City Research Online

City, University of London Institutional Repository

Citation: Pearce, W. (1995). A wind tunnel investigation of the internal pressure dynamics of a single-cell building fitted with a flexible roof and a dominant opening. (Unpublished Doctoral thesis, City, University of London)

This is the accepted version of the paper.

This version of the publication may differ from the final published version.

Permanent repository link: https://openaccess.city.ac.uk/id/eprint/29992/

Link to published version:

Copyright: City Research Online aims to make research outputs of City, University of London available to a wider audience. Copyright and Moral Rights remain with the author(s) and/or copyright holders. URLs from City Research Online may be freely distributed and linked to.

Reuse: Copies of full items can be used for personal research or study, educational, or not-for-profit purposes without prior permission or charge. Provided that the authors, title and full bibliographic details are credited, a hyperlink and/or URL is given for the original metadata page and the content is not changed in any way.

City Research Online: http://openaccess.city.ac.uk/ publications@city.ac.uk

A Wind Tunnel Investigation of the Internal Pressure Dynamics of a Single-Cell Building Fitted with a Flexible Roof and a Dominant Opening.

by

W. Pearce B.Sc. (Hons)

A thesis submitted for the degree of Doctor of Philosophy
in the Centre for Aeronautics, City University, London.

October, 1995

Contents

Acknowledgements

The work reported in this thesis was carried out in the Centre for Aeronautics, City University, London where the author was funded for three years by a departmental research studentship.

The author wishes to acknowledge the technical staff, past and present, within the Centre for Aeronautics, namely Mike Smith, Chris Barber and Keith Harvey, for their invaluable advice and assistance throughout his time at City.

Thanks also to Mr D.M. Sykes for a number of things; instigating an interest in the field of Wind Engineering/Industrial Aerodynamics, reading and criticising the manuscript, and for being so patient.

Declaration

"I grant powers of discretion to the University Librarian to allow this thesis to be copied in whole or in part without further reference to me. This permission covers only single copies made for study purposes, subject to normal conditions of acknowledegement."

Abstract

Wind tunnel tests were conducted in a simulated atmospheric boundary layer on a model of a circular, single-cell building possessing a dominant circular wall opening. The roof of the model was either rigid or made from a flexible membrane material with a variable tension and the internal volume of the model was also adjustable in discrete increments. A total of one hundred and fifty model configurations were investigated; five different roof tensions, three cavity volumes, two windspeeds and five opening azimuth angles.

The local mean external pressure distribution around the model was insensitive to changes in Reynolds number over the range $1.4\times10^5 < Re < 2.5\times10^5$, whereas, the mean internal pressure distributions were self-similar for Reynolds numbers above 1.8×10^5. Reynolds numbers were based upon the diameter of the model and the mean windspeed at roof height and for Reynolds numbers above 1.8×10^5 the mean internal pressures were equal to those measured on the external walls.

Attention was focussed on the steady-state dynamic response of the cavity pressure within the model and its sensitivity to changes in the flexibility of the roof. It was shown that turbulent buffetting present on the external wall pressure spectra was transmitted to the internal pressure fluctuations and that the phenomenon of Helmholtz oscillation, due to resonance of the air contained within the dominant opening, occurred for all the configurations tested.

Increased damping of the Helmholtz mode was effected by increasing the flexibility of the roof, increasing the mean windspeed, increasing the cavity volume and rotating the opening away from the line of the approach flow. Indeed, differences in the magnitudes of the internal and external root-mean-square pressures were attributed to changes in the magnitude of the resonant peak due to Helmholtz oscillation. An apparently universal relationship between the magnitude of the measured spectral response at the Helmholtz frequency and cavity volume scaling was determined.

Comparisons between the measured and predicted magnitudes of the ratio of internal to external pressure fluctuations, using the theoretical approach of Vickery & Bloxham (1992), were satisfactory when the opening was oriented to windward whilst at other azimuth angles the theory overestimated the root-mean-square cavity pressure. However, it was concluded that accurate determination of the empirical loss and inertia coefficients may improve these comparisons.

Notation

a	area; 1/dispersion
c	damping factor
c_o	sonic velocity
d	displacement thickness; opening diameter
f_o	frequency
k	stiffness
k_1, k_2	empirical coefficients
l_{eff}, l_e	effective length of opening
l_o	length of opening
n	frequency
m	mass
p	probability; pressure
p_f	peak factor
p_{at}, p_o	atmospheric pressure
q	dynamic pressure; generalised co-ordinate of roof displacement
r	radius; frequency ratio
t	membrane thickness; time
t_g	period of peak pressure
u_*	friction velocity
x	displacement
y	reduced variate
z	vertical distance
z_o	roughness length

A	area
C_1, C_2	empirical coefficients
C_d	orifice discharge coefficient
C_I	orifice inertia coefficient
C_p	mean pressure coefficient
C_p'	root-mean-square pressure coefficient
D	diameter of wind tunnel model
E	elastic modulus
F	flexibility factor
G_1, G_2, G_3	gain functions
H	height of model; frequency response function
J_o	Bessel function of first kind, zero order
K_a	bulk modulus of air

K_a'	effective bulk modulus
K_b	building bulk modulus
L_x	longitudinal turbulence length scale
M_1, M_2	empirical coefficients
N	no. of sample points
"ORDR"	orifice-resonator dimension ratio
P	probability
Re	Reynolds number
S{n}	power spectral density
S_o	normalised power spectral density at the natural frequency, w_o
T	roof tension
U	mode, mean windspeed
U_{ref}, U_{roof}	mean reference windspeed (roof height of model)
V	cavity volume; flow velocity through opening
a	power law exponent
b	refere to chapter 2
f	azimuth angle of opening
g	ratio of specific heats
l	scale factor
m	mass/area
q	azimuth angle of external pressure; phase angle
r	air density
s	standard deviation
w, W	circular frequency
y	roof mode shape
z	damping factor (as a fraction of critical)

Chapter 1: Introduction & Literature Survey

[1-1] Introduction

The distribution of external pressures over low and high-rise buildings has undergone considerable investigation at both model and full-scale and the results from this research permit the overall wind loads on many different structures to be determined. However, when considering the loads sustained by individual walls, windows or across a roof, then the net load is dependent upon the pressure differential across the individual partition and the magnitude of the internal pressure is potentially as significant as the external loading. Nevertheless, quantification of an internal pressure for the purposes of design is complicated by the variability of the factors which influence the magnitude of the internal pressure. The internal pressure is principally a function of the external pressure distribution (assuming that any mechanical pressurisation by ventilation systems is small or non-existent) which is transmitted to the interior of the building by openings and porosity in the envelope of the building; thus, the area, length, number and location of these openings is important and the designer is faced with the problem of choosing a worst-case loading scenario in order to obtain a conservative estimate of the likely maximum in-service loading. The influence that the location of an opening has on internal pressure and consequently, the net loading across individual walls is illustrated in figure 1.1,

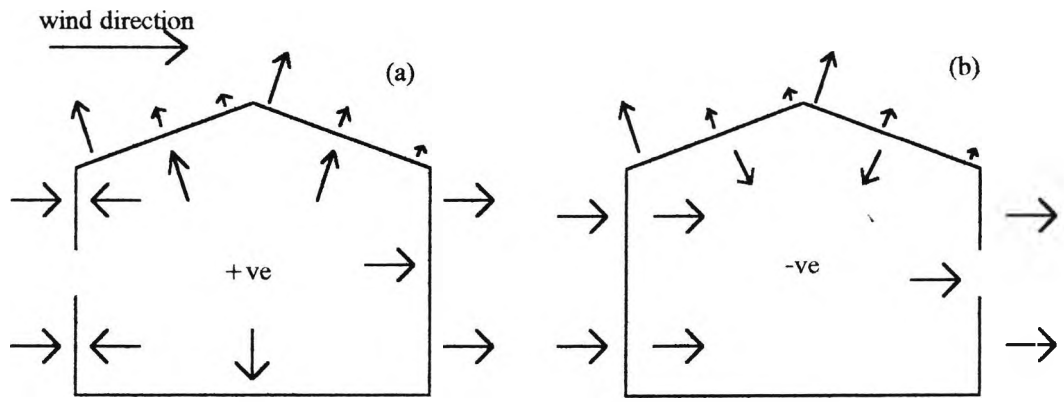

Figure 1.1: Influence of a windward and leeward opening on internal pressure

In addition to the simple examples shown above it has been shown at both model and full-scale that the presence of a dominant opening can bring about a resonant phenomenon called Helmholtz oscillation due to the motion of the mass of air contained within the opening. There are likely to be two different, yet significant, structural loading problems associated with this so-called Helmholtz resonance phenomenon; the amplification of internal pressure fluctuations at the Helmholtz frequency to levels where failure of structural components may occur and/or fatigue

failure of structural components due to the effects of repeated loading and unloading at the Helmhotz frequency even when the amplitudes of the pressure fluctuations are relatively small. The former loading mechanism can be controlled by increasing the damping of the system to minimise the amplitude of the oscillation and/or measures can be taken at the design stage to select an opening geometry such that the natural frequency of the oscillation is out in the tail-end of the wind-spectrum and therefore, unlikely to be excited to large amplitude.

The fatigue loading aspect of Helmholtz resonance is difficult to quantify from the results of wind tunnel experiments but may make a contribution to the failure of certain fixtures and fastenings on full-scale buildings in strong winds, though this is unconfirmed in practice. During a storm it is frequently observed that windborne projectiles cause failure of windward glass cladding thus raising the load on the roof and leeward walls (see figure 1.1) as well as creating conditions which are conducive to the occurrence of Helmholtz oscillation. If the latter does occur then it is not inconceivable that the cyclic loading due to the resonance may result in weakening and even failure of local fixtures and fastenings and thus reduce the ability of the primary components to withstand the already high net loading across certain parts of the building envelope. The possibility for the above as a mechanism for failure is lent some credence by the fact that the more catastrophic failures of major building components during storms occur some time after the inital appearance of a windward opening. In the above scenario it is assumed that after the failure of the windward opening the building envelope remains effectively sealed until the primary failure occurs. In reality it is likely that other local failures may occur, for example failure of a leeward window, which would generally relieve the maximum net loads across the building envelope.

If the building envelope is relatively flexible, then the Helmholtz mode is perceived as a heaving motion of the skin of the structure (not dissimilar to the collapse and expansion of a paper bag if one places a bag over the mouth and breathes). It has been shown that this flexibility can be treated theoretically as an effective increase in the cavity volume and as a consequence, reductions in the resistance of the building envelope to variations in the internal pressure bring about a decrease in the Helmholtz frequency. Although there have been numerous papers concerned with the dynamics of internal pressure inside building cavities and some of these have dealt exclusively with Helmholtz resonance it was felt that there was a need to experimentally quantify the influence that flexibility of the building envelope has on internal pressure variations and this forms the main subject of this thesis.

There are many conventional buildings which are relatively flexible, e.g. industrial prefabricated buildings, but there has also been an increase in the number of civil engineering structures of extended lifespan, which may loosely be defined as a life span in excess of twenty years, which utilise membrane materials as primary or secondary load bearing components. The remainder of this chapter contains a review of the loading characteristics and properties of membrane structures with particular emphasis on buildings which form an effectively enclosed cavity covered by a flexible roof. In addition, the existing body of knowledge concerned with the internal pressure fluctuations of buildings is briefly discussed (more detailed analysis is presented in chapter 2) and finally, the factors affecting the external flow around surface-mounted, low-rise bluff bodies are presented.

[1-2] Membrane Structures in Civil Engineering Applications

[1-2-1] Introduction

In many branches of engineering it would appear that the mass of structures is continually being reduced with more lightweight and flexible components replacing the relatively massive and stiff older designs. This process is certainly true in the aerospace and civil engineering industries. The main reasons for the reductions in structural mass are improvements in the understanding of in-service loading mechanisms, which have lead to improved design procedures, and advances in materials technology, which have improved the range, quality, and material properties available to the structural engineer and architect.

Focussing on composite materials as applied to civil engineering structures it is apparent that one of the significant advances over the past thirty years has been the success of composite fabric membranes as a primary load bearing material in the design of extended life span structures. Indeed the advent of materials such as PVC coated polyester and Teflon coated glass fibre has opened the door to a completely new sphere of architectural design with particular successes in the design of large span lightweight membrane roof structures.

Clearly, thin fabric materials, with an area density of order $1 kg/m^2$, are highly susceptible to static loads caused by wind, rain and snow and by the dynamic loads due to wind alone. The structure must be designed so that under all anticipated loadings the fabric remains in tension and consequently, the membrane must be pretensioned by a cable system or by an over pressure within the building cavity (or some hybrid of the two) which is capable of sustaining the membrane tension over the whole surface of the membrane under all conditions of loading. In addition the

maximum tension induced within the fabric should not exceed the breaking stress of the fabric.

The often unique forms that tensile structures take are generally unsuitable for inclusion in wind loading codes of practice and, therefore, a wind tunnel investigation is required to obtain a realistic estimate of the mean pressure distribution around the structure; the mean pressure coefficient data can subsequently be used as loading terms in computer analyses of mean membrane stress and deflection. However, the inherent flexibility of membrane structures implies that they could undergo relatively large structural deflections compared with the response of conventional buildings such that the deflection causes a significant change in the pressure field on the membrane surface which then feeds back to change the deflected shape of the membrane. This feedback loop could produce an aerodynamic instability that would, at least, increase the fatigue load on the membrane and in the worst case produce membrane stresses in excess of the design values and lead to failure of the fabric material. Aerodynamic instabilities as described above are not generally amenable to theoretical analyses and consequently, the use of an aeroelastic wind tunnel model becomes a viable option for the structural engineer. Nevertheless, construction of an accurately scaled flexible model can be extremely difficult, if not impossible, due to the limitations of material availability, and the modelling requirements need careful assessment (see chapter 2).

One of the more successful applications of civil engineering fabric materials has been in spanning large open areas like sports arenas which can be both physically and mathematically modelled as an enclosed building cavity with vented walls, that represent access points, covered by a flexible membrane roof as shown in figure 1.2. An attractive feature of this particular configuration from the viewpoint of physical modelling is its simplicity because the membrane could be tensioned without the need for modelling a cable support system and no complex cutting pattern is required in order to obtain the correct geometric form of the roof.

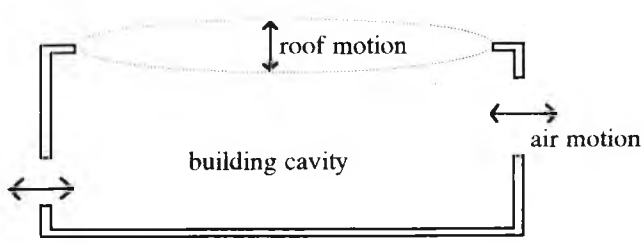

Figure 1.2: Diagram of a vented building cavity with a membrane roof

[1-2-2] Tensile Structures - An Historical Perspective

The use of fabric shelter in the form of tents has been widespread for centuries, however, it is only since the beginning of the twentieth century that applications have been extended to increasingly large architectural forms, mainly as a result of advances in materials technology. The earliest proposal for a pneumatic structure was by Lanchester in 1917 with a patented design for a military field hospital (Dent, 1977). However, it was not until 1950 that Bird designed and produced inflatable, spherical radomes to cover early warning radar antennae for the U.S. Army. The military maintained an interest in pneumatic structures throughout the sixties exploiting their lightweight, low bulk and cubage, ease of handling and logistical support properties (Dietz et al, 1969).

During the fifties and sixties architects like Frei Otto (1967) also began to explore the novel design concepts made possible by membrane materials and in 1967 and 1972 the first and second "International Colloquia on Pneumatic Structures" were held at Stuttgart and Delft respectively. Various aspects of designing with membrane structures were presented at these two Colloquia, but both concluded that more research into the static and dynamic response of the structures to wind loading was necessary. The U.S. Pavilion at Expo'70 in Osaka heightened commercial and architectural interest and was the first glassfibre air-supported structure.

Despite the regulatory limitations placed upon the designer (Parkinson, 1980) and the inherent problems associated with the use of membrane materials such as, fabric tear and fire resistance, concepts for membrane applications in civil engineering have been many and varied ranging from inflatable walkways to the enclosure of city centres (Otto, 1967; Herzog, 1977). Although the latter is probably a long way from realisation there has been considerable success in spanning the roofs of large sports stadia with cable/air-supported hybrid structures, for example the Pontiac Stadium roof in Michigan, the Uni-Dome in Iowa and the Uni of Santa Clara in California (Geiger, 1975). One of the largest cable-tensioned membrane roof structures to date is that of the Haj airport terminal in Jeddah, Saudi Arabia which covers an area of approximately 0.7 square kilometres (Tryggvason et al, 1978).

The codification of data from wind loading research serves to simplify and thus speed up the design process, however, only the more "standard" architectural forms such as cylinders, spheres and their derivatives are suitable for this purpose and the design requirements for air-supported structures of this shape are presented in B.S. 6661. Accordingly, the unusual and often unique designs made possible by membrane materials are likely to require a program of wind tunnel tests in order to quantify the

pressure field around the structure as highlighted by the investigations of Sykes (1992) on rigid models of tensile structures. This procedure will increase the cost of design and delay the construction start date, nevertheless, it is likely that,

> '....due to the following factors; low initial cost, low operating costs, faster erection and erection of the roof occurring simultaneously with other activities below...',

the total cost of the structure will be less than that for a conventional building (Geiger, 1975, discussing the air-supported roof on the Pontiac Metropolitan Stadium).

[1-2-3] Classification of Membrane Structures

The membrane is a flexible surface structure that carries load by developing a two-way tension field and/or tangential shearing stresses; it is unstable, and folds in compression (Schodek, 1980). The tensile state is maintained over the design lifetime in two ways, pre-stressing if the weight of the membrane is smaller than the estimated maximum loads or by internal pressurization. These mechanisms correspond to the building classifications as cable-supported or pneumatic structures respectively. The cable-supported membrane should be distinguished from cable-net constructions because the latter utilise the membrane in a non-structural role as an impervious cover over a load bearing cable net, whereas, the former employs the membrane as a primary load bearing component that is held in tension by a cable framework. Suspended roof systems often comprise a cable-net mesh that is filled in with a relatively heavy covering material, the weight of the roof alone is sufficient to maintain membrane tension for all the anticipated in-service loads over the lifetime of the structure.

Pneumatic structures keep their rigidity by maintaining a pressure differential across the membrane and it is possible to divide pneumatic structures into two groups based upon the magnitude of this differential pressure. The first of these categories is termed air-supported structures and these have been successfully employed as roof structures spanning large arenas (Geiger, 1975). These structures are characterised by a relatively low overpressure, a few centimetres of water is usually sufficient (Dent, 1977), within the building cavity and consequently, the users of the building are in an environment which is above atmospheric pressure. In contrast the second group, termed air-inflated structures, utilise a much larger pressure differential of the order a number of atmospheres (Benjamin, 1982) to inflate a tubular or dual-walled structure which can then be used in a more conventional building role in the form of

inflated beams or arches. Simple examples of the two types of pneumatic structure are presented in figure 1.3.

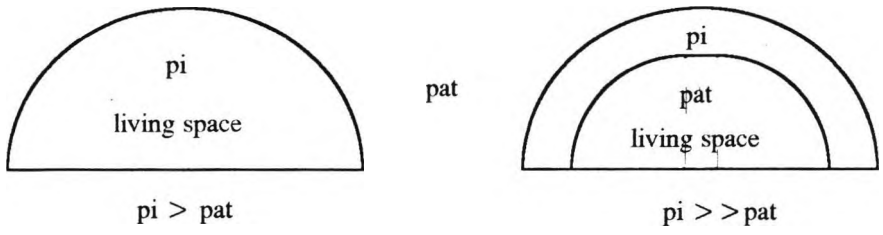

Figure 1.3: An air-supported and air-inflated pneumatic structure.

Pneumatic structures are frequently dome-shaped with only a single direction of curvature apparent over the membrane, as shown in figure 1.3. Structures with single curvature are called synclastic, however, if a tension structure has two directions of curvature over its surface then it is said to be anticlastic. This latter shape is exemplified by the numerous saddle-type geometric forms that appear in the design of cable-supported membrane structures (see Otto, 1967). Large flat areas are generally avoided in design because of the large stresses developed within the membrane to withstand loads that are applied normal to the surface (Benjamin, 1982).

[1-2-4] Properties of Full-Scale Membrane Materials

Generally, a monophase material will not fulfill all the mechanical and resistive requirements necessary for a full-scale membrane structure. Consequently, a composite woven fabric is used as the base fabric which provides stiffness and shear flexibility and this base fabric is coated with a polymer to modify permeability and environmental resistance. A finishing coat may also be applied to the membrane for additional protection. The woven yarn base fibre possesses strength and elongation characteristics that vary with direction and this directionality combined with a non-linear stress-strain curve usually requires that a representative design value for elastic modulus is chosen (Irwin et al, 1979). A selection of the different components currently used to manufacture a membrane along with their relative benefits is presented in Figure 1.4, and Table 1.1 summarises the desired properties of the base fabric, polymer coat and finishing coat.

Stress relaxation characteristics, of which creep is a particular form, are also significant and will result in a reduction of prestress tension over the lifetime of the structure. This problem is alleviated by increasing the prestress loading at the design stage to take account of any creep that will occur or by incorporating a "jack" system

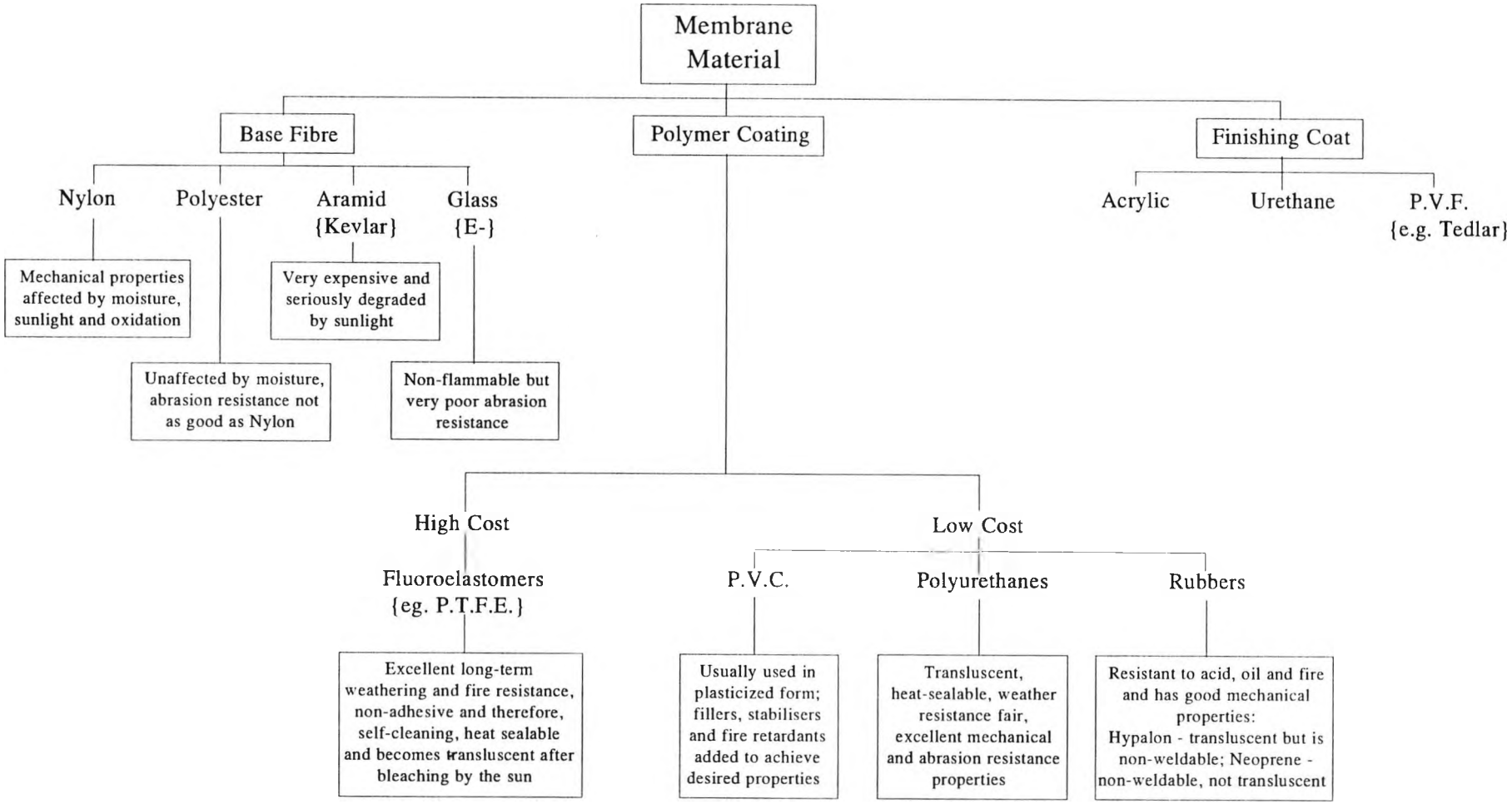

Figure 1.4: Materials for civil engineering membranes

into the structural design so that the tension in the membrane can be periodically increased. Clearly, the latter technique complicates the structure and increases maintenance costs (Benjamin, 1982). Material transluscency and solar reflectivity can be varied by polymer coat modifiers offering economic benefits on daytime lighting and cooling costs respectively (Morrison, 1980).

Base Fabric	Polymer Coating	Finishing Coat
low cost		used as a buffer if polymer coating has limitations eg. prevention of loss of plasticiser
lightweight		
durable		
high tensile strength		
high tensile stiffness		
low shear stiffness		
low susceptibility to ageing, weathering & discontinuous loading	good weather resistance	
resistance to degradation by U.V. light, moisture, biological & chemical attack		
dirt repellant		
negligible permeability to air & moisture, controllable transluscency		
weldable (heat sealable)		
resistant to extremes of temperature & loading		
non-flammable		
capable of erection, dismantling & relocation	able to protect base fabric from abrasive damage	

Table 1.1: Desired design properties of full-scale membrane materials

Reference	Material	m (kg/m^2)	t (mm)	E (GPa)	Tensile Strength (N/m)
Jackson (1983)	Glass/PTFE	1.25 to 1.50	0.8 to 1.0		$1.4x10^5$
Irwin et al (1979)	Kevlar 49/ PVC	1.1 1.1			$1.6x10^7$
Geiger (1975)	Glass/Teflon	4.9	3.0		$3.5x10^4$ to $1.75x10^5$
Ansell (1980)	Nylon Polyester Aramid Glass	mass increases on moving from top to bottom		5.5 13.8 62.1 68.9	

Table 1.2: Typical full-scale membrane properties

Two membrane materials dominate the field of fabric structures at the present time; P.V.C. coated polyester and Teflon/P.T.F.E. coated glassfibre. The glass/P.T.F.E. has proven very successful for extended lifespan structures, defined as a design lifespan in excess of twenty years (Jackson, 1983), because it is both durable and self-cleaning (Geiger, 1975; Morrison, 1980). Unfortunately, it is also expensive, brittle in failure, suffers if the structure is demountable and is less forgiving of cutting pattern errors because of its higher shear rigidity (Parkinson, 1980; Dumbleton, 1986). The polyester/P.V.C. system is chiefly used for temporary or short-life applications and is significantly cheaper (Parkinson, 1980). A list of some of the materials and properties used in constructing pneumatic structures, circa 1972, can be found in Dent (1977) and, in addition, typical full-scale values of membrane properties are presented in table 1.2. It should be noted that for a monophase material the mass per unit area of the membrane is a linear function of membrane thickness.

[1-2-5] Loading of Membrane Structures

The atmospheric climate is of great importance when considering the likely mechanisms for loading a membrane structure. Both rain and snow can cause difficulties due to accumulation of either on the membrane surface and the risk of localised buckling because of the increase in deadweight. Snow loading is not a serious design problem because generally the snow will slide off curved surfaces under its own weight or melt due to heat loss through the membrane, however, the difficulties associated with the static problem of "ponding" rainwater have received attention (Malcolm & Glockner, 1981). Consequently, the dynamic effects due to wind are the major concern for designers and wind loading criteria should be accurately known if the need for excessively complex and heavy cable systems and prohibitively expensive fabrics is to be avoided.

[1-2-6] Wind Tunnel Investigations on Aeroelastic Models of Membrane Structures

It is convenient to discuss the existing papers concerned with the results of experiments on aeroelastic models of membrane structures in the following general groups,

- tests on air-supported membrane models (generally spherical or cylindrical)
- tests on models of structures with hanging/suspended roofs
- design studies on proposed "real" structures

[1-2-6-1] Air-Supported Membranes

Early wind loading tests on flexible models of air-supported buildings seem to provide much of the information on which B.S. 6661 is based e.g. the tests of Beger and Macher (1967) and Niemann (1972) which were conducted in uniform, low turbulence flows. However, the results of wind tunnel tests on rigid models of dome shaped buildings by Nakayama et al (1986) in which the mean pressure distribution in three different approach flows (uniform, low turbulence; grid generated turbulence; sheared, turbulent flow) were measured seem to imply that in a uniform, low turbulence flow the maximum mean suctions tend to be higher than those measured in flow simulations more representative of the atmospheric boundary layer. This effect was most pronounced for domes where h/d (defined in figure 1.5) was greater than 0.5 and reductions in h/d generally caused a reduction in the magnitude of the loading over the whole roof. Tests by Kawamura & Kiuchi (1986b) showed that the maximum mean suctions on rigid dome-type models in a simulated atmospheric boundary layer approach flow were similar in magnitude (around -0.7 to -0.9 at the top of the dome) to the values reported by Nakayama et al (1986).

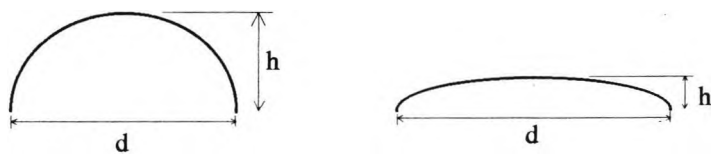

Figure 1.5: Definition of the height-to-diameter ratio

B.S. 6661 permits the minimum inflation pressure to be determined as a function of the design value of the dynamic pressure, q, for different dome shapes and dome-cylinder combinations; the design tensions induced within the membrane are also expressed in terms of q and a building dimension. Newman et al (1984) derived an expression for the minmium internal gauge pressure of spherical inflated domes in terms of the height-to-diameter ratio and the skin friction at the ground, τ_w, where p_{imin} is equal to $180(h/d)\tau_w$ and h and d are defined in figure 1.5.

Regarding the effect that membrane deflection has on the pressure distribution over the models, B.S. 6661 states that,

> "....In general, deflection results in lower wind pressures but higher wind suctions than those that would be obtained on a rigid structure of the same initial shape. The lower the inflation pressure, the higher the wind suction becomes....'

The above is confirmed by the results of Srivastava et al (1984) on a hemispherical inflated membrane model where reduction of the pressure ratio, p_i/q, caused the peak suction on the "along-wind" meridian to double in magnitude and move some 30° toward the windward face. Srivastava et al (1984) also showed that the deflection of the membrane, at a number of points over the surface of the membrane, followed a near exponential decrease as the internal pressure ratio, p_i/q was increased. Similar behaviour was reported by Kawamura & Kiuchi (1986b) on wind tunnel models of low-rise, air-supported buildings.

Kawamura and Kiuchi (1986 (a&b)) reported that increases in internal pressure caused the natural frequency of the building to increase because of the increase in pneumatic stiffness, a result that was subsequently confirmed by Mataki et al (1988) who added that their medium sized field model (25mx25m plan dimension) of a building with an air-supported roof did not vibrate in volume displacing modes. In addition, both of the above teams of investigators reported that increases in the internal pressure caused the damping of the membrane to be reduced. This is most likely due to a reduction in the component of damping due to acoustic radiation, ζ_a, which is strongly dependent upon the volume of air displaced by the membrane movement (assuming the vibrating membrane to be like an acoustic source (see chapter 2)); increasing the internal pressurisation of the building increases the pneumatic stiffness and thus reduces membrane deflections.

Finally, the most recent investigation on a model of a hemispherical air-supported building was conducted by Kassem & Novak (1992) where the response of the internal pressure and the membrane was monitored in a series of atmoshperic boundary layer simulations for variations in the internal pressurisation, gradient windspeed and internal volume. They found that generally rms deflections of the membrane were small compared with mean deflections and that increasing the mean internal pressure caused a reduction in the rms internal pressure fluctuations as did reducing the internal volume of the model (though sensitivity of the fluctuations to the volume change was not as great as the sensitivity to the internal pressurisation).

[1-2-6-2] Suspended Roofs

A section through a suspended or hanging roof structure is shown in figure 1.6 and the plan of this building is typically rectangular. Uchiyama et al (1979) showed that in a "smooth" approach flow (i.e. low turbulence, uniform velocity from left to right in figure 1.6) there was separation from the leading edge of the building and a dominant periodicity in the free-shear layer which grew from this separation point. However, this regularity in the velocity fluctuations was not apparent in the

separation bubble which filled the region beneath the shear layer. Nevertheless, when a membrane roof was fitted to the models the response of the roof was categorised into three distinct types of motion, which were bounded by quite distinct mean windspeeds which were in turn dependent upon the sag ratio, S/L.

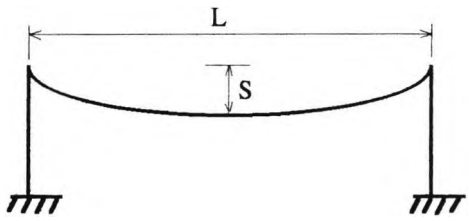

Figure 1.6: Diagram of a suspended/hanging roof structure

A series of papers by Kimoto and Kawamura (1983, 1986) and Kawamura and Kimoto (1979) on wind tunnel models of suspended roof structures, which were again predominantly conducted in a uniform, low turbulence approach flow, revealed an aerodynamic stability in the response of the roof which was characterised by a change in the amplitude of the dynamic component of the deflection of the roof as shown in figure 1.7. The velocities U_s and U_p were defined as the starting and peak windspeeds at which the instability began and reached a maximum respectively. Experiments conducted on a medium-scale field model under the action of a real wind showed similar characteristics to the wind tunnel models, though scatter in the results was large. Although of interest, the results described in the above series of experiments occurred in somewhat idealised circumstances because it was also reported that increases in the turbulence intensity of the approach flow reduced the peak amplitude and addition of a simple cable truss along the edges of the roof practically eliminated the instability.

Matsumoto (1983, 1990) also reported an aerodynamic instability in the first asymmetirc mode of model of suspended membrane roofs structures under the action of a "smooth" approach flow (in a turbulent shear flow the oscillation did not appear). Matsumoto (1983) determined that the self-excited oscillation occurred at a reduced velocity, U/fL, of around 1.6 and later (Matsumoto, 1990) proposed a mechanism for the instability which was based upon a vortex produced at the upstream edge of the roof, through fluid elastic interaction between the roof motion and the flow, being convected downstream at a speed roughly equal to the mean speed of the approach flow.

Finally, results presented by Uematsu and Uchiyama (1986) on the response of an hyperbolic-paraboloid roof to the action of wind also showed evidence of an

aerodynamic instability which was highly dependent upon the wind incidence. Two approach flows were used, one was uniform and of low turbulence (0.5%) whilst the other had a turbulence intensity of 6% (it was not clear whether this flow was sheared). The instability was dependent upon the reduced velocity, but was also mode dependent in that the first instability, which occurred at a relatively low value of reduced velocity, induced oscillations in the first asymmetric mode and subsequent increases in the reduced velocity produced instabilities in higher modes. It was noted that tests on a rigid model to measure the surface pressure fluctuations showed no dominant periodicity at any location for any wind direction.

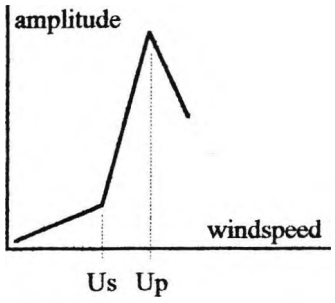

Figure 1.7: Typical behaviour of roof amplitude as a function of windspeed.

[1-2-6-3] Tests on Models of Prototype Structures

A number of investigations involving aeroelastic models of prototype membrane structures have been carried out by Tryggvason & Isyumov (1977), Tryggvason et al (1978), Irwin et al (1979) and Kind & Wardlaw (1981). The scaling requirements which were complied with in each of the above tests were discussed in detail in the relevant reports and will be summarised later in chapter two. The first of the above investigations was performed on a 1/330th scale model of the proposed Dalhousie sports stadium which had an air-supported roof. The model was completely sealed and the results from the wind tunnel tests showed that the roof was aerodynamically stable for all the wind directions and speeds that were tested. The response of the roof was, in the main, due to buffetting of the wind with no large resonant components. The mean deflection of the roof was generally upward with a maximum mean deflection at the centre of the roof which is in qualitiative agreement with the rigid model results on dome buildings by Nakayama et al (1986).

Tests on an aeroelastic model of a part of the roof of the Haj airport Terminal in Jeddah, Saudi Arabia (Tryggvaon & Isyumov (1978)), showed a similar broad-band response of the fabric to buffetting by the wind with no apparent aerodynamic instabilities. All the measured responses, membrane deflection and bending moments

and strains in the supporting pylons, showed fairly smooth, monotonic increases with windspeed.

Tests for the retractable roof on the Montreal Olympic Stadium, which was a cable-supported roof with no internal pressurisation, were reported by Irwin et al (1979) and Kind & Wardlaw (1981). As in the other investigations, no aerodynamic instability was found and deflections and forces on the roof and cable system were found to increase monotonically with windspeed. It was noted by Irwin et al (1979) that excitation of the membrane by acoustic noise within the circuit of the wind tunnel was responsible for much of the measured roof response. The importance of carefully selecting the most relevant scaling parameters when modelling an aeroelastic building was highlighted in the discussion on scaling requirements by Kind & Wardlaw (1981) (see chapter two).

In reality most buildings require openings for access and ventilation and thus the use of an essentially air-tight model, with an additional and large pneumatic stiffness due to the air contained within the cavity of the building, is not a good representation. Although the results reported by Elashkar & Novak (1983) and more recently by Novak & Kassem (1990a; 1990b) and Kassem & Novak (1990) were conducted on relatively idealised representations of buildings with membrane roofs which had no supporting cable network, it could be argued that these models were more realistic because they attempt to investigate the effect that venting of the building has on the response of the membrane. Kassem and Novak (1990) reported that the response of the roof of their model, which was similar to that shown in figure 1.2, under zero wind conditions was dependent upon the total area of the openings and could be modelled as a two-degree-of freedom system with a fundamental mode due to Helmholtz resonance and a second mode attributed to the "kettledrum" frequency (see Kinsler & Frey, 1962). The investigations of Novak & Kassem traverse a gap between the response of membranes to wind and the role played by internal pressure fluctuations on the motion and loads across both membrane and/or the walls of a building. Clearly, the motion of both the building envelope and the flow through an opening somewhere in the walls of the structure are coupled by the internal pressure which leads us onto the next section of this review.

[1-3] Building Internal Pressures

The internal pressure within a building is dependent upon the size and distribution of dominant openings as well as the relative distribution of background porosity, the magnitude of which is dependent, in general terms, upon the function and age of the building. The recommendations for mean internal pressure in the British Standard

Code of Practice, CP3: Chapter V: Part 2: 1972, are dependent upon the relative permeability of the walls of a building and the relative location of any dominant openings. However, if the permeability is not known then there are two cases to consider,

- if the probability of a dominant opening occurring is small then Cp_i should be taken as the more onerous of +0.2 or -0.3
- if a dominant opening is likely to occur then $Cp_i = 0.75xCp_e$, where Cp_e is the external pressure coefficient at the location of the opening.

The significance of distributed porosity on the internal and external presssure distributions of low rise buildings in two types of simulated atmospheric boundary layer flows (open country and urban) was investigated by Stathopoulos et al (1979). The results were quite extensive, but the main points relating to internal pressure may be summarised as

- the internal pressure was dynamic though the magnitude of the fluctuations were smaller than those measured on external walls
- the spatial correlation of the fluctuations within the building cavity was high except in regions very near dominant openings.
- the largest internal pressure coefficients occurred with openings to windward but for small windward openings combined with a large leeward porosity the internal pressure became negative
- configurations with an impermeable windward wall and openings in the lee of the building had internal pressure coefficients that were generally insensitive to the size of the openings and the porosity
- generally, with openings greater than 20% of the wall area the internal pressure coefficient was effectively independent of further increases in opening size.

It was also stated that comparison of spectral measurements of the internal and external pressures on the models showed a high correlation between the two, though typical spectra were not presented; there was no report of any resonant peaks on the internal pressure spectra.

Holmes (1979) was the first investigator to report that a rigid-walled wind tunnel model with a dominant windward opening, under the action of a turbulent wind, sufferred from resonance of its internal pressure. The cause of this resonance was

attributed to the inertia of the air contained within the opening which was excited by buffetting of the turbulence in the incident wind. The system was theoretically described by treating the building as an Helmholtz resonator of classical acoustics (eg. Kinsler & Frey, 1962). Although the resonance was apparent in the results, Holmes (1979) concluded its contribution to the total r.m.s. internal pressure fluctuation was relatively small because it occurred out in the tail-end of the wind spectrum and that in reality flexibility of the walls was likely to have a significant effect by increasing damping and thus reducing any oscillation. (This latter point seemed to be confirmed by the full-scale measurements of Fahrtash & Liu (1990) on three different structures, a garage, a sports arena and an observatory). Nevertheless, the frequency at which the Helmholtz oscillation occurs is dependent upon the volume of the internal cavity as well as the geometry of the openings so that for certain types of building the resonant frequency may lie within the higher energy part of the wind spectrum.

This hypothesis appears to be corroborated by the full-scale measurements on an industrial barn at A.F.R.C., Silsoe (Hoxey, 1991; Robertson, 1992) where a periodic heaving motion of the structure was observed when the door of the barn was left open. Spectral division of the internal pressure fluctuations (door open) by those measured on the external walls of the building, over a common bandwidth, produced gain functions with a peak at a frequency of around 1.0Hz which was attributed to Helmholtz resonance. This peak was not apparent in the gain of the internal pressure fluctuations that was obtained when the barn door was closed. Robertson (1992) concluded that the effect of the resonance needed to be taken into account during the design process because of the significant increase in peak stresses that could occur.

Liu & Rhee (1986) described results obtained from a rigid wind tunnel model of a low-rise building with a single dominant opening of square cross-section (and dimensions of 10, 20, 30 and 40mm) located in the centre of either the windward or leeward wall. A resonant peak due to Helmholtz oscillation was measured on the internal pressure spectra even when the approach flow was of uniform velocity distribution with a longitudinal turbulence intensity of around 1%. There was also evidence that increasing the size of the dominant opening enhanced the intensity of the resonance as well as raising the frequency at which the oscillation occurred. This result was in agreement with the conclusions of Holmes (1979) who reported that increases in the size of the opening reduced damping. Liu & Rhee (1986) also addressed the problem of vortex shedding from an upstream body impinging upon a windward opening of a building and found if the frequency of the shedding was near that of the Helmholtz frequency, then a large amplitude double resonance occurred,

i.e. an excitation force with high energy near the natural frequency of the building cavity produced large oscillations of the internal pressure.

Vickery (1986) also considered the effect of internal pressure fluctuations with a dominant opening assuming the equations of Holmes (1979) but incorporating the influence of building flexibility into an effective cavity volume which was dependent upon the ratio of the building to air bulk moduli, K_a/K_b, (see chapter 2). Estimates for the bulk modulus ratio were around 0.2 for stiff buildings but nearer five for low, large span structures. Vickery concluded that generally, resonant amplification of the internal pressure would be insignificant except for large, flexible structures.

A loading problem related to the appearance of a windward opening is the maximum internal pressure attained shortly after the opening appears, and more specifically the question of whether this so-called overshoot phenomenon will exceed the peak pressures which occur in the building cavity during the steady-state oscillations. This problem was considered theoretically by Liu & Saathoff (1981, 1982) and later by Stathopoulos & Luchian (1989) who conducted a series of wind tunnel experiments on rigid models where the sudden appearance of windward opening was simulated. Calculations to find the maximum (overshoot) internal pressure after a breakage as a function of cavity volume, wind speed and size of opening showed that the maximum induced internal pressure was increased if the area of the opening was increased or the speed of the incident wind or the volume of the cavity were reduced. Furthermore, from the point of view of building design, it was found that in all the configurations tested the peak internal pressures that occurred shortly after the appearance of the opening (i.e. during the transient phase of the response of the internal pressure) was exceeded by the peak pressures attained during the steady-state internal pressure fluctuations.

Vickery & Bloxham (1992) also studied the transient and steady-state internal pressure dynamics after the sudden occurrence of a single windward opening on a rigid-walled model. Both the peak pressure during the steady-state fluctuations and the maximum overshoot pressure attained during the transient phase were found to reduce as the background leakage was increased. This implied that the theoretical predictions of overshoot for a rigid building were conservative and should be considered during the design of a building (the relevant theory will be summarised in chapter 2). Finally, mention will be made of the theoretical analysis by Harris (1990) where the relation between an unsteady external pressure and the internal pressure within a building was investigated; however, the inertia of the air within the openings was omitted in order to simplify the problem so that any resonant effects were neglected.

The following section will summarise the salient features of the flow around circular cylinders with emphasis on more recent results from tests on surface-mounted circular cylinders in simulated atmospheric boundary layer flows.

[1-4] The Flow Around Surface-Mounted Bluff Bodies

[1-4-1] Sensitivity to Reynolds Number

The flow around a bluff body is a highly complex phenomenon that is a function of the shape of the body and the nature of the flow in which the body is immersed. Sharp-edged bodies have associated flow patterns that are generally insensitive to changes in Reynolds number over a wide range because separation is fixed by the geometry of the bodies. However, flow separation from spherical, circular or gently curving surfaces is greatly influenced by the Reynolds number, surface roughness and the turbulence content of the incident airflow. The Reynolds numbers associated with the flow around full-scale buildings are typically of the order 10^6 to 10^8, whereas, the maximum attainable Reynolds numbers in wind loading tests on models are typically of the order 10^5 to 10^6, largely because the dimensions of the model are restricted by tunnel blockage constraints. Nevertheless, it is generally accepted that empirical determination of a mean pressure distribution over the surface of the model that is broadly unchanging with increases in the Reynolds number is sufficient to ensure that the test results are applicable for full-scale design purposes.

Roshko (1961) concluded that the dependence on Reynolds number of the mean drag coefficient, and hence the mean pressure distribution, of a smooth circular cylinder in a uniform, low turbulence (often referred to as smooth) flow was due to the form of the boundary layer around the cylinder. At "subcritical" Reynolds numbers the boundary layer remained laminar and separated from the windward side of the cylinder, some 70^o aft of the windward generator, to produce a wide wake with an associated high drag. At higher Reynolds numbers flow conditions were described as "supercritical" and shortly after separation of the laminar boundary layer the free-shear layer became turbulent and reattached to the surface of the cylinder; the reattached turbulent boudary layer was more capable of withstanding the adverse pressure gradient around the leeward side of the cylinder and did not separate until around 120^o from the windward generator. At still higher Reynolds numbers Roshko (1961) defined a "transcritical" flow regime which was characterised by purely turbulent separation of the boundary layer at around 100^o to 110^o. The dependence of the drag coefficient on Reynolds number is shown in figure 1.8 (from Panton (1984)), whereas figures 1.9 show the form of the different separation processes as depicted by Basu (1985).

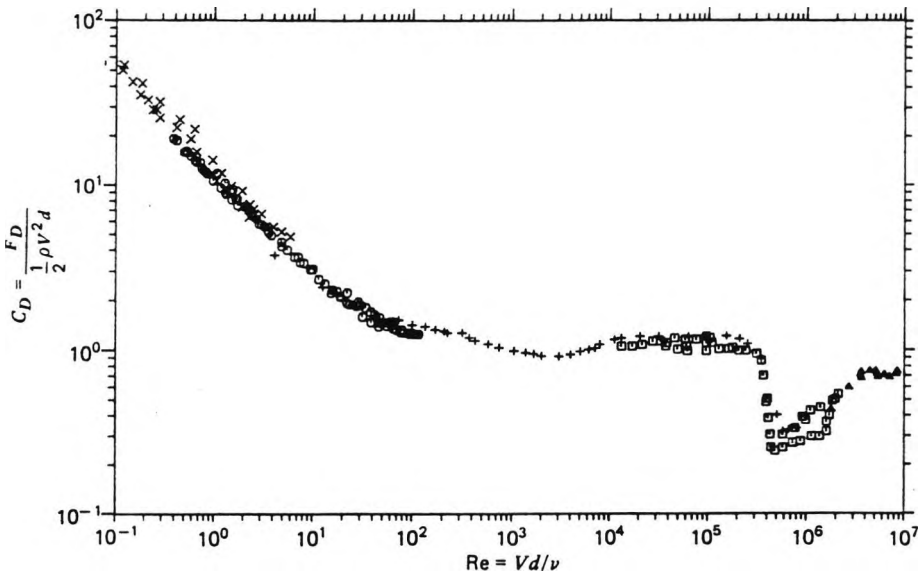

Figure 1.8: Reynolds dependence of the mean drag coefficient of a circular cylinder.

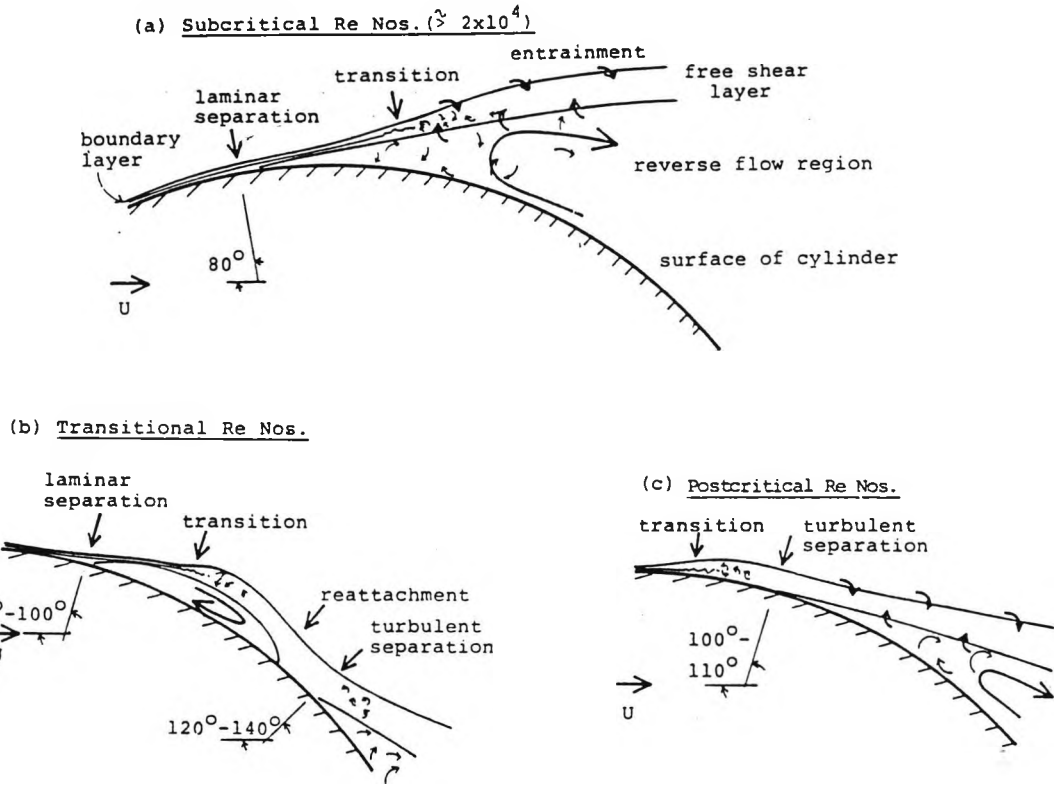

Figure 1.9: Flow separation from a circular cylinder at different Reynolds number (after Basu (1985))

[1-4-2] Sensitivity to Free-Stream Turbulence

Bearman and Morel (1983) present a detailed discussion of the effect of free-stream turbulence (F.S.T.) on a variety of bluff body flows and concluded that there were three basic mechanisms by which F.S.T interacts with the overall mean flow

- accelerated transition to turbulence
- enhanced mixing and entrainment
- distortion of the F.S.T. itself by the mean flow

and that the overall effect of F.S.T. was likely to be some combination of the three mechanisms. However, the only generalisation that was drawn about the influence of F.S.T. was that if some effect was measured, then increases in the intensity of the turbulence increased the effect.

A good example of this latter point is provided by a selection of the results from wind tunnel tests on a smooth, two-dimensional circular cylinder in uniform flow fields of different turbulence intensities, presented by Cheung & Melbourne (1983). They reported that increases in the F.S.T. from 0.4% to 9.1% reduced the mean minimum pressure and increased the base pressure at subcritical Reynolds numbers but had the reverse effect under supercritical conditions. The consequence of the above results on the mean drag coefficients are clearly shown in figure 1.10. Increases in the turbulence intensity of the approach flow effect a drop in the mean drag coefficient at a lower Reynolds number (i.e. induce an increase in the effective Reynolds number of the flow), but the high Reynolds number flow thus attained is different from that found around a smooth cylinder in a "smooth" flow. Similar limitations should be noted when the surface of the cylinder is artificially roughened as shown in the early results of Fage & Warsap (1929) (see figure 1.11 (from Szechenyi, 1975)). Turbulence length scales were kept at approximately constant values by Cheung & Melbourne (1983) and the conclusions in table 2 of Bearman & Morel (1983) seemed to imply that the influence of length scales on the flow around circular cylinders is unclear.

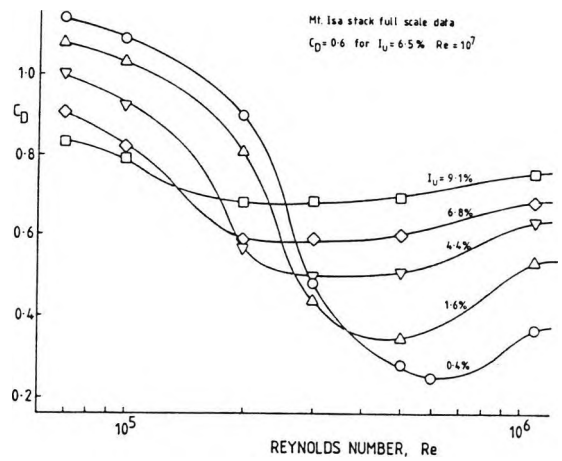

Figure 1.10: Influence of approach flow turbulence on the mean drag coefficient of a circular cylinder over a range of Reynolds numbers.

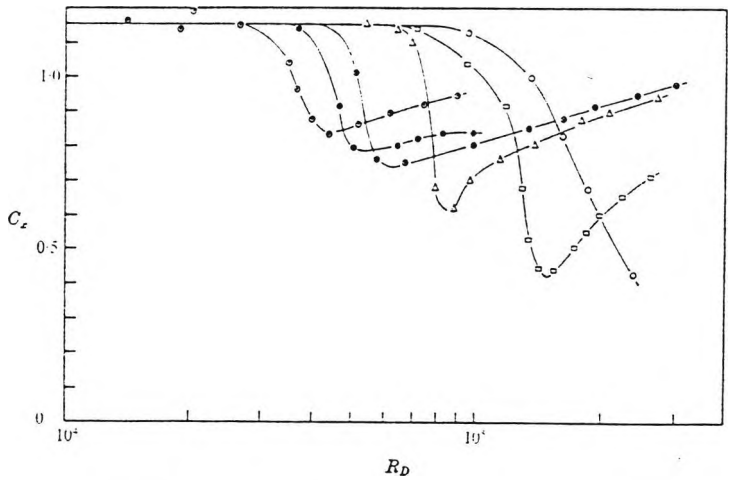

Fage & Warsap's results for the steady drag coefficient. ○, smooth cylinder; □, $\delta/D = 2 \times 10^{-3}$; △, $\delta/D = 4 \times 10^{-3}$; ▽, $\delta/D = 7 \times 10^{-3}$; ●, $\delta/D = 9 \times 10^{-3}$; ▽, $\delta/D = 2 \times 10^{-2}$.

Figure 1.11: Influence of surface roughness on the mean drag coefficient of a circular cylinder for a range of Reynolds numbers.

[1-4-3] Sensitivity to Turbulence Length Scale

The theory of Hunt (1973) states that the presence of a body in an isotropic turbulence field will cause a disturbance of the turbulence on the upstream stagnation line as the body is approached and the nature of this disturbance is dependent upon the scale of the turbulence. As L_x/D (where L_x is the longitudinal length scale and D the plan dimension of the body) tends toward infinity the flow behaves quasi-statically and the turbulence intensity diminishes as the body is approached, whereas, L_x/D tending toward zero brings about an amplification of the intensity of turbulence as the body is approached. This theory has been used by a number of investigators, e.g. Lee (1977), to explain the empirical dependence of the base pressure on the length scales measured for cylinders of rectangular planform (see figure 1.12).

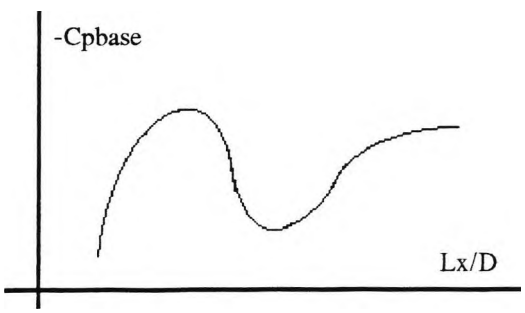

Figure 1.12: Influence of length scale on base pressure behind a rectangular cylinder (after Lee, 1977)

Flow separation from the windward face of the cylinder reattaches to the sides of the body because amplification of the intensity at small length scales causes an increase in the entrainment of the shear layer. The flow remains attached until the trailing edge of the cylinder is reached whereupon it again separates and the unstable free shear layers eventually roll-up to form wake vortices some distance downstream of the body. The further away these vortices form the higher is the base pressure. Larger length scales diminish the turbulence intensity around the body so that the shear layers separating from the front face will have a larger radius of curvature and eventually roll-up a short distance downstream of the leeward face of the cylinder so that the base pressure is correspondingly low. Although the above discussion strictly applies to a cylinder of rectangular cross-section it is possible that similar trends are apparent on circular bodies, however, this author knows of no studies which show that this is the case.

[1-4-4] Flow Around Surface-Mounted Circular Cylinders

Attention will now be focussed on the results of recent studies which deal with more "realistic" representations of wind loading on wind tunnel models of silos and storage tanks of circular cross-section. The flow around these surface mounted bodies is complicated by the formation of horseshoe vortices around the base of the buildings as well as the flow "up-and-over" the free ends, indeed for cylinders of low aspect ratio it is likely that these three dimensional flow phenomena will interact so that the features common to two dimensional flows are suppressed altogether. Holroyd (1983) presents the results of a comprehensive study into the flow field around a circular cylinder of aspect ratio, height to diameter, 0.2 and figure 1.13 is an interpretation, by Holroyd, of the flow around the cylinder.

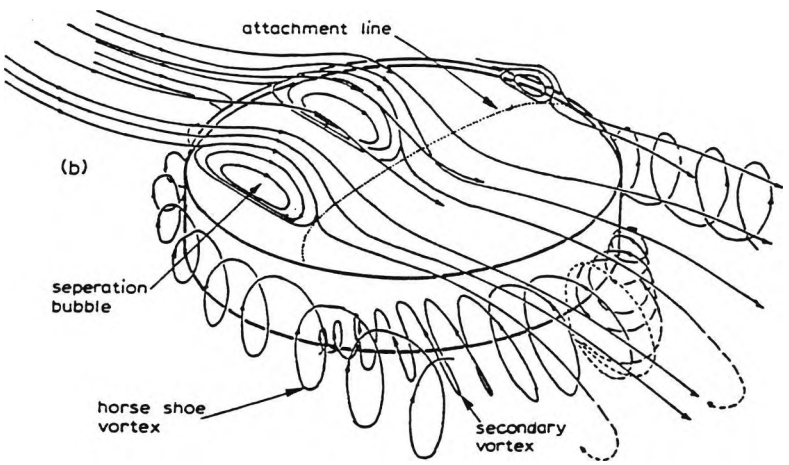

Figure 1.13: Flow around a low aspect ratio, surface mounted circular cylinder

The boundary layer in which the tests were conducted was representative of open countryside and the length scale ratio, L_x/D, was 0.75. Tests were conducted at a Reynolds number of 1.65x105. The flow over the roof separated at the leading edge and reattached approximately D/10 upstream of the centre of the of the roof. It was noted that the pressure over the roof was negative and that the pressure gradient in the along-wind direction was also negative so that the attached turbulent boundary layer which grew over the rear of the roof was in an adverse pressure gradient. The pressure on the vertical walls of the cylinder did not exhibit a constant pressure wake region for azimuth angles greater than 130^o, typical of two-dimensional studies, but instead steadily recovered to a base pressure coefficient of around -0.2. This result implied the existence of the secondary vortex shown in figure 1.13. The root-mean-square pressure coefficients reduced from around 26% at the front stagnation point to around 12% in the base region.

The Reynolds numbers of the tests reported by Sabransky & Melbourne (1987) ranged from $1.0x10^5$ to $3.0x10^5$ and were shown to be supercritical, i.e., the pressure distribution around the walls of the cylinders was insensitive to Reynolds number over this range. The boundary layer was again representative of open country terrain with a turbulence intensity at roof height of 15%. Cylinders of aspect ratio 1.16, 0.78 and 0.66 were tested and the main conclusion from the pressure distributions on the vertical surfaces of the cylinders was that the models were completetly enveloped in a three-dimensional flow so that the flow behaviour was not equivalent to that observed on two-dimensional models.

Finally, MacDonald et al (1988) reported that Reynolds number independence was achieved for Reynolds numbers greater than $1.0x10^5$ in an open countryside boundary layer simulation with turbulence intensity of aound 15% at roof height. The aspect ratios of the cylinders ranged from 0.5 to 2.0 and it was clear that an increase in the aspect ratio brought about an increase in the maximum mean suction (this was also evident in the results of Sabransky & Melbourne (1987) (see also figure 5.3)). The vertical change in the mean pressure distribution around a cylinder of aspect ratio 1.0 is shown in figure 1.14. The results clearly show the effect of the shear in the approach flow, but significantly it should be noted that the uppermost measuring station ($z/H=0.94$) shows a steady pressure recovery around to the base region. MacDonald et al were able to distinguish three regions up the height of the cylinder such that the middle region exhibited flow characteristics which were two-dimensional in nature.

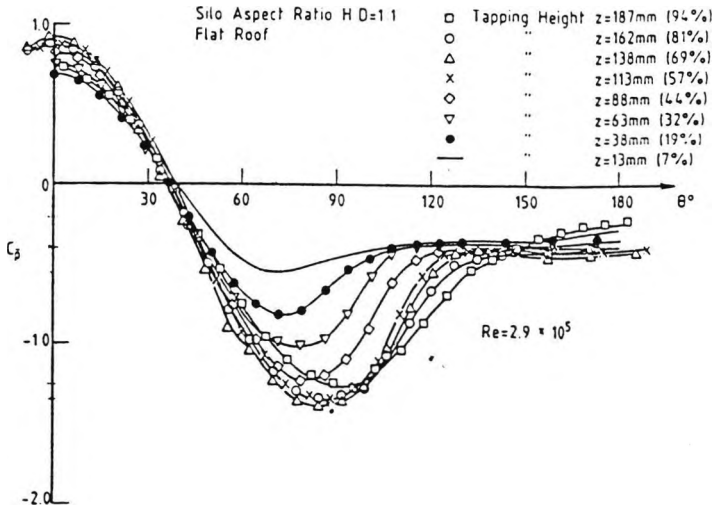

Figure 1.14: Mean pressure distribution around the circumference of a circular cylinder at different heights up the cylinder.

[1-5] The Scope of this Thesis

A number of wind tunnel investigations to quantify the wind loading on rigid models of tension structures have been conducted at City University (e.g. Sykes, (1992)). In order to complement and expand on the experience gained during these investigations a survey of the existing literature concerned with wind tunnel tests on aeroelastic models of tension sturctures was instigated with a view to defining a research programme from the results of the survey (sections 1-2, 1-3 & 2-3).

It transpired that one of the more successful applications of membrane materials in civil engineering was in covering large span arenas but as reported by both Novak & Kassem (1990) and Vickery & Georgiou (1991) significant dynamic interactions between the motion of the roof and the internal pressure was possible if these structures were vented. Indeed, the resonant phenomenon of Helmholtz oscillation, first reported by Holmes (1979) on a rigid model of a conventional building, occurred in a form that was modfiied by the flexibility of the roof. Vickery (1986) extended the original analysis of Holmes (1979) to include the effects of flexibility in the building envelope of more conventional but flexible buildings. Vickery (1986) stressed that the analysis was not suitable for membrane roof structures but, unfortunately, precise limits on the range of applicability of the analysis were not defined.

As a result, there appeared to be a need to quantify the effect that variations in the flexibility of the building envelope had on internal pressure fluctuations. An idealised building could be tested comprised of a single-cell cavity with a single dominant

opening and an envelope of variable stiffness representing a range of building types from the more conventional (stiff) to the more exotic (flexible). The simple drum-type model of Novak & Kassem (1990) was well-suited to this purpose and a design based upon that used by these investigators was manufactured according to the description presented in chapter 2.

Preliminary free-vibration tests on the model were conducted in still-air (c.f. Novak & Kassem (1990)) in order to quantify the damping of the Helmholtz mode and relate the free-vibration frequency of the isolated membrane roof to the corresponding bulk modulus ratio, K_a/K_b, of the building as defined by Vickery (1986). These data are reported in chapter 4.

When a building is submerged in a boundary layer flow then the changes in internal pressure are primarily a function of the external pressure distribution. The pressure field that exists adjacent to a dominant opening is particularly significant because the opening provides a relatively direct connection to the internal cavity. Measurement of parameters such as the mean, r.m.s. and spectra of the external pressure quantify the excitation force for the internal pressure fluctuations. For the model used in this investigation these quantities are discussed in chapter 5.

In chapter 6 the magnitude of the mean and dynamic components of the cavity pressure are presented for changes in the Reynolds number of the external flow, cavity volume, azimuth angle of the dominant opening and roof flexibility. When these results were compared with those of chapter 5 a number of inferences were drawn about the form of the cavity response in the frequency domain. These inferences were corroborated by the spectral data of chapter 7 where the sensitivity of the magnitude of the resonant peak due to Helmholtz oscillation to the physical changes listed above was summarised.

As shown in figure 1.1, the magnitude of the mean internal pressure is important when estimating the net loading across individual walls and roof surfaces. However, for the case of a single-cell building with a dominant opening the rate at which the external pressure fluctuations adjacent to the opening are transmitted to the cavity is high so that relatively large peak internal pressures may also occur. Consequently, an extreme value analysis of the cavity pressure data was conducted for gusts of five different sizes corresponding to 0.003s, 0.006s, 0.012s, 0.024 & 0.048s at model scale. The sensitivity of the extreme value parameters of the internal pressure, namely the mode and dispersion, to changes in the physical configuration of the model were discussed and summarised.

[1-6] Summary

A brief introduction to the main areas of research which the author believes are pertinent to the work presented in this thesis is given. Although the coverage is somewhat scant in certain areas more detail will be given in subsequent chapters where the specific results of previous investigations are directly relevant to the findings of the present study. The purpose of this chapter was interpreted as an introduction to results presented in later chapters.

Chapter 2: Experimental Models, Scaling Requirements & Theoretical Analysis

[2-1] Introduction

This chapter is divided into three sections. Initially, details of the two physical models used in the experimental work will be presented. This will be followed by a discussion of the physical scaling requirements necessary for conducting a wind tunnel test on a model with a flexible roof based upon the findings of previous investigators. Finally, a theoretical treatment of a single-cell building as an Helmholtz resonator is presented.

[2-2] Description of the Experimental Models

The model used in the wind tunnel experiments, model A, was based upon that used by Novak & Kassem (1990b) and was representative of a large arena type building with openings. However, the theoretical analysis presented in section 2-4 includes a selection of empirical coefficients (e.g. the inertia coefficient, C_i) which are sensitive to both flow conditions and model geometry and some of these were quantified using a second model, model B.

[2-2-1] Model A

Model A, shown in figures 2.1(a) and 2.1(b) and plates 2.1(a) and 2.1(b) was a circular cylindrical drum-type model of plywood construction with a height, H, to diameter, D, aspect ratio of 0.25. The upper one third of the model was detachable which permitted either a rigid plywood roof or a flexible membrane roof section to be fitted. The interchangeable roof enabled variations in building envelope flexibility to be made so that the model configuration was representative of a range of buildings from conventional types with relatively rigid roofs to those with more exotic and flexible membrane roofs.

The external diameter of the model was 300mm and the walls were 50mm thick so that the span of the membrane was only 200mm; the tension of the membrane was continuously adjustable by raising or lowering the height of the tension ring (figure 2.1(a)). The base of model A was vented by sixteen identical and symmetrically arranged circular orifices with diameters of 19mm and length to diameter ratios, l_o/d, of 2.6. The orifices were centred at a height of 0.27H and whilst the internal edges of these orifices were sharp, the external edges had a small, sharp-edged, rebate in order to accommodate sealing plugs. The orifices could be opened or closed in any combination and the maximum vented area of the orifices was 6.4% of the area of the

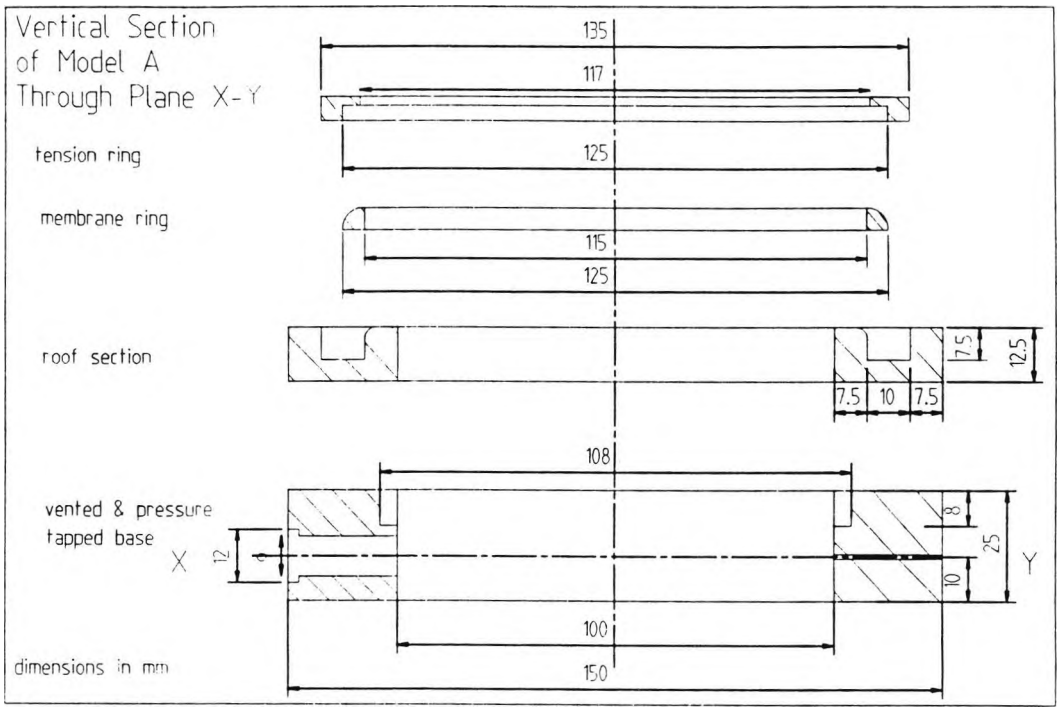

Figure 2.1(a): Cross-sectional view through model "A".

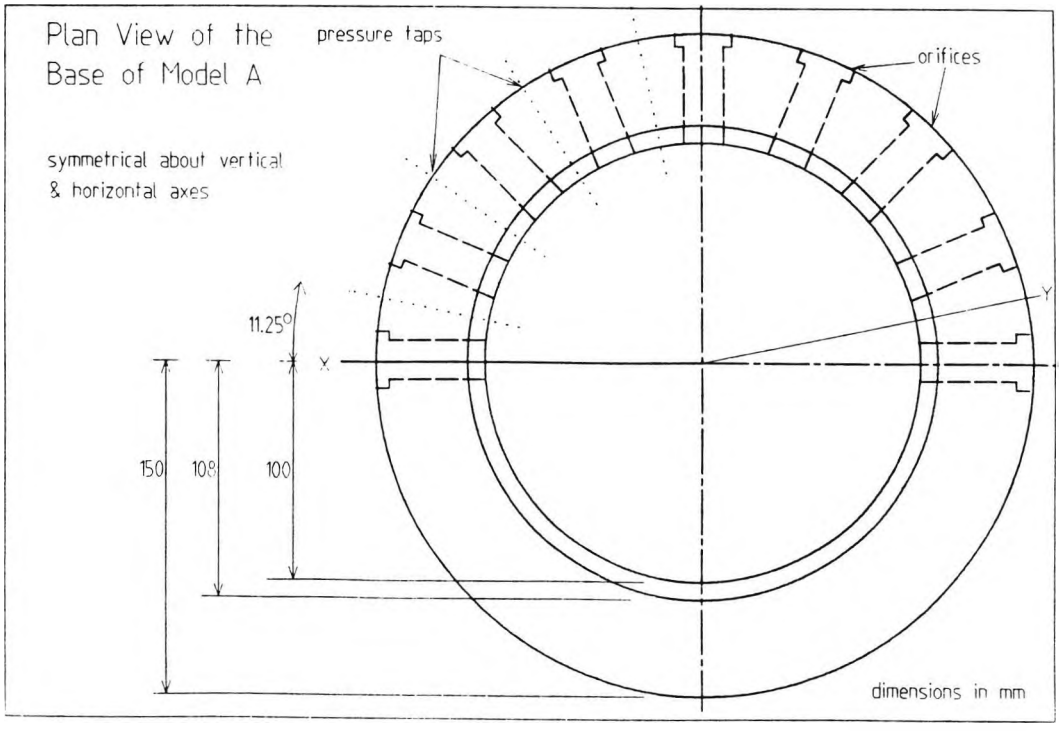

Figure 2.1(b): Plan View of Model "A".

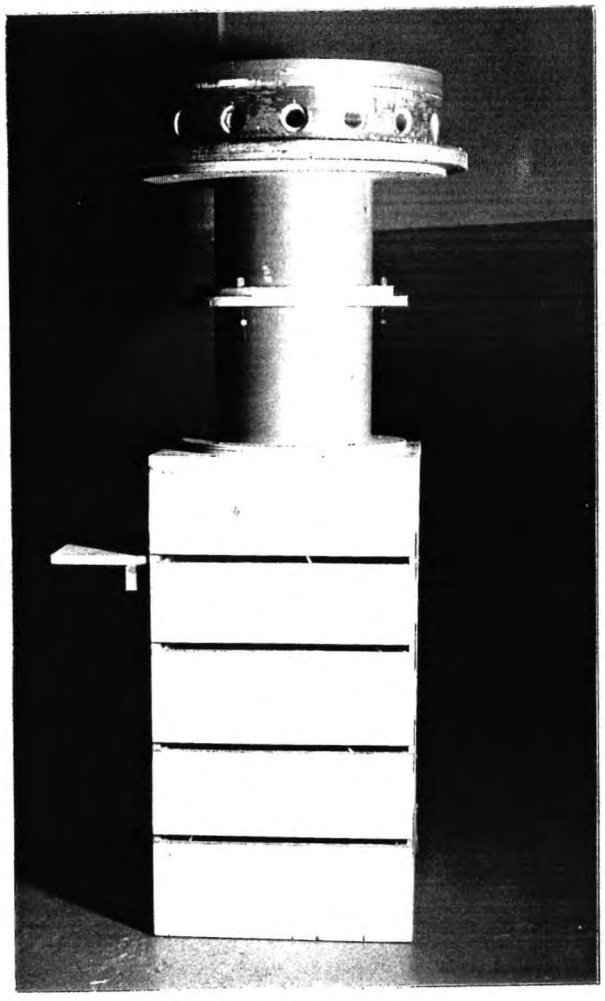

Plate 2.1(a): View of model "A" showing the exaggerated volume box.

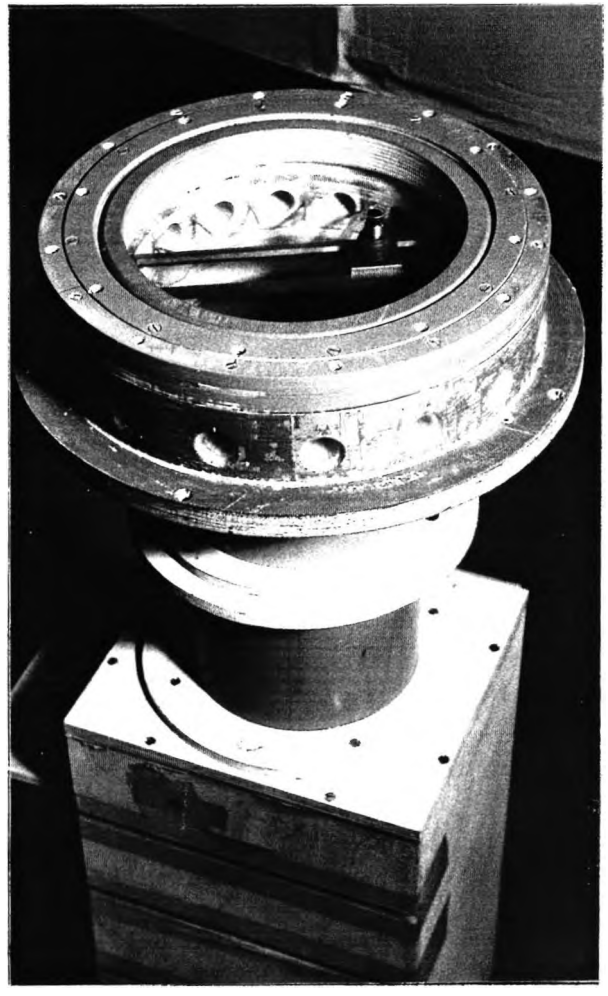

Plate 2.1(b): View of model "A" showing the membrane roof.

wall of the model, or 6.4% of the plan area of the model, or 14.4% of the area of the membrane roof. The internal volume of the basic model, as described so far, will be denoted as V_o and was approximately $0.0024m^3$. The base of model A was also pressure tapped with sixteen taps of internal diameter 1.0mm and length 55mm which were located at a height of 0.27H, midway between adjacent orifices. An additional, single pressure tap was located above the centre of one of the orifices at a height of 0.55H.

A cylindrical wooden box of rectangular cross-section was manufactured, for attachment to model A, which permitted a ten times exaggeration of the internal volume of the model in discrete increments of two, four, six, eight and ten times V_o. This "box" was rigidly closed at one end. When the wind tunnel tests on model A were conducted, it was necessary to construct a connecting pipe between the base of the "basic" model (ie. $V_o=0.0024m^3$) and the underside of the tunnel floor where the exaggerated internal volume "box" was situated (see Plates 2.1(a) and (b)). The internal volume of the additional pipe was approximately $0.0059m^3$, that is $2.5V_o$, so that cavity volumes "A", "B" and "C", referred to in later chapters, corresponded to $4.5V_o$, $8.5V_o$ and $12.5V_o$ respectively. When the model was being tested all joints were sealed using an industrial strength sticking tape and a plastiscene filler. The reasons for exaggerating the cavity volume will be discussed in section [2-3-2-3-3].

[2-2-2] Model B

Model B (not shown) was a rigid plywood box of square planform with a fixed internal volume of $0.005m^3$ and internal cavity dimensions of .2x.2x.12 metres. A sharp-edged, circular orifice of diameter 40mm was drilled in the centre of each of the four sidewalls of model B. The aspect ratio, l_o/d, of these holes was approximately 0.25, and as with model A, the orifices could be opened or sealed in any combination. A series of "plugs" was manufactured from "ABS" plastic which could be slotted into the orifices or stuck to the external walls in order to vary the orifice dimensions. The aspect ratios of the orifices on model B ranged from 0.25 to 4.0 as shown in table 2.1 and once again every effort was made to ensure that all joints were air-tight.

[2-3] Scaling Requirements

Data obtained from wind-tunnel tests should be representative of events at full-scale and for dynamic similarity to exist between the two systems the relative magnitudes of all forces, excitation, inertia, damping and stiffness should be equal. Dimensional analysis is a powerful technique for obtaining a set of non-dimensional similarity

parameters for scaling, provided all relevant physical quantities are included in the analysis. Unfortunately, it is seldom possible to accurately match all the derived scaling parameters and an order-of-magnitude assessment of the non-dimensional constants will usually permit either complete or partial relaxation of the less influential parameters. Consequently, it is important for an a priori judgement to be made about the mechanisms which will affect the response of a particular physical model and to determine the degree of scaling relaxation that will still provide acceptable results.

	length (mm)		
diameter (mm)	10	20	40
10	1.0	2.0	4.0
20	0.5	1.0	2.0
40	0.25	0.5	1.0

Table 2.1: Orifice Aspect Ratios, l_o/d for model B

[2-3-1] Scaling the Atmospheric Boundary Layer

Mixing in the atmospheric boundary layer can be attributed to forced (or mechanical) convection and thermal convection and generally both these physical processes are at work simultaneously. However, for wind loading tests the thermal convective processes are ignored because it is assumed that the maximum design load will occur under the action of a strong wind where mechanical mixing is dominant and the boundary layer is neutrally stratified. A neutral atmospheric boundary layer is both sheared and turbulent and strict scaling necessitates reproduction of both these properties of the boundary layer.

Traditionally, the mean windspeed profile was characterised by the power law exponent, α, but this has been superseded by the log-law format which is characterised by the roughness length, z_o and the friction velocity, u_* (section 3-3-1-2). The ratio of building height, H, to z_o is called the Jensen number and this ratio matches the form of the mean windspeed profile to the size of the building under investigation.

Correctly scaling the three orthogonal components of turbulence is an exacting requirement and the modeller is often limited to matching only the longitudinal component of turbulence and even then the length scale may be some two to three times less than desired. Ideally, both the length scales of turbulence and the roughness length should match the geometric scale of the model, λ_L, however, refer to sections [1-4-2] and [1-4-3].

Once a suitable geometric length scale has been selected, often based upon the size of wind tunnel working-section, blockage constraints and the form of the simulated atmospheric boundary layer, then the velocity scaling, λ_V, must be set. For low-rise buildings a good collapse of the pressure coefficient data has been found when the dynamic pressure at roof height is used as the reference pressure and this is almost universally used as the reference windspeed height. Selection of a minimum reference windspeed is generally dictated by the magnitude of the Reynolds number for tests on bluff bodies, with particular problems occurring for buildings with curved surfaces (see also section [1-4-1]). Reynolds number scaling ensures similitude of the ratio of inertia to viscous forces in a fluid medium.

[2-3-2] Scaling the Model

The following discussion draws chiefly on the reports of Irwin et al (1979), Kind & Wardlaw (1981) and Tryggvason (1978) which were primarily concerned with the necessary scaling of actual prototype membrane structures, namely the roof of the Montreal Olympic Stadium and the roof of the Haj Airport Terminal at Jeddah, Saudi Arabia, rather than the idealised building described in section [2-2].

[2-3-2-1] Froude Number

The Froude number describes the ratio of the inertia of the air to the gravitational force of a structure and may be expressed as U^2/bg, where U is the mean windspeed, b, a length and g, gravitiational acceleration. Accurate scaling of the Froude number is not required for a pre-tensioned membrane because movement of the membrane will only become significant when aerodynamic or inertia forces are much greater than those due to gravity. The upshot of this is that higher model-scale windspeeds can be used, which is desirable if prohibitively low Reynolds numbers are to be avoided. In addition constraints on elastic scaling are reduced. However, a hanging membrane that is not pre-tensioned will require similitude of the Froude numbers between the model and prototype.

Pneumatically tensioned membranes require scaling of gravitational and internal pressurisation forces, expressed as $(\rho/\rho).U^2/bg$ and $p_{int}/(\rho U^2/2)$ respectively, but a simplification can be made if these two parameters are combined to form an effective pressure coefficient, $(p_{int}-\mu g)/(\rho U^2/2)$. The mass/area term, μ, is derived from the product ρb. Clearly, if the membrane is highly tensioned by a large internal pressure then Froude number scaling is not significant.

[2-3-2-2] Mass

Depending upon the structure some or all of the following non-dimensional mass parameters may require scaling, $m_1/\rho b^3$, $m_2/\rho b^2$ or $\mu/\rho b$. The first of these, m_1, refers to the actual mass of a structure such as a tall building or tower, whereas m_2 has units of mass/length and should be applied to line-like structures such as cables. μ is the mass per unit area and is the mass scaling parameter for shell and membrane structures.

It is apparently very difficult to accurately scale μ whilst simultaneously maintaining strict scaling of the stiffness because of the limited availability of model-scale materials. However, relaxation of the mass/area scaling is permissible because the area density of a typical full-scale membrane roof is approximately equal to that of the surrounding air and estimates have shown that the mass of the surrounding air that vibrates with the roof, the added mass, is an order of magnitude greater than the membrane mass. A means of quantifying the added mass will be described in section [2-4-2-3]. Consequently, when scaling the mass/area of a membrane the virtual mass should be considered and not simply the membrane mass, where the term virtual mass is defined as the sum of the membrane mass and the added mass of the surrounding air.

[2-3-2-3] Stiffness

Correct scaling of elastic or stiffness forces is necessary to match the relative magnitude of restoring forces between model and full-scale. The discussion on stiffness scaling will be divided into three sections.

[2-3-2-3-1] Tensile Stiffness

As for the mass scaling three non-dimensional stiffnesses are usually considered, $E/\rho U^2$, $Et/\rho U^2 b$ & $EA/\rho U^2 b^2$ with the latter two quantities applying to membranes and cables repectively. However, experience and analysis has shown that elastic scaling can be considerably relaxed without significant errors in the simulated response being incurred and the following paraphrases a general argument presented by Tryggvason (1982) in support of the relaxation of elastic scaling of membrane roof structures. A membrane that is displaced from its static equilibrium position is subjected to two restoring forces due to changes in surface geometry and increased tension as a result of increased strain; these two forces are termed geometric and elastic stiffness respectively. Analyses show that in general geometric stiffness is the dominant restoring force and this can be correctly reproduced by ensuring similarity of surface shape and tensioning permitting the elastic scaling, $Et/\rho U^2 b$, to be relaxed.

[2-3-2-3-2] Bending Stiffness

In general, it was argued by Irwin et al (1979) that the bending stiffness of a membrane surface is not a significant parameter to model because the radii of curvature of the membrane are usually very large. However, under certain conditions the non-dimensional folding height of a membrane material, h_m/b, where h_m is approximately equal to $[Et^2/(20\rho_m g)]^{1/3}$, is significant and should be modelled (Kind (1981)). The significance of using a model-scale membrane material that is too stiff in bending is that small-scale, localised deflections of the membrane would not occur.

[2-3-2-3-3] Pneumatic Stiffness

Vibrations of a membrane roof can occur in either volume displacing or non-volume displacing modes, i.e. symmetric or asymmetric modes respectively, and the former result in a dynamic component of internal pressure. The compression and expansion of the internal air gives rise to a pneumatic stiffness term which will reduce in magnitude as the building becomes more open, but which can be correctly scaled by maintaining similitude of the following non-dimensional parameters;

$(\pi b^4 \rho c^2)/(T_o V_o)$ - Elashkar (1983)

$(2A^{3/2} p_o)/(\rho U^2 V_o)$ - Holmes (1979)

$(2p_o/\rho U^2)/(\Delta v/V_o)$ - Tryggvason (1982).

These three independently derived parameters each lead to the same cavity volume scaling factor,

$$\lambda_{vol} = (V_o)_{model}/(V_o)_{full\text{-}scale} = \lambda_L^3/\lambda_U^2$$

where λ_L and λ_U are the geometric length and windspeed scaling respectively. This means that the cavity volume dynamics can be reproduced at model-scale by exaggerating the volume of the model by a factor equal to the square of the velocity scaling, however, if the velocity scaling is much less than unity then difficulties of model size might occur.

[2-3-2-4] Damping

In general, reproduction of damping forces at model-scale is complicated not least because it is often difficult to quantify the principle damping mechanisms that occur

at full-scale. Consequently, after some assessment of the major sources of damping has been made, the design philosophy appears to be to construct a wind tunnel model which is lightly damped so that the resultant response of the model will be conservative.

The energy contained in the motion of a membrane roof is dissipated by structural damping and acoustic radiation damping into the surrounding air. The structural damping term is used to describe energy absorbed by the deformation of the membrane material itself and by the motion of the fixtures that keep the roof on place. However, a roof used to span a large arena is likely to be chiefly damped by acoustic radiation which can be quantified by treating the roof as a simple acoustic source (e.g. Novak & Kassem (1990a)).

In addition, the motion of air in and out of openings in the walls beneath the membrane roof further damps the overall dynamic system by acoustic radiation from the openings and by pneumatic or viscous losses due to the flow through the openings. The former can be estimated using the same mathematical model as for the acoustic radiation from the roof whilst the latter damping mechanism is a complex function of opening geometry and flow conditions but methods for its estimation have been proposed (e.g. Vickery & Bloxham, (1992)). Further details of how these modes of damping are quantified are presented in section 2-4.

[2-4] Theoretical Analysis

[2-4-1] Introduction

The analogy of the Helmholtz resonator of classical acoustics has been successfully employed in describing the response of the internal pressure of rigid-walled, single-celled buildings to an external excitation applied at a single opening representative of an open door or window (Holmes, 1979). Flexibility in the building envelope, perhaps caused by a flexible membrane roofing material, modifies the response of the internal pressure and this can be treated as a change in the effective volume of the building cavity (Vickery, 1986; Vickery & Bloxham, 1992), or by treating the roof as an additional degree of freedom and analysing the building as a multi-degree-of freedom system with stiffness coupling through the cavity pressure (Novak & Kassem, 1990a; Vickery & Georgiou, 1991).

The response, to an external excitation, of a rigid-walled cavity containing a single opening is documented in texts on classical acoustics (e.g. Kinsler & Frey (1962)) as the Helmholtz resonator. Fluid contained within the opening is treated as a lumped

mass whose motion is determined by the pressure differential across the opening (figure 2.2). The Helmholtz mode of oscillation is physically different from higher cavity modes which are due to the formation of standing waves within the cavity and are generally characterised by a frequency that is an order of magnitude greater than that of the Helmholtz mode; these higher modes are of little interest to the structural engineer because they lie beyond the high energy range of the turbulent wind spectrum.

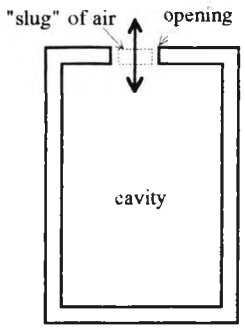

Figure 2.2: A simple Helmholtz resonator

Under the action of a steady-state external stimulus, motion of the lumped mass is sustained by the "stiffness" of the air contained within the cavity; an incoming mass compresses the contained air and consequently increases the cavity pressure until an overpressure exists and the motion of the "slug" is reversed. The system is damped by acoustic radiation of pressure from the opening into the surrounding medium and by losses due to the flow of air through the opening.

[2-4-2] Treatment of an Helmholtz Resonator as a Single-Degree-of-Freedom System

The following analysis is largely based upon the work reported by Vickery & Bloxham (1992). The equation relating the fluid flow through an opening of area A to the pressure difference across the opening is

$$\Delta p_j = p_e - p_i = \frac{1}{2}\rho\, C_L\, V_j \left|V_j\right| + \rho\, l_{eff} \frac{dV_j}{dt} \qquad (2.1)$$

where suffix "j" refers to the jth opening, V_j is the flow velocity through the jth opening and C_L is a loss coefficient. If the air in the opening is considered as a lumped mass that moves an incremental distance x due to the existence of a pressure differential then (2.1) can be rewritten as

$$\rho\, l_{eff} \frac{d^2x}{dt^2} + \frac{1}{2}\rho\, C_L \frac{dx}{dt}\left|\frac{dx}{dt}\right| + p_i = p_e \qquad (2.2)$$

because $V_j = dx/dt$.

Movement of the air contained within the opening causes compression or expansion of the air contained within the building cavity and it may be assumed that this process is isentropic so that $p_o V_o^{\gamma} = \text{constant}$. Differentiation of this expression permits the incremental volumetric changes, dV_o, to be related to the incremental changes in cavity pressure, dp_i

$$dp_i = -\frac{\gamma p_o}{V_o} dV_o \qquad (2.3a)$$

and the volume change dV_o is equal to the product of the area of the opening and the displacement of the air mass within the opening, x,

$$dp_i = -\frac{\gamma p_o A}{V_o} x \qquad (2.3b)$$

Equation (2.3b) and the definition of a pressure coefficient (equation A.1) can be used to transform equation (2.2) into the following expression

$$\frac{1}{\omega^2} \ddot{C}_{p_i} + \frac{\beta^2}{\omega^2} \dot{C}_{p_i} \left|\dot{C}_{p_i}\right| + C_{p_i} = C_{p_e} \qquad (2.4)$$

where ω is the circular frequency and β a constant defined by

$$\omega^2 = \frac{\gamma p_o A}{\rho V_o l_e}$$

$$\beta^2 = \frac{1}{4} \frac{C_L}{l_{eff}} \frac{V_o}{A} \frac{\rho}{\gamma p_o} U_{ref}^2 \qquad (2.5)$$

Equation 2.4 is similar in form to the equation of the Helmholtz resonator derived in texts on acoustics (Kinsler & Frey, 1962) and to the differential equation governing the response of the internal pressure of buildings with dominant openings reported by Holmes (1979) and Liu & Saathoff (1981, 1982). (The reader is directed to Vickery (1991) for a discussion on the differences between the approaches of the latter investigators). Nevertheless, the non-linear damping term in equation (2.4) dictates that closed form solutions can not be obtained and the use of the equation as a

predictive tool is limited unless, for a sealed building where the mean C_{pi} is zero, a linear approximation is made which yields

$$\dot{C}_{p_i} \left| \dot{C}_{p_i} \right| = \sqrt{\frac{8}{\pi}}\, \dot{C}'_{p_i}\, \dot{C}_{p_i} \tag{2.6}$$

where the prime refers to the root-mean-square derivative of the pressure coefficient (Vickery & Bloxham, 1992). Substituting (2.6) into (2.4) gives

$$\frac{1}{\omega^2}\, \ddot{C}_{p_i} + \frac{\beta^2}{\omega^2} \sqrt{\frac{8}{\pi}}\, \dot{C}'_{p_i}\, \dot{C}_{p_i} + C_{p_i} = C_{p_e} \tag{2.7}$$

and it is a trivial matter to show that the damping factor as a fraction of critical, ζ, for the system is given by

$$\zeta = \frac{\beta^2}{\omega} \sqrt{\frac{2}{\pi}}\, \dot{C}'_{p_i} \tag{2.8}$$

When the resonant component is significant, C_{pi}' can be approximated by the expression

$$\dot{C}'_{p_i} \approx C'_{p_e}\, \omega \sqrt{\frac{\pi\, S_o}{4\, \zeta}} \tag{2.9}$$

(Vickery & Bloxham, 1992), so that

$$\zeta^{3/2} = \beta^2\, C'_{p_e} \sqrt{\frac{S_o}{2}} \tag{2.10}$$

and the response of the cavity pressure can be estimated entirely from the dimensions of the building and the magnitude and frequency content of the external pressure outside the opening. The parameter S_o is the magnitude of the spectral energy contained in the external pressure spectrum at the resonant frequency, ω, when the pressure spectrum is plotted in the normalised format of $n.S\{n\}/\sigma^2$.

Equation (2.7) may be compared with the equation of motion of the familiar spring-mass-damper (e.g. Craig, 1981; Thompson, 1988)

$$m\, \ddot{x} + c\, \dot{x} + k\, x = 0 \tag{2.11}$$

which under the action of a complex harmonic excitation, $F_o.e^{i\Omega t}$, can be assumed to have a steady-state solution of the form

$$x = H(i\Omega).F_o.e^{i\Omega t} \qquad (2.12)$$

where $H(i\Omega)$ is the complex frequency response function which is defined by

$$H(i\Omega) = \frac{1}{(k - m.\Omega^2) + i(c)\,\Omega} \qquad (2.13)$$

From (2.11) the natural frequency, ω, and damping factor, ζ, are defined by the expressions

$$\omega^2 = k / m \quad \& \quad 2\zeta w = c/m \qquad (2.14)$$

If the frequency ratio r is defined as Ω/ω, then substitution of (2.14) into (2.13) permits the modulus of the frequency response function to be determined

$$|H(i\Omega)| = \frac{1}{k\sqrt{(1 - r^2)^2 + (2\,\zeta\, r)^2}} \qquad (2.15)$$

and the output lags the input by a phase angle, θ, where

$$\tan\theta = \frac{2\zeta\, r}{(1-r^2)} \qquad (2.16)$$

From equation (2.15) the non-dimensional amplitude ratio is expressed as $k\,.\,|H(i\Omega)|$.

[2-4-2-1] Empirical Coefficients

The parameters ω and β defined in equations (2.5) contain empirical coefficients C_I & C_L which until recently have been assumed to take values of 0.886 and 2.679 based upon idealised theoretical analyses (see for example Vickery (1991)). The inertia coefficient, C_I, can be visualised as an extension of the length of air contained within the opening because the external air immediately adjacent to the opening is forced to move by the contained air. The parameter C_L is a loss coefficient and is related to the steady flow dicscharge coefficient, C_d ($C_L=1/C_d^2$).

The values commonly allotted to these two coefficients, quoted above, are strictly applicable to steady flows through circular openings whereas for an oscillating flow the geometry of the opening, local Reynolds number, reduced frequency, ratio of the flow velocity through the opening to that of the external flow and the magnitude of the oscillation can all be expected to influence the actual values of these coefficients. Vickery & Karakatsanis (1989) reported on a series of tests where the discharge coefficient of a circular opening was measured as the ratio of the velocity of the external flow past the opening to the flow velocity through the opening was changed. They found that marked changes occurred with variations in the discharge coefficient up to a factor of five, but even in these tests the flows were not oscillatory.

In light of the above there does appear to be a need to systematically measure the dependence of both C_I and C_L for different opening geometries under varying flow conditions in order to better define these parameters. In chapter 4 the inertia coefficients for openings of different geometry were measured under a zero wind condition.

[2-4-2-2] Building Envelope Flexibility

For a rigid building the inflow of air through an opening leads to compression of the air contained within the building cavity, according to equation (2.3a), and the "stiffness" of the air is quantified by the bulk modulus of air, K_a (equal to γp_o). However, if the envelope of the building is flexible then compression of the contained air is accompanied by deformation, or displacement, of the flexible component and the resultant interactions between the cavity pressure and the building envelope may result in relatively complex dynamic phenomena as described by Vickery & Georgiou (1991).

Nevertheless, provided that the lowest natural frequency of the envelope is high compared with the rate at which pressure changes occur within the building cavity, as in a highly tensioned membrane roof, then the influence of the building envelope flexibility can be accounted for by defining an effective bulk modulus of air, K_a', where

$$K_a' = \frac{K_a}{(1 + K_a/K_b)} \qquad (2.17)$$

and K_b is the bulk modulus of the building (Vickery & Bloxham, 1992). Substitution of (2.17) into equations (2.5) leads to the conclusion that for conventional buildings the

influence of building flexibility on internal pressure dynamics is to increase the effective cavity volume by a factor equal to $(1+K_a/K_b)$ as reported by Cook (1989).

Vickery (1985) and Vickery & Bloxham (1992) stress that the definition of an effective bulk modulus in order to account for any flexibility in the walls of a building is strictly applicable to more conventional type buildings and not to large span membrane roof structures. However, the approach does not appear to have been corroborated by experimental results and precise limits on the permissible degree of envelope flexibility have not been prescribed.

[2-4-2-3] Acoustic Damping

The damping, as a fraction of critical, defined in equation (2.10) is concerned with the losses due to flow through an opening. However, the internal pressure fluctuations of buildings with openings covered by a membrane roof may be damped to a significant degree by acoustic radiation from both the openings and the roof into the surrounding medium. This form of damping was successfully modelled by Novak & Kassem, (1990a & b) and Kassem & Novak, (1990) as that from a simple acoustic source.

Damping due to acoustic radiation from a simple acoustic source contained in an infinite baffle is given by

$$c_a = \rho_o c_o A F\left\{ 2 r \frac{\omega}{c_o} \right\} \qquad (2.18)$$

where c_a is the acoustic damping coefficient, c_o is sonic velocity, r is the radius of radiating source of area A and the function F{x} is defined by the series

$$F\{x\} = \frac{x^2}{2.4} - \frac{x^4}{2.4^2.6} + \frac{x^6}{2.4^2.6^2.8} - \ldots \qquad (2.19)$$

{Note that "x" in equation (2.19) is nothing to do with displacement}.

For an opening, A is simply the area of the opening which has a radius r, whereas, for an oscillating circular membrane A is the generalised area associated with each of the symmetric membrane mode shapes under consideration. The magnitude of the acoustic radiation is dependent upon the amount of air displaced by the motion of the membrane and not on the exact shape of the vibrating surface. Consequently, the membrane can be replaced by an analogous rigid piston which has a volumetric displacement

equivalent to that of the actual membrane. Finally, it should be noted that the first symmetric mode of a vibrating circular membrane rigidly fixed at its circumference is the most efficient radiator of acoustic energy because the only nodal line is fixed at the circumference of the roof (Kinsler & Frey, (1962)).

The small size of the openings used on the models (sections 2-2-1 & 2-2-2) and the damping results shown in chapter 4 implied that acoustic radiation damping from a single opening was small. Consequently, damping due to the motion of the roof will be focussed on and compared with the results obtained using equation 2.10.

The displacement of the roof is

$$x_2(r_2, t) = \psi(r_2)\ q(t) \tag{2.20}$$

where the suffix "2" denotes roof motion, $\psi(r_2)$ is the mode shape and q(t) the generalised co-ordinate. The mode shape, $\psi(r_2)=J_0(k'r_2)$, is defined so that $\psi(0)=1$. The boundary condition at the edge of the membrane ($r_2=R_2$) is $x_2(r_2,t)=0$ which implies that

$$J_0(k'R_2) = 0 \quad \text{and hence} \quad k'R_2=2.405,\ 5.520,\ 8.654.... \tag{2.21}$$

The generalised mass and area of the roof are

$$m_2 = \int_{A_2} \mu\ (r_2)\ \psi^2\ (r_2)\ dA_2 \quad \text{and} \tag{2.22}$$

$$A_2 = \int_{A_2} \psi\ (r_2)\ dA_2 \tag{2.23}$$

respectively, where $\mu(r_2)$ is the area density of the membrane roof including the external added mass of the surrounding air.

Lightweight roof structures possess an area density which is comparable with the surrounding air and consequently when excited the contribution of the adjacent air to the effective mass of the roof is significant. Indeed estimates show an order of magnitude difference in the ratio of added mass to fabric mass (Irwin et al, 1979) on full-scale structures. The generalised piston analogy for the vibrating roof described

above permitted the added mass to be computed using formulae derived for oscillating discs (Blevins, 1979).

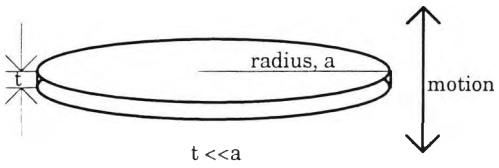

Figure 2.3: Diagram of oscillating disc.

For a thin disc oscillating in the direction shown in figure 2.3 the added mass on a single side of the disc is given by

$$m_a = \frac{8 \rho_c a^3}{3} \qquad (2.24)$$

where in the present analysis the radius "a" is the radius of the generalised area of the roof, $a=[A_2/\pi]^{1/2}$.

Computing the generalised area of the roof for the first symmetric mode permitted the added mass for an equivalent rigid piston to be estimated and subsequently the generalised mass of the membrane roof was determined. This mass was then used to estimate the acoustic radiation damping for the vibrating roof using equation (2.18) and the expression

$$\zeta_a = \frac{1}{2} \frac{c_a}{m_2 \omega} \qquad (2.25)$$

where m_2 and ω are defined by equations (2.22) & (2.5) respectively.

[2-4-2-4] Theoretical Damping Predictions & Comparisons with Experimental Data

Acoustic radiation damping from the roof and damping due to flow through the opening were computed and the results are shown below in table 2.2 for a selection of model configurations only.

The estimates of ζ_a were independent of opening azimuth angle and windspeed and showed that acoustic radiation losses from the roof were less than 1% for most of the model configurations tested and consequently were of secondary importance.

	ζflow			9.4 m/s					13.0 m/s		
	ϕ	R	Ta	Tb	Tc	Td	R	Ta	Tb	Tc	Td
Va	0	.003	.016	.036	.075	.125	.009	.042	.096	.197	.331
	90	.001	.006	.013	.025	.049	.004	.016	.035	.065	.129
	180	.001	.006	.012	.021	.035	.004	.017	.031	.055	.093
Vc	0	.014	.038	.084	.106	.193	.038	.101	.223	.282	.510
	90	.006	.011	.025	-	-	.015	.028	.066	-	-
	180	.005	.011	.024	.030	.049	.014	.030	.062	.079	.129
Va	ζa	-	.009	.007	.007	.005	-	.009	.007	.006	.005
Vc	ζa	-	.008	.006	.006	.005	-	.008	.006	.006	.005

Table 2.2: Theoretical damping factors due to flow losses and acoustic radiation losses at the resonant frequencies.

It is now convenient to compare the theoretical estimates of damping factor using equation (2.10) and the results of chapter five with the estimates of the experimental data obtained from the cavity pressure spectra results of chapter 6. In addition the measured and predicted ratios of external to internal cavity pressure will be compared using equation (2.9) and the relevant results of chapters 5 and 6. Results were obtained for a limited set of model configurations only.

Figures 2.4 showed that increasing the flexibility of the roof increased the damping and that for the majority of cases the theoretical estimates of damping were less than the measured damping factors. The comparison was best when the opening was oriented to windward, that is $\phi=0^o$, poorest for $\phi=90^o$ and was fair when the opening was in the base region.

These results were reflected in figures 2.5 where the root-mean-square pressure ratios, internal divided by external at 0.27H, were compared. With a windward opening the predicted fluctuating cavity pressure was generally within plus or minus 10% of the experimental value, whereas an opening at 180^o and 90^o lead to progressively greater overestimates of the magnitude of the cavity pressure fluctuations. The precise reasons for these discrepancies were not clear, however, there were a number of possible sources of error.

The half-power method (Craig, 1981) was used to determine experimental damping factors from the gain functions of cavity pressure spectra compiled in appendix C. Most of the resonant peaks on these plots were well-defined but for the purposes of determing the damping factors the definition was enhanced by additional smoothing along the gain function. However, even allowing for a plus/minus 30% margin of error in the empirical estimates of damping does not account for the discrepancies shown in figures 2.4(b) and (c).

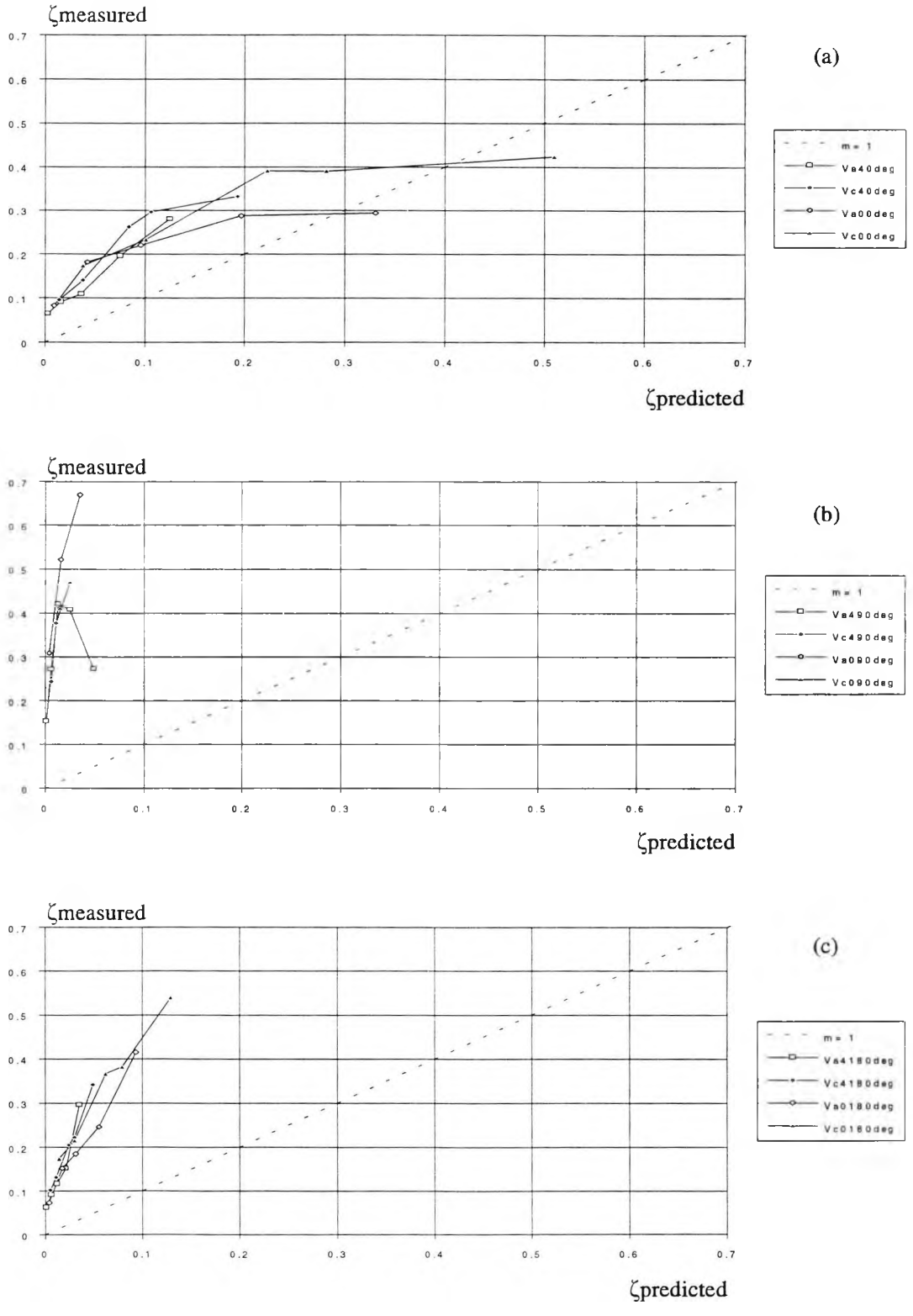

Figure 2.4: Comparison of the measured & predicted damping factors as a fraction of critical for different roof tensions and volumes and with ϕ equal to (a) 0 degrees, (b) 90 degrees, (c) 180 degrees.

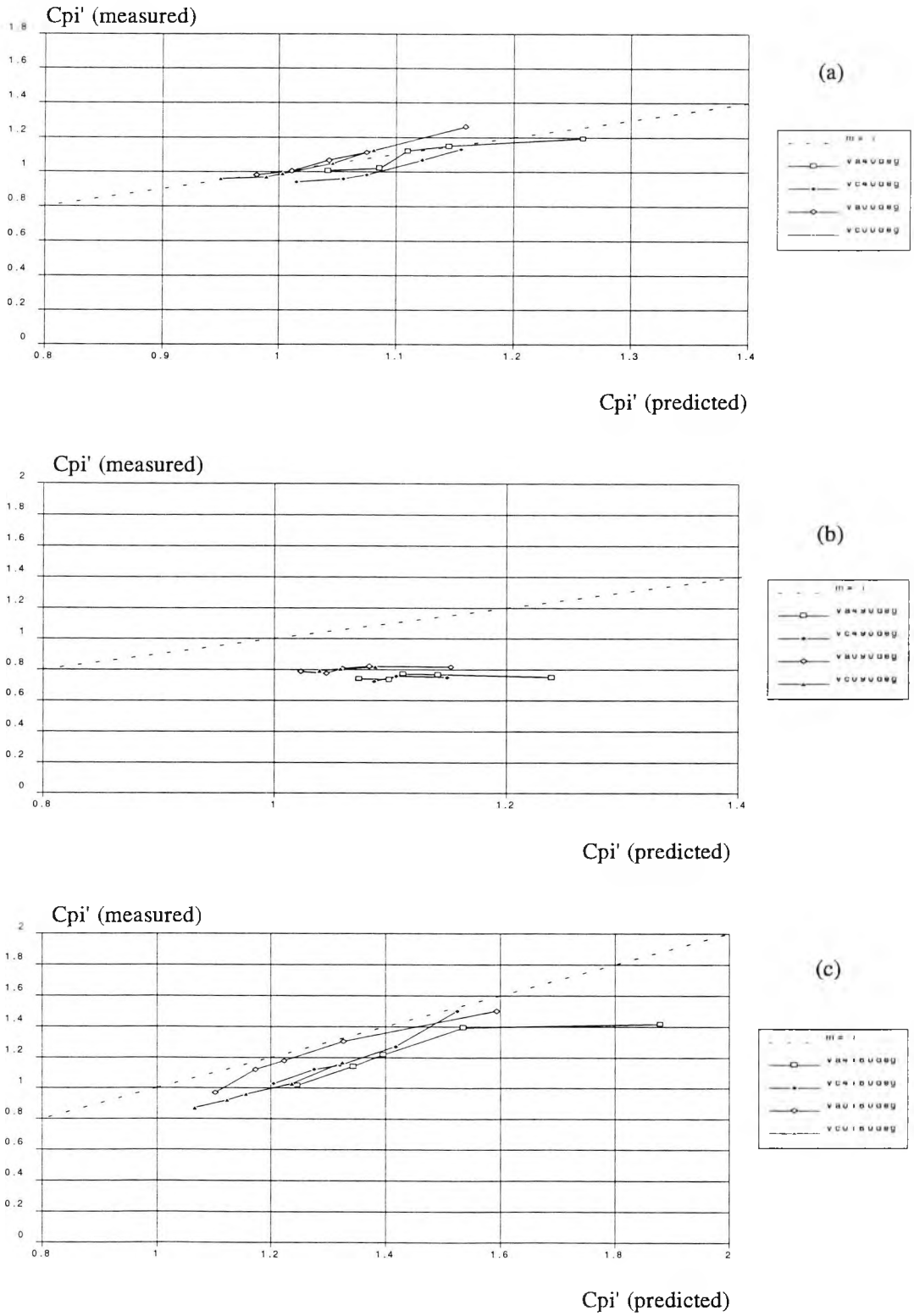

Figure 2.5: Comparison of the measured & predicted ratios of r.m.s. cavity pressure fluctuation to external r.m.s. pressure fluctuation for different roof tensions and volumes and with ϕ equal to
(a) 0 degrees, (b) 90 degrees, (c) 180 degrees.

The theoretical damping predictions only considered losses due to flow through the opening which was shown to be a reasonable approximation by the results of table 2.2. Nevertheless, the "standard" value for the loss coefficient, C_L=2.68, was used to derive the theoretical estimates and this value is known to be sensitive to flow conditions (refer to section 2-4-2-1). A procedure was implemented to fit the theoretical damping factors to the empirical values by changing the magnitude of the loss coefficient but this yielded values of C_L ranging between 1.8 to 22 just by changing the tension in the membrane roof!

Notwithstanding the above the theoretical predictions may be considered conservative in that damping is underestimated which leads to an overestimate of the response of the cavity pressure fluctuations.

[2-4-3] Treatment of a Flexible-Roofed Helmholtz Resonator as a Two-Degree-of-Freedom System

Finally, a brief mention will be made on the work of Novak & Kassem (1990a & b), Kassem & Novak (1990) and Vickery & Georgiou (1991) who modelled the flexible membrane roof backed by a cavity with openings as a two and many degree of freedom system respectively. The roof was treated as a generalised piston similar to that discussed in the previous section and a diagram of the idealised system is shown in figure 2.2.

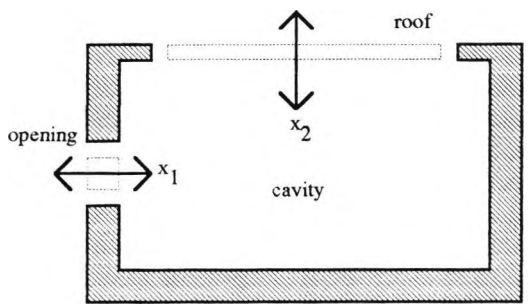

Figure 2.2: Idealisation of an Helmholtz Resonator with a Flexible Roof

Suffices "1" and "2" will be used to describe the motion of the "slug" of air and the roof motion respectively. Preliminary visual tests on a model fitted with a membrane roof indicated that the roof response in its first two resonant modes was dominated by the first volume-displacing symmetric mode. The symmetrical, volume displacing modes of a circular membrane rigidly clamped around its circumference are described by a Bessel's function of the first kind, zero order, $J_o(k'.r_2)$, (Kinsler & Frey (1962))

where the parameter k' is a function of the tension/length, area density and frequency of vibration of the membrane and has dimensions of [length]$^{-1}$ (see equation (2.21)).

Consequently, the theoretical analysis was restricted to considerations of only a single roof mode and the resonator was completetly described by a two-degree-of-freedom system. The full theoretical model presented by Vickery & Georgiou (1991) allows for any number of openings and roof modes.

If the generalised structural stiffness of the roof is

$$k_s = m_2 . \omega_r^2 \tag{2.26}$$

where ω_r is the natural frequency of the isolated roof (Novak & Kassem, 1990b) and the pneumatic stiffness is inferred from equation (2.3a) as

$$dP = -\frac{\gamma . P_{at}}{V_o} (A_1 . x_1 + A_2 . x_2) \tag{2.27}$$

then the equations of motion of the two-degree-of-freedom system are

$$\begin{aligned} m_1 \ddot{x}_1 + (c_{a_1} + c_F) \dot{x}_1 + \frac{\gamma P_{at} A_1^2}{V_o} x_1 + \frac{\gamma P_{at} A_1 A_2}{V_o} x_2 = 0 \\ m_2 \ddot{x}_2 + (c_{a_2} + c_s) \dot{x}_2 + k_s x_2 + \frac{\gamma P_{at} A_2^2}{V_o} x_2 + \frac{\gamma P_{at} A_1 A_2}{V_o} x_1 = 0 \end{aligned} \tag{2.28}$$

However, the treatment of the roof response using the equations 2.28 will not be considered further because the spectral results in chapters 6 and appendix E showed that the response of the cavity pressure and roof were dominated by the lower frequency Helmholtz mode (see also Appendix E).

[2-5] Summary

Initially, a description of the experimental models was presented and this was followed by a discussion of the necessary requirements for "correctly" scaling a wind tunnel model of a membrane structure with a membrane roof.

The second half of this chapter was concerned with formulating the theoretical treatment of the response of the cavity pressure to turbulent pressure fluctuations

outside a dominant opening. This analysis was drawn from the results of previous investigators, principally Vickery & Bloxham (1992), and was found to give good to overly conservative estimates of the cavity pressure fluctuations based upon the measured external pressures acting on the wind tunnel model. Vickery & Bloxham (1992) presented experimental results for a model with a dominant windward opening which supported their theoretical analysis and they stated that the analysis was generally applicable for openings at different orientations. However, the results in section [2-4-2-4] imply that this may not be the case, although accurate determination of the two empirical coefficients, C_L and C_I and their sensitivity to different flow conditions might significantly improve the theoretical predictions.

Chapter 3: Data Acquisition & Approach Flow Characteristics

[3-1] Introduction

This chapter summarises the instrumentation, data acquisition and data analysis procedures used in both the "still-air" and the wind tunnel portions of the test programme. This is followed by a description of the boundary layer profile used in the wind tunnel test programme.

[3-2] Data Acquisition

[3-2-1] "Still-Air" Free-Vibration Tests

The free-vibration tests (chapter 4) were conducted using a low frequency square wave pulse to excite the air within the cavity of the two models tested (refer to chapter 2). A flush-mounted Setra 237 pressure transducer, referenced to atmosphere, monitored the decay in the response.

Power spectra and time domain data were measured "on-line" by the GenRad PDP-11 data acquisition system and each frequency and damping factor was determined from an average of eight separate pressure pulses. Helmholtz frequencies were obtained directly from power spectra whereas, damping factors were estimated by fitting an exponential function to the decay curves. The time series also permitted estimates of the oscillation frequency to be made by measuring the length of time taken for a number of complete oscillations to occur. The GenRad system digitised the analogue transducer signals at 2.56 times the maximum frequency of interest. Depending on the resonator configuration the measured Helmholtz frequencies covered the range from 20Hz to 110Hz.

[3-2-2] Wind Tunnel Tests

[3-2-2-1] Pressure Measurements

The internal and external surface pressures on the model were measured using two separate Setra 237 differential pressure transducers. The transducer for measuring internal pressure was flush mounted in the wall of the model whereas the external pressure transducer was connected via a short length of tubing, 60mm long, to a brass pressure tap, 55mm long, of internal diameter 0.5mm. The response of the transducer/tube system was measured prior to testing [see Appendix A] and was used to correct the distortion of the pressure spectra. No pneumatic response optimisation

devices, such as restrictors, were incorporated into the system. The flush-mounted transducer was assumed to possess a flat frequency response well in excess of the bandwidth of interest in the tests.

Pressures were normalised by referencing the transducers to the static pressure at an upstream reference location and dividing the pressure by the dynamic pressure at that same location. The resultant coefficient was corrected following the procedure outlined in Appendix A. The reference static pressure connection was comprised of a series of interconnected, flexible plastic tubes with different internal diameters running to an overall length in excess of four metres. Consequently, any static pressure fluctuations were heavily damped.

[3-2-2-2] Storage and Processing of Data

During the running of the wind tunnel tests, mean and root-mean-square internal pressure coefficients were computed and output by the GenRad PDP-11 data acquisition system. In addition data was recorded on magnetic tape for subsequent analysis "off-line". Reynolds number sensitivity tests were conducted "on-line" with continuous sampling of both the reference dynamic pressure and the point pressure of interest on the model. Contiguous blocks of 512 samples were collected at a sampling frequency of 256Hz which was equivalent to two seconds of real time data (model scale). Averages were computed along each of these time series and the results stored until thirty seconds of data was obtained. The fifteen values were then averaged and output by the computer. This process was repeated three times giving mean and r.m.s. pressure coefficients obtained over a period of one-and-a-half minutes at each wind azimuth angle.

A fourteen channel FM tape recorder recording at a tape speed of $1^{7}/_{8}$ inch/sec was used to store the reference dynamic pressure and both unconditioned and conditioned internal pressure and external pressure (at z/H=0.55). The conditioned signals had their mean values "backed off" and the remaining signal was amplified and low pass filtered at 500Hz by a filter with a sharp cut-off of 18db/octave.

To speed-up the "off-line" analysis process the playback speed of the tape was doubled to $3^{3}/_{4}$ inch/sec. A 486-33MHz personal computer fitted with an A/D card was used to digitise up to three data channels. The data was collected in contiguous blocks of 4096 points and for the spectral analysis the data was further low-pass filtered at a cut-off frequency of 315Hz which was equivalent to 157.5Hz in real (wind tunnel) time. The sampling frequency was set to 333.33Hz per channel (real time) which was 2.12 times the cut-off frequency. Generally, twenty five blocks of

data were collected, processed individually and eventually ensemble averaged in order to smooth the result. However, the original time series were split into smaller blocks of 2048 points before being Fast Fourier Transformed, thus doubling the number of spectra to be ensemble averaged to increase the smoothing.

[3-3] Characteristics of the Approach Flow

The industrial aerodynamics wind tunnel at City university is of closed return type with the return circuit mounted above the working section. The working section is 9m x 3m x 1.5m and details of the tunnel construction and performance were discussed by Sykes (1977). A non-specific atmospheric boundary layer simulation was desired for the wind tunnel test programme and so existing "hardware" was used for development of the boundary layer.

A full width, straight-edged barrier of height 90mm with eight equi-spaced triangulated spires of height 760mm was located at the exit from the contraction followed by a 5m fetch of uniform roughness. The function of the barrier was to trip the approach flow and provide an initial momentum deficit which was subsequently distributed through the boundary layer by the spires (or mixing devices). The floor roughness sustained the turbulence as the boundary developed downstream and to a large extent determined the value of the scaling parameters z_0 and $u*$. Summaries of the "standard" techniques used to simulate the atmospheric boundary layer in both long and short wind tunnels were given by Cermak (1982) and Cook (1982).

The turntable on which the model was mounted was a painted wood surface not covered by roughness elements and the development of a secondary inner boundary layer was noted in the results. Nevertheless, assuming a geometric scale factor of 1/200, the resultant boundary layer was deemed to be typical of the flow over a rural/suburban terrain with a model-scale surface roughness of 0.94mm and a longitudinal turbulence length scale of around 0.4m. A summary of the measured boundary layer characteristics and the apparatus used for boundary layer development is given in table 3.1.

[3-3-1] Vertical Boundary Layer Profiles

[3-3-1-1] Measurement Technique

The mean velocity profile was measured using a 0.5m pitot-tube rake which was connected to an inclined manometer and positioned on the centreline of the tunnel nearly 3.5D upstream of the centre of the turntable. Two reference pitot-static

tubes were positioned symmetrically 2.5D on either side of the rake at a height of 75mm, corresponding to the height of the roof of the model. These reference probes were downstream of the rake in the same cross-section as the centre of the turntable and the rake pressures were referenced to the average of the static pressures obtained from the two pitot-static probes. The mean windspeed profile was measured at four different windspeeds and the results were averaged. A difference in the static pressure at the rake location and that measured by the reference pitot-static probes caused an offset in the results when the mean windspeed profile was referenced to the mean windspeed at roof height. Consequently, a small correction was made by back-calibrating the two reference pitot-static probes against a third probe situated at a height of 75mm in lieu of the pitot rake.

simulation hardware:		
	barrier height	90mm
	no. of triangular spires	8
	height of spires	762mm
	height of roughness elements	33mm
	packing density based upon average plan area)	2.5%
	length of fetch (uniform roughness)	5m
	turntable diameter	2.4m
boundary layer characteristics:		
uniform roughness	power law exponent, α	0.18
	roughness length, z_o, (model scale)	0.94mm
	$u*/U_{roof}$	0.091
turntable	power law exponent, α	0.11
	roughness length, z_o, (model scale)	0.002mm
	$u*/U_{roof}$	0.035
turbulence intensities at :-	z/H = 0.27	21.5%
	z/H = 0.55	21.0%
	z/H = 1.0	19.5%
	boundary layer depth	>4.5H
	model blockage ratio	0.5%

Table 3.1: Summary of boundary layer characteristics

The vertical longitudinal turbulence intensity profiles were measured using a linearised D.I.S.A. constant temperature hot-wire anemometer which was positioned at the centre of the turntable and traversed over a height of approximately 4.5H using a D.I.S.A.

Sweep Drive Unit. The tunnel temperature during these tests changed by approximately 10°C but no corrections were made to the results following the findings of Bearman (1969).

[3-3-1-2] Profile Results

Traditionally, the shape of the mean velocity profile in a neutrally buoyant strong wind was fairly well represented by an empirical power law of the form

$$U/U_{ref} = (z/z_{ref})^{\alpha} \qquad (3.1)$$

where the power law exponent, α, was dependent upon the roughness of the surface over which the boundary layer developed. However, this formulation for the boundary layer profile was gradually replaced by the theoretically more rigorous log-law

$$U/u* = 2.5 \ln \{ (z-d)/z_0 \} \qquad (3.2)$$

where $u*$ is the friction velocity, z_0 the roughness length and the factor of 2.5 is the inverse of the von Karman constant, k. The length, d, is an empirical constant called the displacement thickness which was set equal to zero in the present tests because Lawson (1980) stated that it was insignificant for roughness elements with an area density <10%. Equations 3.1 and 3.2, or variations of these, are both commonly quoted in the literature, e.g. Deaves & Harris (1976), and consequently both were used to quantify the form of the mean windspeed profile.

In figure 3.1(a) the natural logarithm of z was plotted against $\ln\{U/U_{roof}\}$ and an estimate for the value of α was obtained from the gradient of the graph. The two different slopes in figure 3.1(a) implied that the mean windspeed profile was composed of two distinct regions because of the change in roughness at the upstream edge of the turntable. Two estimates for the roughness length were calculated from figure 3.1(b) which also showed the boundary layer to be a hybrid with a well developed upper region due to the uniform roughness which was gradually being displaced by a profile characteristic of the relatively smooth surface of the turntable. Results from tests using a combination of different size roughness elements (not reported here) confirmed that the changes in the profiles were due to step changes in the roughness.

The boundary layer was predominated by the rougher profile and was subsequently graded as typical of a rural/suburban boundary layer with a full-scale z_0 of 0.19m (using E.S.D.U 82026 and assuming a 1:200 scale factor). This grading was further corroborated by the estimated power law exponent of 0.18 following the early results

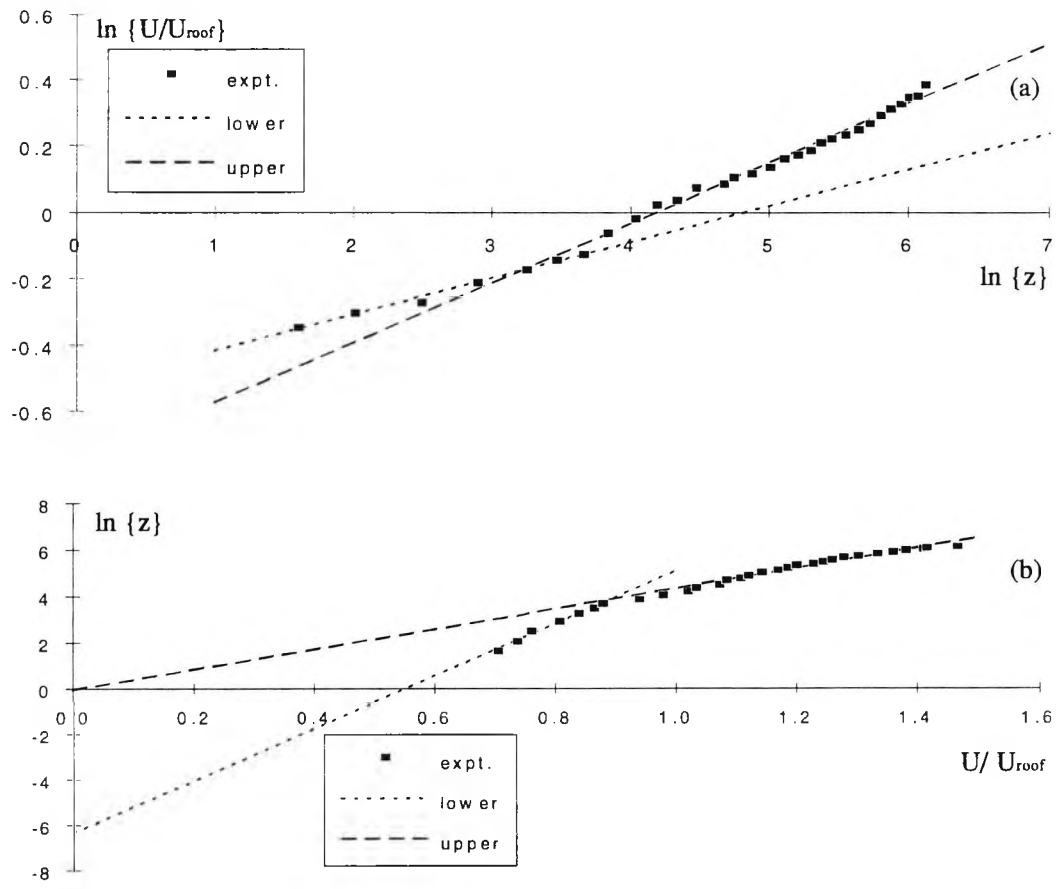

Figure 3.1: (a) Graphical representation of equation 3.1; slope equals power law exponent.
(b) Graphical representation of equation 3.2; intercept equals roughness length, z_o.

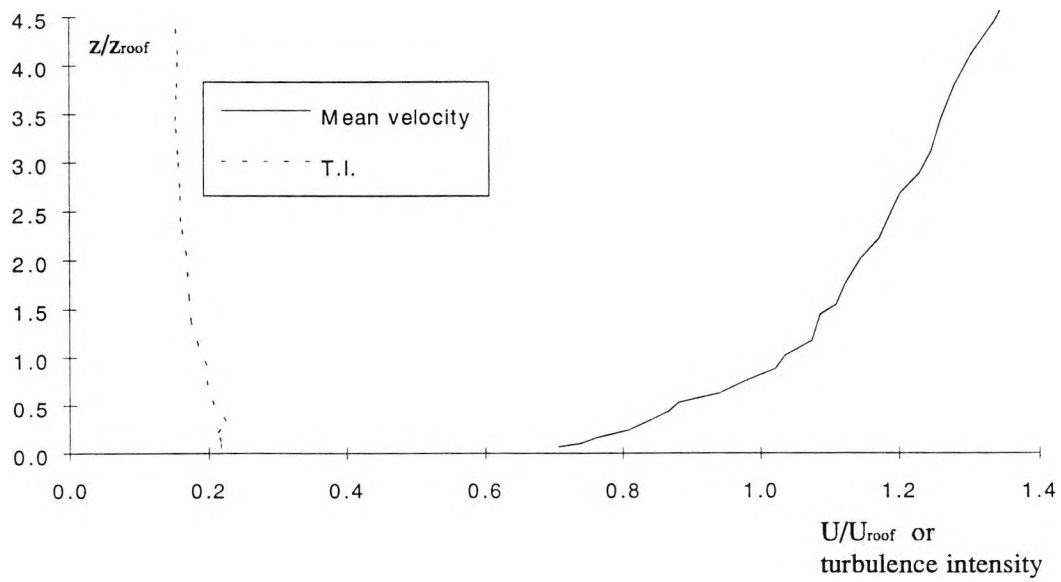

Figure 3.2: Mean windspeed and longitudinal turbulence intensity profiles

of Davenport (1965) which are reproduced below in table 3.2. The longitudinal turbulence intensity profile and the mean windspeed profile are shown in figure 3.2.

roughness description	power law exponent, α
open water	0.16
town suburb	0.28
city centres	0.40

Table 3.2:- Mean windspeed profiles (after Davenport (1965))

[3-3-2] Turbulence Length Scale

The spectrum of the longitudinal turbulence was not directly measured by the conventional hot-wire technique. Instead the scale of turbulence was estimated from the normalised pressure spectrum in the windward stagnation region of the model. This enabled a direct measure of the dynamic excitation acting on the orifice of the model to be made after the turbulence in the approach flow had been distorted by the presence of the building. Fitting the curve for the normalised longitudinal wind spectrum (E.S.D.U. 85020) to the normalised pressure spectrum in the windward stagnation region provided an estimate for the turbulence length scale acting on the orifice. The E.S.D.U. curve is given by the expression

$$n.\ S(n) / \sigma^2 = 4\ .\ (n\ L_x / U) / [1 + 70.8\ (n\ L_x / U)^2\ ]^{5/6} \qquad (3.3)$$

where σ^2 is the variance, U is the reference windspeed (U_{roof}) and L_x is the integral length scale. When expressed in this normalised format the area under the spectrum is equal to unity.

The results of the pressure spectra measured at z/H=0.27 and 0.55 at the two reference windspeeds of 9.4m/s and 13.0m/s with θ equal to zero degrees are shown in figures 3.3 and 3.4. The length scale appeared to be independent of both windspeed and height and an average value for L_x was calculated as 0.43m. The length scales were obtained by fitting the theoretical curves (equation 3.3) to the experimental data by eye such that the low frequency peaks of the spectra were matched as closely as possible.

The work of Rao (1986) was consulted to corroborate this estimate for the length scale. Using the same roughness elements and mixing devices but with a slightly taller barrier (114mm) Rao reported that the longitudinal turbulence length scale, measured using a linearised hot-wire anemometer, was 0.653m. This estimate was obtained at a height of 50mm using a reference windspeed of 10m/s. However, it appeared that the reference speed was measured at a height of approximately 370mm

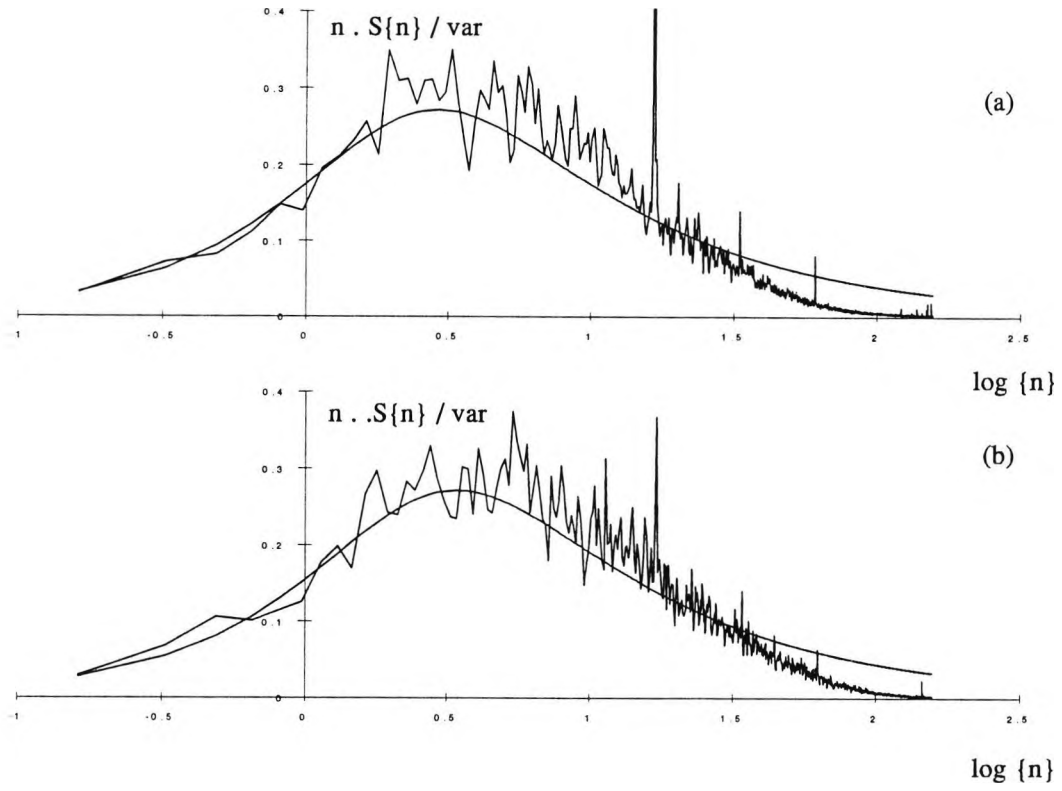

Figure 3.3: (a) Normalised external pressure spectrum at z/H = 0.27, U_{roof} = 9.4 m/s, θ = 0 degrees.
(b) " " " " at z/H = 0.55, U_{roof} = 9.4 m/s, θ = 0 degrees.

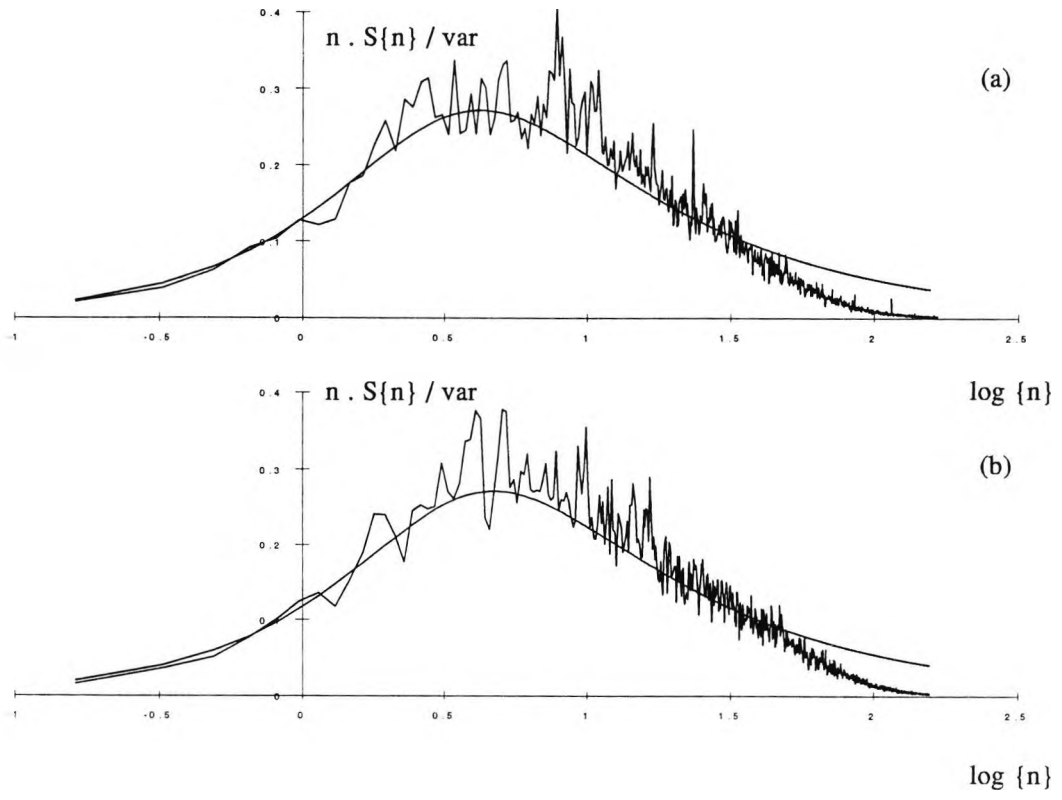

Figure 3.4: (a) Normalised external pressure spectrum at z/H = 0.27, U_{roof} = 13.0 m/s, θ = 0 degrees.
(b) " " " " at z/H = 0.55, U_{roof} = 13.0 m/s, θ = 0 degrees.

in a boundary layer where U/U_{ref} was equal to 0.65 at a height of 77mm. This enabled a "corrected" length scale of 0.42m to be computed which compared very well with the result of the present tests.

A final check on the form of the pressure spectra was made by re-plotting the spectral data as $\log\{Sp(n)/\sigma^2\}$ versus $\log\{n\}$ in order to determine the rates of decay of the turbulent fluctuations (figures 3.5 & 3.6). Slopes of -5/3 and -3.5 were fitted (by eye) to the spectra and are shown in figures 3.5 & 3.6 for comparison and table 3.3 summarises the approximate frequency bandwidths over which these two rates of decay best fitted the individual spectra.

slope	$\theta=0^o$; z=0.27H		$\theta=0^o$; z=0.55H	
	Re=181000	Re=250000	Re=181000	Re=25000
-5/3	3Hz to 35Hz	8Hz to 35Hz	6Hz to 35Hz	8 to 45Hz
-3.5	45Hz to 150Hz	50Hz to 150Hz	50Hz to 150Hz	50 to 150Hz

Table 3.3: Rates of decay of turbulent pressure fluctuations on the windward wall of the model

[3-4] Summary

The data acquisition and analysis equipment were described. The turbulent shear layer in which model A was submerged was characterised by a roughness length, z_o, of 0.94mm (model scale) a longitudinal length scale of 0.43m and a longitudinal turbulence intensity at roof height of approximately 20%. The pressure spectra showed the decay rates of the turbulent energy to be comparable with those of other investigators.

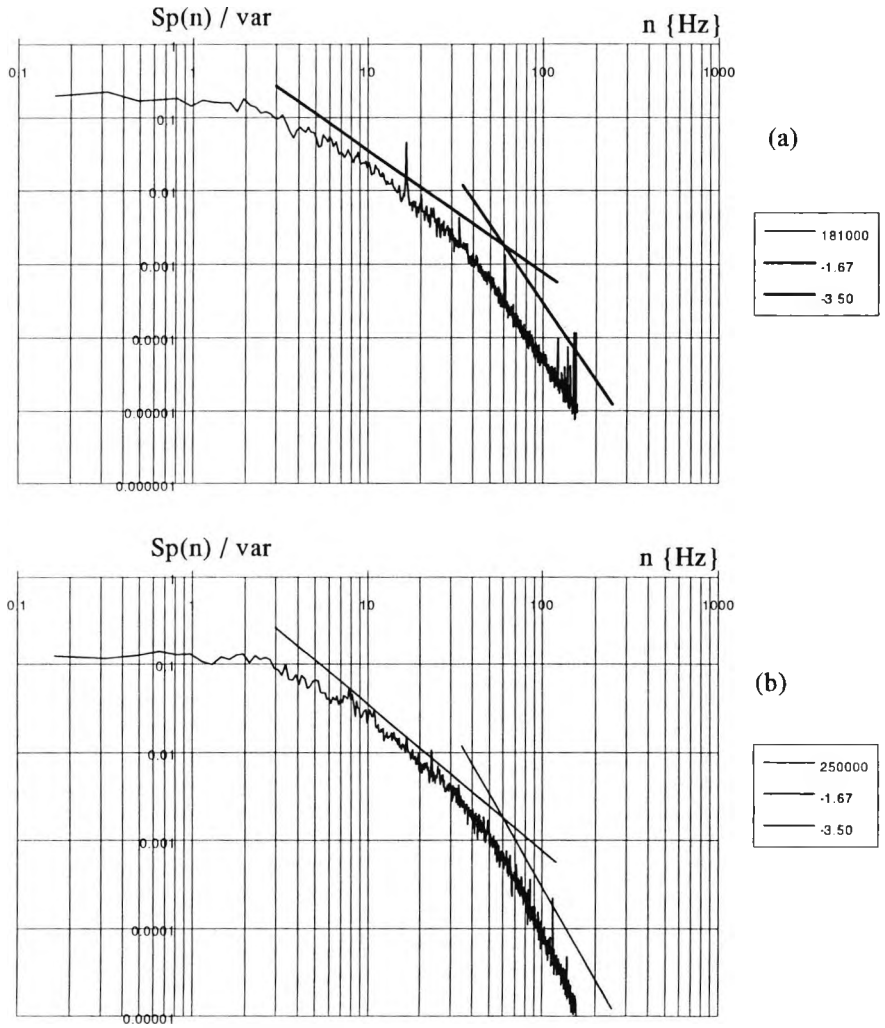

Figure 3.5: Normalised external pressure spectra (at 0.27H & θ = 0 degrees) showing rates of decay of turbulent fluctuations; (a) Re=181000, (b) Re=250000

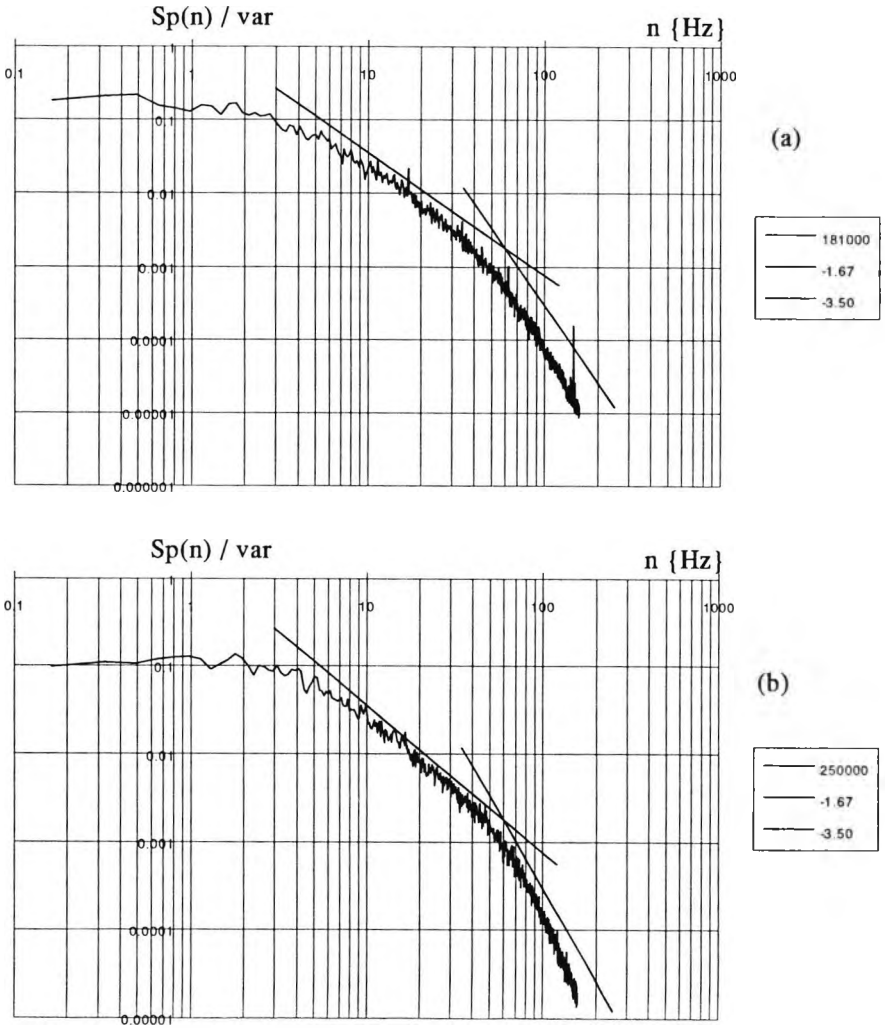

Figure 3.6: Normalised external pressure spectra (at 0.55H & θ = 0 degrees) showing rates of decay of turbulent fluctuations; (a) Re=181000, (b) Re=250000

Chapter 4: Free-Vibration Tests in Still Air

[4-1] Introduction

The results presented were obtained from the damped response of the internal cavity pressure to an excitation in the form of an external pressure pulse. Tests were conducted on two models "A" and "B" in still air. In the majority of cases only the first resonant frequency (ie. the Helmholtz frequency) of each cavity was measured and the associated damping as a fraction of critical was estimated from amplitude decay curve data. The main objectives of the tests reported in this chapter were to obtain realistic estimates of the inertia coefficient, C_I, and to quantify the magnitude of the bulk modulus ratio for models with different envelope flexibilities.

[4-2] Processing of the Results

[4-2-1] Introduction

In the theoretical analysis of chapter two a number of parameters required empirical determination in order for the response of the cavity pressure to be accurately determined. These parameters were the total damping factor at the Helmholtz frequency, ζ_H, the inertia coefficient of the open orifices, C_I, the loss coefficient, C_L, and the bulk modulus ratio, K_a/K_b. Although values for the above quantities have generally been assumed or estimated by previous investigators (e.g. Holmes, 1979; Vickery 1986; Novak & Kassem, 1990(a) & (b)) it was the objective of this chapter to obtain experimental values pertinent to the models under test.

[4-2-2] Determination of C_I and K_a/K_b

The rigid-walled rectangular box, model "B", was used to determine the value of orifice inertia coefficients for orifices of different aspect ratio, defined as the ratio of length to diameter. The resonant frequency for each model configuration was measured and substituted into equation (2.5) in order to calculate the inertia coefficient C_I. It was assumed in this analysis that the flexibility parameter K_a/K_b was zero. Subsequent measurement of the Helmholtz frequency for resonator "A" fitted with a flexible roof enabled K_a/K_b to be estimated (table 4.1) assuming a suitable value for C_I from the results for model "B".

Volume	Tension	f_1 [Hz]	f_2 [Hz]	ζ_1	ζ_2	K_a/K_b
A	Rigid	29.0	N/A	0.039	N/A	0.23
	A	18.4	160.0	0.062	0.022	2.04
	B	15.0	150.0	0.068	0.019	3.59
	C	13.1	141.9	0.073	0.017	5.05
	D	11.0	140.0	0.079	0.017	7.54
B	Rigid	21.3	N/A	0.052	N/A	0.10
	A	16.1	111.6	0.076	0.023	0.91
	B	13.0	96.0	0.078	0.014	1.94
	C	11.2	92.0	0.086	0.013	2.96
	D	10.6	92.0	0.084	0.013	3.45
C	Rigid	17.9	N/A	0.054	N/A	0.02
	A	14.4	95.4	0.056	0.016	0.58
	B	11.8	79.6	0.067	0.014	1.36
	C	10.9	77.3	0.065	0.017	1.76
	D	9.4	72.8	0.067	0.015	2.71

Table 4.1: Results of free-vibration tests on model "A" located in the wind tunnel in still air

[4-2-3] Determination of ζ_H

The damping factors, as a fraction of critical, at the Helmholtz frequency were estimated from the shape of the decay curve envelope, which was assumed to be exponential, after the raw experimental data had been corrected for an off-set in the "zero" value. This correction procedure caused the somewhat "bumpy" appearance of some of the "corrected" decay curves shown in figure 4.1. The assumption of an exponential decay in the magnitude of the pressure fluctuations within the cavity of the resonators appeared to be justified by the linearity exhibited in figure 4.1. Equivalent results for model "A" in the wind tunnel (in still air) are shown in figure 4.2.

[4-3] Presentation of the Results

[4-3-1] Inertia Coefficients & Damping Factors

In an attempt to present the results in a concise manner, both the measured damping factor at the Helmholtz frequency, ζ_H, and the inertia coefficients of the openings, C_I, were expressed as functions of a novel non-dimensional geometric quantity that was dependent only upon the relative physical dimensions of the orifice/s compared with those of the resonator. This quantity was called the "**O**rifice-**R**esonator **D**imension **R**atio" [ORDR], and was defined as,

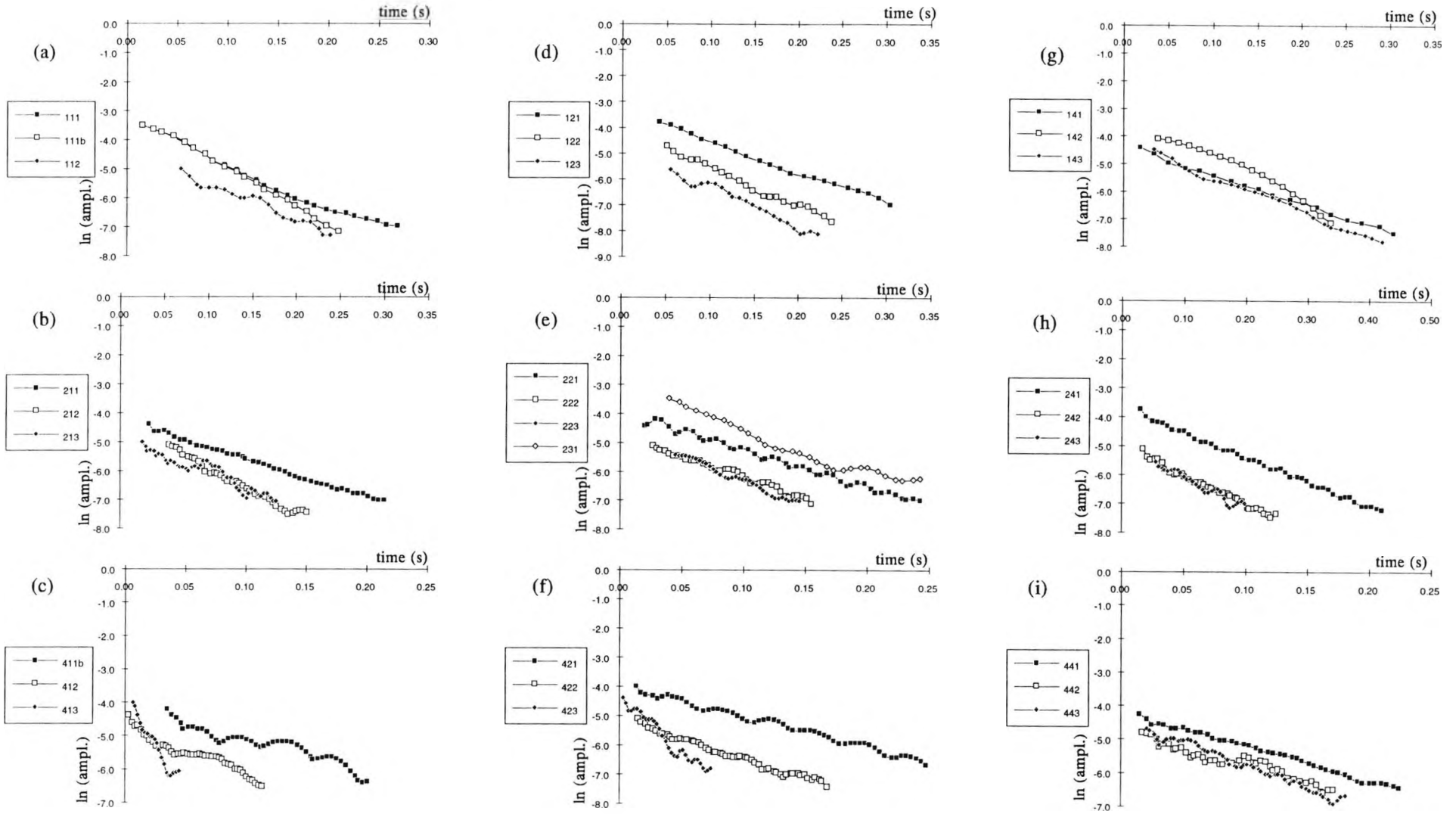

Figure 4.1: Internal pressure damped decay curves for model B (after correction for zero offset). The legends describe the box configuration, e.g. 423 indicates an orifice diameter of 40mm, length 20mm with three identical orifices open.

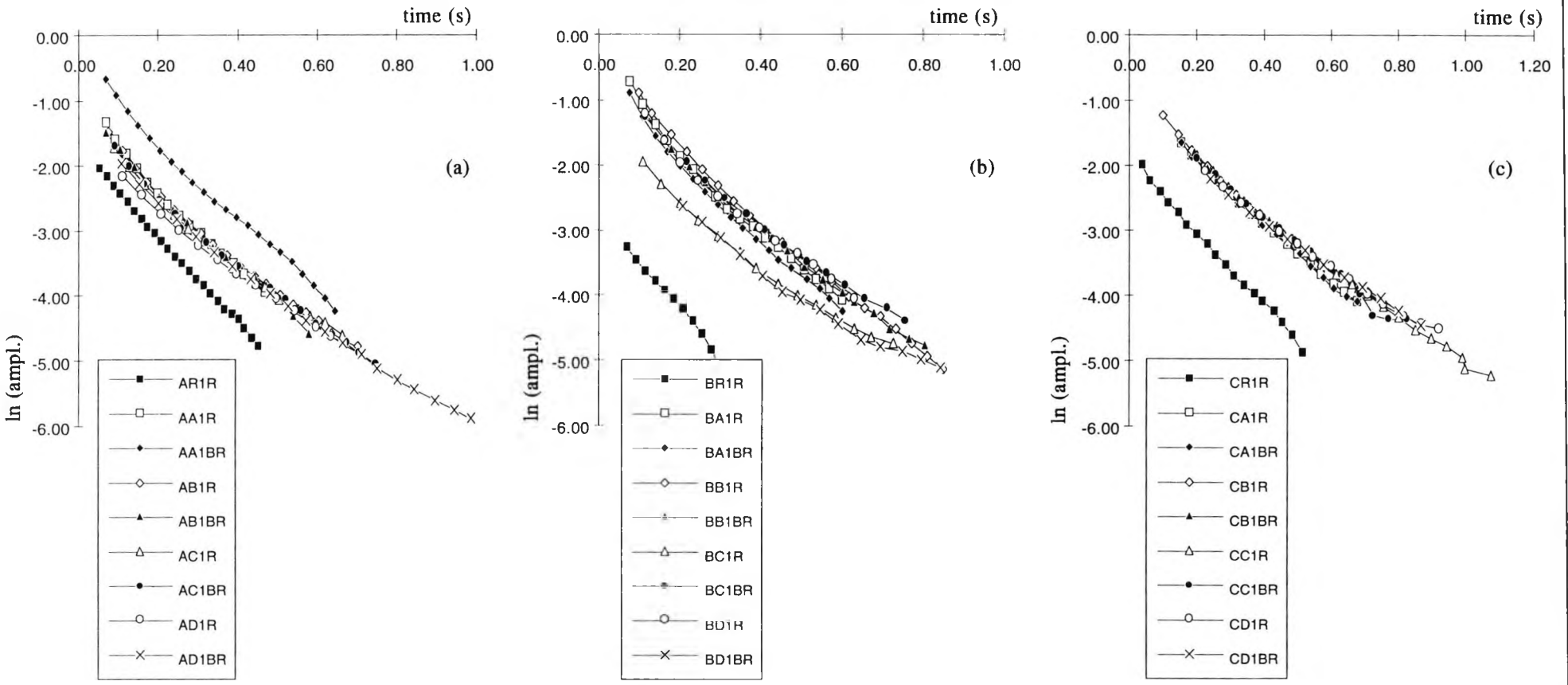

Figure 4.2: Internal pressure damped decay curves (after correction for zero-offset) for model "A". The legends (e.g. "CD1R") refer to the cavity volume (C), the roof tension (D) and "IR" or "1BR" refer to before and after the wind tunnel tests respectively.

$$\begin{aligned} \text{"ORDR"} &= \text{[orifice aspect ratio] x [orifice area/wall area] x [orifice volume/cavity volume]} \\ \text{"ORDR"} &= [l_o/d] \times [NA/A_{wall}] \times [NAl_o/V_i] \\ \text{"ORDR"} &= [Nl_o A]^2 / [dA_{wall} V_i] \end{aligned} \qquad (4.1)$$

where A_{wall} is the total external area of the walls of the resonator that contain the orifices. A_{wall} did not include the area of the "roof" of the model or the additional external wall area due to exaggeration of the internal volume. Figures 4.3 (a-c) and 4.4 (a-c) show the orifice inertia coefficients and damping factors for resonator "B" plotted against "ORDR" on a semi-logarithmic scale. The damping factor estimates of model "A" fitted with a rigid roof are plotted against $\log_{10}$ (ORDR) in figure 4.5.

[4-3-2] Bulk Modulus Ratio

The bulk modulus ratio is a measure of the compressibility of the air contained within the cavity, K_a, compared with the flexibility of the envelope of the building. An estimate for the stiffness of the roof on model "A" was obtained by measuring the natural frequency of the isolated roof, f_{Mi}^2, that is the natural frequency of the membrane with an infinite cavity volume and all orifices open. Figure 4.6 was constructed from the results of experiments on model "A" where the natural frequency of the isolated membrane was measured before attaching any cavity walls to the "basic" model and subsequently related to the estimates of K_a/K_b obtained from the measured Helmholtz frequency (section [4-2-2]).

During the wind tunnel tests it was not convenient to dismantle the model and measure the natural frequency of the "isolated" membrane and so figure 4.6 was utilised to obtain estimates of f_{Mi}^2 from the measured Helmholtz frequency and the physical dimensions of the model. It is apparent that the experimental measure of f_{Mi}^2, included the effects of external added mass and as such cannot be used to directly estimate the roof tension unless the added mass of the membrane can be quantified.

[4-3-3] Free-Vibration Results on the Wind Tunnel Model

Model "A" alone was utilised in the wind tunnel tests but only for the case of a single dominant opening; the results reported above included tests where numerous orifices were open.

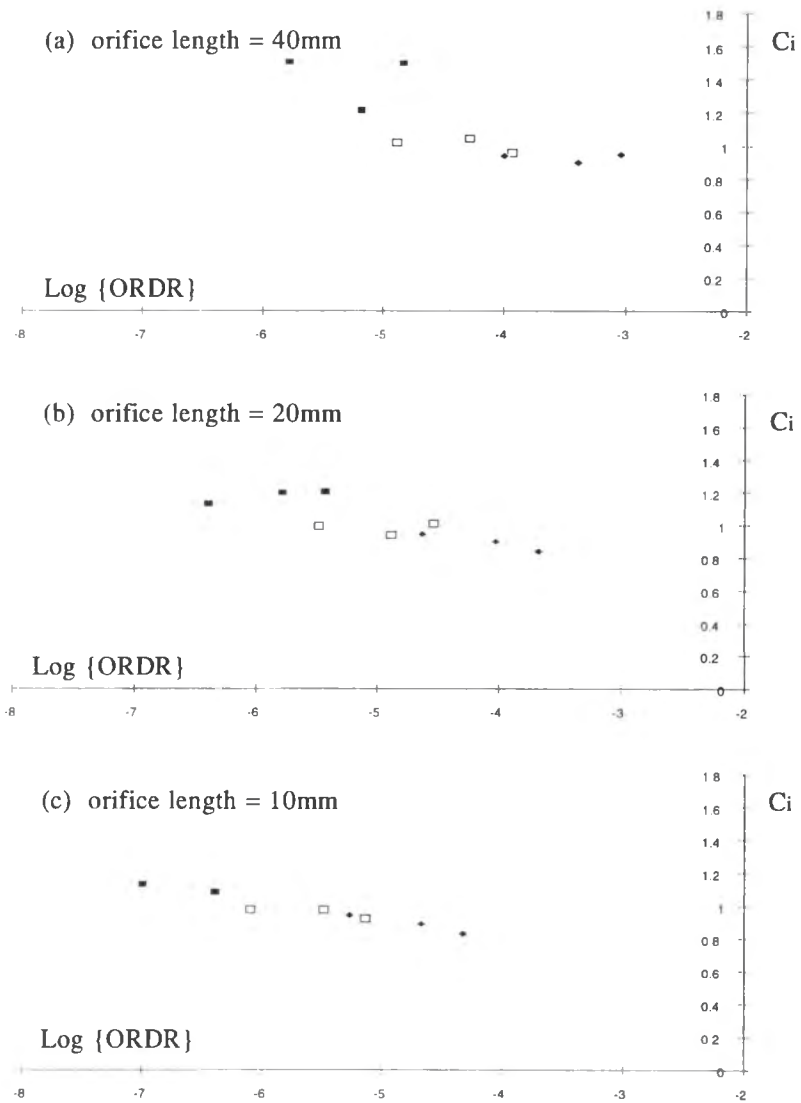

Figure 4.3: Empirical estimates of inertia coefficient from the Helmholtz frequency results for model B.

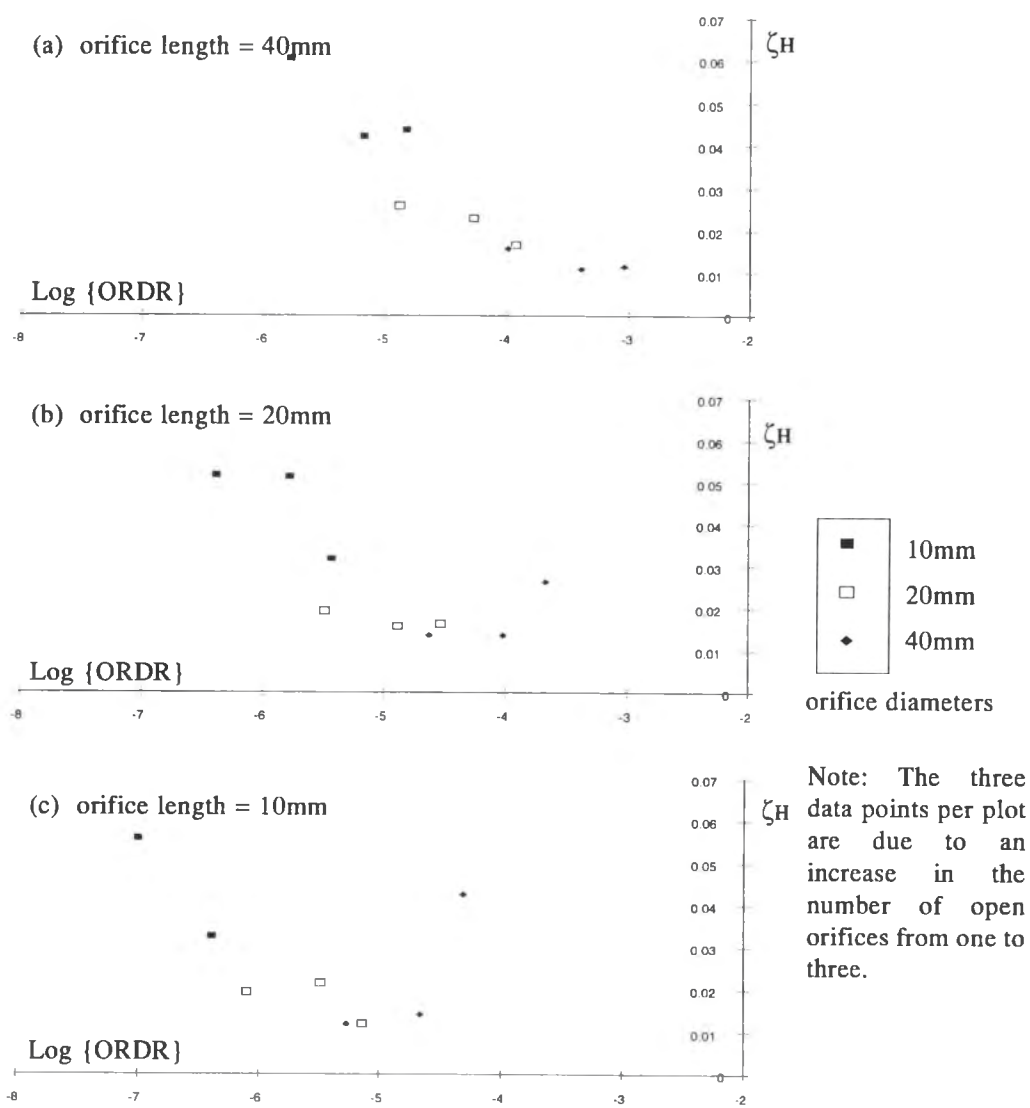

Figure 4.4: Empirical estimates of the damping factor at the Helmholtz frequency for the box model B.

Note: The three data points per plot are due to an increase in the number of open orifices from one to three.

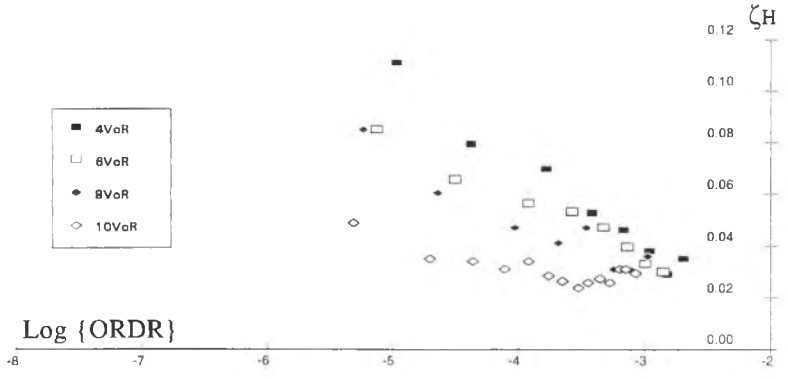

Figure 4.5: Experimental values of damping factor at the Helmholtz frequency for model A fitted with a rigid roof. The independent variable is defined in equation (4.1). Increases in "ORDR" are due to increases in N for four different cavity volumes as indicated in the legend.

Table 4.1 summarises the results from the free-vibration tests on model "A" in situ in the wind tunnel, where estimates for damping and bulk modulus ratio are presented for both rigid and membrane roof configurations.

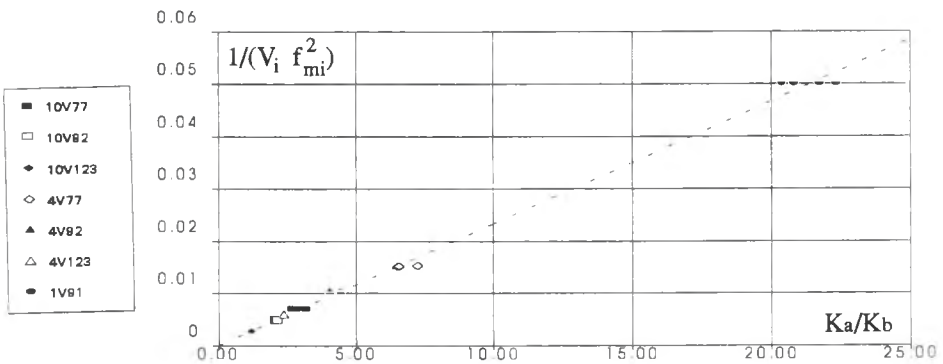

Figure 4.6: Dependence of bulk modulus ratio on cavity volume and frequency of vibration of the isolated membrane roof. The legend denotes the cavity volume, eg. 4V, and natural frequency of the isolated membrane, eg, 123Hz.

[4-4] Discussion of Results

All the results presented in this chapter were obtained in still air for openings of circular cross-section.

[4-4-1] Rigid Model "B"

The results of figure 4.3 showed that for a particular length of orifice, increases in the open area, either by increasing the number of openings or by increasing the diameter of the openings, generally reduced the value of the inertia coefficient. The rate of this reduction was dependent upon the length of the orifice being approximately

linear for openings of length 10mm and increasingly non-linear for orifices of length 20mm and 40mm. The commonly quoted theoretical inertia coefficient of 0.89 for circular orifices (eg. Holmes, 1979) appeared to coincide with the lower limit of the results in figure 4.3. A possible explanation for the correlation between large values of C_I and orifices of high aspect ratio (see figure 4.3) may be the existence of a more stable "jet-type" flow in the immediate vicinity of the exit plane of the longer openings. This hypothesis is illustrated in figure 4.7.

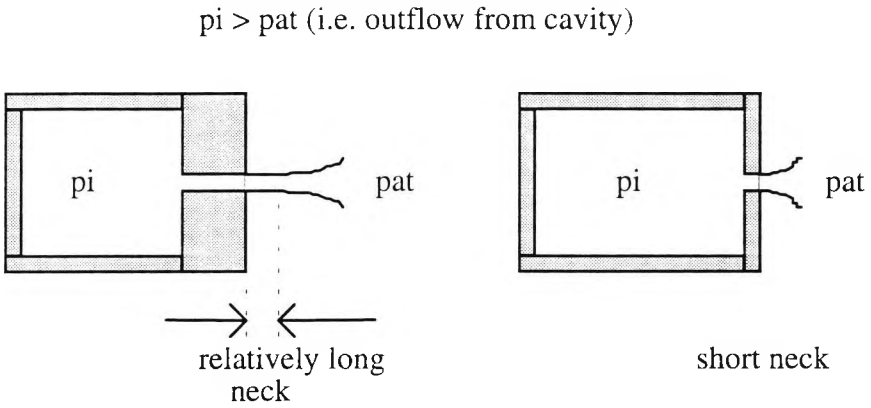

Figure 4.7: A diagram of the possible differences between the flows for high aspect ratio and low aspect ratio orifices.

The total damping at the Helmholtz frequency also showed a systematic dependence upon ORDR and l_o (figure 4.4). Starting with openings of diameter 10mm, it was apparent that an increase in the ORDR generally diminished the total damping at each value of l_o. This change was attributed to a reduction in the flow losses due to viscous dissipation. However, there was a limit to this drop in damping which was characterised by a minimum value of ζ_H at a "critical" value of ORDR where the critical ORDR appeared to be dependent upon the orifice length, l_o.

Increases in ORDR beyond $[ORDR]_{crit}$ effected an increase in total damping for orifices of length 10mm and 20mm but for for openings of length 40mm the critical ORDR was not exceeded. The magnitude of the minimum value of ζ_H was independent of l_o and marked the boundary between damping at the Helmholtz frequency that was dominated by viscous losses and damping that was dominated by losses due to acoustic radiation. This result is summarised in figure 4.8.

The apparent relationship between $[ORDR]_{crit}$ and l_o is shown more clearly in figure 4.9 which was constructed from the results in table 4.2. A comparison was made between the results from rigid model "B" and from rigid model "A" (figure 4.5) and an estimate of ORDR assuming N=3 for the model used by Kassem and Novak (1990) [K&M] was also included. K&M concluded that the Helmholtz mode of their model

model was principally damped by acoustic radiation a conclusion that appeared to be consistent with the results of the present tests for openings of length 10mm.

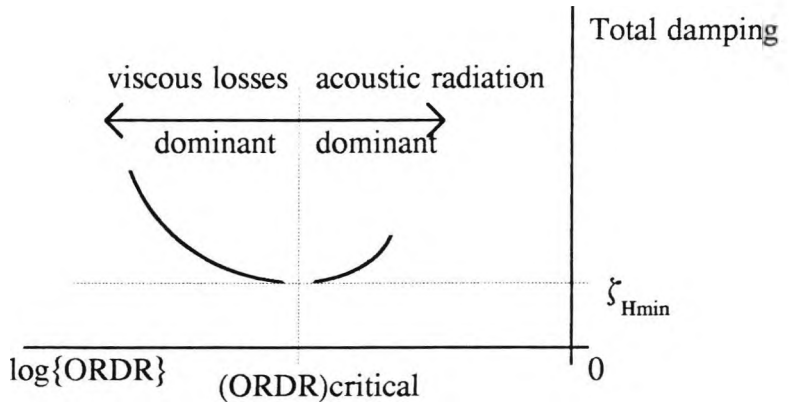

Figure 4.8: Diagram of the behaviour of the total damping at the Helmholtz frequency versus the ORDR.

$\log_{10}[ORDR]_{crit}$	l_o (mm)	source
-3.2 to -2.9	40	fig. 4.4a
-4.46	20	fig. 4.4b
-5.14	10	fig. 4.4c
-2.4 to -2.7	50	fig. 4.5
-5.80	10	N&K (1990) for N=3

Table 4.2: Estimates of the critical ORDR for openings of different length

It is evident from the above discussion that the orifice length, l_o, is a significant parameter in determining the magnitude of the damping for an Helmholtz resonator. Although the orifice length was not normalised, the results in figure 4.9 may be used as a guide when designing a scale model building with openings if the internal pressure dynamics are of interest. In general the philosophy applied to damping of physical models is to ensure that the scaled damping is less than that which is likely to occur at full-scale so that the resultant response will be conservative. Employing this practice here would mean that, within the constraints of wall flexibility, the wall thickness (ie. length of orifice) should be selected so that the ORDR is critical.

A direct extension of the above findings to actual buildings would require investigation of the dominant mechanisms that dissipate internal pressure fluctuations at full-scale. Normalisation of l_o by a suitable reference length may permit extrapolation of the above results, however, a suitable reference length was not identified and this process is not recommended without the support of full-scale data. Novak & Kassem (1990(a) & (b)) cite structural and acoustic radiation damping as the principal damping mechanisms at work in a membrane roof structure backed by a cavity with openings, whereas, Vickery & Georgiou (1991) in a theoretical analysis

of a similar structure consider only the losses due to flow through the openings. A qualitative assessment of the above comments using the results of figure 4.4 would seem to imply that both sets of authors are correct.....dependent upon the geometries of the openings on the building.

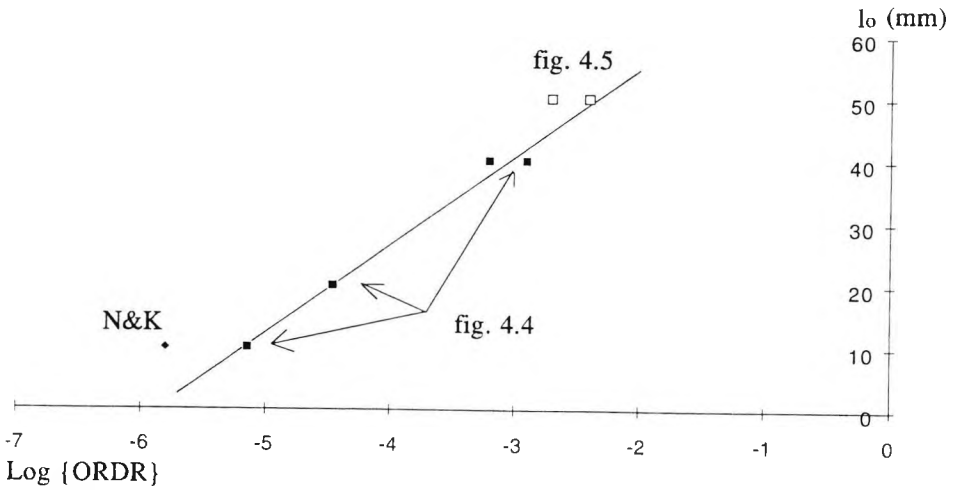

Figure 4.9: Relationship between orifice length and $[ORDR]_{crit}$

[4-4-2] Model "A"

Based upon the generel trends exhibited in figure 4.4 it was possible to infer from figure 4.5 that: damping for resonator "A" was subcritical for small open areas (ie. viscous losses predominated), increases in cavity volume caused a reduction in the total damping, and increases in ORDR reduced ζ_H to a minimum the magnitude of which appeared to be independent of cavity volume.

Table 4.1 summarises the range of bulk modulus ratios that was covered during the wind tunnel tests and is a useful introduction to the "wind-on" results presented in the remaining chapters. Three different cavity volumes, denoted as $A < B < C$, were tested in the wind tunnel and at each volume five different roof tensions were tested, denoted in order of decreasing tension as RIGID, T_A, T_B, T_C, and T_D. Although there were some difficulties in obtaining identical values of membrane tension for each size of cavity (ie. T_A for volume A equal to T_A for volumes B and C) this was approximately achieved using the results of figure 4.6 to determine the natural frequency of the isolated membrane roof (table 4.3). Linear regression analysis of the data points in figure 4.6 produced a "best-fit" line with a gradient of 1/428.33. The frequencies contained in the first column of table 4.3 may be thought of as those for an equivalent membrane roof and were computed as a check on the similarity of experimental conditions between rigid roof configurations. It was noted that the

frequency estimate for volume C was roughly a factor of two greater than that for volumes A and B!

	Rigid	Ta	Tb	Tc	Td
Va	*419.1*	140.7	106.1	89.4	73.2
Vb	*462.5*	153.3	105.0	85.0	78.7
Vc	*852.7*	158.3	103.4	90.9	73.3

Table 4.3: Estimated natural frequencies (in Hz) of the "isolated" membrane roof on model "A" in the wind tunnel

The frequencies and damping factors in table 4.1 denoted by the subscript "$_1$" are those for the Helmholtz mode (1st mode), whereas values for the second mode are denoted by the subscript "$_2$". The latter set of results are included for the sake of completeness and as a reference to the spectral and gain results presented in later chapters where these higher modes can be seen but their significance is small because of the low energy content of the wind at these higher frequencies. The damping results for the Helmholtz mode showed an increase as the roof tension was reduced for volume A because of additional damping due to the roof displacement, however, this trend was not repeated for volumes B or C. The bulk modulus results showed that for the "same" membrane tension increases in cavity volume reduced the measured K_a/K_b as shown earlier in figure 4.6. Both modes exhibited a reduction in frequency as the cavity size increased.

[4-5] Summary

The orifice inertia coefficients and the total damping factors at the Helmholtz frequency were expressed in terms of a novel non-dimensional parameter called the "ORDR". The total damping was comprised of acoustic radiation damping and losses due to viscous dissipation and a critical value of the ORDR marked the boundary between the predominance of either of these two mechanisms. Longer orifices were associated with higher values of inertia coefficient. The results of table 4.3 should be referred to in conjunction with the "wind-on" results presented in subsequent chapters. It was shown that damping at the Helmholtz mode for resonator "A", fitted with a rigid roof, was dominated by viscous losses. Addition of a flexible roof to model "A" with a cavity volume of A caused an increase in total damping as tension was reduced, however, such a trend was not observed for volumes B or C.

Chapter 5: External Pressure Distribution

[5-1] Introduction

This chapter presents the results for the external pressure distribution around the model. Initially, the pressure acting on the vertical walls is described and this is followed by a summary of the pressures acting on the rigid roof of the model. Mean and root-mean-square pressure coefficients are presented as well as the power spectra in the familiar $n.S\{n\}/\sigma^2$ versus $\log\{n\}$ format.

[5-2] Wall Pressures

[5-2-1] Mean Wall Pressures

The surface-mounted circular cylinder used in the wind tunnel tests was categorised as a squat cylinder based upon its slenderness ratio, H/D, of 0.25. Cook (1989) defined squat cylinders as having $2H/D < 1$. Vertically mounted cylinders are also characterised by a mean pressure distribution which for design purposes may be assumed to be invariant over the height of the cylinder. Collation of experimental results from a number of sources, e.g. Sabransky & Melbourne (1987) and MacDonald et al (1988), permitted Cook (1989) to conclude that in the range $0.5 < H/D < 2$ the mean circumferential pressure distribution can be represented by the expression

$$C_p = k \sum [A_n \cos n\theta]. \qquad (5.1)$$

where k is a factor, A_n are the Fourier coefficients, θ is the angular position of the point of interest measured from the windward stagnation point and n are the harmonics which are reproduced in table 5.1 together with the pertinent Fourier coefficients. The factor k is a function of the sign of the mean pressure; it is equal to one for +ve mean pressures and $1+\log\{H/D\}$ for suction pressures. Cylinders with a slenderness ratio greater than two or less than a half were catered for by assuming that the wind loading was the same as that for $H/D=2.0$ and 0.5 respectively.

Using equation (5.1) the "theoretical" pressure distributions for three cylinders of aspect ratio 0.5, 1.0 and 2.0 were computed and the results are shown in figure 5.1. The primary effect of reducing the slenderness ratio was to reduce the magnitude of the suction lobe as an increasing proportion of the flow went over the top of the cylinder. The pressure distribution in the positive pressure region was independent of

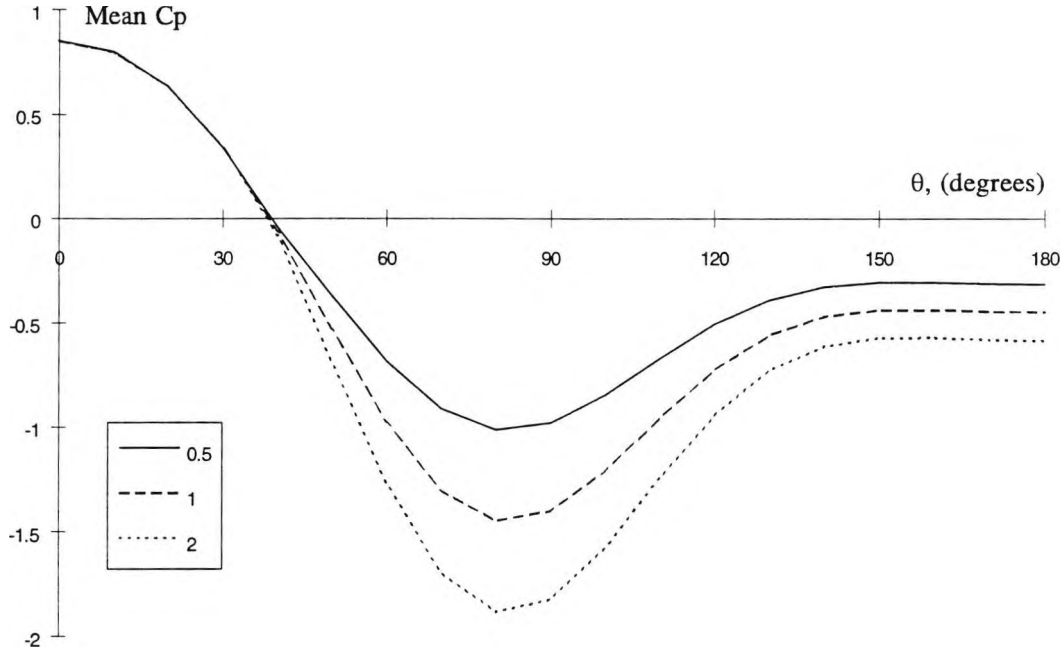

Figure 5.1: Theoretical mean pressure distribution (using equation 5.1) around circular cylinders of different slenderness ratio, H/D.

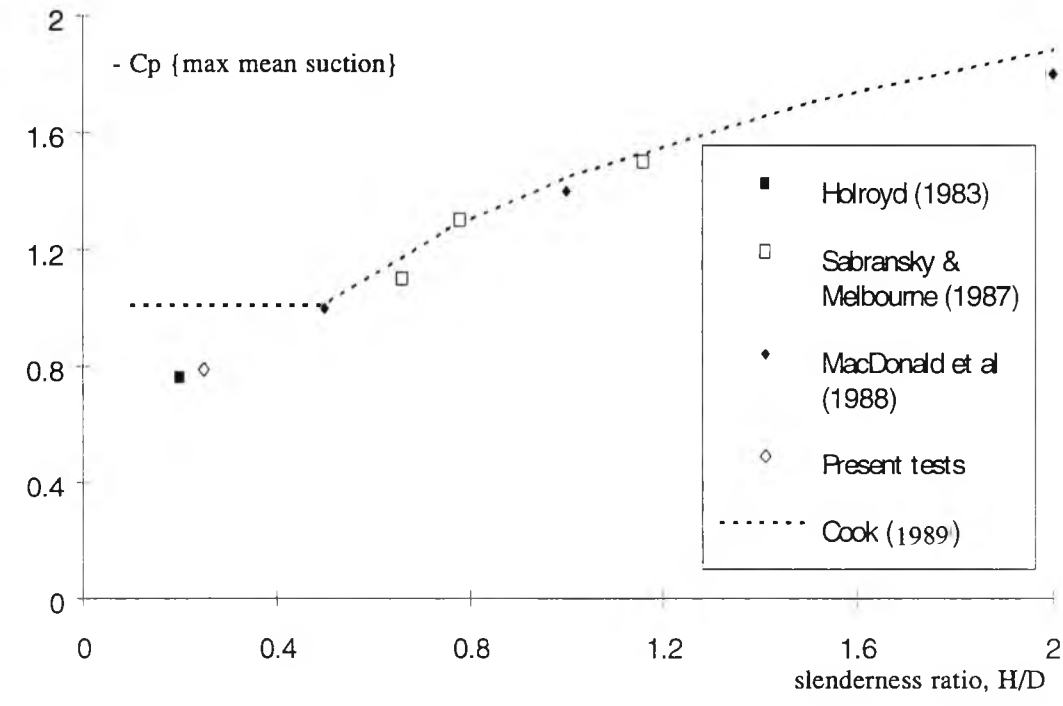

Figure 5.2: Maximum mean pressure coefficient as a function of circular cylinder slenderness ratio

the slenderness ratio and flow separation was evident in the lee of the cylinder by a constant pressure region over the range $140^{o}<\theta<180^{o}$.

Harmonic, n	Fourier coefficient, An
0	-0.5
1	0.4
2	0.8
3	0.3
4	-0.1
5	-0.05
6	0
7	0

Table 5.1: Fourier coefficients for use in equation 5.1

The form of the mean pressure distribution around a circular cylinder at full-scale Reynolds numbers ($2x10^{7}$) was shown in Batham (1985) where the results obtained by Tunstall (1974) on a chimney at Fawley power station were reproduced. At the front stagnation point the pressure coefficient was 1.0 and this fell to zero at around 33^{o}. The flow continued to accelerate around the chimney until the peak suction Cp of around -1.7 was reached at $\theta=78^{o}$. The adverse pressure gradient around the lee of the chimney decelerated the flow until separation occurred at $\theta=120^{o}$ forming a relatively constant-pressure wake region where Cp=-0.3. This description is generally applicable to "infintely" long cylinders where the flow is essentially two-dimensional and supercritical.

Based upon the above it was clear that for structural loading the two most significant regions of the flow were near the front stagnation point and some 80^{o} aft of this point where the maximum suction occurred. The former load was invariant with changes in H/D, whereas, the maximum suction load was dependent upon H/D as shown in figure 5.1 and in more detail in figure 5.2. The results from Sabransky & Melbourne (1987) and MacDonald et al (1988) were plotted against slenderness ratio and as expected the predictions using equation (5.1) were seen to closely follow the experimental results for maximum mean pressure coefficient (see figure 5.2). However, further reductions of the slenderness ratio to 0.25 and 0.2 by this author and Holroyd (1983) respectively implied that for squat cylinders the "theoretical" method outlined above overestimated the maximum mean suction by around 20%. It should be noted that Holroyd used a reference dynamic pressure postitioned at H/2; the value shown in figure 5.2 was corrected to a reference location at H for consistency with the other results.

Comparison of the theoretical and experimental mean pressure distributions shown in figures 5.1 and 5.3(a)-(c) revealed a fundamental difference in the flow regimes around the cylinders. The results using equation 5.1 all exhibited a constant pressure wake region which occurred some 130^{o} to 140^{o} aft of the front stagntion point, whereas, the present tests did not reproduce this characteristic of the flow at either of the two vertical stations 0.27H or 0.55H. Instead there was a steady recovery of the pressure around the leeward side of the model to a base pressure ($\theta=180^{o}$) only slightly less than the local static pressure. The question then arose as to the cause of this recovery? Was it due to the proximity of the ground-based families of horseshoe vortices (see Baker (1980)) or to the flow over the free end of the cylinder both of which are highly three-dimensional flow phenomena.

Closer investigation of the results of MacDonald et al (1988) (in particular the family of plots reproduced in figure 1.14) showed that near the free end of a vertically mounted circular cylinder with H/D=1 there was a steady recovery in pressure right around the the cylinder into the base region. Furthermore, full-scale results of the mean pressure distribution around a 240m tall chimney stack (Sageau (1977/78)) exhibited a steady pressure recovery into the base region at a height of 0.98H which was not evident in measurements made at 0.57H and 0.79H.

To this author's knowledge this phenomenon does not appear to have been commented on at any length by previous investigators possibly because for tall cylinders the size of the suction lobe near the free end of the cylinder is reduced by flow over the free end and consequently, the design loads occur some distance from the free end. However, as the slenderness ratio of the cylinder is reduced so the influence of the free-end eventually appears to "swamp" the flow regime up the complete height of the cylinder and thus reduce the overall wind loading experienced by the cylinder. The result presented in figure 5.2 is corroborated by Holroyd (1983) and seems to imply that current design recommendations (Cook, (1989)) lead to overly conservative design loads on cylinders with a slenderness ratio <0.5.

[5-2-1-1] The Effect of Reynolds Number on Mean Wall Pressure

Referring back to figures 5.3(a), (b), & (c) it can be seen that the mean pressure distribution on the external wall of the cylinder was essentially independent of Reynolds number in the range $1.35\text{x}10^{5}$ to $2.55\text{x}10^{5}$. The flow accelerated around the cylinder and reached a minimum Cp of -0.8 some 90^{o} from the windward stagnation point. The adverse pressure gradient around the leeward side of the cylinder decelerated the flow but did not appear to cause the classic separation of the turbulent boundary layer to form a constant pressure wake region for azimuth angles

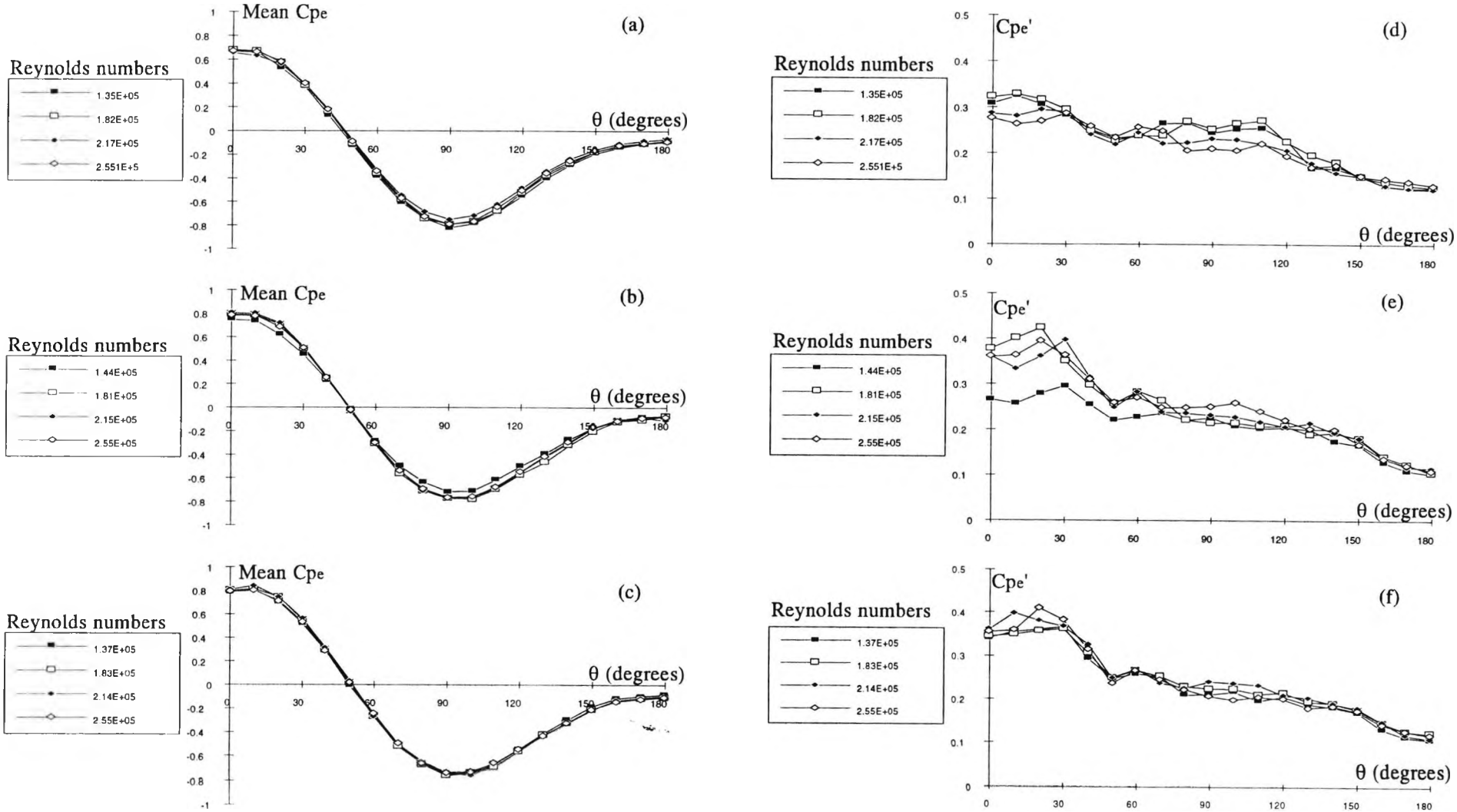

Figure 5.3: Mean (L.H.S.) and r.m.s. (R.H.S.) external, circumferential wall pressure coefficients over a range of Reynolds numbers (shown in legend): z/H = 0.27 (orifice closed) - top; z/H = 0.55 (orifice closed) - middle; z/H = 0.55 (orifice open) - bottom.

greater than 120^{o}. This phenomenon has been widely reported in tests performed on the flow around two-dimensional cylinders (e.g. Panton (1984)). As discussed in the previous section the gradual pressure recovery into the base region of the cylinder was attributed to the proximity of the free-end of the cylinder to the tunnel floor.

In figure 5.3(b), mean pressure distribution at 0.55H, there was a slight reduction in the magnitude of the mean pressure coefficients at the lowest Reynolds number of 1.44×10^5. Because this reduction was experienced right around the cylinder it was attributed to a processing error when applying the correction procedure to the raw data (see Appendix A) and not a Reynolds number effect. Nevertheless, when conducting the main series of experiments, reported in subsequent chapters, Reynolds numbers of 1.8×10^5 and 2.5×10^5 were used.

As discussed in chapter one the concensus from previous investigations is that the mean pressure distribution around a vertically mounted circular cylinder in a sheared flow with a longitudinal turbulence intensity of 15% (measured at roof height) is self-similar for Reynolds numbers greater than 1.0×10^5. This result was corroborated by the present tests which implied that the flow regime was supercritical and thus similar to that expected at full-scale.

[5-2-2] Unsteady Wall Pressures

The root-mean-square (rms) pressure coefficients at 0.27H and 0.55H are shown in figures 5.3(d) and (e). The form of the distributions is not dissimilar to that reported by Holroyd (1983) and to a first approximation could be represented as a linear reduction in the magnitude of the unsteady component of pressure on moving from the windward to the base region. The rms pressure ($\theta = 0^{o}$) at 0.27H is slightly less than that measured at 0.55H whereas in the base region ($\theta = 180^{o}$) this situation is reversed, however, these differences are relatively small.

There is no generally recognised limiting form of the the unsteady pressure distribution around a vertically mounted circular cylinder that implies independence of the external flow from the effects of Reynolds number. However, there does appear to be a degree of self-similarity in the profiles shown in figures 5.3(d) & (e).

[5-2-3] Power Spectra of Wall Pressures

The power spectrum shows the distribution of energy contained within the pressure fluctuations measured at a point (or finite area) over a specified frequency range.

Spectra were measured at five incidences from 0^o to 180^o in 45^o increments and at two different windspeeds of around 9.0m/s and 13.0m/s measured at roof height. The spectra shown are the raw results of the ensemble averages of fifty individual spectral estimates and have not undergone any further form of smoothing (unless stated otherwise).

The spectra at 0.27H (figs. 5.4 and 5.5) generally exhibited a series of very sharp peaks which were attibuted to acoustic noise within the working section of the tunnel (see Appendix A). Nevertheless, it was easy to distinguish the broad-band turbulent energy component of the signals and so no attempt was made to remove the noise for fear of losing a desired part of the signal. The acoustic noise was not so prevalent in the spectra obtained at the higher windspeed (figs. 5.5).

At an azimuth angle of 0^o (figs 5.4(a) & 5.5(a)) the spectra exhibited a broad peak at low frequencies which steadily decayed to zero at higher frequencies. This behaviour was typical of pressure spectra on the windward face of a bluff body where the turbulent energy of the wind at lower frequencies is fully transmitted to the pressure fluctuations acting on the surface of the body. However, at higher frequencies the pressure flucutations generally decay at a faster rate than the velocity fluctuations of the approach flow; a phenomenon which is easily visualised by plotting the spectra in the form $S\{n\}/\sigma^2$ versus $\log\{n\}$. The ratio of the normalised pressure and velocity spectra can be computed to form an admittance function (see for example Simiu & Scanlan (1987)). The effect of the admittance function is equivalent to applying a low-pass filter to the velocity fluctuations in order to obtain the pressure spectrum. Unfortunately, such an admittance function could not be derived from the present tests because an approach flow spectrum was not measured, however, a similar concept was used in this and later chapters to determine the gain function (square root of admittance) of the ratio of two spectra.

The spectra at 45^o, 90^o and 135^o azimuth angles all contained the low frequency peak associated with the integral length scale of the approach flow. However, at 135^o there was an additional marked increase in the energy at higher frequencies implying that smaller scale turbulence was influencing the pressure fluctuations in the lee of the model. This increase in energy at higher frequencies was attributed to building-induced turbulence as described by Eaton & Mayne (1975) on the full-sized two-storey house at Aylesbury. In the base region, the maximum energy in the spectrum had shifted completely to higher frequencies and showed no evidence of the large scale peak associated with the turbulence of the approach flow. This implied that the pressure fluctuations in the wake of the building were generated by relatively small eddies whose scale was related to the dimensions of the wake.

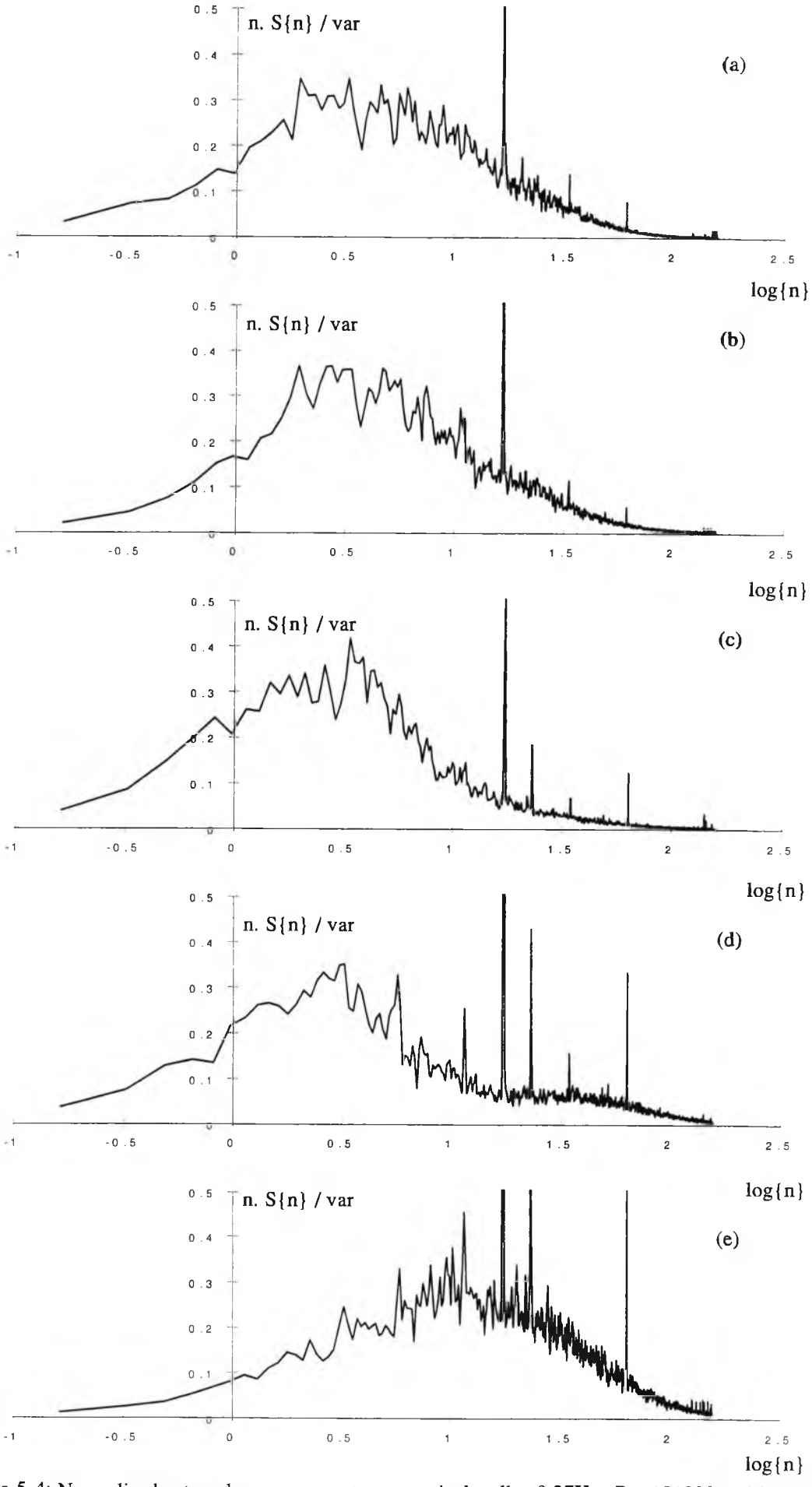

Figure 5-4: Normalised external pressure spectra on vertical wall at 0.27H at Re=181000 and θ equal to (a) 0 degrees, (b) 45 degrees, (c) 90 degrees, (d) 135 degrees & (e) 180 degrees

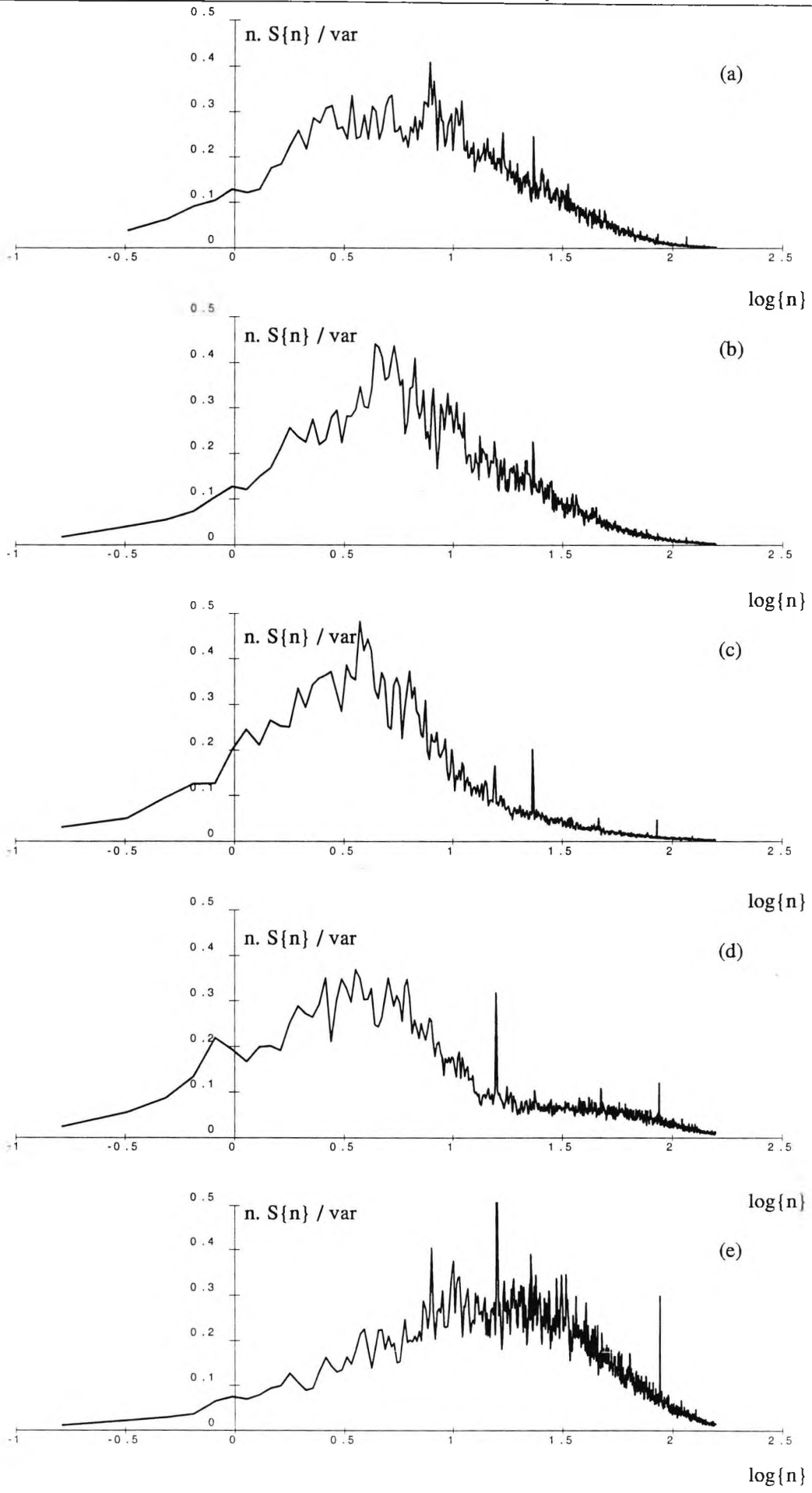

Figure 5.5: Normalised external pressure spectra on vertical wall at 0.27H at Re=255000 and θ equal to (a) 0 degrees, (b) 45 degrees, (c) 90 degrees, (d) 135 degrees & (e) 180 degrees

[5-2-4] Influence of an Open Orifice on External Wall Pressures

[5-2-4-1] Pressure measured directly above an open orifice

A limited series of tests was performed in order to assess the impact of an open orifice in the sidewall of the model on the pressure distribution. Referring to figures 5.3(c) & (f) it was apparent that the presence of the open orifice had little affect on either the mean or the unsteady pressures at a point directly above the open orifice (at 0.55H or 1.1d above the centre of the opening). The Reynolds number independence was maintained along with the overall profile shapes. However, there was a slight increase in the mean pressure on moving from 0^o to 10^o (fig. 5.3(c)) which may have been due to the inflow into the orifice deflecting higher momentum air downwards.

Spectra measured at 0.55H with the orifice open showed no signs of resonance due to the periodic motion of air into and out of the cavity of the model (figs 5.6 & 5.7) and were essentially the same as the spectra measured at 0.27H. A more detailed comparison of the two sets of spectra was made by deriving a gain function as defined below,

$$Gain,\ G2 = \sqrt{\frac{(n.S\{n\}/\sigma^2)_{0.27H}}{(n.S\{n\}/\sigma^2)_{0.55H}}} = \frac{\sigma_{0.55H}}{\sigma_{0.27H}} \cdot \sqrt{\frac{S\{n\}_{0.27H}}{S\{n\}_{0.55H}}} \qquad (5.2)$$

and the graphical results are shown in figures 5.8 and 5.9 (a) to (e).

In the base region the gain functions showed that the spectra at 0.27H and 0.55H were essentially the same at both windspeeds. However, rotating from 0^o to 135^o it was increasingly apparent that there was more energy contained within the small scale turbulence at the higher location and that the rate of decay of this energy across the spectrum was less than that at 0.27H. These effects were most noticeable at $\theta=135^o$.

[5-2-4-2] Pressure Measured Downstream of an Open Orifice at 0.27H

The mean and unsteady pressures were measured (but not spectra) downstream of an open orifice with the orifice orientated at a number of different azimuth angles from 0^o to 180^o in 10^o increments at a single Reynolds of 2.54×10^5. (In the figures ϕ was used to denote the azimuth angle of the orifice and θ denotes the location of the pressure tap; for comparison the reference pressure distributions at 0.27H with the orifice closed are shown as dashed lines).

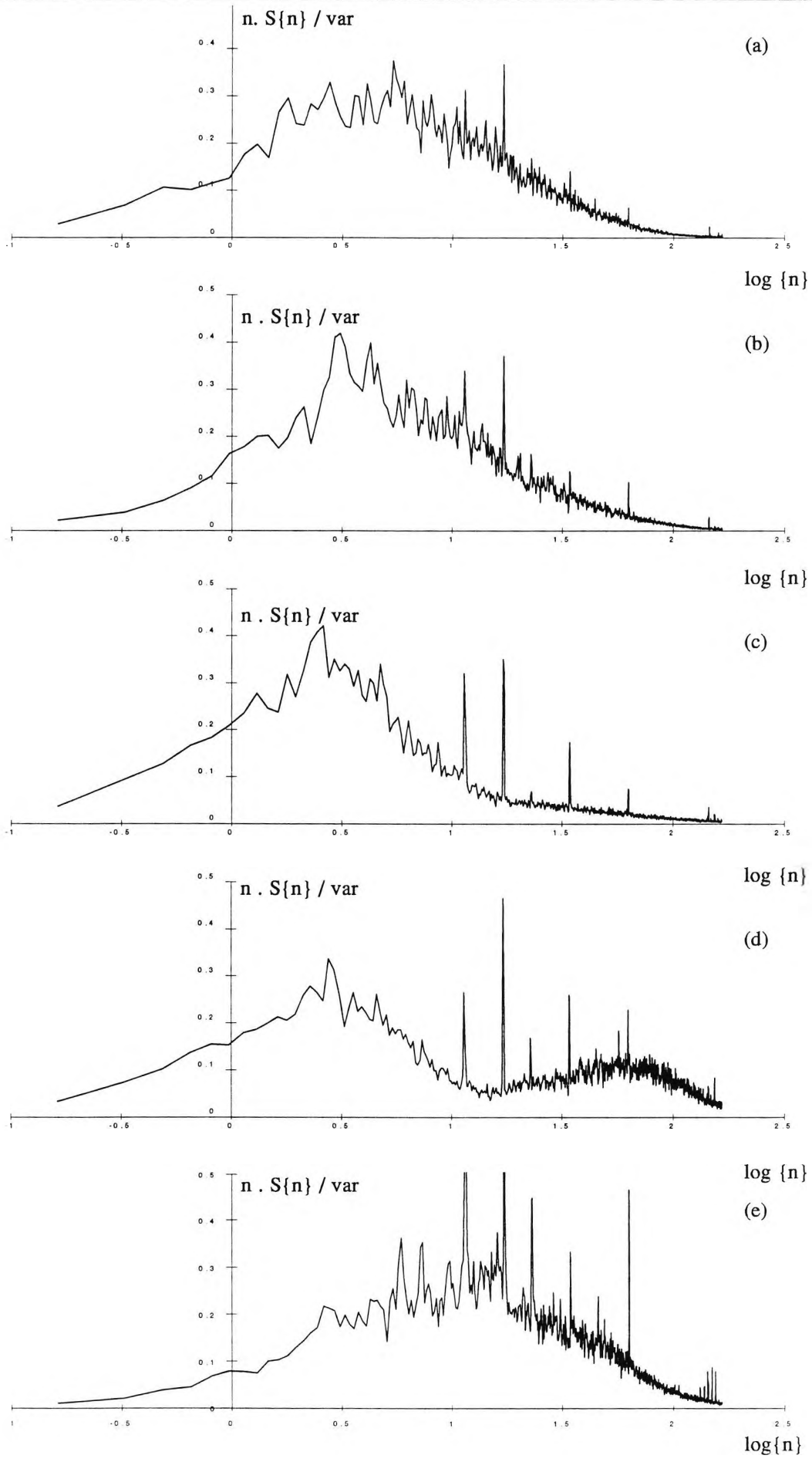

Figure 5.6: Normalised external pressure spectra on vertical wall at 0.55H at Re=181000 and θ equal to (a) 0 degrees, (b) 45 degrees, (c) 90 degrees, (d) 135 degrees & (e) 180 degrees

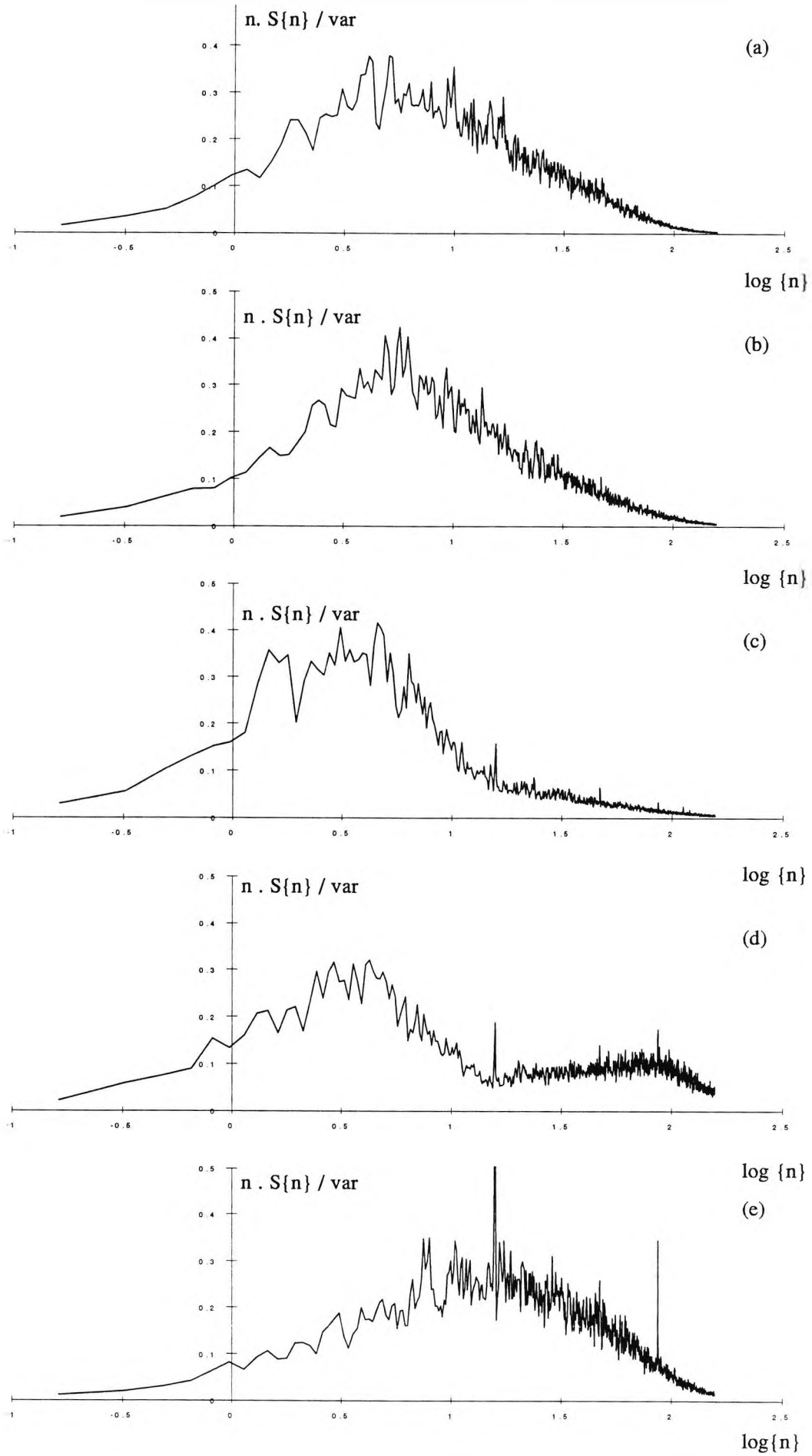

Figure 5.7: Normalised external pressure spectra on vertical wall at 0.55H at Re=255000 and θ equal to (a) 0 degrees, (b) 45 degrees, (c) 90 degrees, (d) 135 degrees & (e) 180 degrees

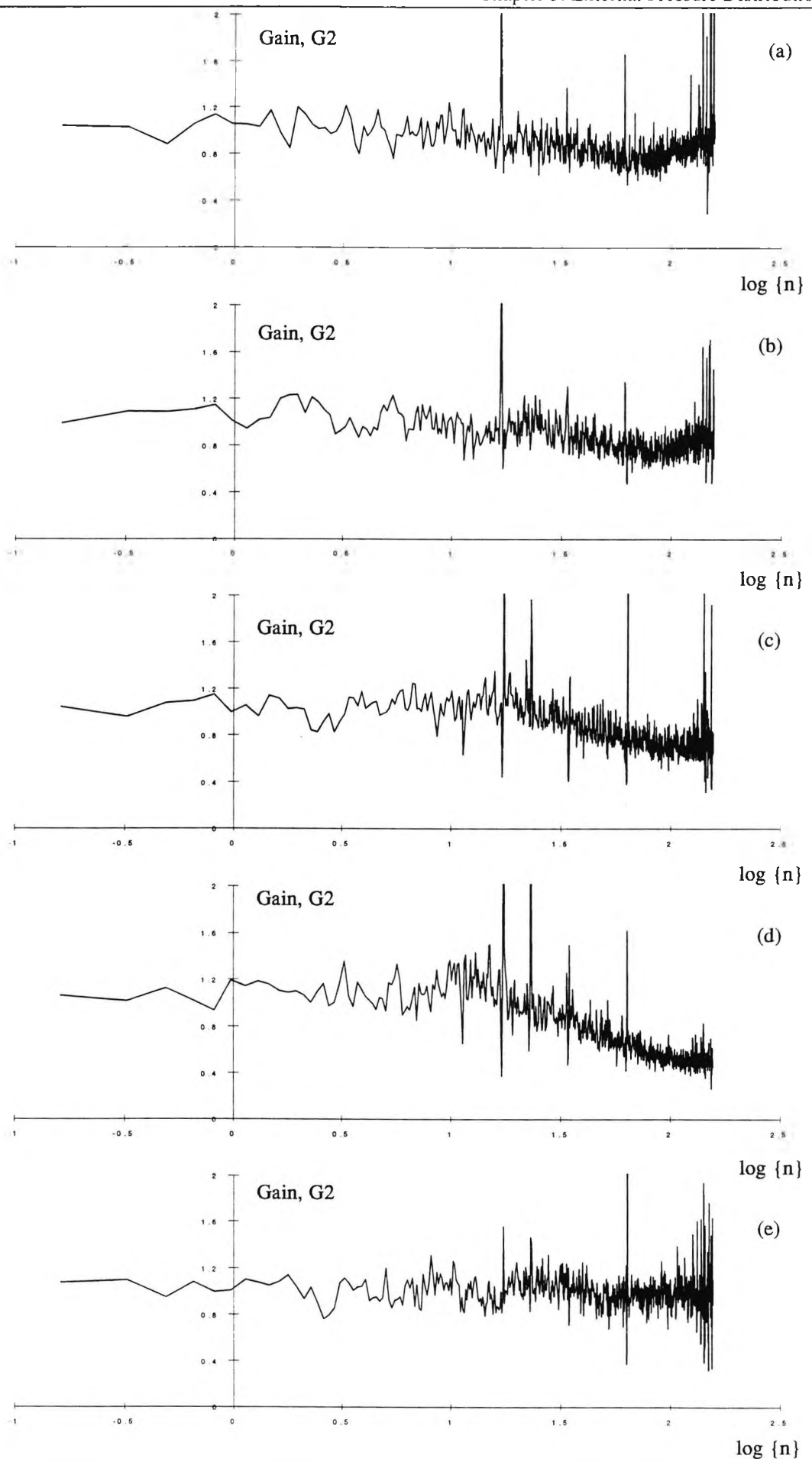

Figure 5.8: Gain functions (equation (5.2)) of pressure spectra on vertical wall at Re=181000 and θ equal to (a) 0 degrees, (b) 45 degrees, (c) 90 degrees, (d) 135 degrees & (e) 180 degrees

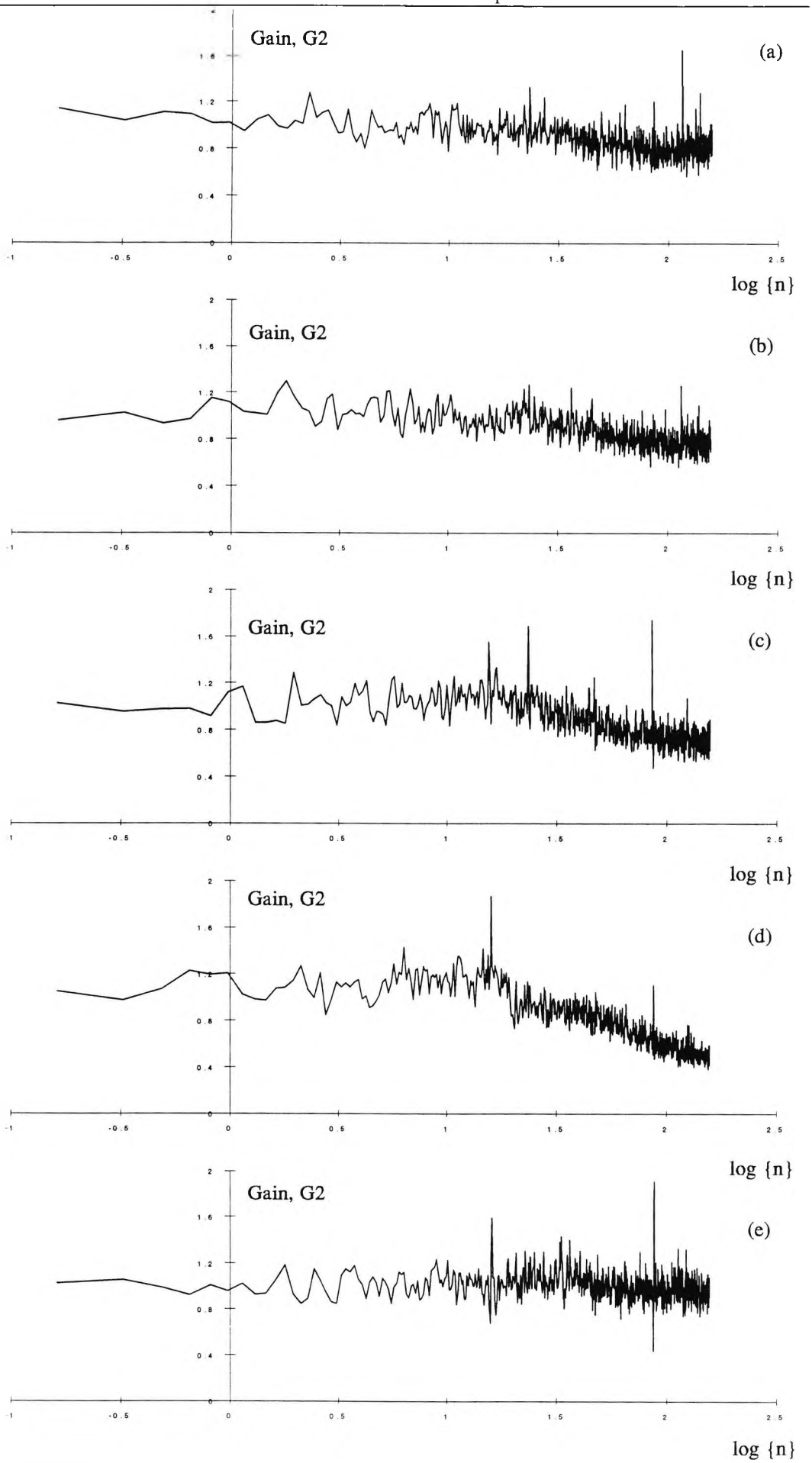

Figure 5.9: Gain functions (equation (5.2)) of pressure spectra on vertical wall at Re=255000 and ϵ equal to (a) 0 degrees, (b) 45 degrees, (c) 90 degrees, (d) 135 degrees & (e) 180 degrees

The mean pressure downstream of the open orifice (fig 5.10) was little affected by the presence of the opening apart from a slightly increased rate of pressure recovery around the leeward face of the cylinder. The magnitudes of the windward stagnation pressure, maximum mean suction and base pressure were all unchanged by the presence of the opening. For the sake of clarity, the unsteady pressure results have been divided into three groups (figs 5.11(a) to (c)). With the orifice oriented between 0^o to 50^o the rms pressure coefficients were seen to follow the reference profile (dashed line) quite well until $\theta=70^o$. Between the limits of $70^o<\theta<120^o$ there was a marked increase in the unsteady pressure which eventually rejoined the reference pressure profile into the base region. For orifice incidences greater than 60^o the presence of the opening did not influence the magnitude of the rms pressure fluctuations further downstream.

The reasons for the increased unsteady pressures may have been twofold. Firstly, the mere presence of the opening would have introduced an irregularity on the surface of the model and thus increased the unsteady pressure fluctuations downsteam of the orifice. Secondly, the oscillating "slug" of air contained within the orifice may have added a resonant component to the downstream fluctuations. Both these processes would have been relatively small-scale phenomena characterised by the size of the opening and the wavelength of the Helmholtz frequency respectively, however, without spectral evidence it was not possible to be any more specific. The constancy of the unsteady pressure in the lee of the model, $110^o<\theta<180^o$, may indicate that the small-scale disturbances introduced by the presence of the opening were either rapidly dissipated or, more likely, were lost in the free-shear layer which formed the boundary to the wake of the cylinder.

[5-2-4-3] Pressure Measured at 0.27H Midway Between Two Open Orifices

Spectral measurements of the pressure fluctuation between *two* open orifices were also made at Reynolds numbers of $1.8\text{x}10^5$ and $2.5\text{x}10^5$ for azimuth angles, θ, (measured between the windward stagantion point and the pressure tap) between 0^o to 180^o in 45^o increments (The corresponding orifice incidences were equal to θ plus and minus 11.25^o. The raw spectral data were converted directly to gain functions defined by

$$Gain,\ G3 = \sqrt{\frac{(n.S\{n\}/\sigma^2)_{0.27H_{open}}}{(n.S\{n\}/\sigma^2)_{0.27H_{closed}}}} = \frac{\sigma_{0.27H_{closed}}}{\sigma_{0.27H_{open}}} \cdot \sqrt{\frac{S\{n\}_{0.27H_{open}}}{S\{n\}_{0.55H_{closed}}}}. \qquad (5.3)$$

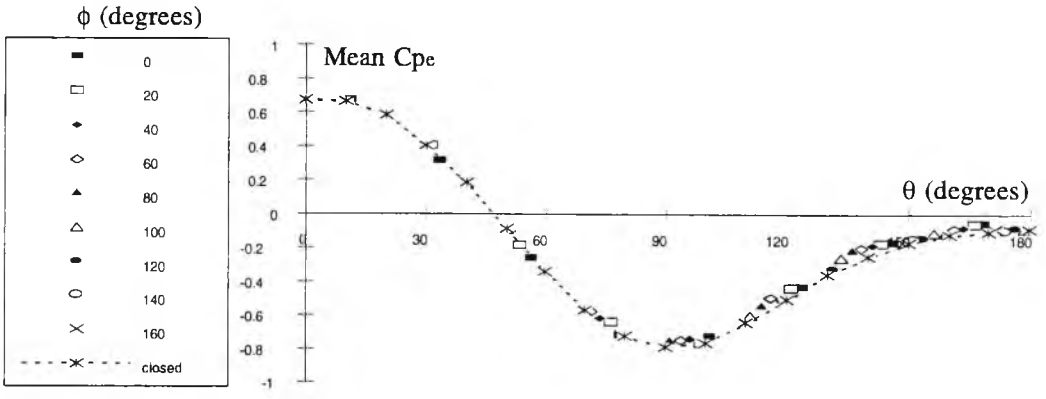

Figure 5.10: Mean pressure distribution at 0.27H downstream of an open orifice at a Reynolds number of 254000. The dashed line is the reference case.

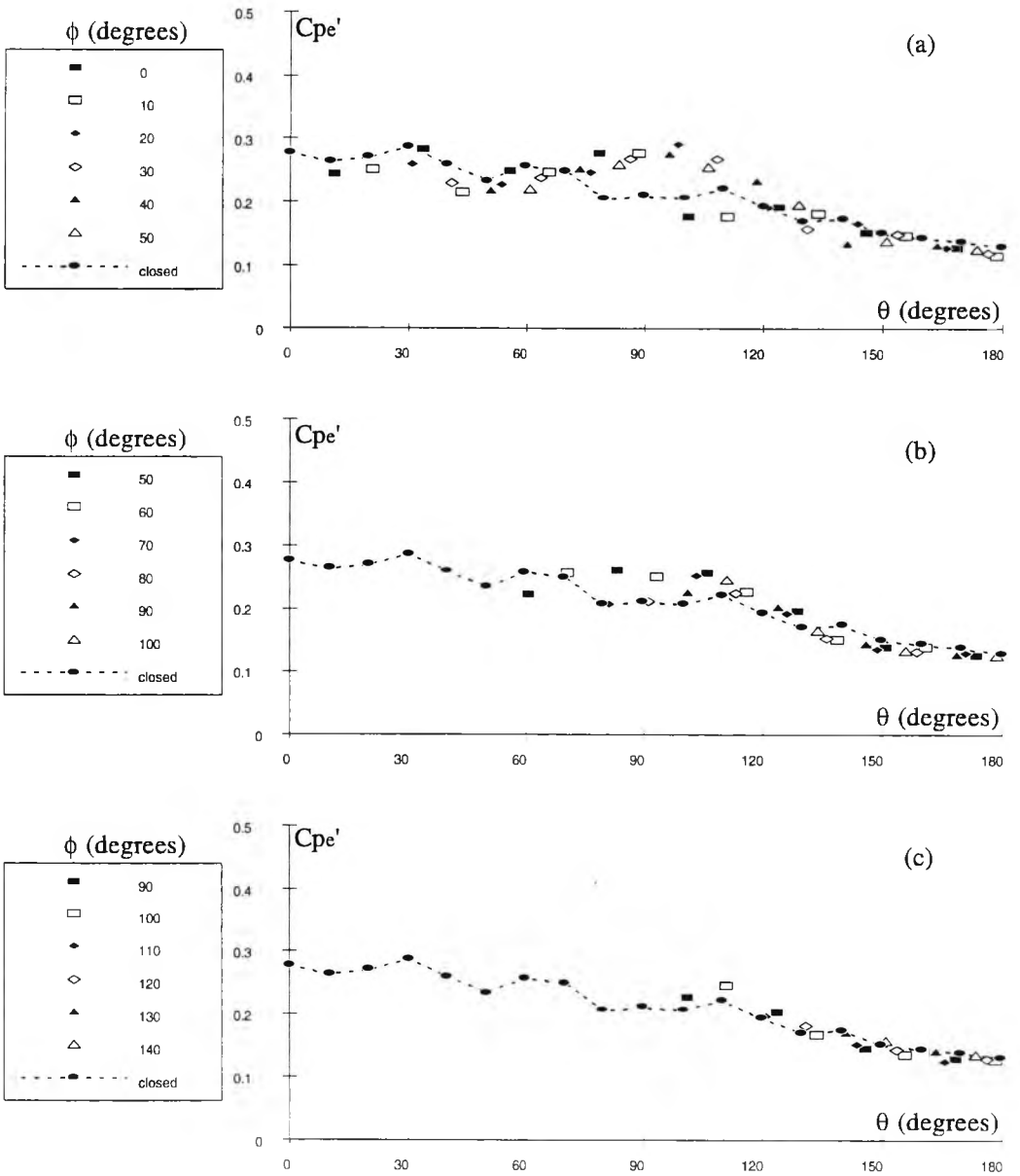

Figure 5.11: Root-mean-square pressure distribution at 0.27H downstream of an open orifice at a Reynolds number of 254000. The dashed line is the reference case.

In contrast to the "G2" functions (figures 5.8 & 5.9) the "G3" gains (figs 5.12 & 5.13) were additionally smoothed by computing the nine-point moving average across the whole frequency range.

At 0^o, 45^o and 180^o the "G3" functions were flat across the whole frequency range. At 90^o the presence of the openings brought about an increased gain at frequencies above 80Hz (approximately) with this increase being greater at the lower Reynolds number. When θ was equal to 135^o the "G3" again showed increased energy levels over the top end of the spectrum, but in addition there was a significant resonant component corresponding to the Helmholtz frequency (shown by the vertical dashed line).

Now whilst, the configuration of the tests reported here differed slightly from those described in the previous section (5-2-4-2) the results seem to confirm that the principal effect of an opening/s was to increase the energy of the small-scale pressure fluctuations over a broad bandwidth and to impart a resonant component to the external pressure fluctuations at certain azimuth angles (narrow-band process).

[5-3] Roof Pressures

[5-3-1] Mean Roof Pressures

Nine pressure taps were equispaced along a radius of the rigid roof of the model beginning at the centre of the roof and ending at D/3 from the centre; this span corresponded to the radius of the flexible roof (see chapter 2). The mean roof pressures were measured at an early stage in the experimental programme using a bank of inclined multitube manometers so unsteady pressure measurements were not obtained. Tests were conducted at a single Reynolds number of 2.5×10^5 because the windward sharp-edge of the roof effectively fixed flow separation at this location. The model was rotated through 180^o in 10^o increments and the corrected pressure coefficients were plotted against radial position for each azimuth angle. Interpolation between data points enabled a contour plot of mean pressure coefficients to be constructed (figure 5.14).

The area of the roof covered by the pressure taps was under a suction pressure. The maximum suction occurred on the upwind side of the roof (top of figure 5.14) and an adverse pressure gradient existed along the roof in the direction of the mean flow. The magnitude of this gradient was reduced on moving downstream.

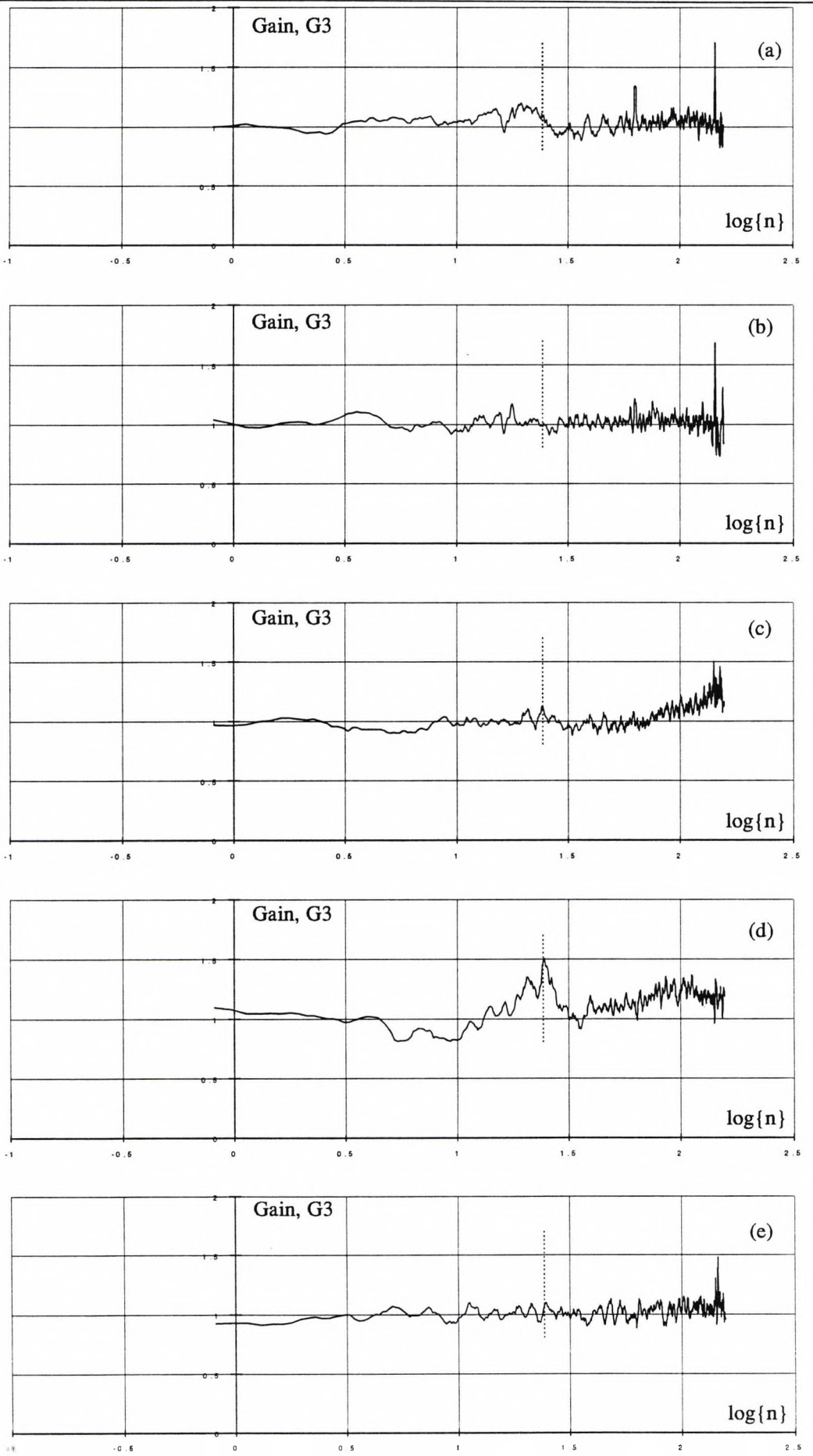

Figure 5.12: Gain functions (see equation (5.3)) of external pressure spectra at 0.27H and incidences of (a) 0 degrees, (b) 45 degrees, (c) 90 degrees, (d) 135 degrees & (e) 180 degrees. Reynolds number of tests was 181000.

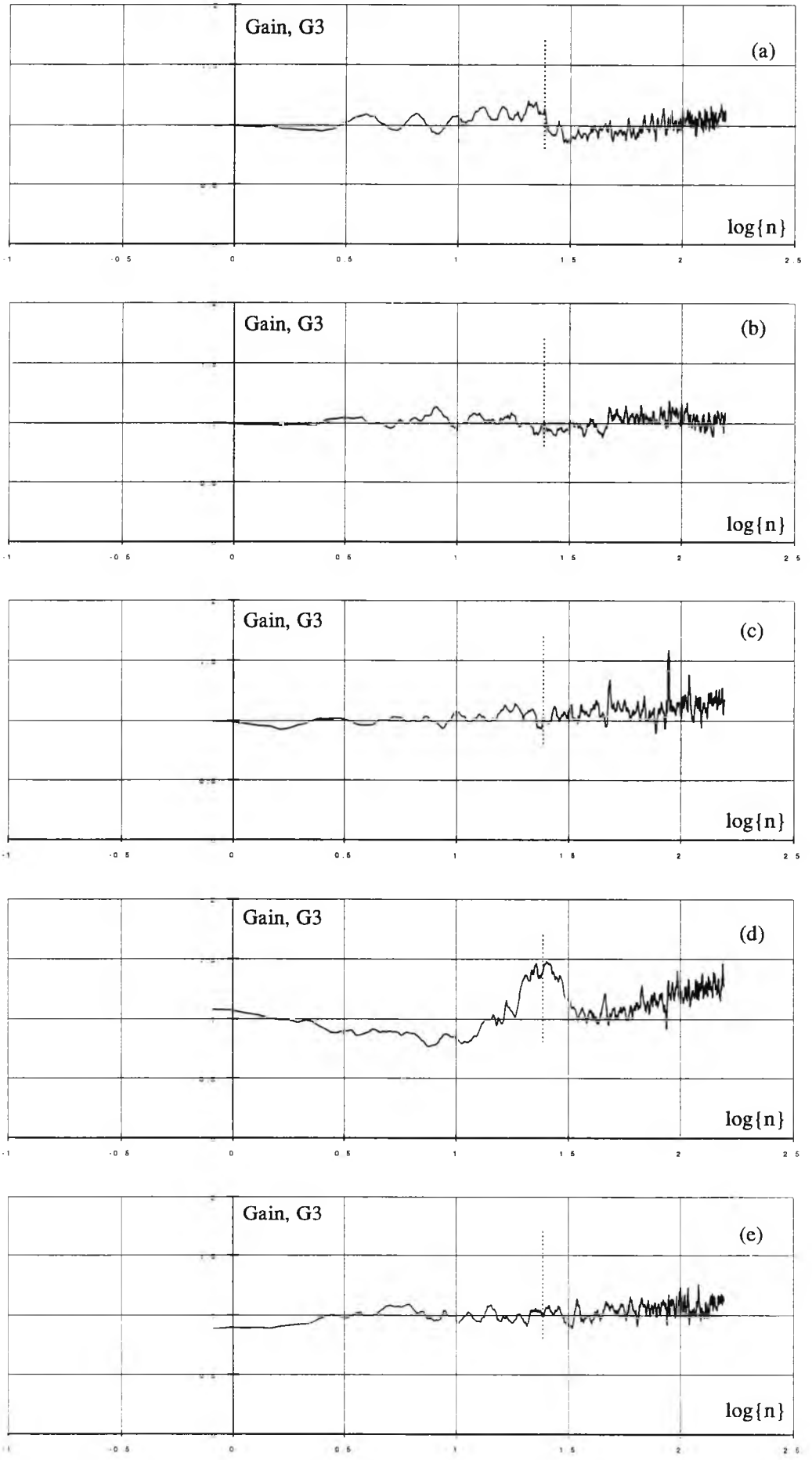

Figure 5.13: Gain functions (see equation (5.3)) of external pressure spectra at 0.27H and incidences of (a) 0 degrees, (b) 45 degrees, (c) 90 degrees, (d) 135 degrees & (e) 180 degrees. Reynolds number of tests was 255000.

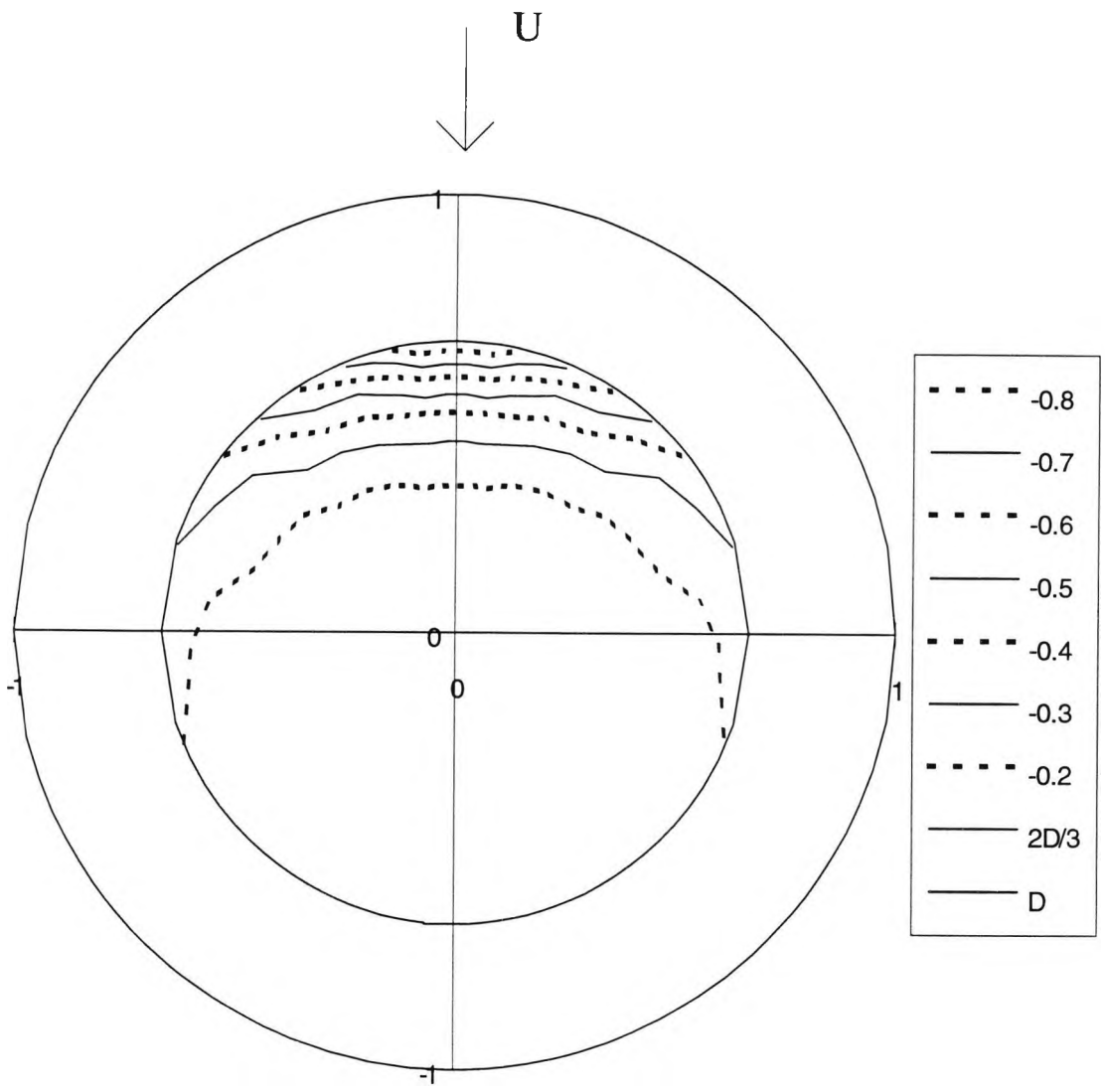

Figure 5.14: Mean pressure contours on the roof of the model (measured in the central portion of the roof only). Legend denotes the mean pressure coefficient commencing with the most upwind value of -0.8; the diameter of the model is also shown for comparison.

The form of the mean pressure distribution was similar to that obtained by Holroyd (1983) with fairly flat pressure contours at right angles to the mean flow which gradually turned into the downstream direction near the edges of the roof. However, whereas the maximum mean suction shown in figure 5.14 was around -0.8, at a similar location Holroyd reported a mean pressure coefficient nearer to -1.0. This discrepancy might be explained by differences in the two boundary layer simulations where the roof height longitudinal turbulence intensity was 22% in the present tests as opposed to a value nearer 14% in the tests of Holroyd. Purdy et al (1967) showed that increasing the turbulence intensity promoted earlier reattachment of the shear layer (which had separated from the leading edge of the roof) and shifted the maximum roof suction in an upstream direction. Such a movement was implied by the results of figure 5.14.

[5-3-2] Unsteady Roof Pressures & Power Spectra

Root-mean-square pressure coefficients at a single radial location of D/6 from the centre of the roof were determined at two Reynolds numbers of 1.8×10^5 and 2.5×10^5 and azimuth angles of approximately 26^o, 71^o, 116^o, 154^o, and 161^o. The r.m.s. pressure coefficients are presented in table 5.2 where it was noted that a reduction in the unsteady roof pressure occurred in the along-wind direction. The magnitude of the rms pressure coefficient was independent of the Reynolds number for the two test cases.

Azimuth (degrees)	Reynolds number = 1.8×10^5	Reynolds number = 2.5×10^5
26	.18	.18
71	.16	.17
116	.12	.12
154	.09	.08
171	.09	.09

Table 5.2: Unsteady pressure coefficients (r.m.s.) on the roof of the model

The unsteady pressures were obtained as a by-product of the spectral measurements shown in figures 5.15 and 5.16. The spectra at the lower Reynolds number (figure 5.15) contained sharp peaks associated with acoustic noise within the wind tunnel but were to a large extent invariant with changes in θ. Re-examination of figure 5.14 showed that the spectra were measured over an area on the roof where the mean pressure coefficients changed by less than 0.1 which was reflected in the fixed frequency distribution of the pressure fluctuations in this region.

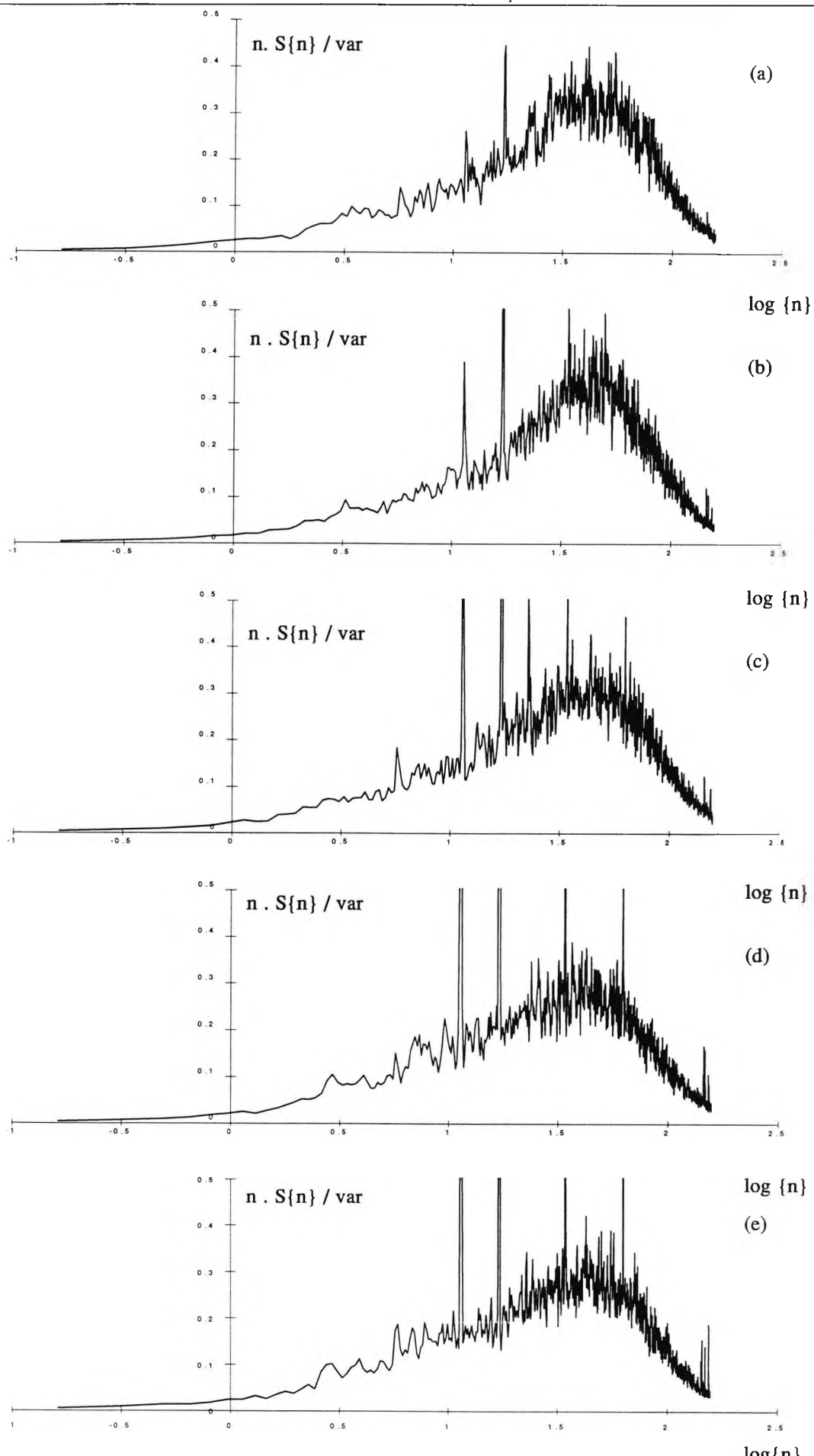

Figure 5.15: Normalised external pressure spectra on roof at x/D=0.17, Re=181000 and θ equal to (a) 26 degrees, (b) 71 degrees, (c) 116 degrees, (d) 154 degrees & (e) 161 degrees.

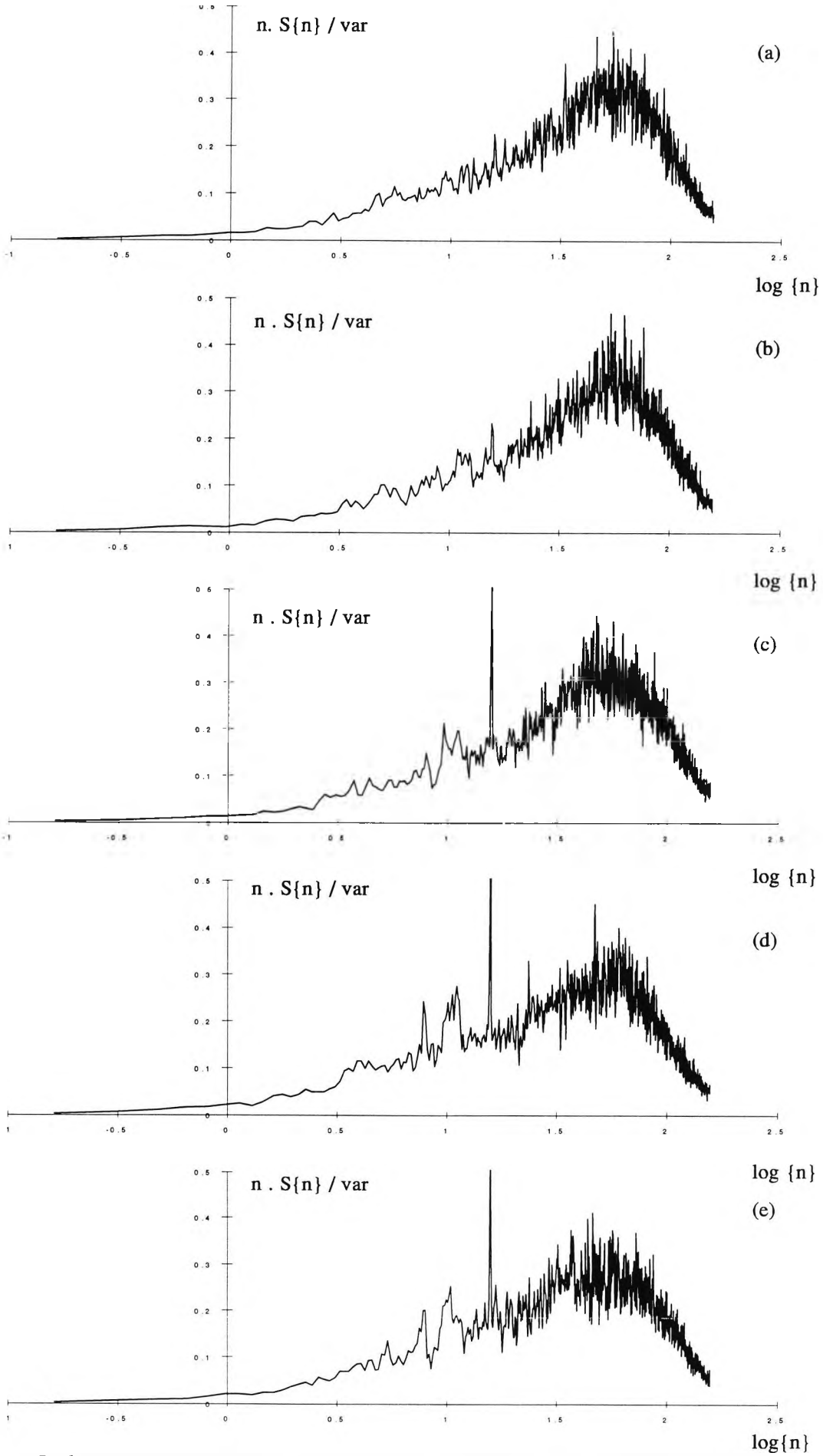

Figure 5.16: Normalised external pressure spectra on roof at x/D=0.17, Re=255000 and θ equal to (a) 26 degrees, (b) 71 degrees, (c) 116 degrees, (d) 154 degrees & (e) 161 degrees.

The above characteristics were also apparent in spectra measured at a Reynolds number of $2.55x10^5$ (figure 5.16) apart from an apparent periodicity in the pressure fluctuations at around 10Hz which was present for azimuth angles of 116^o and greater. This peak was not thought to be of acoustic origin because it was different in appearance to the very narrow band peaks previously described. The squat slenderness ratio of the cylinder precluded any notion of coherent vortex shedding in the wake of the cylinder so the precise origin of this peak was not identified.

When plotted in the $S\{n\}/\sigma^2$ versus $\log\{n\}$ format the roof spectra at both Reynolds numbers collapsed and were described by decay rates given in table 5.3.

Reynolds number = $1.8x10^5$		Reynolds number = $2.5x10^5$	
bandwidth	decay rate	bandwidth	decay rate
upto 4Hz	flat	upto 4Hz	flat
4Hz to 30Hz	$n^{-0.35}$	4Hz to 50Hz	$n^{-0.35}$
40 Hz to 85Hz	$n^{-1.67}$	40Hz to 90Hz	$n^{-1.67}$
90Hz to 155Hz	$n^{-4.0}$	90Hz to 155Hz	$n^{-3.8}$

Table 5.3: Decay rates for roof pressure spectra

[5-4] Summary

Results for the external pressure distribution around the wind tunnel model were presented and discussed in context with the results from previous investigators. The external pressure characterisitcs needed to be determined as these were the primary sources of excitation for the pressure variations within the cavity of the model. The characteristics of the internal cavity pressure are described in the following chapters.

Chapter 6: Mean and Unsteady Cavity Pressure Measurements

[6-1] Introduction

The pressure characteristics of the internal volume of the model were to a large extent dependent upon a number of geometric parameters, namely cavity volume, roof flexibility, number of open orifices and orifice orientation. Reynolds number also influenced the internal pressures. This chapter quantifies how the above parameters influenced mean and root-mean-square cavity pressures. The majority of tests where cavity pressure fluctuations were monitored were conducted with only a single opening connecting the internal volume to the external flow. Great care was taken to ensure that all joints on the model were rigidly sealed to minimise the background leakage on the model.

[6-2] Mean Cavity Pressures

[6-2-1] General Characteristics of the Mean Cavity Pressures

The mean cavity pressure distributions (fig 6.1) were obtained by rotating the open orifice from 0^o to 180^o in discrete increments. The angle between the windward stagnation point and the centre of the orifice defined the azimuth angle, ϕ.

The mean pressure distributions were broadly similar in shape to the external distributions (compare with figures 5.3) which implied that the cavity pressure was directly related to the external pressure via the open orifice. The front stagnation pressures lay somewhere between the mean external pressures measured at 0.27H (centre of opening) and 0.55H (above the opening) which implied that the mean cavity pressure was a spatial average of the external pressure across the area of the opening. The minimum mean pressure coefficient was around -0.8 and there was a steady pressure recovery into the base region. Indeed the final recovery was greater than that measured on the external walls of the model.

[6-2-2] Mean Cavity Pressure as a Function of Reynolds Number and Cavity Volume

The two parameters cavity volume and Reynolds number (based upon the mean windspeed at roof height and the diameter of the cylinder) were found to be interlinked (figure 6.1). Whilst a fair degree of confidence was assumed about the Reynolds number sensitivities of the external flow (section 5-2-1-1] the small size of the openings in the model caused some concern about local Reynolds number effects on the flow through

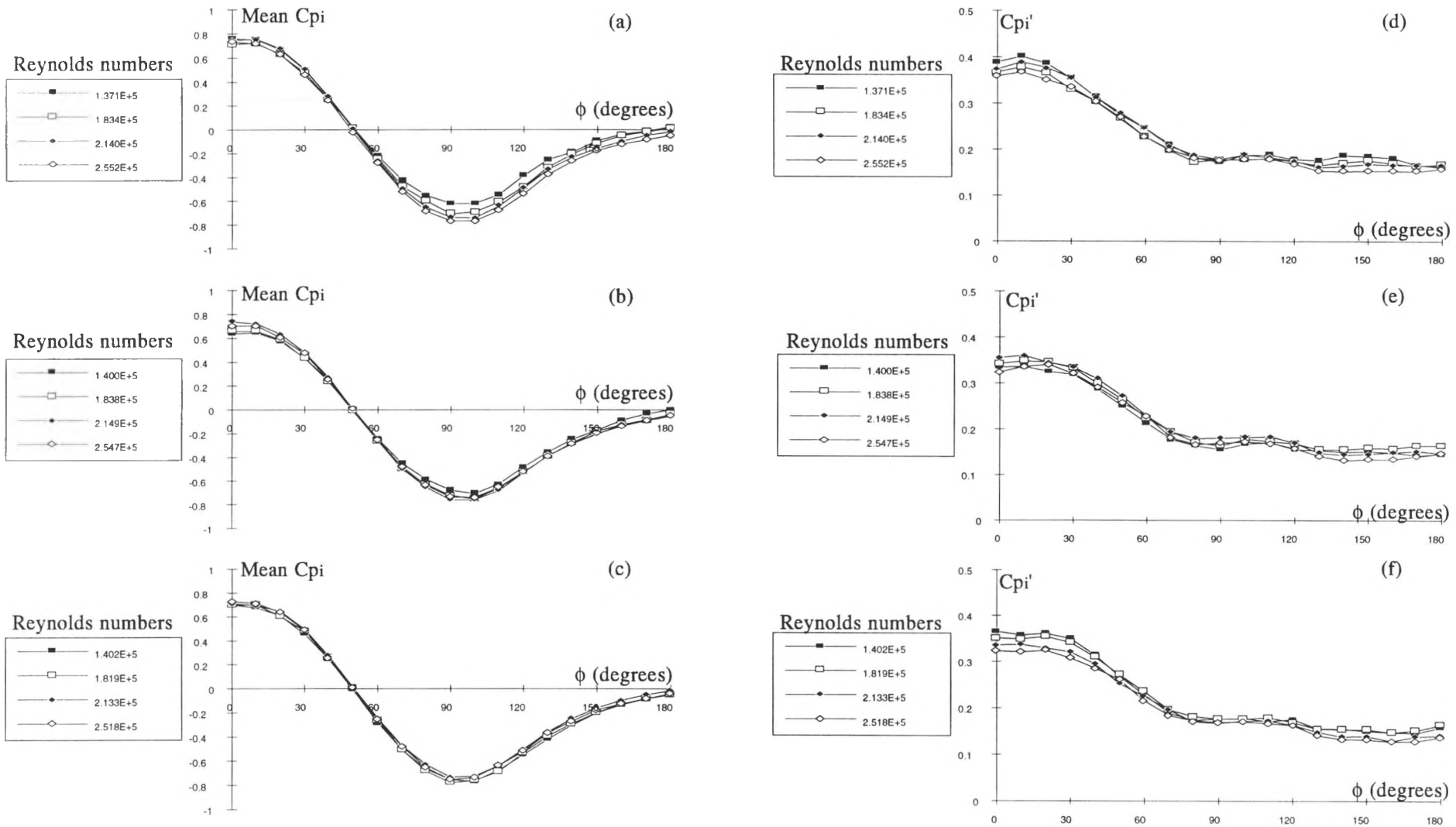

Figure 6.1: Mean (L.H.S.) and r.m.s. (R.H.S.) internal pressure coefficients as a function of orifice incidence over a range of Reynolds numbers (refer to the legend) for three different internal volumes: volume A (top) < volume B (centre) < volume C (bottom).

the orifice. This situation was further complicated by the nature of the orifice flow which was rapidly reversing due to resonance within the cavity. At the largest cavity volume (V_c) the mean cavity pressure distribution was self-similar for Reynolds numbers in the range $1.4x10^5<Re<2.52x10^5$ (fig 6.1(c)). However, as the cavity volume was reduced through volume B (V_b) and on to volume A (V_a) a sensitivity to Reynolds number became apparent around the leeward face of the cylinder where increases in the Reynolds number brought about an increase in suction around the model.

The implications of this result were more clearly seen by replotting the mean pressure distributions for different cavity volumes at similar Reynolds numbers (fig. 6.2). A good collapse of the data was evident at the two largest Reynolds numbers but at a Reynolds number of $1.8x10^5$ the mean cavity pressure for V_a showed signs of Reynolds number sensitivity. At the lowest Reynolds number the mean cavity pressure for both V_a and V_b sensitive to Reynolds number. Consequently, the earlier conclusion to run the main set of tests at Reynolds numbers of $1.8x10^5$ and $2.5x10^5$ based upon external flow sensitivities (section 5-2-1-1) was just sufficient to satisfy the local Reynolds number sensitivities of the orifice flow.

[6-3] Unsteady Cavity Pressures

[6-3-1] General Characteristics of the Unsteady Cavity Pressures

The r.m.s. cavity pressures showed a fairly rapid reduction between $0^o<\phi<70^o$ after which they remained fairly constant apart from an additional slight reduction around $\phi=130^o$ (figure 6.1). This behaviour contrasted with the almost linear reduction of the external unsteady pressures with increasng azimuth angle.

[6-3-2] Unsteady Cavity Pressure as a Function of Reynolds Number and Cavity Volume

There were ranges of azimuth over which the r.m.s. pressures coefficients showed a systematic variation with changes in Reynolds number (figs 6.1(d), (e) & (f)). Although not clear for each internal volume these ranges seemed to be confined to the windward (overpressure) region and the base region for angles between 0^O to 40^O and 130^O to 180^O respectively. Between these two zones the unsteady cavity pressure was independent of the Reynolds number.

As the cavity volume was increased there was a gradual flattening of the profile shape over the sector from $0^o<\phi<30^o$ sector (figure 6.1). In addition there was a slight

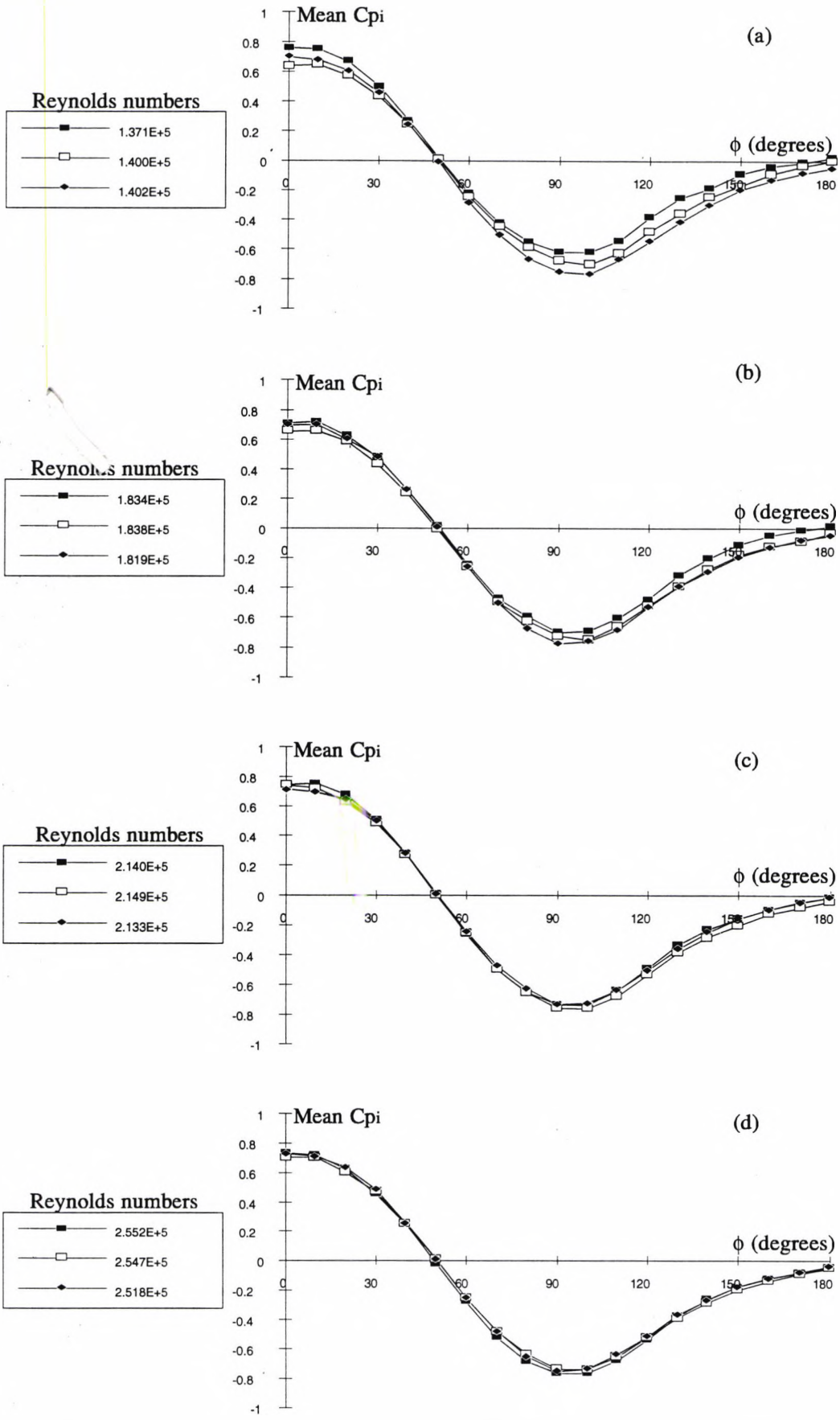

Figure 6.2: Mean internal pressure coefficients as a function of orifice incidence for different internal volumes at approximately constant Reynolds numbers: the legends display the Reynolds numbers for the different volumes with volume A (top) < volume B (centre) < volume C (bottom).

reduction in the r.m.s. pressure flucutations in the base region from around 0.18 to 0.14 as the cavity volume was increased. Further examination of the unsteady pressure coefficients by computing the ratio of the r.m.s. cavity pressure to the external r.m.s. pressure (at 0.27H) identified distinct sectors where cavity pressure fluctuations exceeded external pressure fluctuations (figure 6.3). From 0^o to 50^o the pressure fluctuations measured in the internal volume of the model were greater than those measured on the external wall. However, between 60^o and a larger azimuth angle, termed ϕ_{upper} (or θ_{upper}), the r.m.s. cavity pressure was less than the external wall pressure and the value of θ_{upper} was dependent upon the cavity volume as shown in table 6.1.

Cavity Volume	θ_{upper}
V_a	130^o
V_b	150^o
V_c	160^o

Table 6.1: Estimated values of θ_{upper} from figure 6.3.

The cavity pressure fluctuations were shown to be sensitive to Reynolds number in figure 6.1 and were also a function of the azimuth angle as shown in figure 6.3. Changes in the variance (or its square root) of the cavity pressure fluctuations will be reflected in the distribution of energy in the power spectra (whose area is equal to the variance) whereby the sensitivities discussed above may be related to the magnitude of the Helmholtz oscillation. There was evidence to support this proposition in the spectral data (chapter 7).

[6-3-3] Unsteady Cavity Pressures as a Function of Roof Flexibility

The influence of wall flexibility on resonance at the Helmholtz frequency was alluded to by Liu & Rhee (1986), however, no experimental evidence was presented. In order to directly assess the effects of roof flexibility on the cavity pressure fluctuations the r.m.s. cavity pressure measured when the roof of the model was rigid was used as a reference value for each configuration where "configuration" was defined by a Reynolds number, orifice azimuth angle, ϕ, and cavity volume. For each configuration four different roof tensions were tested and the resultant unsteady pressure coefficients, $C'pi_{flex}$ expressed as a fraction of $C'_{p_{rigid}}$. Azimuth angles from 0^o to 180^o in increments of 45^o were tested. The results were tabulated (table 6.2) and expressed in the form of histograms in

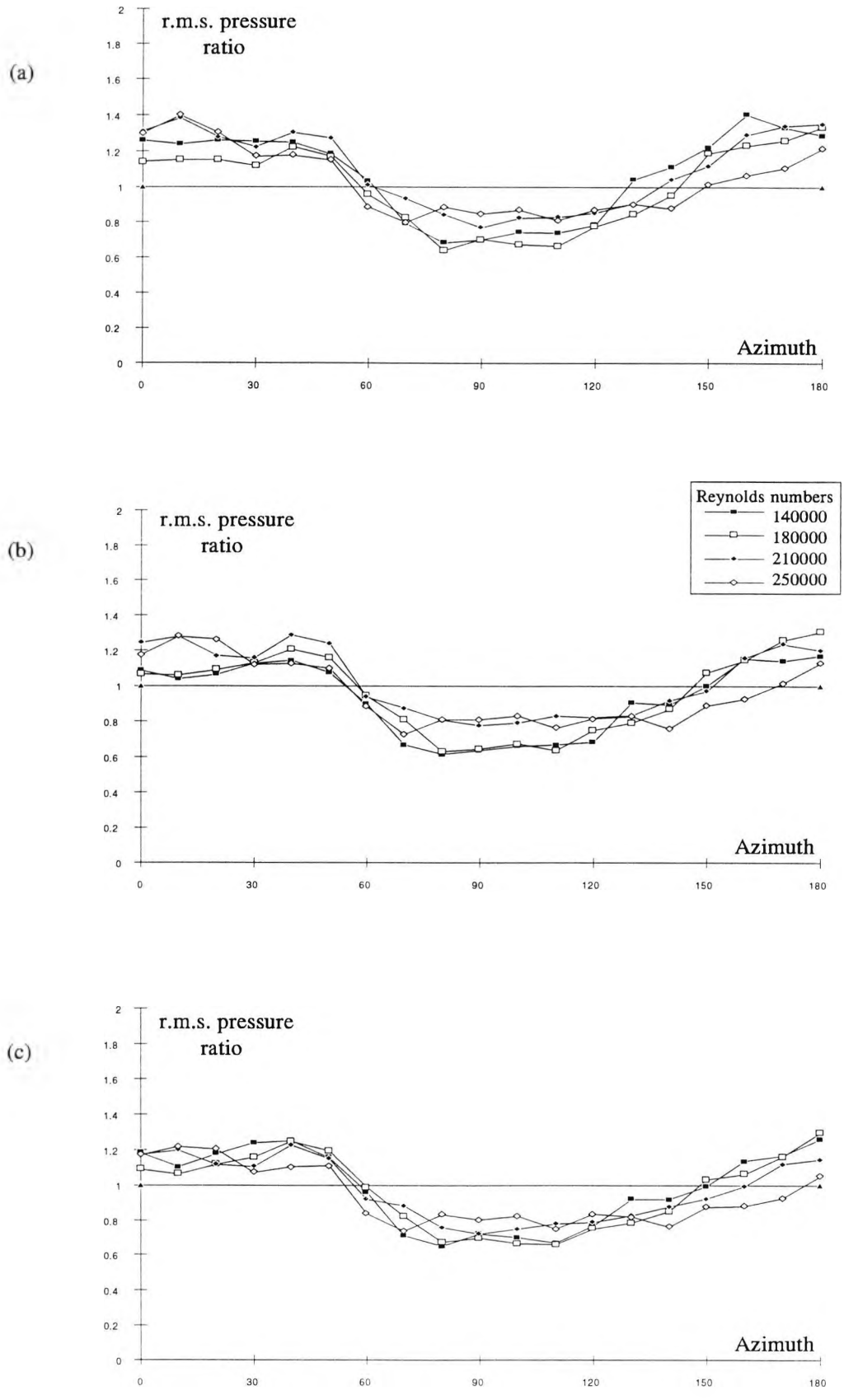

Figure 6.3: R.m.s. pressure ratios expressed as cavity pressure divided by external pressure (at z/H=0.27) versus orifice azimuth angle for (a) volume A, (b) volume B and (c) volume C

figure 6.4 (Note: The roof tensions are shown in qualitative terms only going from relatively rigid, T_a to the most flexible, T_d).

Orifice Incidence [degrees]	Cavity Volume A							
	Re 1.8 x10^5				Speed 2.5 x10^5			
	T_A	T_B	T_C	T_D	T_A	T_B	T_C	T_D
0	0.961	0.937	0.854	0.842	0.879	0.843	0.794	0.776
45	**1.019**	0.989	0.916	0.880	0.913	0.857	0.811	0.760
90	**1.023**	**1.030**	0.981	0.987	**1.006**	0.988	0.950	0.963
135	0.960	0.917	0.879	0.818	0.813	0.774	0.732	0.687
180	0.983	0.859	0.805	0.719	0.869	0.784	0.746	0.646

Orifice Incidence [degrees]	Cavity Volume B							
	Re 1.8 x10^5				Re 2.5 x10^5			
	T_A	T_B	T_C	T_D	T_A	T_B	T_C	T_D
0	0.956	0.879	0.820	0.815	0.907	0.835	0.818	0.808
45	0.993	0.905	0.834	0.857	0.920	0.833	0.797	0.796
90	0.968	0.940	**1.016**	0.979	0.972	0.960	0.959	0.961
135	0.899	0.842	0.809	0.837	0.923	0.899	0.871	0.851
180	0.883	0.786	0.717	0.744	0.883	0.778	0.785	0.788

Orifice Incidence [degrees]	Cavity Volume C							
	Re 1.8 x10^5				Re 2.5 x10^5			
	T_A	T_B	T_C	T_D	T_A	T_B	T_C	T_D
0	0.945	0.868	0.848	0.831	0.932	0.879	0.861	0.854
45	0.954	0.895	0.917	0.841	0.937	0.860	0.841	0.797
90	**1.009**	0.963	0.967	0.949	0.983	0.968	0.971	0.954
135	0.940	0.884	0.860	0.829	0.942	0.918	0.877	0.841
180	0.847	0.766	0.748	0.686	0.881	0.822	0.788	0.746

Table 6.2: Ratio of r.m.s. cavity pressures; flexible roof/rigid roof configurations

In nearly all the test cases increasing the flexibility of the roof attenuated the intensity of the pressure fluctuations within the cavity of the building. Generally, the smallest attenuation ocurred for the cases $\phi=90^o$ where the fluctuation ratio was near to unity, i.e. the unsteady cavity pressure was least affected by roof flexibility.

At the lower Reynolds number (figures 6.4(a) to (c)) the attenuation increased in a systematic way from $\phi=90^o$ to $\phi=0^o$ and similarly from $\phi=90^o$ to $\phi=180^o$. For each cavity volume the maximum attenuation generally occurred when the orifice was in the

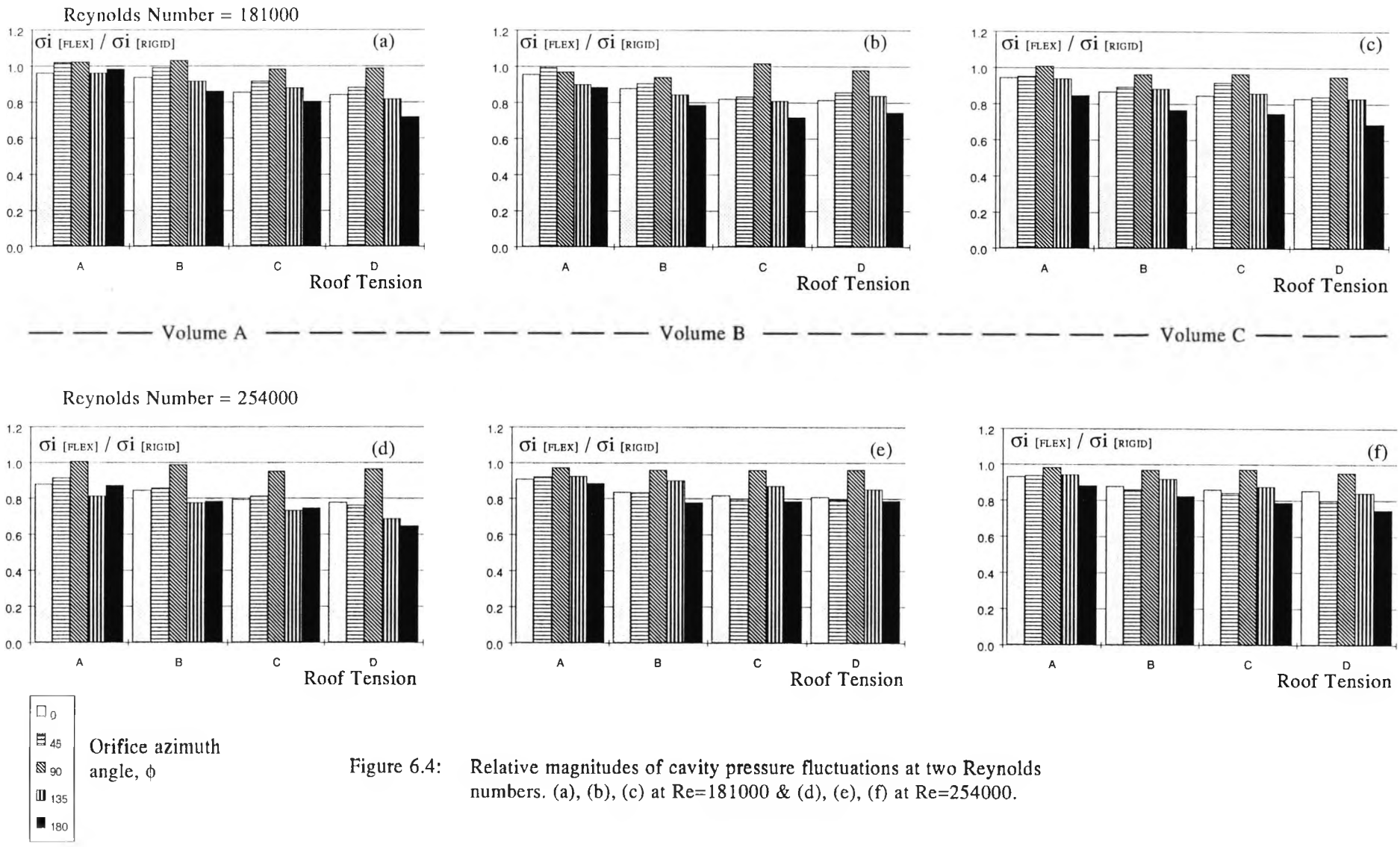

Figure 6.4: Relative magnitudes of cavity pressure fluctuations at two Reynolds numbers. (a), (b), (c) at Re=181000 & (d), (e), (f) at Re=254000.

the base region of the cylinder (ϕ=180°). Similar trends to the above were noted in the results obtained at the higher Reynolds number, however, these results were less consistent.

A final manipulation of the data contained in table 6.2 was made by using the bulk modulus ratios, K_a/K_b (defined in section 2-4-2-2), estimated from the "still-air" Helmholtz frequencies. K_a/K_b is a measure of the relative compressibilities of the building envelope and the air within the cavity. Increasing the flexibility of the roof increased the value of K_a/K_b and a relative increase was obtained at each value of roof tension by defining a flexibility factor, F, where

$$F = \frac{(K_a / K_b)_{flex}}{(K_a / K_b)_{rigid}} \quad . \qquad (6.1)$$

The estimate of the rigid roof building bulk modulus ratio for V_c was very small, only 0.02, which gave rise to correspondingly large values of F of between 30 and 130. These values were some three to four times bigger than the equivalent flexibility factors computed for volumes A and B. Consequently, for the purposes of a comparison the estimate of $(K_a/K_b)_{rigid}$ for V_c was (somewhat arbitrarily) doubled to 0.04 (but see also table 4.3).

At the lower Reynolds number the results of unsteady pressure ratio as a function of the change in roof flexibility were "well-behaved" and collapsed onto a single curve that was independent of cavity volume (figure 6.5). Reductions in the tension of the roof generally brought about an attenuation of the r.m.s. cavity pressures for each orifice azimuth apart from ϕ=90° where roof flexibility had practically no effect on the cavity pressure fluctuations. At the higher Reynolds number (figure 6.6) the data appeared to collapse for configurations where the orifice was on the windward side of the model but when in the lee of the building the results were more scattered.

The general conclusions from figures 6.5 and 6.6 were that increases in the flexibility factor to around twenty reduced the cavity pressure fluctuations by 20% and further reductions in the rigidity of the roof had a negligible effect on the unsteady cavity pressures.

[6-4] Summary

The mean cavity pressures were to a large extent dependent upon the pressures acting on the external walls of the model. Some degree of local Reynolds number sensitivity

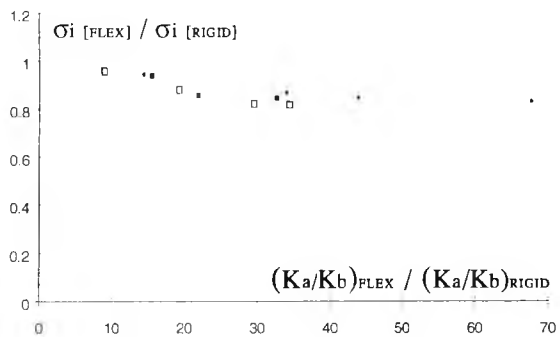

(a) ϕ = 0 degrees

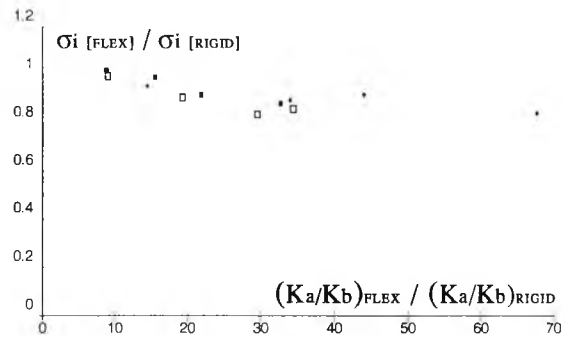

(b) ϕ = 45 degrees

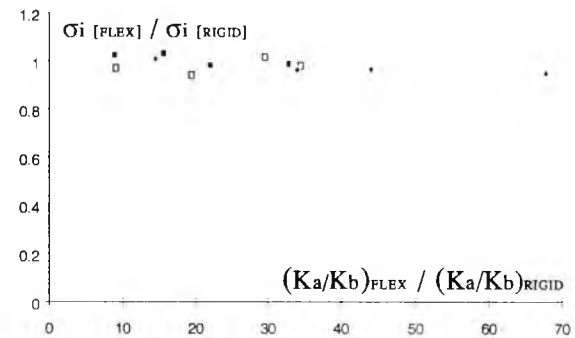

(c) ϕ = 90 degrees

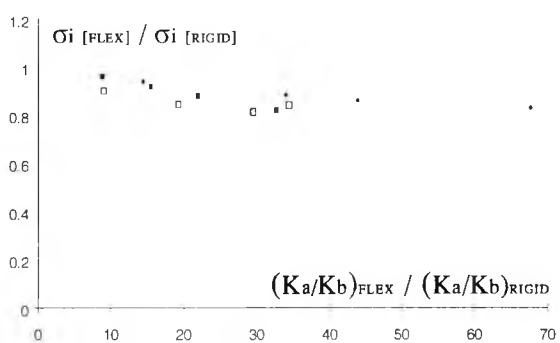

(d) ϕ = 135 degrees

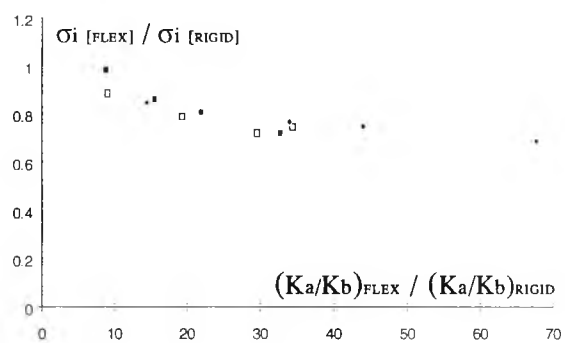

(e) ϕ = 180 degrees

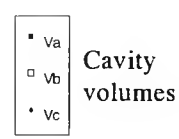

Figure 6.5: Relative unsteady cavity pressure coefficients as a function of the relative increase in bulk modulus ratio for three cavity volumes and different orifice azimuth angles.

Reynolds number = 181000

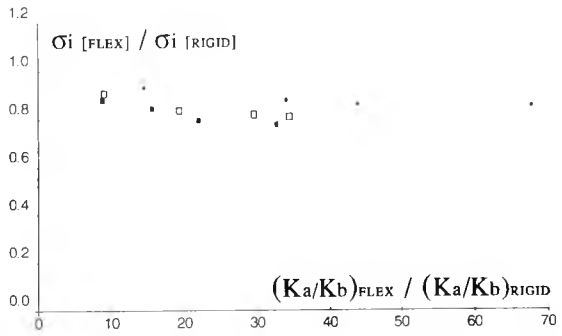

(a) ϕ = 0 degrees

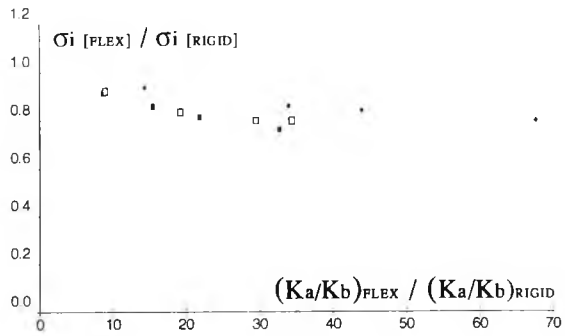

(b) ϕ = 45 degrees

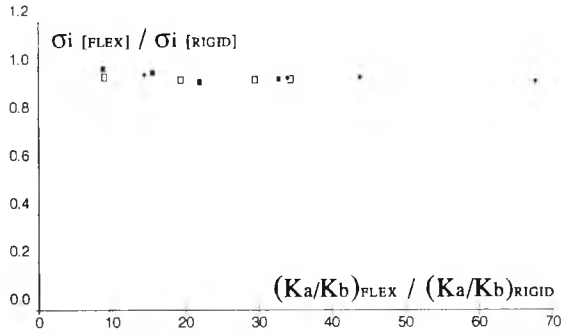

(c) ϕ = 90 degrees

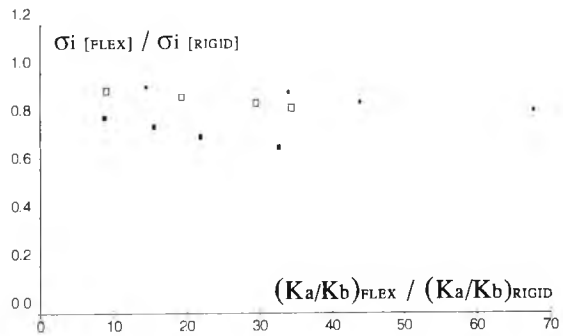

(d) ϕ = 135 degrees

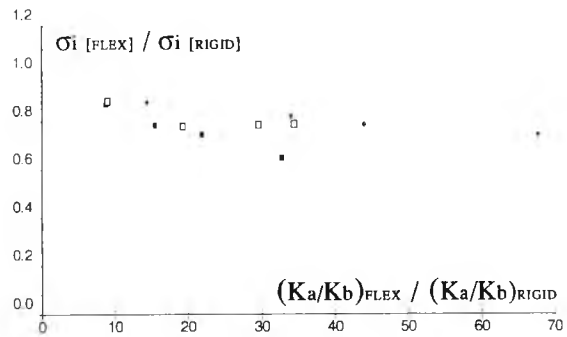

(e) ϕ = 180 degrees

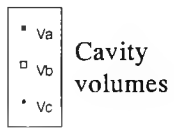

Figure 6.6: Relative unsteady cavity pressure coefficients as a function of the relative increase in bulk modulus ratio for three cavity volumes and different orifice azimuth angles.

Reynolds number = 254000

was noted in the flow through the openings but for Reynolds numbers (based upon the mean roof height windspeed and diameter of the model) of 1.81×10^5 and above these effects were minimal. It was suggested that variations in the unsteady cavity pressures might well be reflected in the degree to which the Helmholtz mode of oscillation was excited within the cavity. This suggestion will be discussed further in the next chapter.

Chapter 7: Cavity Pressure Results in the Frequency Domain

[7-1] Introduction

A significant amount of research has been reported on the phenomenon of Helmholtz resonance, a phenomenon which was categorised as a fluid-resonant behaviour in the review paper of Naudascher & Rockwell (1978). A particularly successful application of the Helmholtz resonator appears to be as a means of suppressing duct noise where holes in the wall of a duct communicate with resonator cavities of different size. This type of research is generally restricted to the case of an external flow moving perpendicular to the longitudinal axis of the opening (equivalent to the "90°" case in the present tests) for which both the interactions between the external flow and the cavity and the sensitivity of the cavity response to changes in the opening geometry have been investigated.

Baumeister & Rice (1975) captured the exchanges between the external flow and an Helmholtz resonator on camera and the results are summarised below for three stages of the resonant cycle; the arrows show the direction of the flow.

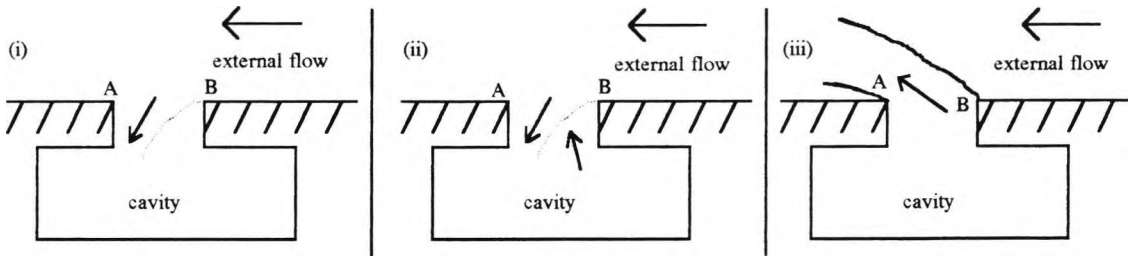

Figure 7.1: Flow mechanism of Helmholtz oscillation under a "grazing" flow (after Baumeister & Rice, 1975).

The sequence shown in figure 7.1 starts on the inflow stage of the resonant cycle (7.1(i)) where separation from point B limits the area available for inflow to the region downstream of the separation line. Eventually, the overpressure within the cavity forces fluid back into the external flow but this outflow begins "beneath" the shear layer (as indicated on figure 7.1(ii)) where the momentum of the fluid is low compared with the jet of fluid to the left of the shear layer. At this time the net momentum through the opening is zero but two distinct bodies of fluid moving in opposite directions coexist within the opening. The inflow component in figure 7.1(ii) is gradually decelerated until the opening is completely filled with fluid moving from cavity to external flow and the cycle is completed (figure 7.1(iii)).

Baumeister & Rice (1975) concluded that the existence of the external flow reduced the effective area of the opening on both the inflow and outflow parts of the cycle, compared with the zero external flow case, so that the presence of the grazing flow could be viewed qualitatively as a blockage in the opening. In addition, measurements of the discharge coefficients associated with the inflow and ouflow parts of the cycle showed that the energy loss on the inflow exceeded the energy lost on the outflow which implied that the two flow processes were different. However, knowledge of the ratio of the mean jet velocity through the opening to the mean external flowspeed, $V_{jet}/V_{external}$, was sufficient to define the two discharge coefficients.

Panton (1990) considered the influence of the shape of the opening of the resonator on the response of the cavity pressure and found that significant changes occurred for apparently small variations in geometry. The basic experimental configuration was similar to that shown in figure 7.1 and the results clearly demonstrated that the cavity response was increased when modifications were made to the geometry of the opening which facilitated inflow and outflow through the opening. For example, compared with the opening shown in figure 7.2(i), the cavity response was enhanced by making the changes shown in 7.2(ii) and (iii), whereas the geometry shown in 7.2(iv) virtually eliminated the resonant response of the pressure within the cavity.

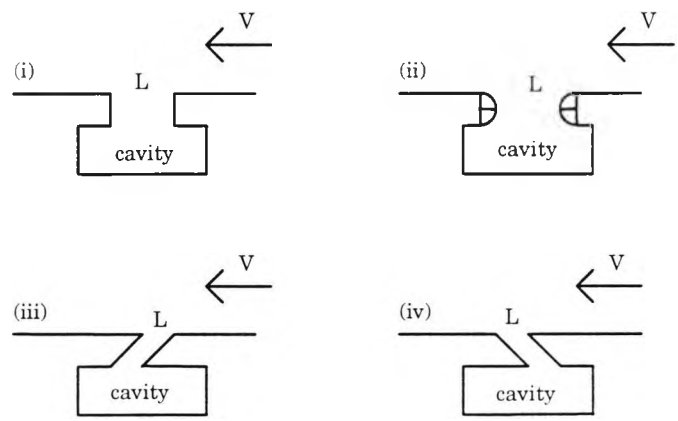

Figure 7.2: Changes in opening geometry investigated by Panton (1990).

The tests of Panton (1990) were conducted for a range of external flow conditions and the results presented in the normalised format of p_i'/q versus the Strouhal number of the opening, $V/(L.f_o)$, where f_o was the *acoustic* Helmholtz frequency. When plotted in this way the response characterisics of the different resonators were generally similar with a peak of around 1.0 (dependent upon the geometry of the opening) occurring at a Strouhal number of approximately 3.8.

The results of the present tests showed an increased cavity response on changing the orientation of the opening from 90° through 45° to 0° and this agreed qualitatively with the results of Panton (1990), as discussed above. However, a significant response was also observed on directing the opening away from the direction of the mean external flow, the 135° and 180° cases, which implied that the reversed flow in the wake of the model produced an inflow component capable of exciting the resonant mode. These general results were applicable to each of the model configurations tested with the minimum response occurring for an opening located at an azimuth angle of 90°.

The spectra of the pressure fluctuations measured within the cavity of the model will initially be presented for tests conducted with a rigid roof and walls and the specific influences of mean reference windspeed, orientation of the opening and cavity volume will be described. Similar sets of data from tests on a model fitted with a flexible membrane roof will then be presented and conclusions drawn regarding the modelling of internal pressure dynamics. A complete set of the cavity pressure spectra are included in appendix B, whilst the gain functions defined by equation (7.1) are presented in appendix C; a small selection of the graphs from these two appendices will be reproduced in this chapter in order to illustrate the points being made in the text.

[7-2] Rigid Roof Results

[7-2-1] The Influence of Mean Reference Windspeed

Each model configuration was tested at two mean reference windspeeds of 9.4m/s and 13.0m/s, however, for volume A with an opening orientated at 0° and 45° tests were run at two additional windspeeds. The cavity pressure spectra for these tests are shown in figures 7.3 and 7.4 where it is clear that reductions in the mean windspeed increased the resonant response at both orientations. This trend was consistently repeated for the pairs of results obtained from tests on other configurations of the model, i.e. the response at 9.4m/s exceeded that measured at 13.0m/s.

The implication of this result was that damping at the Helmholtz frequency was a function of the mean windspeed such that increases in the mean speed increased damping and thus reduced the resonant response of the cavity pressure. Indeed, the damping constants for flow through an opening modelled by Vickery & Georgiou (1991) included a direct relationship between damping and the mean reference windspeed (see equation 2.9) of the external flow. However, it was possible that the changes in the response of the cavity pressure fluctuations might have been caused by

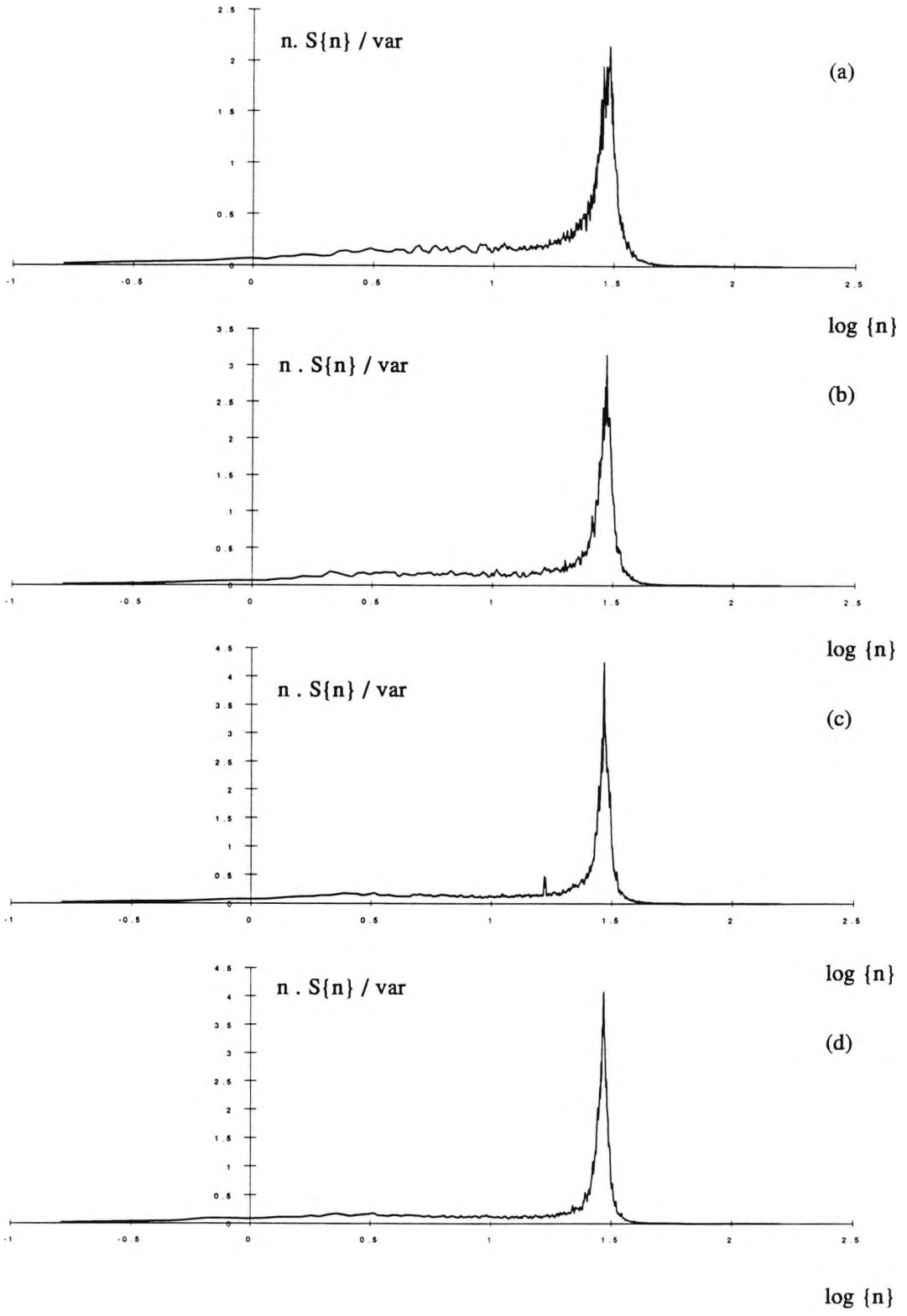

Figure 7.3: Normalised cavity pressure spectra for model fitted with a rigid roof and with an opening azimuth angle of 0 degrees at mean reference windspeeds of (a) 13.0 m/s, (b) 11.3 m/s, (c) 9.4 m/s, (d) 7.2 m/s.

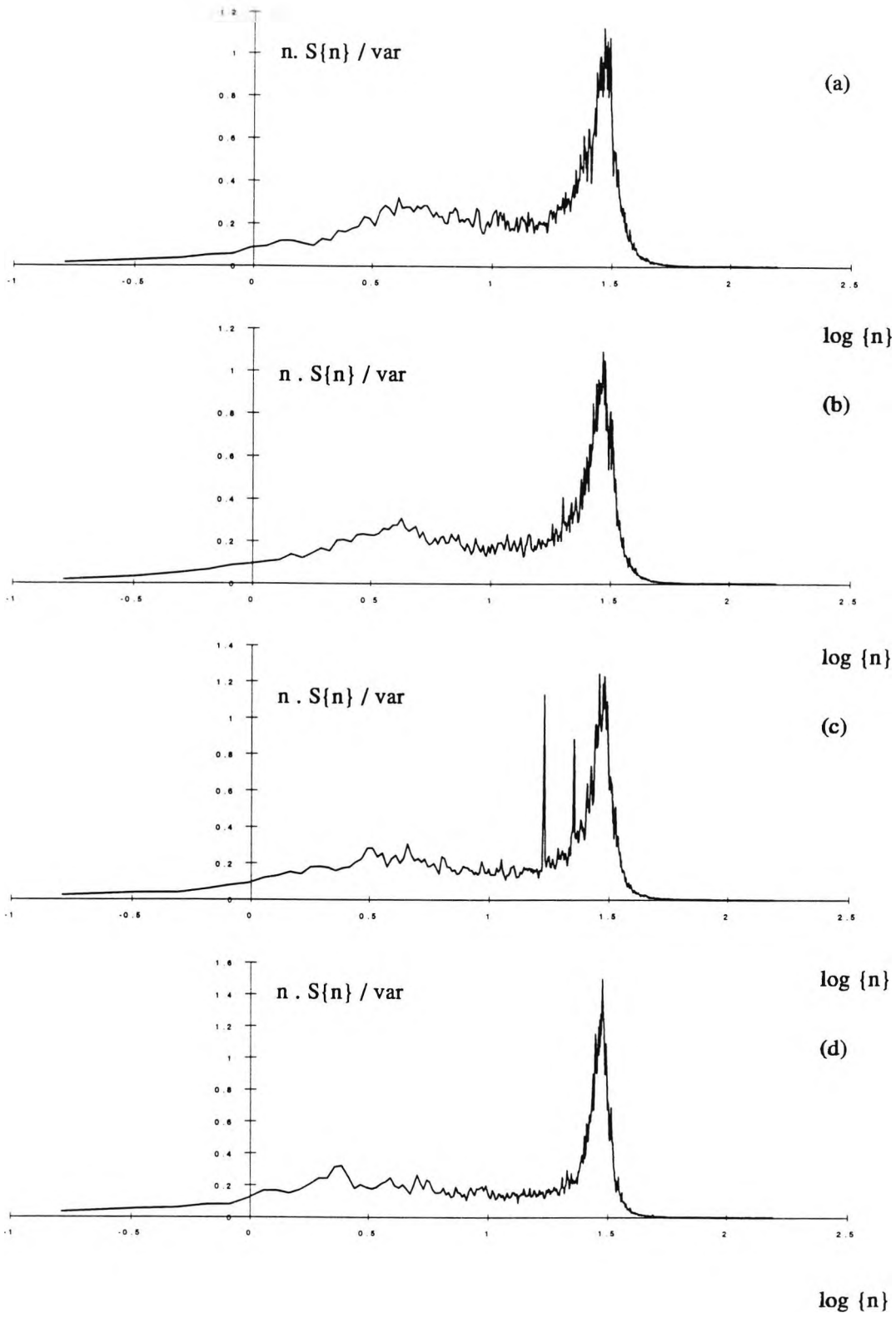

Figure 7.4: Normalised cavity pressure spectra for model fitted with a rigid roof and with an opening azimuth angle of 45 degrees at mean reference windspeeds of (a) 13.0m/s, (b) 11.3 m/s, (c) 9.4m/s, (d) 7.2 m/s.

changes in the external pressure field which were subsequently transmitted to the pressure fluctuations within the cavity. In order to remove this effect, if it were present, a third gain function, G_1, was defined (c.f. the functions G_2 and G_3 defined in chapter 5) which was obtained by narrow bandwidth division of the cavity pressure spectra by the external pressure spectra measured at 0.27H. The function G_1 is defined by

$$\text{Gain, } G_1 = \sqrt{\frac{(n.S_i\{n\}/\sigma_i^2)}{(n.S_e\{n\}/\sigma_e^2)_{0.27H}}} = \frac{\sigma_{e_{0.27H}}}{\sigma_i} \cdot \sqrt{\frac{S_i\{n\}}{S_e\{n\}_{0.27H}}} \qquad (7.1)$$

where the suffices "i" and "e" refer to internal and external pressure respectively. These gain results retained the sensitivity to mean windspeed described above and are shown in figure 7.5.

[7-2-2] The Influence of Cavity Volume

Comparison of the cavity pressure spectra for different cavity volumes showed a reduction in the response at the Helmholtz frequency as the volume was increased. For the convenience of the reader the cases of maximum response (0°) and minimum response (90°) were reproduced in figure 7.6 (similar trends were observed in the additional results shown in appendix B).

Changing the volume of the internal cavity altered the Helmholtz frequency so that for the same turbulent excitation the natural frequency of the cavities were subjected to different levels of turbulent energy. Once again conversion of the spectra to gain functions removed this effect but the results retained the sensitivity to internal volume described above (figure 7.7).

[7-2-3] The Influence of Azimuth Angle

At each cavity volume and windspeed the minimum resonant response of the cavity pressure consistently occurred when the opening in the wall of the model was at 90° to the aproach flow. At 90° a significant broad-band of low frequency energy was apparent on the cavity pressure spectra which had been transmitted from the turbulent pressure fluctuations acting on the outside of the model (figure 7.8). This broad-band response was due to the buffetting effect of the turbulence. The magnitude of the spectral peak associated with turbulence was generally greater than that of the resonant peak due to Helmholtz oscillation when the opening was at an azimuth angle

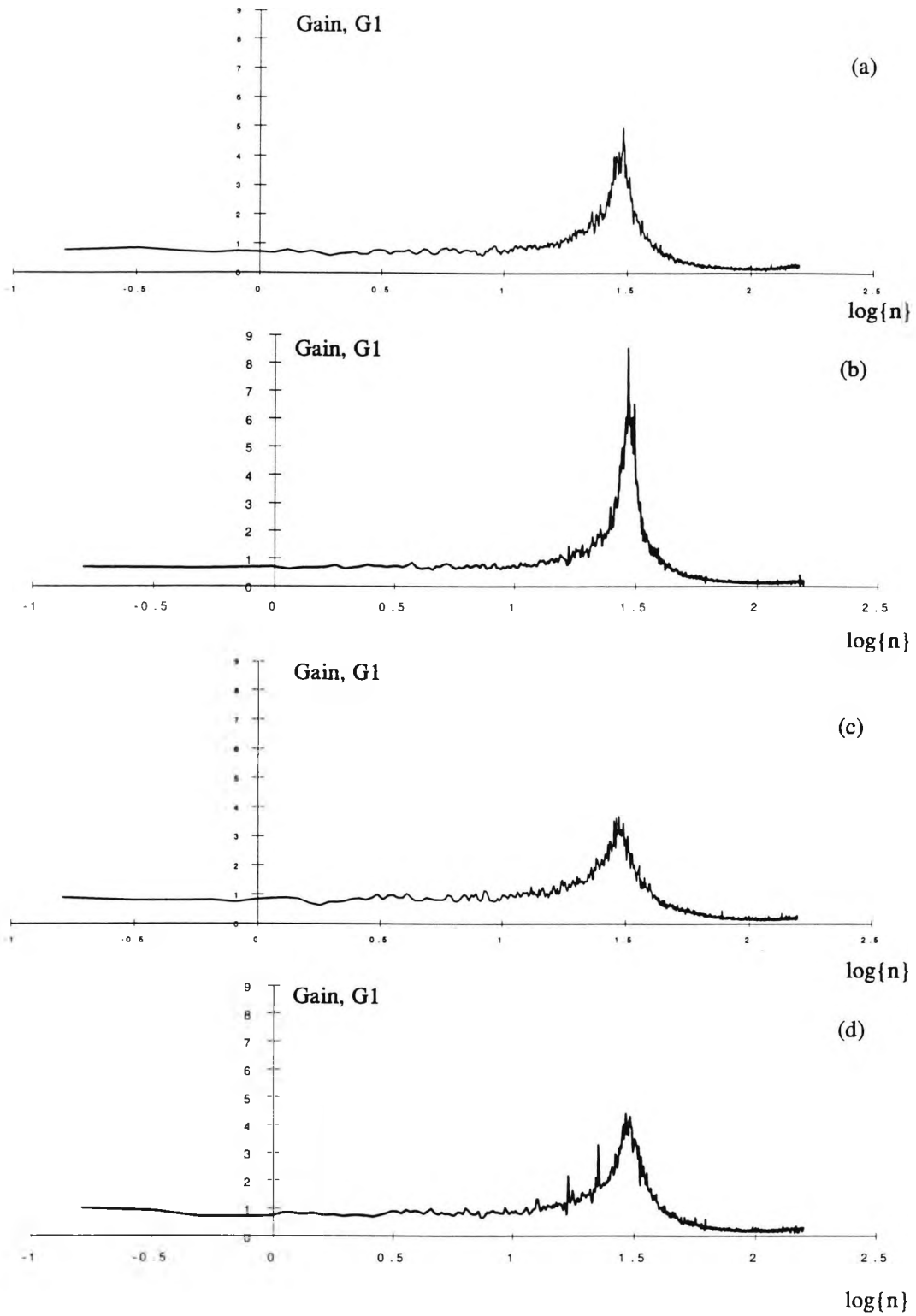

Figure 7.5: Gain functions of cavity pressure for a rigid-roofed model with volume A and :
(a) opening at 0 degrees, windspeed =13.0m/s
(b) opening at 0 degrees, windspeed = 9.4m/s
(c) opening at 45 degrees, windspeed = 13.0m/s
(d) opening at 45 degrees, windspeed = 9.4m/s

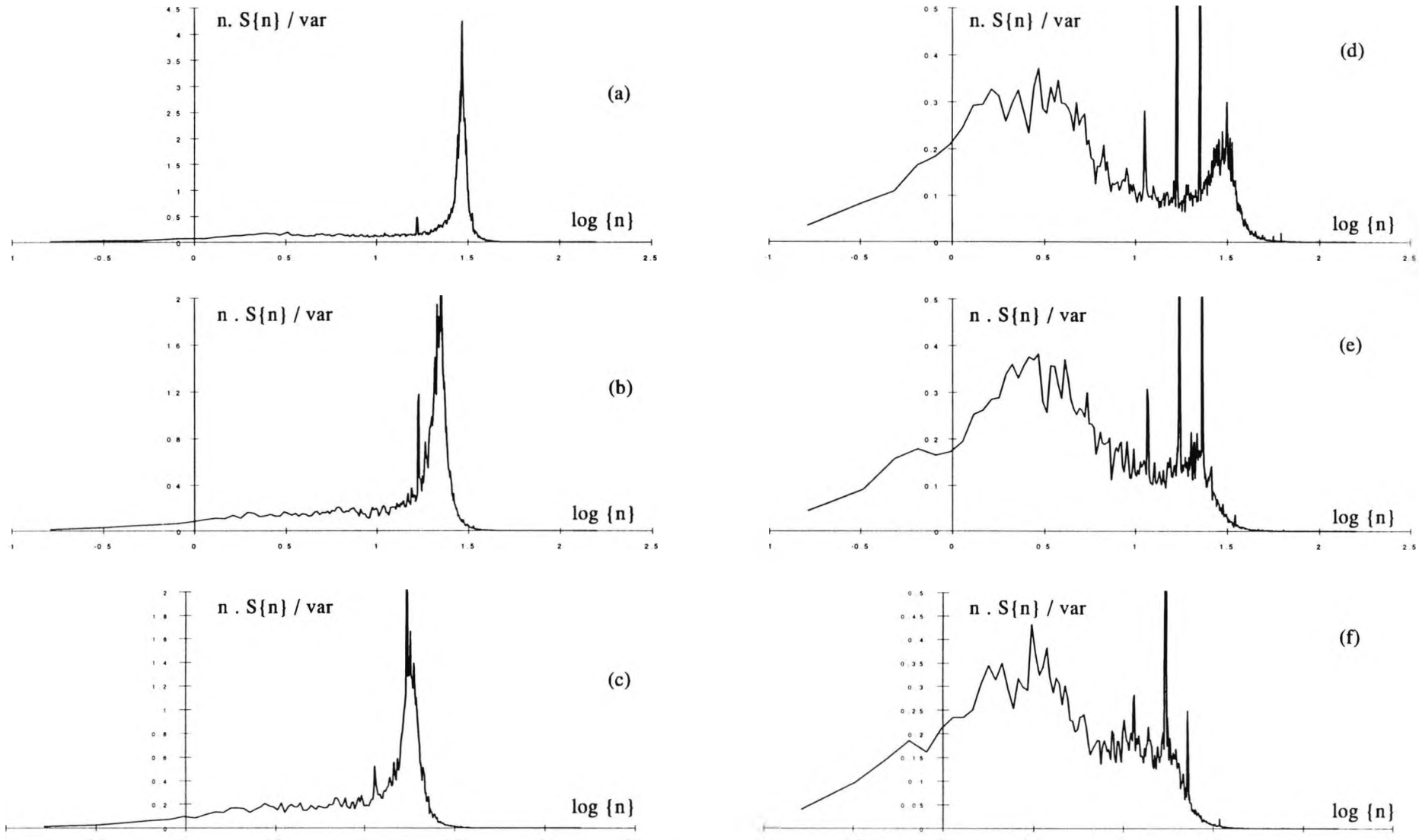

Figure 7.6: Cavity pressure spectra at a windspeed of 9.4m/s for the model fitted with a rigid roof and (a) opening at 0 degrees, volume A, (b) opening at 0 degrees, volume B, (c) opening at 0 degrees, volume C, (d) opening at 90 degrees, volume A, (e) opening at 90 degrees, volume B, (f) opening at 90 degrees, volume C.

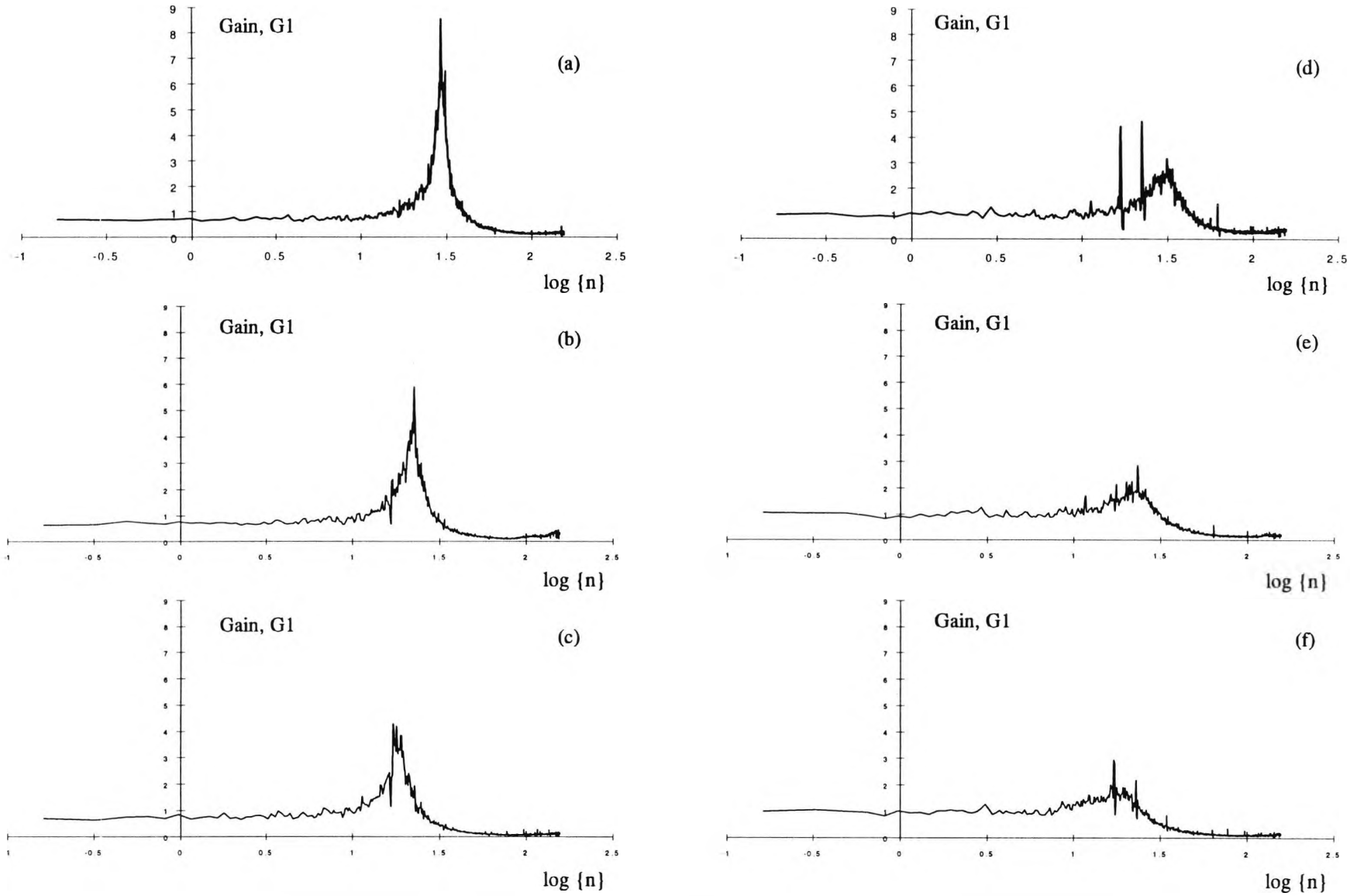

Figure 7.7: Cavity pressure gain functions at a windspeed of 9.4m/s for the model fitted with a rigid roof and (a) opening at 0 degrees, volume A, (b) opening at 0 degrees, volume B, (c) opening at 0 degrees, volume C, (d) opening at 90 degrees, volume A, (e) opening at 90 degrees, volume B, (f) opening at 90 degrees, volume C.

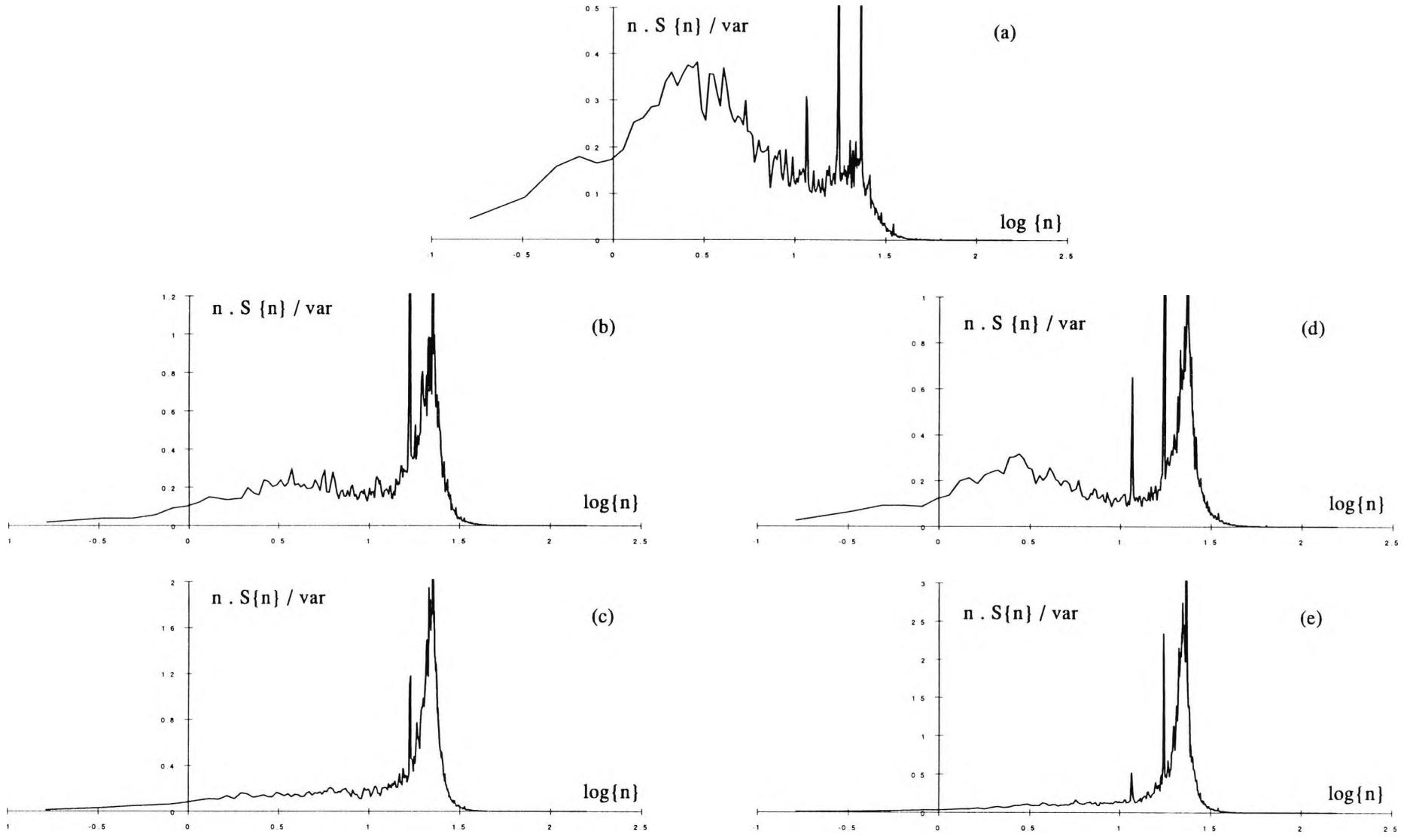

Figure 7.8: Cavity pressure spectra for volume B at a mean windspeed of 9.4m/s with a rigid roof and openings located at (a) 90 degrees, (b) 45 degrees, (c) 0 degrees, (d) 135 degrees, (e) 180 degrees.

of 90°. Rotating the opening to windward through 45° to 0° gradually increased the energy content of the resonant peak because the position of the opening promoted the flow of air into the cavity of the model (Panton, 1990). The broad-band turbulent buffetting response was essentially "swamped" by resonance when the opening was orientated to windward.

However, turning the opening to 135° and then 180° also enhanced the resonant response of the cavity even though the opening was directed away from the approach flow. At these azimuth angles the Helmholtz oscillation again dominated the cavity pressure spectra excited by the inflow components induced by reversed flow on the leeward side of the model. The shift in turbulent energy toward higher frequencies that occurred on the outside walls of the model on moving from windward to leeward (chapter 5) might also have prompted the large resonant response of the cavity pressure for openings situated on the leeward side of the model. The gain function defined in section 7-1 was used to remove this effect and showed that the resonant response of the cavity pressure was high for openings located in this region (figure 7.9).

[7-2-4] Effect of Volume Scaling on the Response of the Cavity Pressure

The scaling requirements for correctly matching the internal pressure dynamics of both full-scale and model buildings (chapter 2) showed that using a velocity scale less than unity meant that the cavity volume of the model had to be exaggerated by a factor equal to the square of the velocity scale. This result (which seems to have been independently derived by a number of different investigators) was corroborated, at least qualitatively, by the results discussed in sections 7-2-2 and 7-2-3, where running a test at a low windspeed increased the resonant response of the cavity pressure fluctuations whilst increasing the volume of the cavity reduced the resonant response of the cavity pressure so that the two phenomena could be used to compensate for one another.

In order to make a more qualitative assessment of this behaviour, one of the model configurations was arbitrarily chosen to be a "correct" representation of some undefined full-scale building; the response and internal volume of this configuration were used as reference values for comparison with the results obtained from the remaining configurations where response was quantified by an estimate of the height of the resonant peak on the cavity pressure spectra. The reference configuration selected was volume B tested at a windspeed of 9.4m/s (denoted by $V_b^{9.4}$). A reference full-scale windspeed of 27.405m/s was derived by equating the 8.5 volume

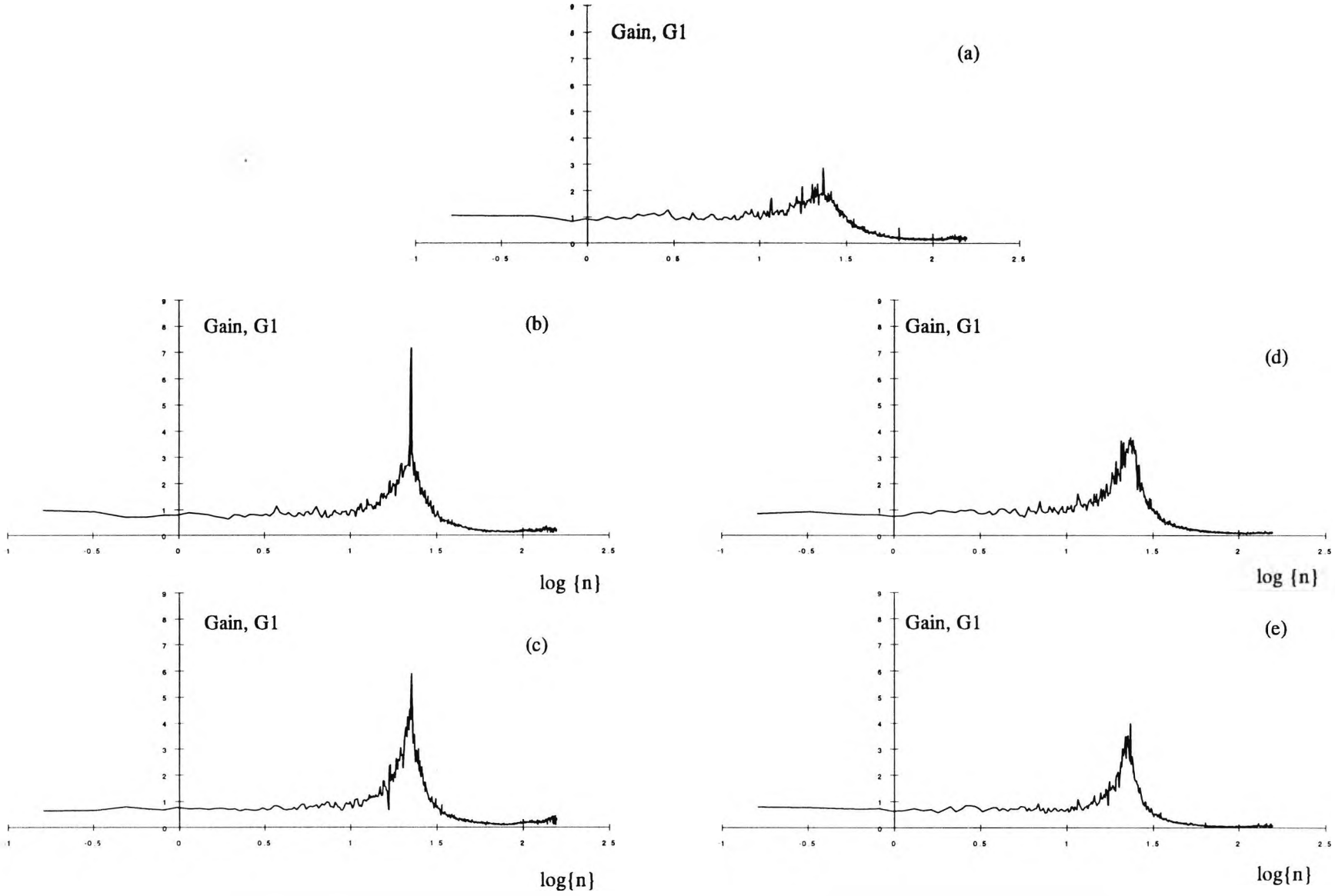

Figure 7.9: Cavity pressure gain functions for volume B at a mean windspeed of 9.4m/s with a rigid roof and openings located at (a) 90 degrees, (b) 45 degrees, (c) 0 degrees, (d) 135 degrees, (e) 180 degrees.

factor of volume B to the inverse of the square of the velocity scale. The relative mismatch in the volume scaling for all other configurations of the tests were obtained by dividing the pertinent volume factors (4.5, 8.5 or 12.5) by $1/\lambda_v^2$. The relative response of the internal cavity pressure was quantified at each azimuth angle by estimating the resonant peak of the Helmholtz oscillation from the spectrum and dividing it by the corresonding response measured for $V_b^{9.4}$.

The results for openings located at five different azimuth angles appeared to collapse onto a single curve as shown in figure 7.10 and were adequately described by the exponential decay curve (shown as the "best-fit" on figure 7.10),

$$y = 1.6338 \, . \, e^{-0.4107 \, x} \qquad (7.2)$$

where y is the relative reponse and x the distortion in the scaling. Exaggerating the scale factor resulted in a reduced response whilst a cavity volume that was too small overestimated the response. It may be argued that the latter error in scaling would produce conservative results at model-scale because of the increased response, however, the exponential nature of the relationship in equation 7.2 produces errors in the response of smaller magnitude for a 50% (say) overestimate of the cavity volume than those for a 50% underestimate. The percentage error bands which enclose all the data points are shown in order to give some feel for the scatter in the data.

[7-3] Flexible Roof Results

[7-3-1] The Helmholtz Mode

Generally for each value of the roof tension, denoted in order of increasing flexibility as T_a, T_b, T_c, T_d, the trends described in section 7-2 were also applicable, namely

- minimum response occurred for openings at 90° to the approach flow
- increased cavity volume reduced the resonant response of the cavity pressure fluctuations
- increased mean windspeed reduced the resonant response of the cavity pressure fluctuations.

However, these effects were generally less pronounced than they were for the rigid roof tests because of the additional damping introduced by the motion of the roof. None of

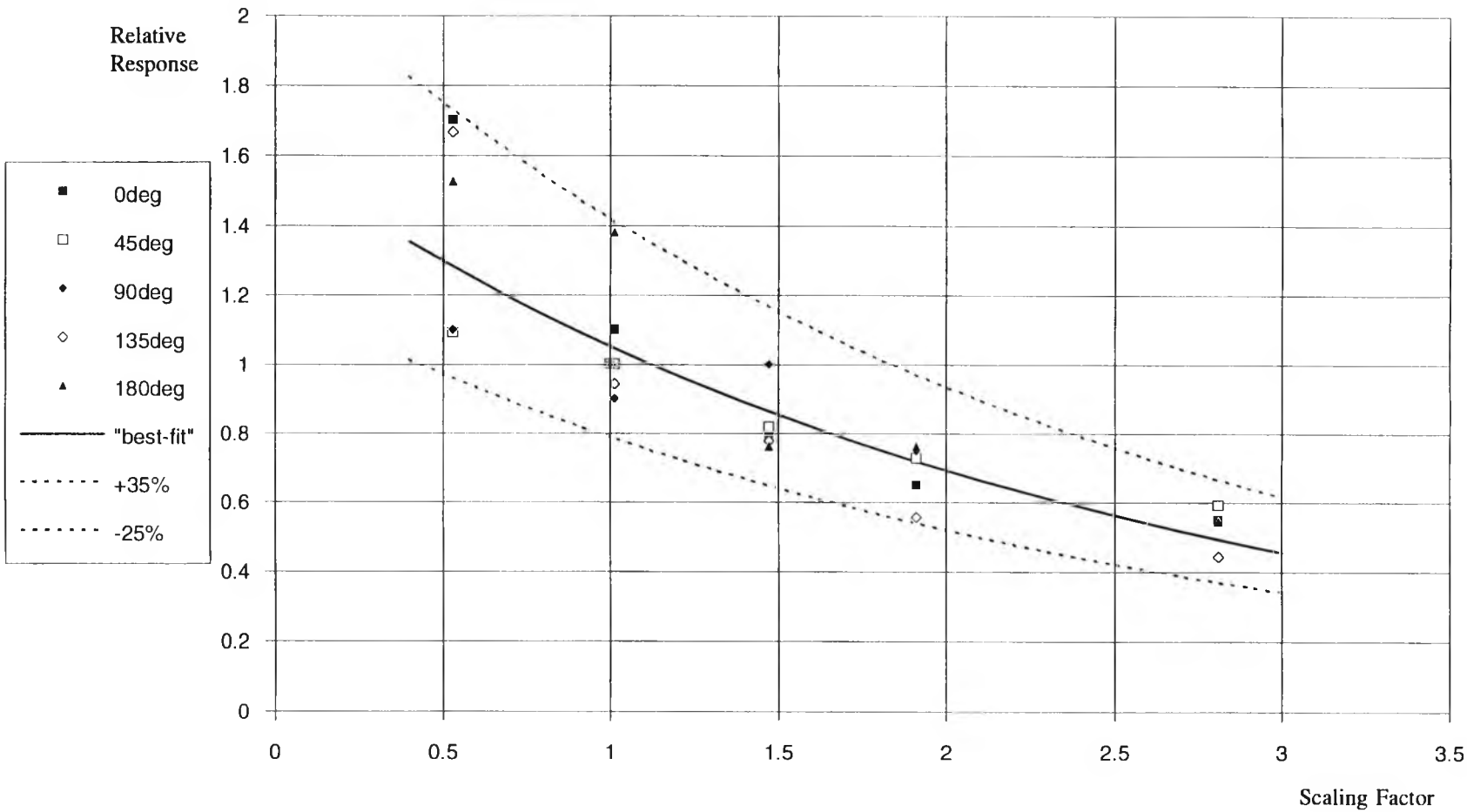

Figure 7.10: Relationship between errors in the internal volume scaling and the resonant response of the cavity pressure fluctuations for a model with a rigid envelope.

None of the results compiled in appendices B & C were reproduced here due to limitations in space.

Nevertheless, in order to summarise the results of this section the analysis of section 7-2-4 was extended to include the effective cavity volume, V_{eff}, defined in chapter 2. Using the volume factors from the previous section and multiplying them by the relevant values of $(1+K_a/K_b)$ (listed in chapter 4) and for each opening azimuth angle using the rigid roof $V_b^{9.4}$ response as a reference value, figure 7.10 was extended to incorporate the flexible roof results. All the data again collapsed onto a single curve (figure 7.11) which was fitted by a function of the form

$$y = 8508 \cdot e^{-9.038\sqrt[16]{x}} \qquad (7.3)$$

where y and x were defined in equation 7.2. The fact that both rigid roof and flexible roof data collapsed so well would seem to corroborate the use of an effective volume when describing the internal pressure dynamics of both rigid and flexible structures. Consequently, similitude of the resonant response of the internal pressure at velocity scales less than unity may be achieved by either exaggeration of the cavity volume at model scale or by introducing some degree of flexibility into the envelope of the model. This idea was alluded to by Pearce & Sykes (1994) from the results of free-vibration tests on the model under zero wind condition.

[7-3-2] Higher Modes of Oscillation

The theory in chapter 2 showed that a rigid-walled Helmholtz resonator can be modelled as a single-degree-of-freedom system and that this analysis may be extended to "conventional" buildings with flexible walls if an effective volume dependent upon the relative stiffnesses of air and the envelope of the building is defined. However, strictly speaking, the additional motion of the flexible components of the building introduce additional degrees-of-freedom to the system which produce higher frequency modes of vibration to which the building can *potentially* respond.

Vickery (1986) stressed that the definition of an effective volume was only applicable to more conventional buildings and should not be applied to the analysis of the dynamic response of large-span roof structures. The reasoning behind this was probably that the inherent stiffness of conventional buildings, even those that were relatively flexible, produced higher frequency modes that were way out in the tail end of the turbulent energy spectrum of the atmospheric boundary layer and were thus

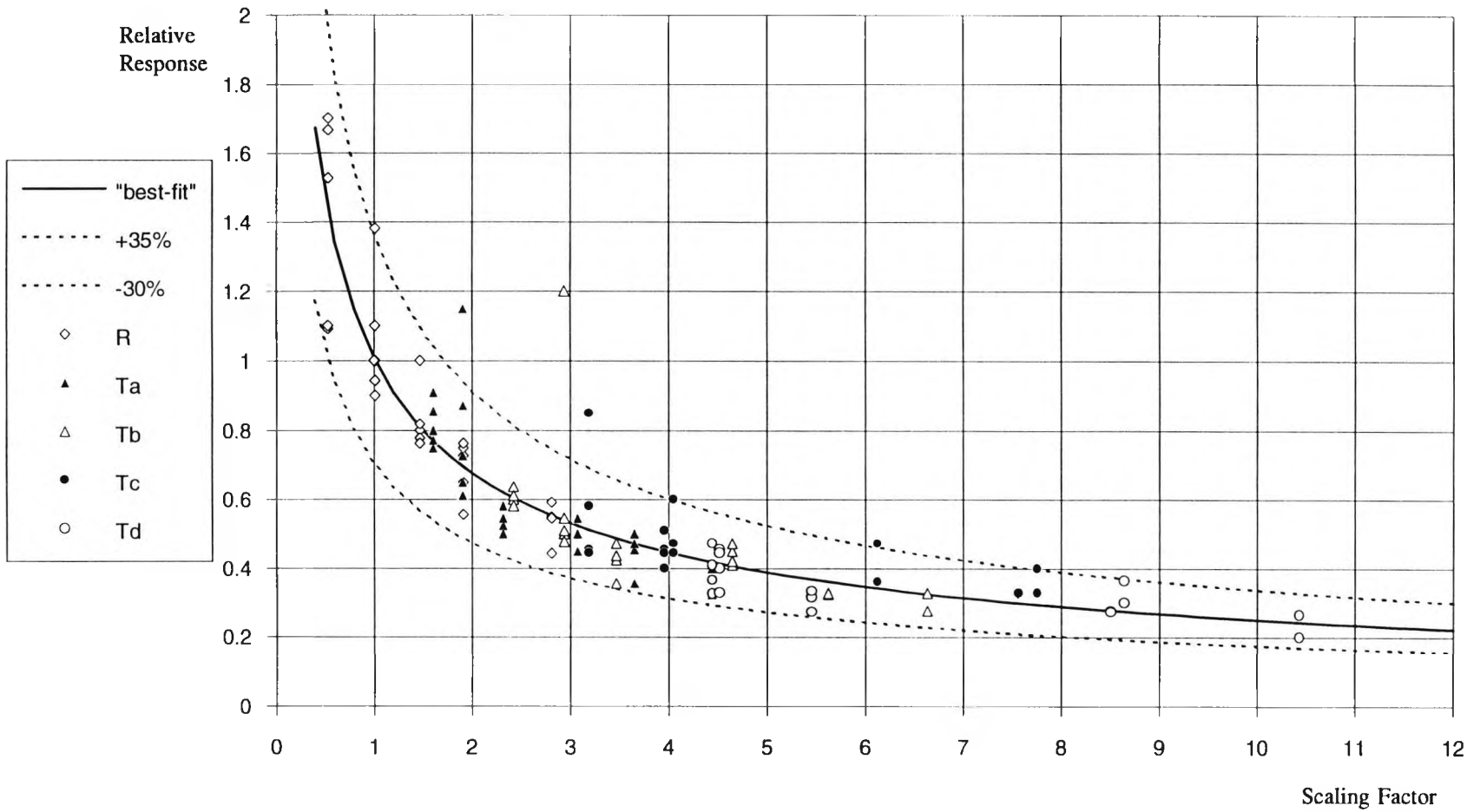

Figure 7.11: Relationship between errors in the internal volume scaling and the resonant response of the cavity pressure fluctuations for models with both rigid and flexible roofs.

unlikely to be excited to a significant degree even if they were only lightly damped modes. The results of the previous section [7-3-1] showed that the definition of an effective volume was a valid means of extending the analysis of an Helmholtz resonator as a single-degree-of-freedom system to fairly "unconventional" buildings with large flexibility in the envelope of the building, however, the spectral results of appendix B showed that such an analysis did not paint the complete picture because higher modes were excited by the turbulent pressure field acting around the model. The reader is again referred to appendices B and C for the relevant results.

[7-3-2-1] Roof Mode Shapes

A simple visualisation study of the motion of the flexible roof of the model in still air was conducted using a loudspeaker emitting a sinusoidal excitation and salt as a marker. This test revealed that for the two modes of oscillation shown on the spectra in appendix C the roof was vibrating in its fundamental mode, i.e. first volume-displacing mode and that no asymmetric roof modes were excited for frequencies up to around 150Hz (at model scale). This simplified the multi-degree-of-freedom analysis of the roof-cavity-opening system, as described by Vickery & Georgiou (1991), to a two-degree-of-freedom system as outlined in chapter 2.

[7-3-2-2] Trends in the Response of the Cavity Pressure

The natural frequency of the higher frequency mode for the model configured as volume A lay just beyond the frequency range covered by the data processing. This was unfortunate but the maximum cut-off frequency of the spectral analysis was limited by the speed of the sampling software. However, based upon the results obtained for cavity volumes A and B a number of general conclusions were drawn .

Similar model configurations showed an increased response at the frequency of the second mode when the windspeed of the external flow was increased. However, there was no discernible trend apparent in the response of the cavity pressure when the volume was increased; some configurations showed an increased response whilst others a reduced response. Increases in the flexibility of the building envelope, for cavity volume C showed an increased response for openings located at most azimuth angles, whereas, for volume B this same trend was restricted to openings positioned at 90°, 135° and 180° (the response was insensitive to changes in roof tension when the openings pointed to windward).

The frequency of the second mode of oscillation was reduced when either the cavity volume was increased or the tension of the roof was decreased and thus followed the same trends as the lower frequency Helmholtz mode. These shifts along the frequency axis moved the frequencies of the second modes to regions where the turbulent energy available for excitation was greater, nevertheless, for most of the results shown in appendix B the response of the cavity pressure at the higher frequency was only a small fraction of the total dynamic response. Indeed comparisons of the areas under the power spectra, by inspection, indicated that the response at the higher mode contributed less than 10% of the total response of the cavity pressure.

[7-4] Summary

The spectral results revealed that the magnitude of the resonant response of the cavity pressure fluctuations was highly dependent upon the location of the single dominant opening present in the wall of the model. The minimum response was found to occur when the opening was orientated such that the component of flow into the opening was at a minimum. These results were in agreement with the root-mean-square pressures reported in chapter 6 where the dynamic component of the cavity pressure was less than that measured on the external walls of the model for azimuth angles centred around 90°.

The cavity pressure spectra measured when the walls of the model were rigid showed that resonance at the Helmholtz frequency dominated the response for certain configurations of the model, but at other times the response was essentially due to broad-band turbulent buffetting. The definition of a gain function, G_1, was useful in isolating changes in the cavity pressure spectra by removing any sensitivities inherent in the external pressure spectra.

When the flexible membrane roof was fitted to the model and tests repeated for varying degrees of roof tension a second, higher frequency mode appeared on the cavity pressure spectra. However, the response of the cavity pressure in this mode was negligible across the range of model configurations tested.

The scaling parameter for modelling internal pressure dynamics was experimentally verified both qualitatively and quantitatively and a general empirical relationship between the resonant response of the cavity pressure at the Helmholtz frequency as a function of errors in scaling was determined from the graphical results of appendix B.

Chapter 8: Probability Distributions & Peak Pressures

[8-1] Introduction

The results presented so far have been concerned with mean values and variance (or standard deviation) of the measured pressure coefficients. However, in the design of a structure the maximum loading likely to be encountered during its lifetime has clear significance. The importance of the mean internal pressure on the net loading across the individual walls of a structure was discussed in chapter 1 (see figure 1.1), but buildings with a dominant opening are also prone to relatively large peak pressures because of the relative ease with which the energy contained in external gusts is transmitted to the building cavity. Whilst theoretical estimates and measurements of the peak internal pressures induced in rigid walled buildings have been reported previously (Liu & Saathoff, 1981, 1982; Stathopoulos & Luchian, 1989) there does not appear to be published data concerned directly with the influence that building envelope flexibility has on the magnitude and distribution of peak internal pressures. The results in this chapter address this gap in knowledge for a limited set of experimental conditions.

An important parameter in terms of obtaining realistic values for the peak net loading is the correlation between occurrences of extreme external pressure and extreme internal pressure. This correlation will in general be a function of the position, size, geometry and lengths of the openings in the walls of the building as well as the geometry of the internal cavity and is likely to be low for relatively airtight structures and high for buildings that are open, or closed but with a dominant opening. Thus, the results presented below may be considered to be representative of a typical worst-case scenario where peak factors (defined in equation 8.2) for internal pressure are high and *assumed* to be well-correlated with the external peak pressures. The actual correlation between external and internal pressure fluctuations was not determined from the experimental results.

The extreme value analysis conducted in the present test programme was restricted to pressures on the vertical walls of model A at a height of z/H=0.55 for wind azimuth angles (θ) of 0^0, 45^0, 90^0, 135^0 and 180^0 at two mean wind speeds of 9.4m/s and 13.0m/s. The peak internal pressures were obtained at the same five orifice azimuth angles, though from the viewpoint of structural loading the results at $\phi=0^0$ and $\phi=90^0$ are the more significant because these two locations represented the two extreme mean loads exerted around the circumference of the model. The peak internal pressure coefficients were obtained for three cavity volumes, A, B & C, five roof tensions, rigid, T_a,T_b,T_c & T_d and two mean reference windspeeds.

[8-2] Data Acquisition and Analysis

The previous chapter was concerned with the transformation of time series data into the frequency domain where the frequency content was quantified and described. However, the same time series may be converted into the amplitude domain where the likelihood of occurrence of data of different magnitudes can be compared by computing the probability distribution. Generally speaking, values around the mean have a high probability of occurrence whilst out in the tail ends of the probability distribution the extreme values have a low probability of occurrence.

Peterka & Cermak (1975) were able to determine the form of the probability density function (p.d.f.) of external pressure from the magnitude of the mean pressure coefficient at the point of interest. If the $C_p > -0.1$ then the flow above the pressure tap was attached and adequately described by a Gaussian distribution, whereas the condition $C_p < -0.25$ implied that the external flow was separated and the p.d.f. approached an exponential form. More recently Holmes (1981) reported that the shape of the p.d.f.s of pressures on windward walls of buildings was also dependent upon the magnitude of the turbulence intensity of the approach flow becoming more exponential as the intensity increased. The significance of the latter result is that assuming a Gaussian form for the p.d.f. increasingly underestimates the magnitude of the extreme pressures.

Despite the sensitivity of the shape of the p.d.f. to the external flow the distribution of extremes for both Gaussian (or normal) and exponential functions can be described by the Fisher-Tippett Type I distribution and this was assumed in the analysis of the following results. Details of the analysis procedure can be found in Cook (1985; 1989) and a summary of the procedure is given in appendix D. Probability distributions of both internal and external cavity pressures were computed for each configuration of the model and compared graphically with the standardised normal distribution. In addition the third and fourth moments of the time series, namely skew and kurtosis, were computed and compared for parametric changes in the configuration of the model.

The extreme values were obtained in the form of pressure coefficients referenced to the dynamic pressure at the height of the model (see appendix A). The mean component of pressure was removed from each sample block so that each peak value was of the form,

$$C_{p_{max}} = C_{p_{peak}} - \overline{C}_p \quad . \qquad (8.1)$$

In regions on the building where the mean pressure was positive then the peak positive pressure was selected as the maximum of interest and in regions of mean suction the peak negative pressure was chosen as the "maximum". The variance of the pressure over each sample period was also computed which enabled the peak factors, p_f, of external and internal pressure to be compared, where

$$p_f = \frac{C_{p_{max}}}{\sigma_{C_p}} \qquad (8.2)$$

As stated in chapter 3 the time series were digitised at 333.33Hz in blocks of 4096 data points. Five different peak values were extracted from each block corresponding to single, two, four, eight and sixteen-point moving averages computed along the time series. For each block the five different peak values were stored until twenty-four blocks had been processed. Each set of extremes was then analysed following the procedure outlined in appendix D. The five different peak values were equivalent to model-scale averages computed over periods of approximately 0.003s, 0.006s, 0.012s, 0.024s and 0.048s being the maxima for individual data blocks that were approximately 12s in length.

[8-3] External Wall Pressure Results

[8-3-1] Probability Distributions

A standardised normal distribution is symmetric about zero and consequently has zero skew. In addition, the "flatness" or kurtosis for the same type of distribution has a value of three so that the differences between the computed skew and kurtosis and these "theoretical" values gives some idea of goodness of fit of the experimental data to a normal distribution.

Table 8.1 contains both the skew and kurtosis data computed for external pressure fluctuations acting on the vertical wall of the model at a height of 0.27H. The skew was positive when the mean external pressure was positive and negative when the pressure was negative. In addition, the magnitude of the skew was high when the magnitude of the mean pressure was high and low when the magnitude of the mean mean was low.

Estimates of the kurtosis of the external pressure fluctuations exceeded those of a Gaussian distribution for all azimuth angles. The magnitude of the kurtosis was high for pressure fluctuations in the stagnation region of the vertical wall and systematically

decreased on moving to leeward; however, in the base region (θ=180°) the kurtosis was at a maximum value.

azimuth angle	Uref = 9.4m/s skew	kurtosis	Uref = 13.0m/s skew	kurtosis
0	0.76	3.93	0.76	3.89
45	0.24	3.75	0.30	3.88
90	-0.66	3.59	-0.66	3.54
135	-0.50	3.58	-0.45	3.54
180	-0.17	4.13	-0.26	4.03

Table 8.1: Estimates of the skew & kurtosis of the external pressures at 0.27H

[8-3-2] Extreme Value Distributions

The acquisition of extreme value data was described in section 8-2 and these data were processed according to the method outlined in appendix D. The analysis of these extreme value peak factors (equation 8.2) produced estimates of the most likely extreme value (mode, U), the spread of extreme values (dispersion, 1/a) and also the dimensionless characteristic product of extremes, aU. Table 8.2 summarises the extreme value analysis data of the external pressure fluctuations on the vertical face of the model at a height 0f 0.55H, for single, two, four, eight & sixteen point extreme values.

	gust -size	1			2			4			8			16		
speed	θ	U	1/a	Ua	U	1/a	Ua	U	1/a	Ua	U	1/a	Ua	U	1/a	Ua
9.4																
	0	4.51	0.50	9.0	4.30	0.50	8.6	3.99	0.44	8.99	3.54	0.45	7.88	2.97	0.40	7.5
	45	4.32	0.35	12.5	4.05	0.32	12.7	3.74	0.34	10.9	3.35	0.26	12.9	2.88	0.24	12.1
	90	4.00	0.44	9.0	3.83	0.38	10.0	3.62	0.42	8.7	3.38	0.44	7.64	3.00	0.47	6.3
	135	4.64	0.65	7.1	4.03	0.62	6.5	3.49	0.57	6.2	3.16	0.51	6.2	2.82	0.46	6.2
	180	4.34	0.39	11.1	3.81	0.39	9.6	3.39	0.31	11.0	2.87	0.28	10.1	2.30	0.30	7.7
13.0																
	0	4.60	0.55	8.3	4.29	0.45	9.4	3.86	0.43	9.0	3.27	0.43	7.7	2.67	0.22	12.1
	45	4.62	0.57	8.1	4.31	0.51	8.5	3.84	0.40	9.5	3.35	0.42	7.9	2.75	0.34	8.1
	90	4.19	0.58	7.3	4.01	0.60	6.6	3.84	0.52	7.4	3.56	0.42	8.5	3.20	0.32	9.9
	135	4.21	0.38	11.0	3.71	0.32	11.8	3.28	0.30	10.8	2.97	0.34	8.7	2.66	0.27	9.7
	180	5.11	1.08	4.7	4.47	0.91	4.9	3.64	0.56	6.5	3.04	0.52	5.8	2.41	0.46	5.2

Table 8.2: Extreme value analysis parameters for extremes of different duration measured on the external wall at a height of 0.55H.

Systematically increasing the size of the moving average from a single point extreme value to the mean of sixteen consecutive data points increased the size of gust under investigation within the cavity of the model. It was clear that this procedure had the effect of smoothing the original time series data so that for a particular time series one

would expect the estimate of the mode to get smaller as the size of gust was increased, i.e. the magnitude of the most likely extreme value decreased with increases in gust size. It was also anticipated that the smoothing process described above would diminish the spread of extremes, 1/a. Reductions in the dispersion parameter implied that the range of extreme values was nearer in magnitude to the magnitude of the mode, a condition that was also implied by a high value for the characteristic product.

The results in table 8.2 were consistent with the expectations described in the previous paragraph with both the mode and dispersion decreasing in magnitude for increases in the duration of the extreme; there was no discernible trend apparent for the characteristic product. As shown in appendix D the estimate of the mode was associated with the smallest margin of error and so the sensitivity of this parameter to changes in the duration of the peak was quantified as follows. At each azimuth angle, the "single-point" mode, $U_{N=1}$, was used to normalise the modes for 2, 4, 8 & 16 point extremes and these data were then plotted against the relative period of the gust, 1, 2, 4, 8 & 16. The resultant curves were approximated by exponential decays of the form

$$\frac{U_{N_{gust}}}{U_{N=1}} = k_2 \, e^{\,k_1 N} \qquad (8.3)$$

where k_2 and k_1 were empirical coefficients and N represents the number of points in the moving average. The linear regression analysis of the data for each configuration of the model showed that the coefficient k_2 was equal to unity to within plus or minus 5%, whereas, the decay rate k_1 was a function of both azimuth angle and windspeed as shown in table 8.3 and figure 8.1.

	Uref = 9.4m/s		Uref = 13.0m/s	
θ	k1	k2	k1	k2
0	-0.027	1.00	-0.035	0.99
45	-0.026	0.99	-0.033	0.99
90	-0.018	0.99	-0.017	1.00
135	-0.029	0.92	-0.027	0.93
180	-0.040	0.96	-0.047	0.95

Table 8.3: k_1 & k_2 (defined in equation 8.3) for external pressure fluctuations at 0.55H

The coefficient k_1 was negative for all cases which implied that increasing the size of the extreme gust reduced the magnitude of the most likely extreme value. Clearly this result implied that even though the spatial correlation of a large gust is greater than that of a smaller gust its overall magnitude is less. Nevertheless, the rate of this reduction

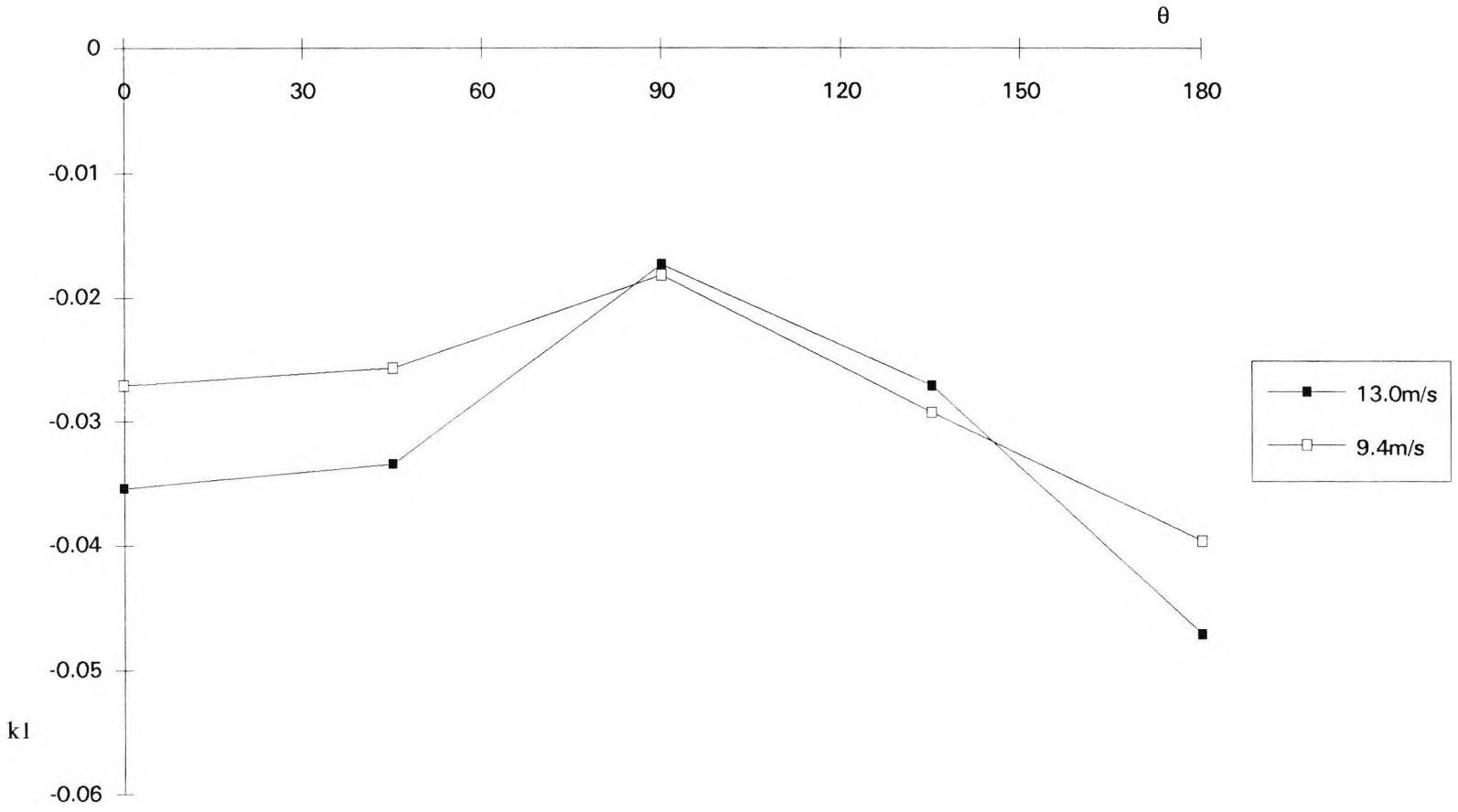

Figure 8.1: The parameter k1 (defined in equation 8.3) as a function of azimuth angle for external pressure fluctuaions on the external wall at a height of 0.55H.

was sensitive to the location of the pressure fluctuations with values ranging between -0.03<k_1<-0.05.

Remembering that high values of k_1, i.e. those approaching zero, suggested that the magnitude of the mode was *not* significantly affected by the size of the peak gust, for the range of gusts covered in this analysis, it was apparent from figure 8.1 that the relationship between the e.v.a. mode and peak duration was not universal and that the nature of peak pressures in the stagnation region was perhaps physically different from the peaks that occurred in the maximum mean suction region (θ=90°).

[8-4] Cavity Pressure Results

[8-4-1] Probability Distributions

Figure (8.2) shows the probability distributions of the cavity pressure measured when the model had a rigid roof and cavity volume A and figure (8.3) shows equivalent results for the same configuration but with the membrane roof fitted at tension D. Inspection of these plots shows that when the mean cavity pressure was positive the skew on the p.d.f. of pressure was positive and for negative mean pressures the skew was negative. These trends agreed qualitatively with the results of table 8.1. The physical significance of positive (or negative) skew is that a higher probability of occurrence of extreme positive (or negative) pressures exists compared with the Gaussian distribution (as illustrated on figures (8.2) & (8.3)).

The degree of skew and kurtosis is quantified in tables 8.4 & 8.5 where neither variations in roof tension nor changes in the cavity volume had any discernible effect on the p.d.f. of the cavity pressure. The trends mentioned in the previous paragraph were apparent in the data and, in addition, increases in the magnitude of the pressure were accompanied by increases in the skew. The estimates of kurtosis were generally high for openings oriented to windward and steadily reduced to values of around 3.0 when the opening was in the base region of the model. Generally the magnitudes of both the skew and kurtosis were less than those measured on the external wall at 0.27H which probably reflects the area-averaging effect of the opening.

In addition to the above the consistency in the measures of both skew and kurtosis permitted these data to be used as a check on the quality of the results obtained for each configuration of the model tested. It can be seen that ten of the experimental runs (highlighted in tables 8.4 & 8.5 by the bold, italicised print) produced values of skew and kurtosis that differed significantly from the majority of the tests which was

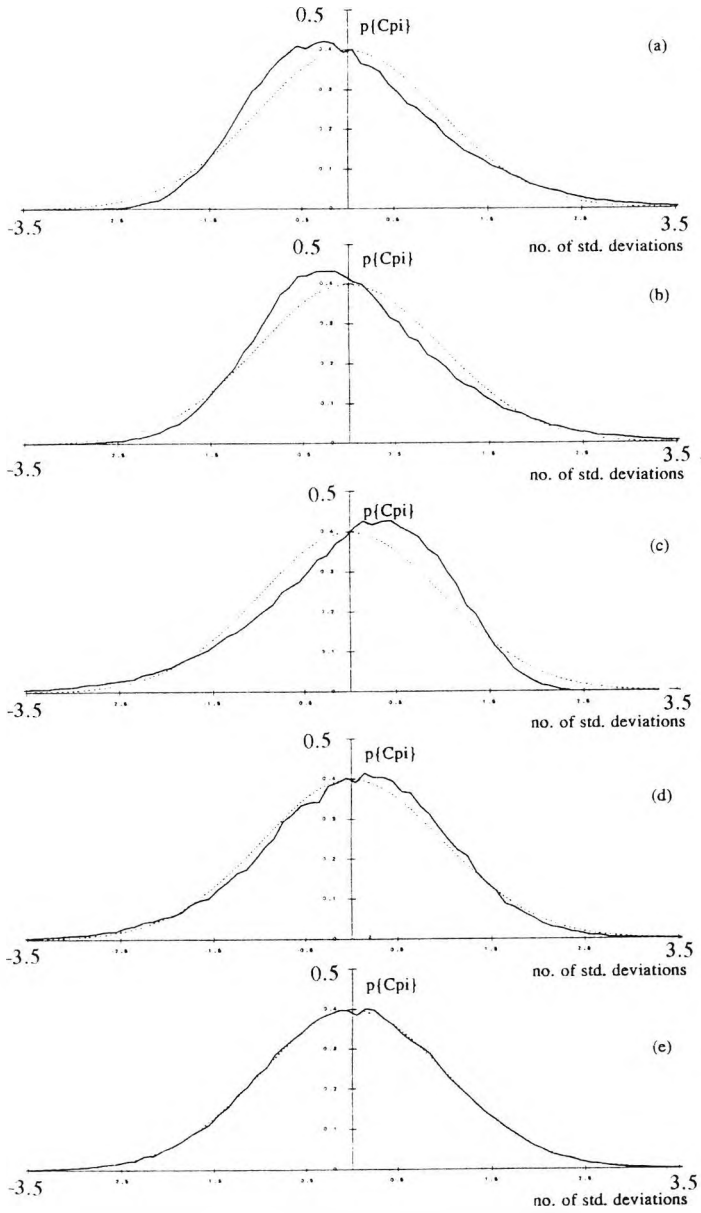

Figure 8.2(i): Probability distributions for cavity pressure fluctuations with Va, mean windspeed of 13.0m/s, rigid roof and (a) ϕ = 0 degrees, (b) ϕ = 45 degrees, (c) ϕ = 90 degrees, (d) ϕ = 135 degrees, (e) ϕ = 180 degrees.

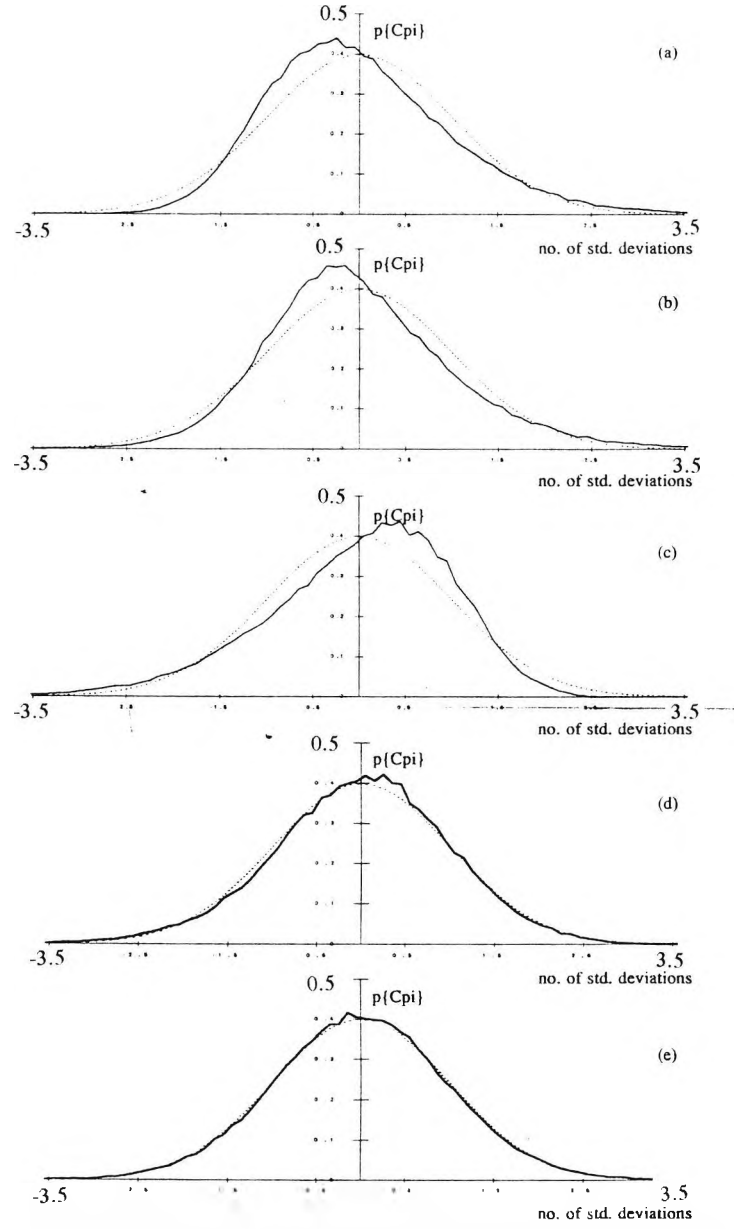

Figure 8.2(ii): Probability distributions for cavity pressure fluctuations with Va, mean windspeed of 9.4m/s, rigid roof and (a) ϕ = 0 degrees, (b) ϕ = 45 degrees, (c) ϕ = 90 degrees, (d) ϕ = 135 degrees, (e) ϕ = 180 degrees.

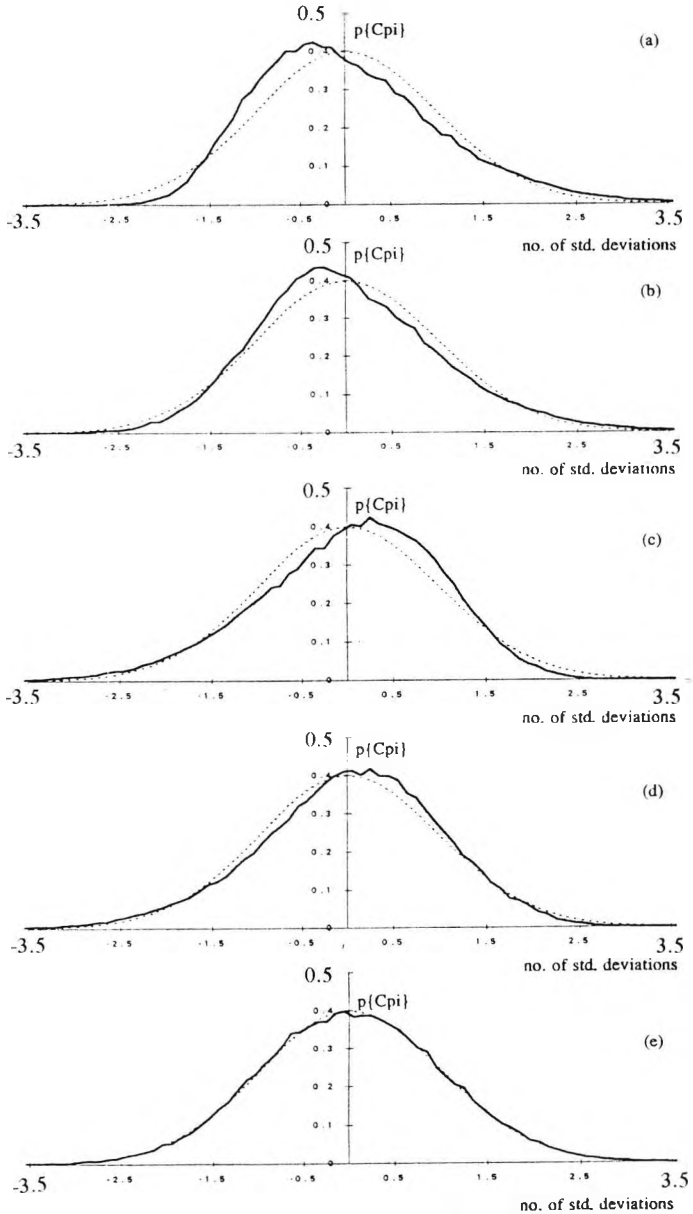

Figure 8.3(i): Probability distributions for cavity pressure fluctuations with Va, mean windspeed of 13.0m/s, roof tension D and (a) ϕ = 0 degrees, (b) ϕ = 45 degrees, (c) ϕ = 90 degrees, (d) ϕ = 135 degrees, (e) ϕ = 180 degrees.

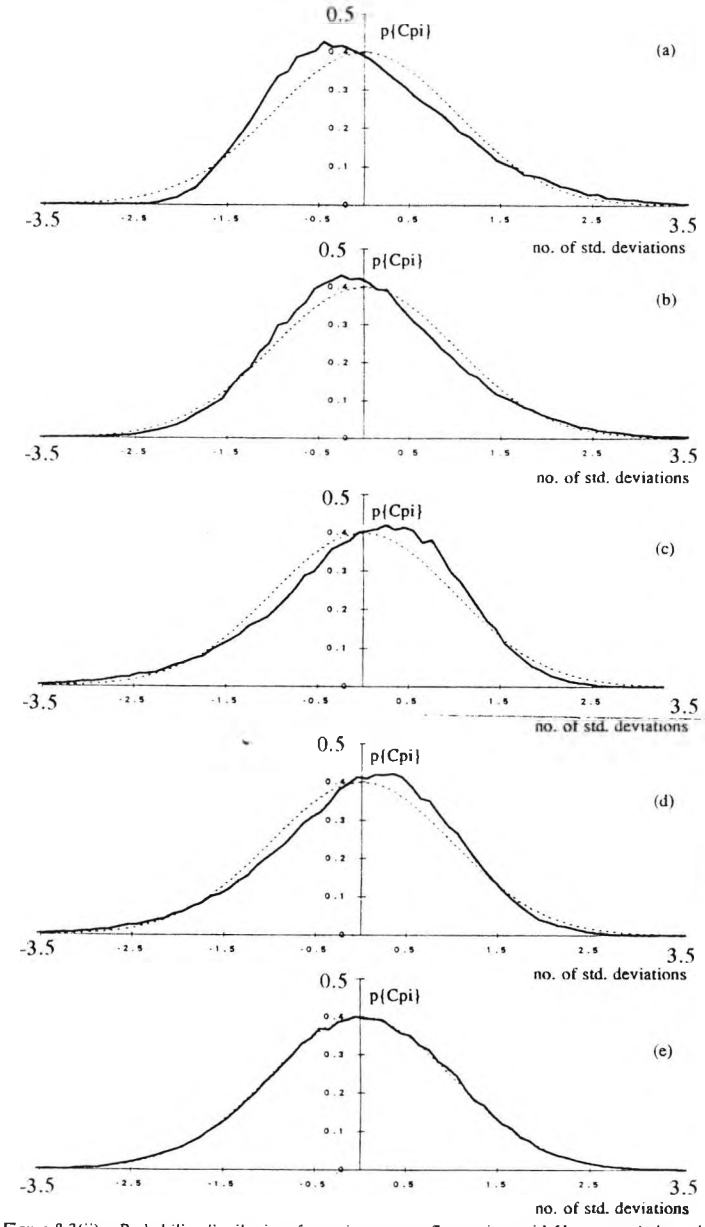

Figure 8.3(ii): Probability distributions for cavity pressure fluctuations with Va, mean windspeed of 9.4m/s, roof tension D and (a) ϕ = 0 degrees, (b) ϕ = 45 degrees, (c) ϕ = 90 degrees, (d) ϕ = 135 degrees, (e) ϕ = 180 degrees.

indicative that during the digitisation process there may have been drop-outs or spikes present on the analog tape. These "errors" were consistent and appeared in both the skew and kurtosis data.

		Va					Vb					Vc				
U	θ	R	Ta	Tb	Tc	Td	R	Ta	Tb	Tc	Td	R	Ta	Tb	Tc	Td
9.4	0	.67	.59	.53	.53	.62	.61	.61	.59	.62	.56	.63	.59	.53	.59	.64
	45	***.62***	***.31***	.44	.43	.40	.54	.44	.36	.35	.41	.43	.42	.41	***-3.6***	.38
	90	-.62	***-.85***	-.50	-.44	-.55	-.62	-.58	-.52	***-1.8***	-.51	-.69	-.62	-.54	-.57	-.52
	135	-.19	-.26	-.26	-.34	-.67	-.25	-.35	-.49	-.35	-.38	-.22	-.35	-.35	***-.63***	-.32
	180	0	-.02	-.05	-.05	-.05	-.03	-.01	-.07	-.04	-.09	-.10	-.07	-.10	-.04	-.05
13	0	.60	.52	***.28***	.59	.61	-	.50	.54	.61	.58	.54	.53	.54	***.37***	.58
	45	.59	.39	.43	.44	.44	.52	.35	***-.07***	.40	.39	.48	.39	.39	.41	.43
	90	-.68	-.48	-.50	-.50	-.47	-.63	-.55	-.52	-.44	-.43	-.54	-.45	-.54	-.42	-.43
	135	-.29	-.33	-.35	-.37	-.34	-.33	-.33	-.37	-.35	-.37	-.32	-.31	***-1.0***	-.35	-.36
	180	-.01	-.06	-.06	-.07	0	-.05	-.05	-.06	-.03	-.06	-.02	-.08	-.07	-.07	-.07

Table 8.4: Estimates of the skew (third mode) for cavity pressure fluctuations.

		Va					Vb					Vc				
U	θ	R	Ta	Tb	Tc	Td	R	Ta	Tb	Tc	Td	R	Ta	Tb	Tc	Td
9.4	0	3.84	3.95	3.34	3.30	3.52	3.58	4.32	3.46	3.54	3.35	3.61	3.49	3.25	3.46	3.54
	45	***4.27***	***5.71***	3.52	4.05	3.61	3.70	3.59	3.42	3.42	3.72	4.44	3.49	3.48	***134.***	3.41
	90	3.59	***6.50***	3.44	3.29	3.59	3.57	3.53	3.45	***56.7***	3.39	3.74	3.71	3.59	4.11	3.40
	135	3.42	3.31	3.23	3.36	7.31	3.34	3.55	3.33	3.25	3.38	3.18	3.38	3.79	***7.58***	3.35
	180	3.26	3.03	3.42	3.09	3.03	3.12	3.37	3.10	3.05	3.06	3.92	3.05	3.06	3.02	3.01
13	0	3.51	3.31	***7.42***	3.36	3.41	-	3.49	3.28	3.40	3.34	3.26	3.28	3.28	***6.47***	3.27
	45	3.97	3.50	3.98	3.55	3.58	3.68	3.41	***10.4***	3.42	3.46	3.53	3.42	3.41	3.31	3.47
	90	3.64	3.29	3.37	3.42	3.28	3.57	3.42	3.63	3.20	3.31	3.28	3.20	5.03	3.17	3.18
	135	3.31	3.34	3.24	3.32	3.29	3.29	3.21	3.31	3.27	3.30	3.38	3.24	***15.0***	3.33	3.32
	180	3.10	3.03	3.06	3.05	3.00	3.04	3.04	3.05	3.03	3.03	2.93	2.95	3.06	2.98	3.00

Table 8.5: Estimates of kurtosis (fourth mode) for cavity pressure fluctuations.

[8-4-2] Extreme Value Distributions

[8-4-2-1] Introduction

Tables 8.6 summarise the extreme value analysis data of the cavity pressure fluctuations for single-point extreme values. Whilst the e.v.a. parameters associated with the larger gusts were obtained they were not tabulated below due to limitations of space. However, these data were used in an extended analysis of the mode parameter where the influence of gust size, cavity volume, roof tension and cavity volume scaling were investigated using equation 8.3. Comparison of the results in tables 8.6 with the single-point extreme external pressure results (table 8.2) indicated that, *for most azimuth angles*, both the mode and dispersion of the external pressure fluctuations exceeded those measured for the cavity pressure.

		R			Ta			Tb			Tc			Td		
speed	ϕ	U	l/a	Ua	U	l/a	Ua	U	l/a	Ua	U	l/a	Ua	U	l/a	Ua
Va																
9.4	0	4.34	0.53	8.15	3.89	0.42	9.2	3.81	0.32	11.8	3.78	0.35	10.7	3.93	0.45	8.8
	45	4.60	0.59	7.77	4.17	0.45	9.4	3.97	0.44	8.9	4.01	0.47	8.4	3.83	0.47	8.2
	90	3.82	0.48	8.35	4.03	0.80	5.0	3.86	0.31	12.3	3.88	0.34	11.3	3.74	0.42	8.8
	135	3.72	0.31	12.1	3.72	0.33	11.2	3.69	0.34	10.7	3.84	0.39	9.8	3.65	0.48	7.6
	180	3.78	0.34	11.2	3.48	0.31	11.1	3.58	0.25	14.1	3.63	0.19	19.1	3.49	0.29	12.2
Vb																
9.4	0	4.05	0.32	12.6	4.04	0.52	7.7	3.75	0.29	12.8	4.00	0.36	11.1	3.66	0.29	12.5
	45	4.14	0.39	10.6	3.77	0.38	9.9	3.72	0.42	8.8	3.63	0.44	8.3	3.75	0.45	8.4
	90	3.65	0.44	8.2	3.64	0.43	8.4	3.68	0.42	8.7	3.85	0.50	7.7	3.57	0.55	6.5
	135	3.54	0.36	9.9	3.77	0.47	7.8	3.89	0.41	9.4	3.55	0.40	8.9	3.74	0.38	9.7
	180	3.65	0.31	11.9	3.46	0.22	15.4	3.44	0.41	8.3	3.39	0.37	9.2	3.54	0.27	12.9
Vc																
9.4	0	4.06	0.37	11.0	3.83	0.37	10.5	3.59	0.35	10.4	3.74	0.46	8.0	3.76	0.45	8.3
	45	4.06	0.44	9.2	3.72	0.40	9.3	3.69	0.40	9.1	4.48	2.24	2.0	3.69	0.39	9.4
	90	3.68	0.48	7.6	3.73	0.49	7.6	3.64	0.43	8.4	3.65	0.35	10.3	3.60	0.36	10.1
	135	3.40	0.31	11.0	3.66	0.34	10.7	3.62	0.35	10.4	3.71	0.81	4.6	3.64	0.34	10.8
	180	3.46	0.34	10.3	3.52	0.34	10.2	3.45	0.29	11.8	3.42	0.20	17.0	3.43	0.26	13.4

Table 8.6(a): Extreme value analysis results for cavity pressure fluctuations using single point extremes at a reference windspeed of 9.4m/s

		R			Ta			Tb			Tc			Td		
speed	ϕ	U	l/a	Ua	U	l/a	Ua	U	l/a	Ua	U	l/a	Ua	U	l/a	Ua
Va																
13.0	0	4.21	0.32	13.1	3.93	0.29	13.5	3.86	0.38	10.0	3.91	0.31	12.5	3.90	0.31	12.5
	45	4.31	0.54	7.9	3.97	0.40	9.86	3.85	0.39	9.9	3.86	0.47	8.1	3.81	0.47	8.1
	90	4.01	0.27	14.7	3.71	0.34	10.8	3.60	0.37	9.8	3.87	0.30	13.1	3.71	0.34	10.8
	135	3.71	0.31	12.1	3.69	0.35	10.6	3.64	0.35	10.5	3.68	0.43	8.6	3.78	0.41	9.3
	180	3.59	0.38	9.4	3.54	0.28	12.7	3.59	0.24	15.0	3.63	0.33	10.8	3.50	0.25	13.8
Vb																
13.0	0	3.89	0.37	10.5	3.83	0.38	10.1	3.72	0.28	13.3	3.87	0.38	10.2	3.89	0.33	11.6
	45	4.17	0.49	8.5	3.82	0.35	10.9	3.75	0.37	10.1	3.74	0.38	9.9	3.72	0.37	9.9
	90	3.91	0.25	15.5	3.79	0.42	9.0	3.73	0.40	9.3	3.63	0.40	9.1	3.60	0.39	9.1
	135	3.68	0.26	15.2	3.50	0.30	11.6	3.67	0.37	10.0	3.72	0.37	10.2	3.75	0.33	11.2
	180	3.47	0.23	14.9	3.48	0.21	16.8	3.56	0.28	12.9	3.54	0.25	14.5	3.56	0.23	15.5
Vc																
13.0	0	3.64	0.35	10.4	3.62	0.39	9.4	3.74	0.30	12.4	3.86	0.38	10.1	3.58	0.34	10.7
	45	3.89	0.47	8.3	3.71	0.47	7.9	3.74	0.39	9.5	3.77	0.35	10.9	3.85	0.43	8.8
	90	3.56	0.27	13.2	3.46	0.34	10.3	3.48	0.48	7.3	3.45	0.33	10.5	3.57	0.35	10.4
	135	3.55	0.36	10.0	3.54	0.38	9.3	3.63	0.27	13.3	3.63	0.28	12.9	3.75	0.42	9.0
	180	3.26	0.25	13.1	3.42	0.24	14.1	3.52	0.20	17.2	3.43	0.22	15.4	3.45	0.23	14.8

Table 8.6(b): Extreme value analysis results for cavity pressure fluctuations using single point extremes at a reference windspeed of 13.0m/s

[8-4-2-2] The Influence of Gust Size on the Magnitude of the Mode

The extreme value modes for cavity pressure fluctuations were analysed employing equation 8.3. Presentation of the mode data in this format permitted the sensitivity of changes in peak gust size for systematic changes in model geometry to be quantified and the "k_l" results are shown in figures 8.4(i) & (ii).

The coefficient k_1 was negative for all cases which implied that increasing the size of the extreme gust reduced the magnitude of the most likely extreme value. However, the rate of this reduction was sensitive to the configuration of the model with values ranging between $-0.01<k_1<-0.06$ dependent upon the cavity volume, azimuth angle of the opening, reference windspeed and roof flexibility.

Generally, for ϕ equal to 90^o, k_1 was a maximum for all the configurations tested; rotating the opening to windward or leeward reduced the value of k_1. This trend was similar to that reported on the external wall (figure 8.1) but the range of the parameter, k_1, was increased for cavity pressure peak factors. This result was also analogous to the cavity pressure spectra of chapter 7 where the minimum resonant response occurred with $\phi=90^o$ and demonstrated a link between peak pressure and the degree of resonant excitation.

Increasing the size of the cavity volume also increased the value of k_1, a trend that was particularly clear for the rigid roof results (figs 8.4(i)a & 8.4(ii)a) at both windspeeds and underlined the link between peak pressure and resonance of the cavity pressure. Increasing the flexibility of the roof of the model systematically reduced the dependence of k_1 on opening azimuth angle such that for the largest building envelope flexibility k_1 was essentially constant for $0^o<\phi<180^o$ at an "averaged" value of around -0.015. A systematic relationship between mean reference windspeed and the parameter k_1 was not identified in figures 8.4.

One of the implications of the results discussed above is that cavity pressure fluctuations caused primarily by turbulent buffetting have a mode, obtained from extreme value analysis of the peak factors, for gusts of different size that is relatively insensitive to the gust-size. However, when the cavity response is dominated by Helmholtz resonance then the mode of the peak factors of the cavity pressure is far more sensitive to gust size. Indeed equation 8.3 and the results shown in figures 8.4 can be used to quantify this effect; assuming a maximum increase in gust-size of sixteen times gives a relative reduction in the mode of around 0.85 for a response that is turbulent (assuming $k_1=-0.01$) but nearer to 0.40 for a more resonant response (assuming $k_1=-0.06$).

[8-4-2-3] The Influence of Cavity Volume Scaling on the Mode

This section investigates the magnitude of the mode of the cavity pressure fluctuations as a function of cavity volume scaling. Data were analysed in five sets based upon the gust-size and as in the previous chapter, section 7-2-4, an arbitrary "reference" model configuration was used to normalise the modes obtained from different model

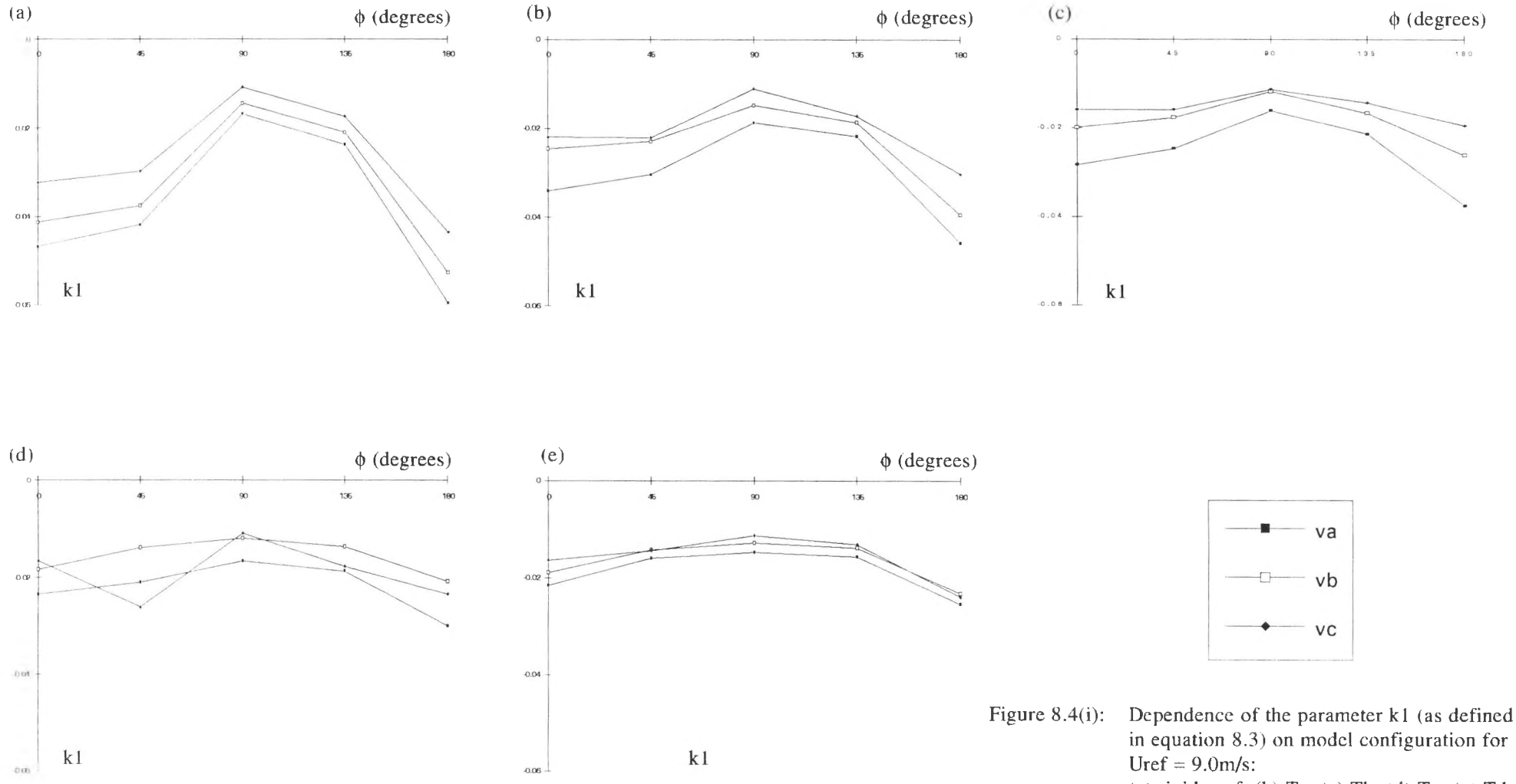

Figure 8.4(i): Dependence of the parameter k1 (as defined in equation 8.3) on model configuration for Uref = 9.0m/s:
(a) rigid roof; (b) Ta; (c) Tb; (d) Tc; (e) Td

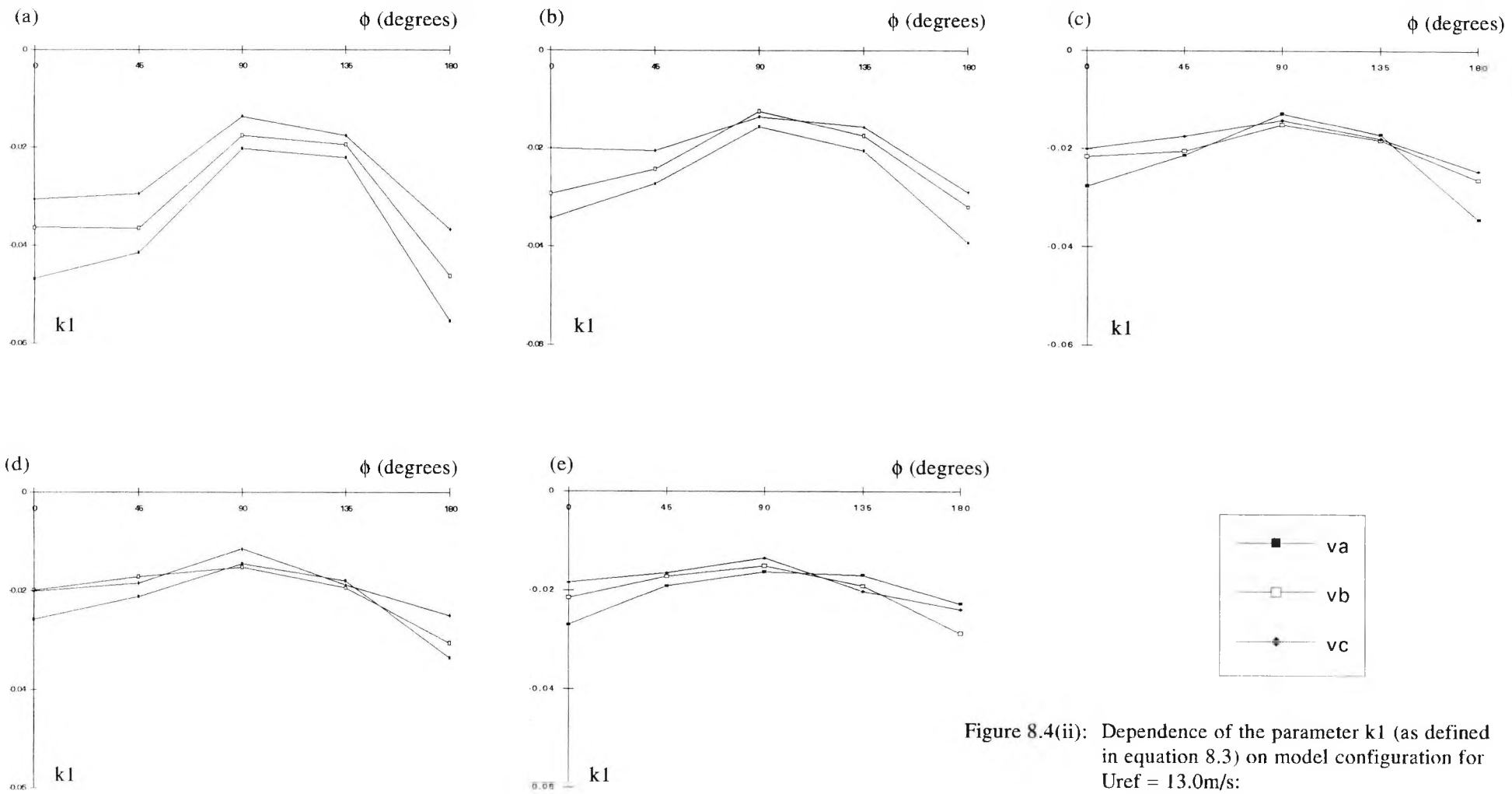

Figure 8.4(ii): Dependence of the parameter k1 (as defined in equation 8.3) on model configuration for Uref = 13.0m/s:
(a) rigid roof; (b) Ta; (c) Tb; (d) Tc; (e) Td

configurations; the reference configuration was cavity volume B fitted with a rigid roof in a boundary layer with a mean reference windspeed of 9.4m/s. The results of this procedure are shown in figures 8.5.

The data were fitted by an exponential curve

$$\frac{U}{U_{R_{b9.4}}} = k_2 \cdot e^{[k_1 \cdot \sqrt[16]{V_{ex}}]} \qquad (8.4)$$

which was similar in form to equation 7.3. The "best-fit" to each set of results was obtained by linear regression and the scatter in the results was quantified by the error bands shown on each figure as the dashed lines.

The volume distortion, shown as the independent variable in figures 8.5, was an effective distortion which took into account both the magnitude of the internal cavity and the apparent increase in this volume due to increased flexibility of the building envelope (see section 7-3-5). Increases in the cavity volume scaling up to a factor of twelve had little effect on the mode of the pressure fluctuations for gusts smaller than 0.024s (model scale), where the magnitude of the mode was changed by less than 10% of the "correct" value. However, the results for the largest gust, 0.048s, showed that a 10% change in the magnitude of the mode was effected by an exaggeration in the cavity volume by a factor of two whilst at an exaggerated cavity scaling of twelve times, the mode was altered by nearly 40%.

Another feature of the results in figures 8.5 was that for peak cavity pressures of duration 0.003s through to 0.012s exaggerating the cavity volume attenuated the extreme value mode, whereas similar changes in the volume scaling amplified the mode when the peaks were 0.024s and 0.048s duration. In order to quantify this effect the parameters k_1 and k_2, as defined in equation 8.4, were plotted against the relative duration of the peak value in figures 8.6. If the duration of the peaks are normalised by the sample period of 12.288s then a non-dimensional gust duration, t_{gnorm}, can be defined which for these tests ranged from 0.0002, 0.0005, 0.0010, 0.0020 to 0.0039.

Figures 8.6 permit the likely error in the mode of the cavity pressure fluctuations for errors in cavity scaling to be estimated based upon the relative period of the extreme pressure. The duration of the peak determines whether exaggerating the cavity volume scaling will amplify or attenuate the measured mode; $t_{gnorm}<0.0015$ attenuates the mode

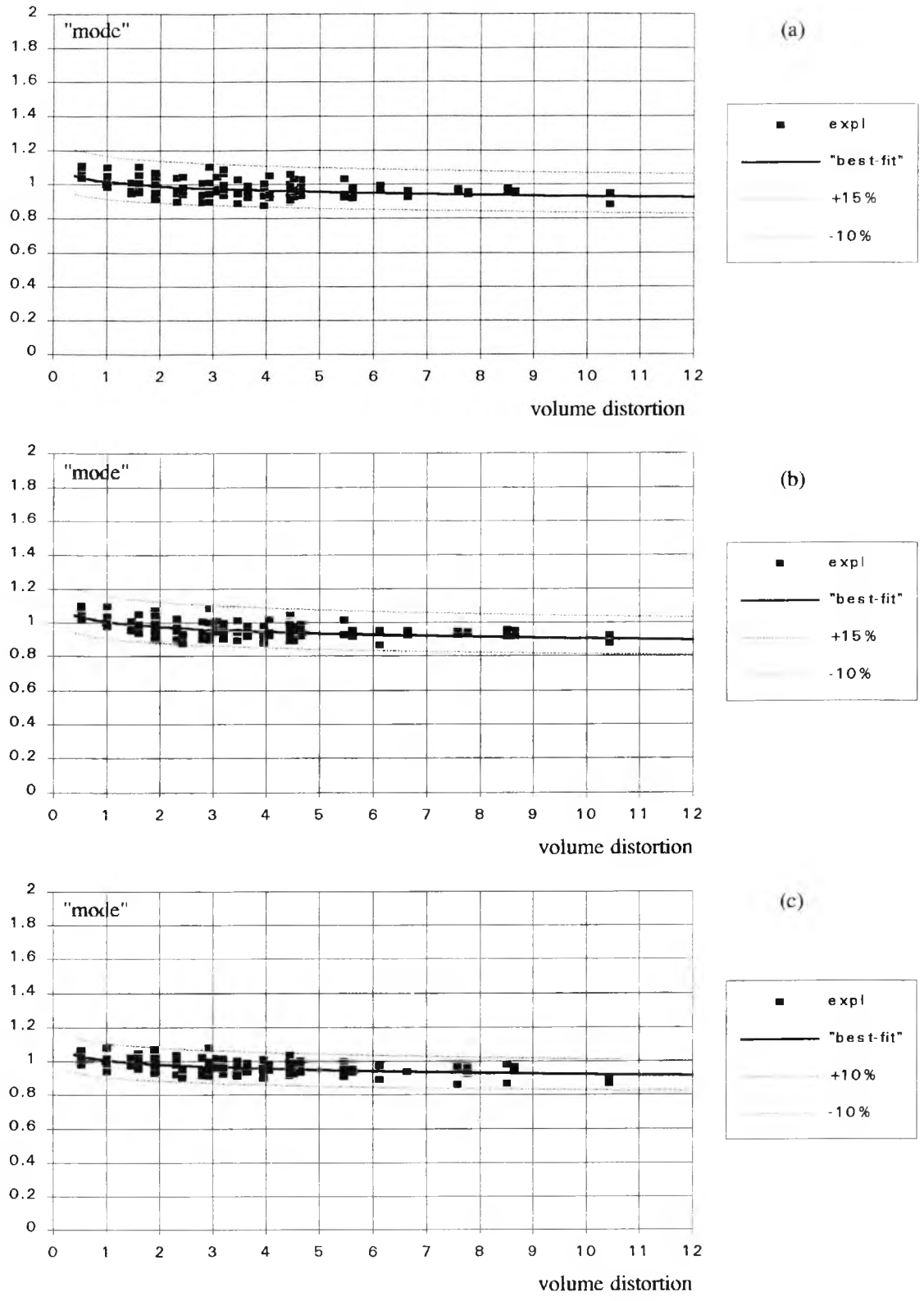

Figure 8.5: Influence of cavity volume scaling on the extreme value analysis estimate of the mode of the cavity pressure fluctuations. Graphs show the mode for each configuration as a fraction of the "correctly" scaled mode [i.e. the mode for a cavity volume B at a reference windspeed of 9.4m/s] as a function of the distorted volume scaling for (a) single point extremes, (b) two-point extremes, (c) four point extremes, (d) eight point extremes & (e) sixteen point extremes.

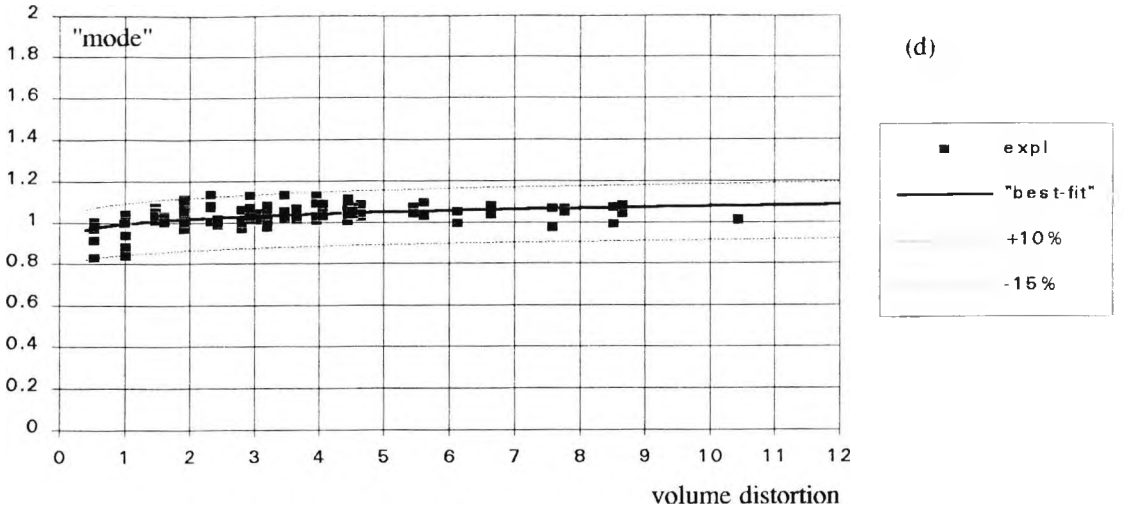

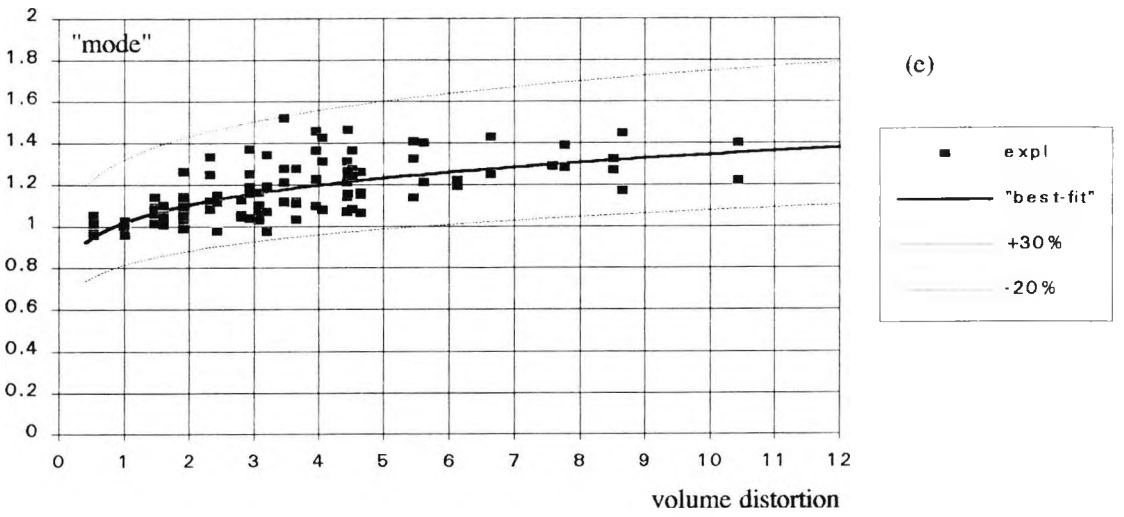

Figure 8.5: continued...

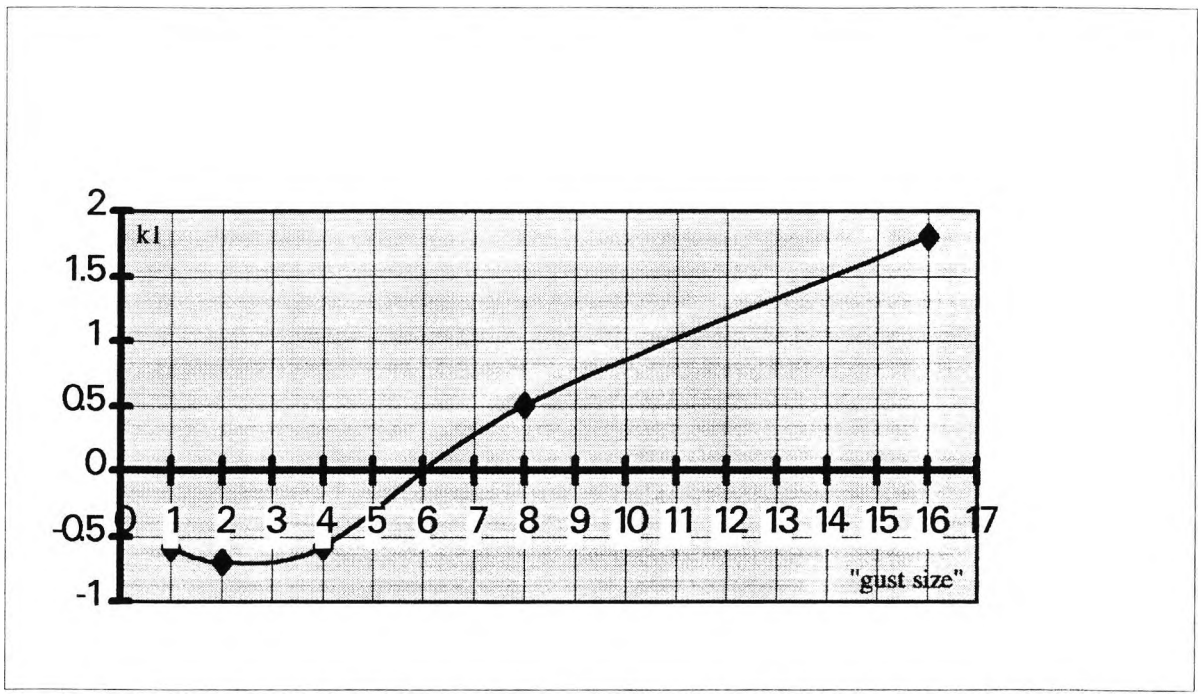

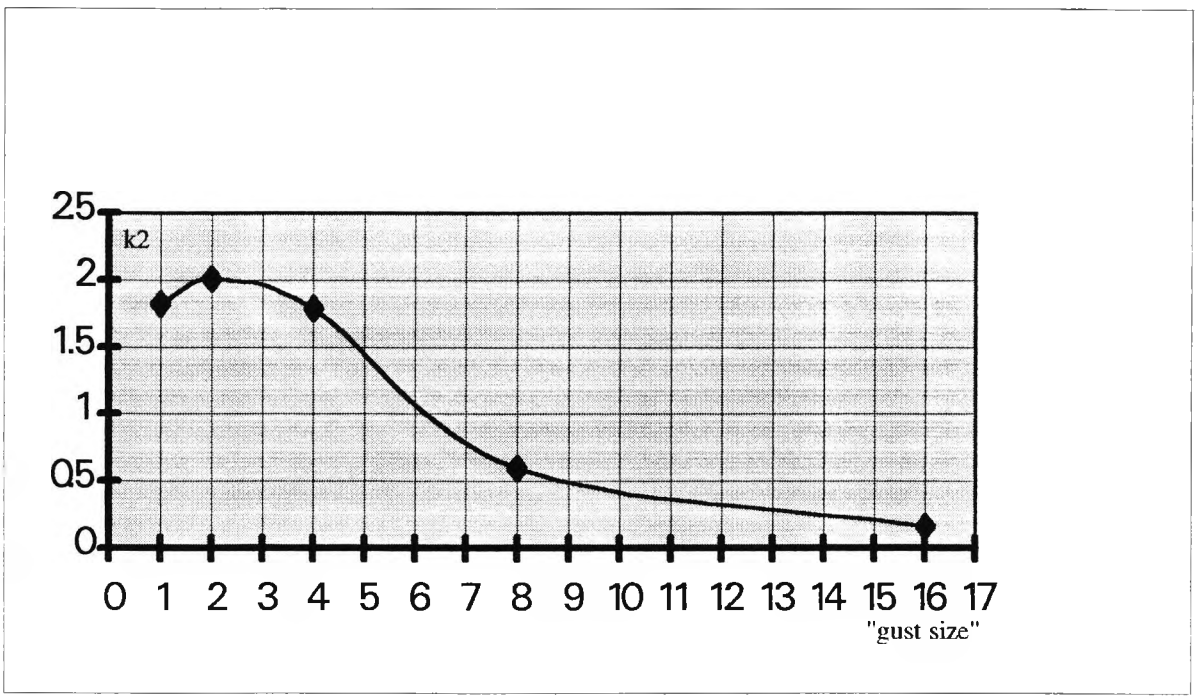

Figure 8.6: Variation of the empirical coefficients k1 and k2 (defined by equation 8.4) with the size of the peak gust moving point average.
(Note: division of the "gust-size" shown on these graphs by the block size of 4096 data points gives the normalised peak period described in the text.)

(because k_1 is negative), whereas $t_{gnorm}>0.0015$ amplifies the mode (because k_1 is positive).

[8-5] Summary

Expression of the time series, of both external wall and cavity pressure fluctuations, in the amplitude domain showed that similar trends were apparent on the probability distributions and in the extreme value analysis of both sets of data.

Positive (negative) skew occurred in regions where the mean pressure was positive (negative) and the magnitude of the skew was proportional to the magnitude of the mean pressure. Measures of the kurtosis were high at the front stagnation region and steadily reduced on moving to windward.

Extreme values were obtained in the form of positive peak factors for five different peak periods corresponding to 0.003s, 0.006s, 0.012s, 0.024s & 0.048s (model scale). These data showed that increasing the duration of the peak reduced the magnitude of the most likely extreme value, the mode, and also reduced the spread of extremes, the dispersion. These trends were not unexpected but it was found that the rate of decay of the mode for increases in peak duration was not a universal function, but depended upon the region in which the pressure fluctuations occurred and on the cavity volume and building envelope flexibility. The rates of decay of the dispersion were not quantified because these changes were attributed to a reduction in the scatter of the extreme values as the duration of the peaks was increased and not a physical process.

Emulating the analysis of the resonant response of the cavity pressure fluctuations (section 7-3-5), the influence of cavity volume scaling on the magnitude of the extreme value mode was investigated. It was found that a critical normalised peak period, t_{gnorm}, existed whereby exaggerating the cavity volume scaling attenuated the mode for $t_g<t_{gnorm}$, whilst the opposite result occurred for $t_g>t_{gnorm}$.

Chapter 9: Overall Summary & Suggestions for Future Work

[9-1] Reasons for this Investigation

Wind tunnel studies to determine the wind loading on rigid models of prototype membrane structures are often necessary because the unique shapes of these structures are beyond the remit of design codes. In addition, if the designer is concerned about the existence of an aeroelastic instability, that could lead to catastrophic failure of the fabric material, then it may be necessary to conduct additional wind tunnel studies using expensive and elaborate aeroelastic models. A number of reports concerned with the results from investigations on aeroelastic models of prototype membrane structures have been cited in this thesis but it is difficult to draw general conclusions from these results.

Consequently, it was felt that a wind tunnel investigation of the fundamental interactions between roof motion and internal building pressure dynamics might provide valuable information of use to both wind tunnel modellers and structural engineers. Indeed, the proliferation of "exotic", lightweight membranes as roofing materials suggests that the need for such information is on the increase.

The principle objective of this thesis was to investigate experimentally the impact of variations in building envelope flexibility on the steady-state internal pressure dynamics of a single-cell building with a single dominant opening. The case of a domainant windward opening is often considered as the worst case scenario for mean net loadings across the roof and windward walls and Holmes (1979) considered that the phenomenon of Helmholtz resonance was similarly intense for a dominant windward opening. Stathopoulos (1989) showed that the peak internal pressure occurred during steady-state fluctuations of the internal pressure and not after the sudden occurrence of a windward opening whilst Vickery & Bloxham (1992) quantified the effect of background porosity on cavity pressure fluctuations. However, experimental results that quantify the effect of envelope flexibility on cavity pressure dynamics have not been reported and the main conclusions of this study are listed below.

[9-2] Main Conclusions

- An extensive series of experiments to define the sensitivities of the empirical coefficients C_I and C_L to different conditions of flow and opening geometry is required. These results would remove the need for assuming "standard" values

for the coefficients and permit a true comparison of theoretical models with experimental results.

- A novel, dimensionless geometric parameter, the ORDR, was defined. This parameter brought about a reasonable "collapse" of both the inertia coefficient and the damping, at the Helmholtz frequency, data obtained from tests conducted in still air and showed that for most of the test configurations acoustic radiation damping was negligible.

- Comparisons of the predicted damping, using the theory of Vickery & Bloxham (1992), with experimental results (wind-on) were fair for the case of a windward opening; however, for openings at other azimuth angles the theoretical damping estimates were very low. These results were reflected in the predicted and measured values of the root-mean-square cavity pressure fluctuations where predictions exceeded the measured results. [Data from point "1" might improve this situation!]

- The local maximum mean suction on the external wall of the model was some 20% less than that predicted by Cook (1990). This result was corroborated by the data of Holroyd (1983) for tests on a ground-mounted circular cylinder, similar to the present model "A", with an aspect ratio less than 0.5.

- The cavity pressures were dynamic and resonant exhibiting a narrow band response at the Helmholtz frequency. Turbulent buffetting, originating from the external pressure spectra, was transmitted to the cavity pressure spectra but in addition resonance of the air contained within the opening was superimposed on the buffetting response. The Helmholtz effect was most heavily damped for an opening located at 90° to the approach flow, whilst peak resonant responses occurred when the opening was aligned with the flow direction (f=0° and 180°).

- Increasing the flexibility of the roof increased the damping at the Helmholtz frequency and consequently reduced the magnitude of the root-mean-square cavity pressure fluctuations. For the most resonant cases, f=0° and 180°, a factor of 30 increase in the flexibility attenuated the root-mean-square cavity pressure by between 20% to 30%.

- The influence of cavity volume scaling on the resonant response was empirically determined as $y = k_1 e^{-k_2 \sqrt[16]{x}}$ where y is the relative resonant response and x the relative *effective* volume of the cavity. The exponential term in this expression dictates that a factor of 2 overestimate of the volume will lead to a

30% underestimate of the response whilst a factor of 2 underestimate of the volume will produce a 50% overestimate of the response.

An extreme value analysis of the peak factors of the cavity pressure for five different gust periods showed that the most likely extreme value, the mode, was attenuated as the gust period was increased. However, the rate of decay of the mode for increases in peak period was not a universal function and appeared to be related to the magnitude of the resonant response.

References

- Armitt J., (1968), 'The Effect of Surface Roughness and Freestream Turbulence on the Flow Around a Model Cooling Tower at Critical Reynolds Number', Symposium on wind effects on buildings and structures, Loughborough University, April 2nd-4th, pp.6.1-6.13.

- Baker C.J., (1980), 'The Turbulent Horseshoe Vortex', Journal of Wind Engineering & Industrial Aerodynamics, Vol.6, pp.9-23.

- Basu R.I., (1985), 'Aerodynamic Forces on Structures of Circular Cross-section. Part 1. Model-scale Data Obtained Under Two-dimensional Conditions in Low-Turbulence Streams', Journal of Wind Engineering & Industrial Aerodynamics, Vol.21, pp.273-294.

- Batham J.P., (1973), 'Pressure Distributions on Circular Cylinders at Critical Reynolds Numbers', Journal of Fluid Mechanics, Vol.57, part 2, pp.209-228.

- Batham J.P., (1985), 'Wind Tunnel Tests on Scale Models of a Large Power Station Chimney', Journal of Wind Engineering & Industrial Aerodynamics', Vol.18, pp.75-80.

- Baumeister K.J. & Rice E.J., (1975), 'Visual Study of the Effect of Grazing Flow on the Oscillatory Flow in a Resonator Orifice', N.A.S.A. Technical Memorandum, TM X-3288.

- Bearman P.W., (1968), 'Some Effects of Turbulence on the Flow Around Bluff Bodies', Symposium on wind effects on buildings and structures, Loughborough University, April 2nd-4th, pp.11.1-11.13.

- Bearman P.W., (1969), 'Corrections for the Effect of Ambient Temperature Drift on Hot-wire Measurements in Incompressible Flow', DISA Information, No. 11, May 1971, pp.25-30.

- Bearman P.W. & Morel T., (1983), 'Effect of Free Stream Turbulence on the Flow Around Bluff Bodies', Progress in Aerospace Science, Vol.20, pp.97-123.

- Beger G. & Macher E., (1967), 'Results of Wind Tunnel Tests on Some Pneumatic Structures', pp.142-146, Proceedings of 1st Colloquim on Pneumatiuc Structures, Stuttgart, 1967.

- Benjamin B.S., (1982), 'Structural Design with Plastics', Van Nostrand Reinhold Company, ISBN 0-442-20167-2

- Blevins R.D., (1979), 'Formulas for Natural Frequency and Mode Shape', Van Nostrand Reinhold, ISBN-0-442-20710-7.

- Bristish Standards Institute, B.S. 6661, 'British Standard Guide for Design, Construction & Maintenance of Single-Skin Air-Supported Structures', 1986.

- Bruun H.H. & Davies P.O.A.L., (1975), 'An Experimental Investigation of the Unsteady Pressure Forces on a Circular Cylinder in a Turbulent Cross Flow', Journal of Sound and Vibration, Vol.40, part 4, pp.535-559.

- Building Research Establishment, (1984), 'The Assessment of Wind Loads', Digest No. 119.

- Cermak J.E., (1982), 'Physical Modelling of the Atmospheric Boundary Layer in Long Boundary Layer Wind Tunnels', in Wind Tunnel Modelling for Civil Engineering Applications, Proceedings of the International Workshop on Wind Tunnel Modelling Criteria and Techniques in Civil Engineering Applications, Gaithersburg, Maryland, U.S.A., April, pp.97-125.

- Cheung J.C.K. & Melbourne W.H., (1983), 'Turbulence Effects on Some Aerodynamic Parameters of a Circular Cylinder at Supercritical Reynolds Numbers', Journal of Wind Engineering & Industrial Aerodynamics, Vol. 14, pp.399-410.

- Christiano P., Seeley G.R. & Stefan H., (1974), 'Transient Wind Loads on Circular Concave Roofs', Proceedings of the American Society of Civil Engineers, Journal of the Structural Division, Vol.100, ST11, November, pp.2323-2341.

- C.I.R.I.A., (1970), 'The Modern Design of Wind-sensitive structures', Proceedings of the Seminar held on 18th June at the Institution of Civil Engineers.

- Cook N.J., (1982), 'Simulation Techniques for Short Test-section Wind Tunnels: Roughness, Barrrier and Mixing-device Methods', in Wind Tunnel Modelling for Civil Engineering Applications, Proceedings of the International Workshop on Wind Tunnel Modelling Criteria and Techniques in Civil Engineering Applications, Gaithersburg, Maryland, U.S.A., April, pp.126-136.

- Cook N.J., (1982), 'Calibration of Techniques for the Prediction of Peak Pressures', in Wind Tunnel Modelling for Civil Engineering Applications, Proceedings of the International Workshop on Wind Tunnel Modelling Criteria and Techniques in Civil Engineering Applications, Gaithersburg, Maryland, U.S.A., April, pp.320-328.

- Cook N.J, (1985), 'The Designer's Guide to Wind Loading of Building Structures: Part 1: Background, Damage Survey, Wind Data & Structural Classification', ISBN 0-408-00870-9, Butterworths.

- Cook N.J., (1989), 'The Designer's Guide to Wind Loading of Building Structures: Part 2: Static Structures', ISBN, 0-408-00871-1, Butterworths.

- Craig R.R. Jnr., (1981), 'Structural Dynamics: An Introduction to Computer Methods', John Wiley & Sons, ISBN 0-471-04499-7

- Davenport A.G., (1965), ' The Relationship of Wind structure to Wind Loading', Proceedings of the Symposium on Wind Effects on Buildings & Structures, Vol.1, National Physical Laboratory, Teddington, U.K., pp.53-102.

- Deaves D.M. & Harris R.I., 'A Mathematical Model of the Structure of Strong Winds', CIRIA Report 76, 49 pages.

- Dent R.N., (1977), 'Principles of Pneumatic Architecture', John Wiley & Sons.

- Dietz A.E., Proffitt R.B., Chabot R.S., Moak E.L. & Monego C.J., (1969), 'Wind-Tunnel Tests and Analysis for Ground-Mounted, Air-Supported Structures (Revised)', Technical Report 70-7-GP, U.S. Army Natick Labs., Contract No. DA19-129-AMC-953(N), 7/69.

- Dumbleton B., (1986), 'Wind Tunnel Tests for Tattered Tent', New Civil Engineer, 3rd April, pp.28-29.

- Eaton K.J. & Mayne J.R., (1975), 'The Measurement of Wind Pressures on Two-Storey Houses at Aylesbury', J.I.A., Vol.1, pp.67-109.

- Elashkar I., (1974), 'Dynamic Response of Tension Roofs to Turbulent Wind', University of Western Ontario, BLWT-3-74.

- Elashkar I. & Novak M., (1983), 'Wind Tunnel Studies of Cable Roofs', Journal of Wind Engineering & Industrial Aerodynamics, Vol.13, pp.407-419.

- E.S.D.U. 82026, 'Strong Winds in the Atmospheric Boundary Layer. Part 1: Mean Hourly Wind Speeds', Engineering Science Data Units.

- E.S.D.U. 85020, 'Characteristics of Atmospheric Turbulence Near the Ground. Part II: Singe Point Data for Strong Winds (Neutral Atmosphere)', Engineering Science Data Units.

- Fage A. & Warsap J.H., (1929), 'The Effects of Turbulence & Surface Roughness on the Drag of a Circular Cylinder', Aeronautical Research Council Research & Memoranda No.1281, H.M.S.O.

- Fahrtash M. & Liu H., (1990), 'Internal Pressure of Low-rise Building - Field Measurements', Journal of Wind Engineering & Industrial Aerodynamics, Vol.36, pp.1191-1200.

- Finnigan J.J. & Longstaff R.A., (1982), 'A Wind-tunnel Model Study of Forced Convective Heat Transfer from Cylindrical Grain Storage Bins', Journal of Wind Engineering & Industrial Aerodynamics, Vol.10, pp.191-211.

- Geiger D.H., (1975), 'Largest and Lightest Fabric Roof to Date', Civil Engineering-American Society of Civil Engineers, November, pp.82-86.

- Gumley S.J., (1983), 'A Detailed Design Method for Pneumatic Tubing Systems', Journal of Wind Engineering & Industrial Aerodynamics, Vol.13, pp.441-452.

- Harris R.I., (1990), 'The Propagation of Internal Pressures in Buildings', Journal of Wind Engineering & Industrial Aerodynamics, Vol.34, pp.169-184.

- Hassan U., (1979), 'Effects of Turbulence Scale on the Correlation of Pressures on Rectangular Section Prisms', Ph.D. Dissertation, City University, London.

- Herzog T., (1977), 'Pneumatic Structures - a Handbook for the Architect & Engineer', published by Crosby, Lockwood & Staples.

- Holdϕ A.E., Houghton E.L. & Bhinder F.S., (1982), 'Some Effects Due to Variations in Turbulence Integral Length Scales on the Pressure Distribution on Wind-tunnel Models of Low-rise Buildings', Journal of Wind Engineering & Industrial Aerodynamics., Vol.10, pp.103-115.

- Holmes J.D., (1979), 'Mean and Fluctuating Pressures Induced by Wind', Proceedings of the 5th International Conference on Wind Engineering, Fort Collins, Colorado, pp.435-450.

- Holmes J.D., (1981), 'Non-gaussian Characteristics of Wind Pressure Fluctuations', J.W.E.I.A., Vol.7, pp.103-108.

- Holmes J.D., (1984), 'Effect of Frequency Response on Peak Pressure Measurements', Journal of Wind Engineering & Industrial Aerodynamics, Vol.17, pp.1-9.

- Holmes J.D. & Lewis R.E., (1987), 'Optimization of Dynamic Pressure Measurement Systems. 1. Single Point Measurements', Journal of Wind Engineering & Industrial Aerodynamics, Vol.25, pp.249-273.

- Holroyd R.J., (1983), 'On the Behaviour of Open-topped Storage Tanks in High Winds. Part I. Aerodynamic aspects', Journal of Wind Engineering & Industrial Aerodynamics, Vol. 12, pp.329-352.

- Hoxey R.P., (1991), 'Structural Response of a Portal Framed Building Under Wind', Journal of Wind Engineering & Industrial Aerodynamics, Vol.38, pp.347-356.

- Hunt J.C.R., (1973) 'A Theory of Turbulent Flow Round Two-Dimensional Bluff Bodies', Journal of Fluid Mechanics, Vol.61, pp.635-706.

- Hunt J.C.R., Abell C.J., Peterka J.A. & Woo H., (1978), 'Kinematical Studies of the Flows Around Free or Surface-mounted Obstacles; Applying Topology to Flow Visualisation', Journal of Fluid Mechanics, Vol.86, part 1, pp.179-200.

- Irwin H.P.A.H., Cooper K.R. & Girard R., (1979), 'Correction of Distortion Effects Caused by Tubing Systems in Measurements of Fluctuating Pressures', Journal of Industrial Aerodynamics., Vol.5, pp.93-107.

- Irwin H.P.A.H., Wardlaw R.L., Wood K.N. & Bateman K.W., (1979), 'A Wind Tunnel Investigation of the Montreal Olympic Stadium Roof', N.R.C.C. Laboratory Technical Report, LTR-LA-228.

- Irwin H.P.A.H. & Wardlaw R.L., (1979), 'A Wind Tunnel Investigation of a Retractable Fabric Roof for the Montreal Olympic Stadium.', Proceedings of the 5th International Conference on Wind Engineering, Fort Collins, Colorado, pp.925-938.

- Jackson N. (ed.), (1983), 'Civil Engineerng Materials', MacMillan Press Ltd., 3rd Edition, pp. 375-376.

- Kandola B.S., (1978), 'Wind Effects on Buildings with Varying Leakage Characteristics - Wind Tunnel Investigation', Journal of Industrial Aerodynamics, Vol.3, pp.267-284.

- Kassem M. & Novak M., (1990), 'Experiments with Free-vibration of Light Roofs Backed by Cavities', Proceedings of the American Society of Civil Engineers, Journal of the Engineering Mechanics Divivsion, Vol. 116, No. 8, August, pp.1750-1763.

- Kassem M. & Novak M., (1992), 'Wind-induced Response of Hemispherical Air-supported Structures', Journal of Wind Engineering & Industrial Aerodynamics., Vol.41-44, pp.177-178.

- Kawamura S. & Kimoto E., (1979), 'Aerodynamic Stability Criteria of One-way Type Hanging Roofs in Smooth Uniform Flow', Proceedings of the 5th International Conference on Wind Engineering, Fort Collins, Colorado, U.S.A., pp.939-953.

- Kawamura S. & Kiuchi T., (1986), 'Wind Design Method of Air-supported Structures', in the I.A.S.S. Symposium "Shells, membranes & space frames", Osaka, pp.233-240.

- Kawamura S. & Kiuchi T., (1986), 'An Experimental Study of a One-membrane Type Pneumatic Structure - wind load and response', Journal of Wind Engineering & Industrial Aerodynamics., Vol.23, pp.127-140.

- Kimoto E. & Kawamura S., (1983), 'Aerodynamic Behaviour of One-way Type Hanging Roofs', Journal of Wind Engineering & Industrial Aerodynamics, Vol.13, pp.395-405.

- Kimoto E. & Kawamura S., (1986), 'Aerodynamic Criteria of Hanging Roofs for Structural Design', Proceedings of the I.A.S.S. Symposium "Shells, Membranes and Space Frames", Osaka, pp.249-256.

- Kind R.J. & Wardlaw R.L., (1981), 'Wind Tunnel Tests on the Behaviour of the Proposed Mobile Roof for the Montreal Olympic Stadium Roof During Retraction and Deployment in Wind', National Research Council of Canada, Laboratory Technical Report, LTR-LA-254.

- Kinsler L.E. & Frey A.R., (1962), 'Fundamentals of Acoustics', 2nd Edition, John Wiley & Sons..

- Kiya M., Suzuki Y., Arie M. & Hagino M., (1982), 'A Contribution to the Free-stream Turbulence Effect on the Flow Past a Circular Cylinder', Journal of Fluid Mechanics, Vol.115, pp.115-164.

- Krishna P., (1989), 'Wind Effects on Curved Roofs', Recent Advances in Wind Engineering, Proceedings of the 2nd Asia-Pacific Conference, Beijing, China, pp.39-53.

- Lawson T.V., (1980), 'Wind Effects on Buildings', Volumes 1 and 2, London, Applied Science Publishers.

- Lee B., (1977), 'Wind Flow Around Bluff Bodies', University of Sheffield, Proceedings of the 6th Post Experience course in building services engineering, 5th-6th January.

- Liu H. & Saathoff P.J., (1981), 'Building Internal Presssure: Sudden Change', Proceedings of the American Society of Civil Engineers, Journal of the Engineering Mechanics Division, Vol.107, April, pp.309-321.

- Liu & Saathoff P.J., (1982), 'Internal Pressure and Building Safety', Proceedings of the American Society of Civil Engineers, Journal of the Engineering Mechanics Division, Vol.108, October, pp.2223-2234.

- Liu & Rhee, (1986), 'Helmholtz Oscillation in Building Models', Journal of Wind Engineering & Industrial Aerodynamics, Vol.24, pp.95-115.

- MacDonald P.A., Kwok K.C.S. & Holmes J.D., (1988), 'Wind Loads on Circular Storage Bins, Silos and Tanks: I. Point pressure measurements on isolated structures', Journal of Wind Engineering & Industrial Aerodynamics, Vol.31, pp.165-188.

- MacDonald P.A., Holmes J.D. & Kwok K.C.S., (1990), 'Wind Loads on Circular Storage Bins, Silos and Tanks. II. Effect of grouping', Journal of Wind Engineering & Industrial Aerodynamics, Vol.34, pp.77-95.

- Maher F.J., (1965), 'Wind Loads on Basic Dome Shapes', Proceedings of the American Society of Civil Engineers, Journal of the structural division, Vol.91, ST3, June, pp.219-228.

- Maher F.J., (1966), 'Wind Loads on Dome-cylinder and Dome-cone Shapes', Proceedings of the American Society of Civil Engineers, Journal of the Structural division, Vol.92, ST5, October, pp.79-95.

- Maher F.J., (1969), 'Wind Loads on Kresge Auditorium and Traveler's Building', Proceedings of the American Society of Civil Engineers, Journal of the structural division, Vol.95, ST1, January, pp.1-15.

- Malcolm D.J. & Glockner P.G., (1981), 'Collapse by Ponding of Air-Supported Spherical Caps', Journal of the Structural Division, Proceedings A.S.C.E., Vol.107, No. ST-9, pp.

- Mataki Y., Iwasa Y., Fukao Y. & Okada A., (1988), 'Wind Induced Response of Low-profile Cable-reinforced Air-supported Structures', Journal of Wind Engineering & Industrial Aerodynamics, Vol.29, pp.253-262.

- Matsumoto T., (1983), 'An Investigation on the Response of Pretensioned One-way Type Suspension Roofs to Wind Action', Journal of Wind Engineering & Industrial Aerodynamics, Vol.13, pp.383-394.

- Matsumoto T., (1990), 'On Self-excited Oscillation of the Cable Trussed Roof with Single Curvature', Journal of Wind Engineering & Industrial Aerodynamics, Vol.33, pp.131-138.

- Morrison A., (1980), 'The Fabric Roof', Civil Engineering-American Society of Civil Engineers, August, pp.60-65.

- Nakayama M., Suzuki T., Ishii K. & Satoh K., (1986), 'Wind Tunnel Test on Spherical Pneumatic Structures', Proceddings of the I.A.S.S. Symposium "Shells, Membranes and Space Frames", Osaka, Vol. 2, pp.225-232.

- Newman B.G., Ganguli U. & Shrivastava S.C., (1984), 'Flow Over Spherical Inflated Buildings', Journal of Wind Engineering & Industrial Aerodynamics, Vol.17, pp.305-327.

- Niemann H.J., (1972), 'Wind Tunnel Experiments on Aeroelastic Models of Air-Supported Structures: Results & Conclusions', paper 5.11, Vol.2, 2nd International Symposium on Pneumatic Structures, Delft, 1972.

- Novak M. & Kassem M., (1990), 'Free-vibration of Light Roofs Backed by Cavities', Proceedings of the American Society of Civil Engineers, Journal of the Engineering Mechanics Division, Vol. 116, No. 3, March, pp.549-564.

- Novak M. & Kassem M., (1990), 'Effect of Leakage and Acoustical Damping on Free Vibration of Light Roofs Backed by Cavities', Journal of Wind Engineering & Industrial Aerodynamics, Vol. 36, pp.289-300.

- Otto F., 1967, 'Tensile Structures - Design structure & Calculation of Cable Nets & Membranes', 2 volumes.

- Panton R.L., (1984), 'Incompressible Flow', published by John Wiley & Sons,

- Panton R.L., (1990), 'Effect of Orifice Geometry on Helmholtz Resonator Excitation by Grazing Flow', A.I.A.A. Journal, Vol.28, January, pp.60-65.

- Parkinson J., (1980), 'Outdated Draft Hinders Airhouse Designers', New Civil Engineer, 12 June, pp22-24.

- Peterka J.A. & Cermak J. E., (1975), 'Wind Pressures on Buildings - Probability Densities', Proceedings of the American Society of Civil Engineers, Journal of the Structural Division, ST6, June, pp.1255-1267.

- Peterka J.A., (1982), 'Predicting Peak Pressures vs. Direct Measurement', in Wind Tunnel Modelling for Civil Engineering Applications, Proceedings of the International Workshop on Wind Tunnel Modelling Criteria and Techniques in Civil Engineering Applications, Gaithersburg, Maryland, U.S.A., April, pp.313-319.

- Pearce W. & Sykes D.M., (1994), 'Free-Vibration Tests on Rigid and Flexible Roofed Cavity Models with Wall Openings', J.W.E.I.A., Vol.52, pp.359-370.

- Purdy D.M., Maher F.J. & Frederick M., (1967), 'Model Studies of Wind Loads on Flat-top Cylinders', Proceedings of the American Society of Civil Engineers, Journal of the Structural Division, Vol.93, ST2, April, pp.379-395.

- Rao K., (1986), (unpublished), 'Boundary Layer Measurements in the Industrial Aerodynamics Wind Tunnel', Centre for Aeronautics, City University, London.

- Robertson A.P., (1992), 'The Wind-induced Response of a Full-scale Portal Framed Building', Journal of Wind Engineering & Industrial Aerodynamics, Vol. 41-44, pp.1677-1688.

- Rockwell D & Naudascher E., (1978), 'Review - Self-Sustaining Oscillations of Flow Past Cavities', Transactions of the A.S.M.E., Journal of Fluids Engineering, Vol.100, June, pp.152-165.

- Roshko A., (1961), 'Experiments on the Flow Past a Circular Cylinder at Very High Reynolds Number', Journal of Fluid Mechanics, Vol.10, pp.345-356.

- Sabransky I.J. & Melbourne W.H., (1987), 'Design Pressure Distribution on Circular Silos with Conical Roofs', Journal of Wind Engineering & Industrial Aerodynamics, Vol.26, pp.65-84.

- Sageau J.F., (1977/78), 'Etude in Situ Du Champ De Pression Stationnaire et Instationnaire Autour D'Une Cheminee De 240m', J.I.A., Vol.2, pp.361-383.

- Savory E.. & Toy N., (1984), 'Investigation of the Wind Loading on Domes in Turbulent Boundary Layers', Proceedings of the 3rd International Conference on Space Structures, Surrey University, September, pp.277-282.

- Schodek D.L., (1980), 'Structures', Prentice-Hall Inc., Chapter 11., pp.398-414.

- Simiu E. & Scanlan R. H., (1987), 'Wind Effects on Structures', 2nd Edition, John Wiley & Sons, ISBN 0-471-86613-X.

- Srivastava N.K., Turkkan N. & Dickey R., (1984), 'Wind Tunnel Study of a Flexible Membrane Structure', Proceedings of the 3rd International Conference on Space Structures, Surrey University, September, pp.785-790.

- Stathopoulos T., (1979), 'Discussion - "Wind effects on Building with Various Leakage Characterstics - Wind Tunnel Investigation"', Journal of Industrial Aerodynamics, Vol.5, pp.191-192.

- Stathopoulos T., Surry D. & Davenport A.G., (1979), 'Internal Pressure Characteristics of Low-rise Buildings Due to Wind Action', Proceedings of the 5th International Conference on Wind Engineering, Fort Collins, Colorado, pp.451-463.

- Stathopoulos T., (1989), 'Transient Wind-induced Internal Pressures', Proceedings of the American Society of Civil Engineers, Journal of the Engineering Mechanics Division, Vol. 115, No. 7, July, pp.1501-1514.

- Sykes D.M., (1977), 'A New Wind Tunnel for Industrial Aerodynamics', Journal of Industrial Aerodynamics, Vol.2, pp.65-78.

- Sykes DM., (1992), 'Wind Loading Tests on Models of Two Tension Structures for Expo'92, Seville', Inaugural Conference of the Wind Engineering Society, 28th-30th September, Downing College, University of Cambridge, U.K.

- Szechenyi E., (1975), 'Supercritical Reynolds Number Simulation for Two-dimensional Flow Over Circular Cylinders', Journal of Fluid Mechanics, Vol.70, part 3, pp.529-542.

- Thomson W.T., (1988), 'Theory of Vibration with Applications', 3rd Edition, Unwin Hyman Ltd., ISBN 0-04-445069-9.

- Tieleman H.W., (1992), 'Problems Associated with Flow Modelling Procedures for Low-rise Structures', Journal of Wind Engineering & Industrial Aerodynamics, Vol.41-44, pp.923-934.

- Tryggvason B.V. & Isyumov N., (1977), 'A Study of the Wind Induced Response of the Air Supported Roof for the Dalhousie University Sports Complex', University of Western Ontario, BLWT-SS7-1977.

- Tryggvason B.V., Surry D. & Davenport A.G., (1978), 'A Study of an Aeroelastic Model of the Haj terminal at Jeddah International Airport', University of Western Ontario, BLWT-SS12-1978.

- Tryggvason B.V., (1982), 'Aeroelastic Modelling of Pneumatic and Tensioned Fabric Structures', in Wind Tunnel Modelling for Civil Engineering Applications, Proceedings of the International Workshop on Wind Tunnel Modelling Criteria

and Techniques in Civil Engineering Applications, Gaithersburg, Maryland, U.SA. April, pp.1061-1072.

- Tunstall M.J., (1974), 'Some Measurements of the Wind Loading on Fawley Generating Station Chimney', Proceedings of the symposium on full-scale fluid dynamic measurements, Leicester University, pp.26-41.

- Uchiyama K., Higuchi Y. & Uematsu Y., (1979), 'On the Wind Induced Dynamic Behaviours of Suspended Roofs', World Congress on Shell and Spatial Structures, 20th Anniversary of the I.A.S.S., Madrid, pp.2.17-2.31.

- Uematsu Y. & Uchiyama K., (1986), 'Aeroelastic Behaviour of an Hyperbolic-Paraboloid-Shaped Suspended Roof', Proceedings of the I.A.S.S. Symposium, "Shells, Membranes and Space frames", Osaka, pp.241-248.

- Vickery B.J., (1986), 'Gust-factors for Internal Pressures in Low-rise Buildings', Journal of Wind Engineering & Industrial Aerodynamics, Vol. 23, pp.259-271.

- Vickery B.J. & Karakatsanis C., (1989), 'Discharge Coefficients & Internal Pressures in Well-Ventialted Buildings', Recent Advances in Wind Engineering, Proceedings of the 2nd Asia-Pacific Symposium on Wind Engineering, (2Vols), June 26th-29th, Beijing, China, pp.557-567.

- Vickery B.J., (1991), 'Comments on "The Propagation of Internal Pressures in Buildings" by R.I. Harris', Journal of Wind Engineering & Industrial Aerodynamics, Vol. 37, pp.209-212.

- Vickery B.J. & Georgiou P.N., (1991), 'A Simplified Approach to the Determination of the Influence of Internal Pressures on the Dynamics of Large Span Roofs', J.W.E.I.A., Vol.38, pp357-369.

- Vickery B.J. & Bloxham C., (1992), 'Internal Pressure Dynamics with a Dominant Opening', Journal of Wind Engineering & Industrial Aerodynamics, Vol. 41-44, pp.193-204.

Appendix A: Calibration of the Reference Static and Dynamic Pressures

[A-1-1] Calibration Procedure

The use of a pressure coefficient as a means of representing the wind load on a structure requires the definition of a reference static and dynamic pressure according to equation A.1.

$$C_p = \frac{(p - p_{sr})}{q_r} \qquad (A.1)$$

where p is the normal surface pressure of interest and p_{sr} and q_r the reference static and dynamic pressures respectively.

The choice of a reference dynamic pressure is often dependent upon the structure under test and for low-rise buildings the windspeed at roof height is a convenient choice for normalisation of wind loads. The reference dynamic pressure may be considered as a measure of the magnitude of the speed of the flow in which a structure is immersed. On the other hand, the reference static pressure should represent the static pressure at the position of interest on the building surface but with the building absent so that subtraction of this pressure from the normal surface pressure provides a measure of the pressure due solely to the action of the wind at that point. It is understood that the presence of the building, and of surrounding obstacles, will distort the static pressure field so that the location of the reference static pressure point should be outside the region influenced by the presence of the building but not so far away that the measured pressure is unrepresentative of that at the site of the building.

Keeping the above in mind, there appear to be two methods by which a measure of the correct reference static pressure can be obtained. Firstly, a direct reading of the static pressure can be made during a test run using a pitot-static probe positioned in the same cross-section as the model but outside the influence of the static pressure field of the model; this technique presumes that any vertical or horizontal variation in static pressure within the working section of the tunnel is relatively small and demands estimation of the extent of the static pressure field of the model. The second technique involves calibration of the static pressure at the position of interest, *with the model absent*, against the static pressure at an upstream location that is well away from the static pressure field of the model. This "false" reference is used as the backing

pressure to any pressure transducers in the model and a small correction to the measured pressure coefficients is then required at the data reduction stage. This latter method was used in the tests presented in this thesis and details of the correction procedure are given below.

Figure A.1 shows the relative locations of the pitot-static tubes used in the calibration tests. Probe #1 was located near a sidewall of the tunnel at a height of 3.5D (where D is the diameter of the model) and approximately 6D upstream of probes #2, #3 and #4. The latter three probes were symmetrically arranged across the tunnel in the same cross-section that the model was to occupy at a height equal to one model height, H. Probe #3 was in the centre of the working-section and probes #2 and #4 were displaced approximately 2.5D to either side.

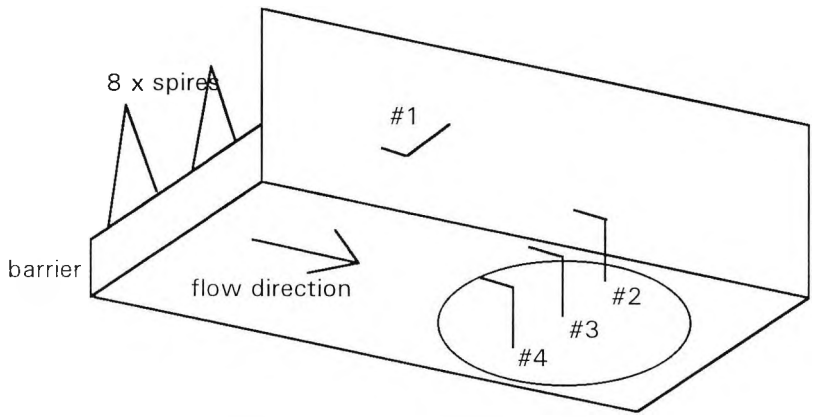

Figure A.1: The relative locations of the reference pitot-static tubes.

The calibration tests comprised measurement of the static and dynamic pressures at the locations of the four pitot-static tubes over a range of tunnel speeds with the boundary layer development "hardware" in place but no model in the tunnel. The dynamic pressure at #3 was expressed as a function of the dynamic pressure measured by tube #1 (see equation A.4) and the difference between the static pressure measured by probe #1 and an average of the three static pressures measured at locations #2, #3 and #4 was also expressed as a function the dynamic pressure measured at position #1 (see equation A.5). The scatter in the static pressure measurements was approximately plus/minus two Pascals across the whole range of dyanmic pressures.

During the wind tunnel tests when the model was at position #3, probe #1 was used as a "false reference" probe because it was well away from the influence of the pressure field due to the model and because it was a permanent fixture in the tunnel. The differential pressure transducers (Setra 237's) used to measure the wind loading around the model were referenced to the static pressure tap on probe #1 and the resultant output from the transducer was normalised by the dynamic pressure measured

by probe #1. The resultant pressure coefficient is described by equation A.3 and the corrected coefficient by equation A.6.

[A-1-2] Analysis

If the "true" pressure coefficient is defined as

$$C_{px} = \frac{(p_x - p_{sx})}{q_x} \qquad (A.2)$$

where suffices "x" and "s" denote the model location and static pressure respectively, then the measured pressure coefficient is given by

$$C_{pm} = \frac{(p_x - p_{sm})}{q_m} \qquad (A.3)$$

where suffix "m" refers to the upstream "reference" location. The results of the calibration tests shown in figures A.2 and A.3 permit the following functions to be determined

$$q_m = M_1.q_x + C_1 \quad \text{and} \qquad (A.4)$$

$$(p_{sx} - p_{sm}) = M_2.q_m + C_2 \qquad (A.5)$$

where M_1, M_2, C_1 and C_2 are constants that are a function of the type of boundary layer and streamwise position of the probes if horizontal and vertical variations of the static pressure are assumed to be negligible. Substitution of A.4 and A.5 into A.3 and manipulation of the resultant equation enables the "true" pressure coefficient to be expressed in terms of C_{pm} and the four constants in equations A.4 and A.5,

$$C_{px} = M_1.\{ q_m.(C_{pm} - M_2) - C_2 \} / \{ q_m - C_1 \} \qquad (A.6)$$

If the "best-fit" line is forced through the origin then the constants C_1 and C_2 are zero and equation A.6 simplifies to,

$$C_{px} = M_1.\{ C_{pm} - M_2 \} \qquad (A.7)$$

It is implicit in the above discussion that the pitot-static tubes will correctly measure the static pressure at a specific site. However, in reality the across-wind fluctuations due to turbulence in the simulated atmospheric boundary layer will increase the apparent static pressure and errors in local pressure coefficient as large as 0.06 are have been estimated typical in flows with 20% turbulence (Cook, 1990).

[A-2-1] Standing Waves in the Test Section

The ducting which forms the circuit of a wind tunnel is prone to "organ-pipe" type resonances due to the superposition of noise waves travelling in opposite directions around the circuit. A simple estimate of the frequencies associated with resonant acoustic phenomena can be obtained from the dimensions of the tunnel if assumptions are made about the form of the standing wave.

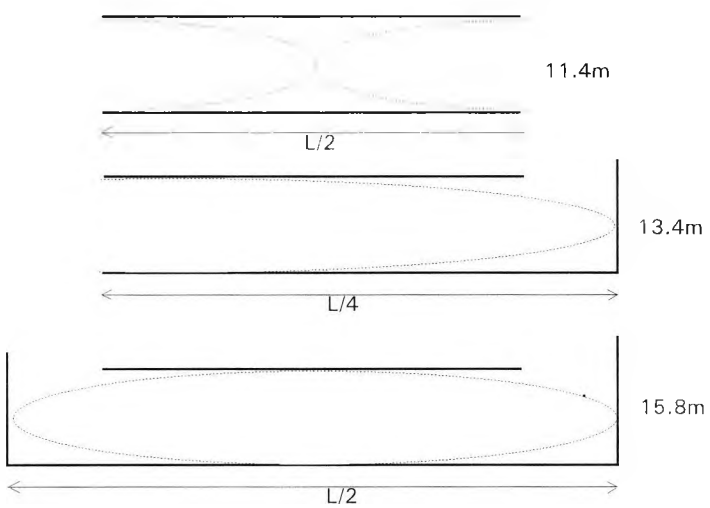

Figure A.2: Fundamental modes of standing waves in different sections of the tunnel corresponding to (top) open-open pipe, (middle) open-closed pipe & (bottom) closed-closed pipe.

In figure A.2 the dotted lines show the form of the fundamental frequency of the standing wave for three different sections of the lower circuit of the industrial aerodynamics tunnel at City University. The top and bottom cases have an associated frequency of 14.9Hz and 10.8Hz (assuming the speed of sound to be 340m/s) with higher modes being 2, 3 & 4 times the fundamental. The middle case has a frequency of 6.3Hz with higher modes at frequencies of 3, 5, 7 & 9 times the fundamental.

The theoretical estimates of the frequencies due to acoustic noise coincided with the range of frequencies at which Helmholtz oscillation occurred. It was not deemed possible to filter out the noise because an integral part of the response signal would be lost and so the noise had to be tolerated.

[A-3-1] Correction of the External Pressure Spectra

The short length of tubing connecting the head of the pressure transducer (Setra 237) to the external pressure tap distorted the pressure signal in a manner that was experimentally determined following the method of Hassan (1979).

A short length of six inch diameter pipe was fitted with a loudspeaker at one end and a flat plate at the other. A reference pressure transducer with a flat frequency response across the range of interest was flush-mounted in the centre of the flat plate whilst a brass tap and flexible tube, identical to that used on the wind tunnel model, was connected to a Setra pressure transducer adjacent to the reference transducer. The loudspeaker was driven by a variable frequency oscillator up to frequencies in excess of 300Hz and the r.m.s. output from each of the pressure transducers was measured. The ratio of the magntitudes of the signals from each pressure transducer was a measure of the distortion due to the tap/tube system (figure A.3). The square of this ratio was used to correct the external pressure spectra shown in appendix B and chapter 5. This technique is similar to that reported by Irwin et al (1979) and Holmes & Lewis (1987).

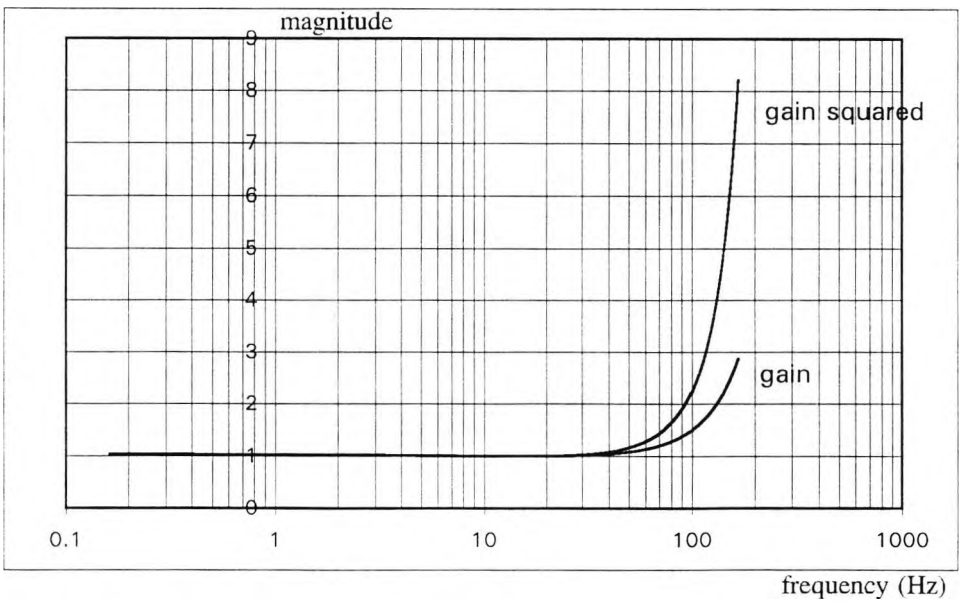

Figure A.3: Experimentally measured gain due to the pressure tap/tubing system.

Appendix B: Cavity Pressure Spectra

The results in this appendix comprise the complete set of power spectra measured inside the cavity of the model.

Results were plotted in the familiar format of frequency multiplied by the power at that frequency on a linear scale against the logarithm to base 10 of the frequency (at model scale). The spectra were all normalised by the variance.

The key to each graph is best explained by giving an example,

Figure B14(e) **B/13.0/A/180** cavity volume **B**,
mean reference windspeed **13.0**m/s,
roof tension, **A** (tension "A"),
opening azimuth angle **180** degrees

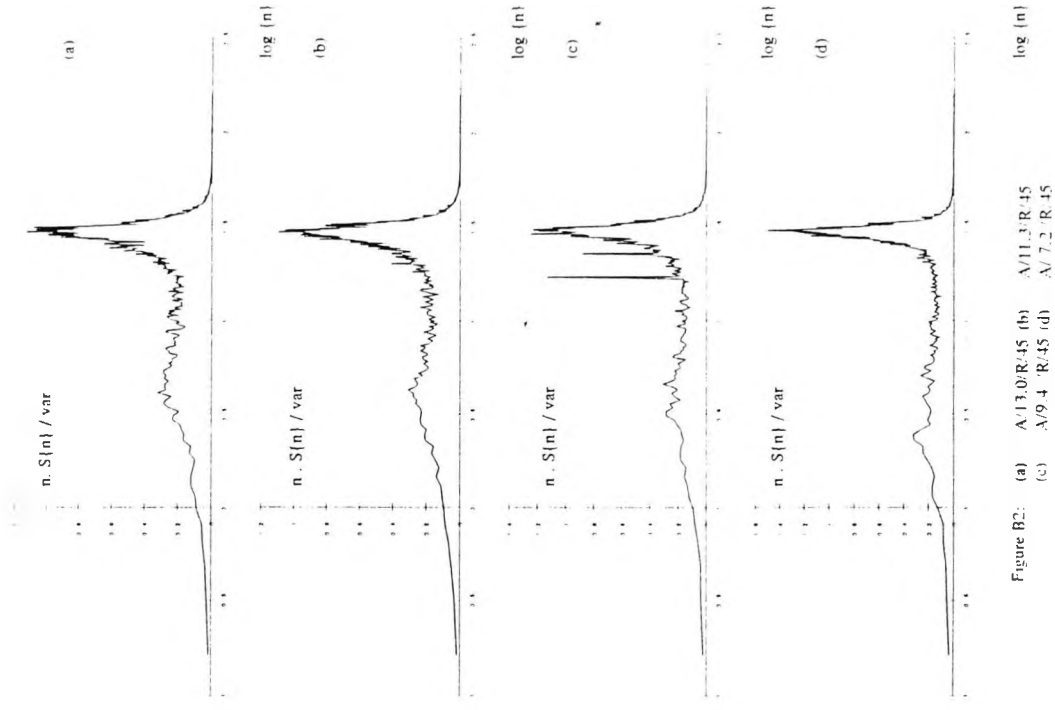

Figure B2: (a) A/13.0/R/45 (b) A/11.3/R/45
(c) A/9.4 /R/45 (d) A/7.2 /R/45

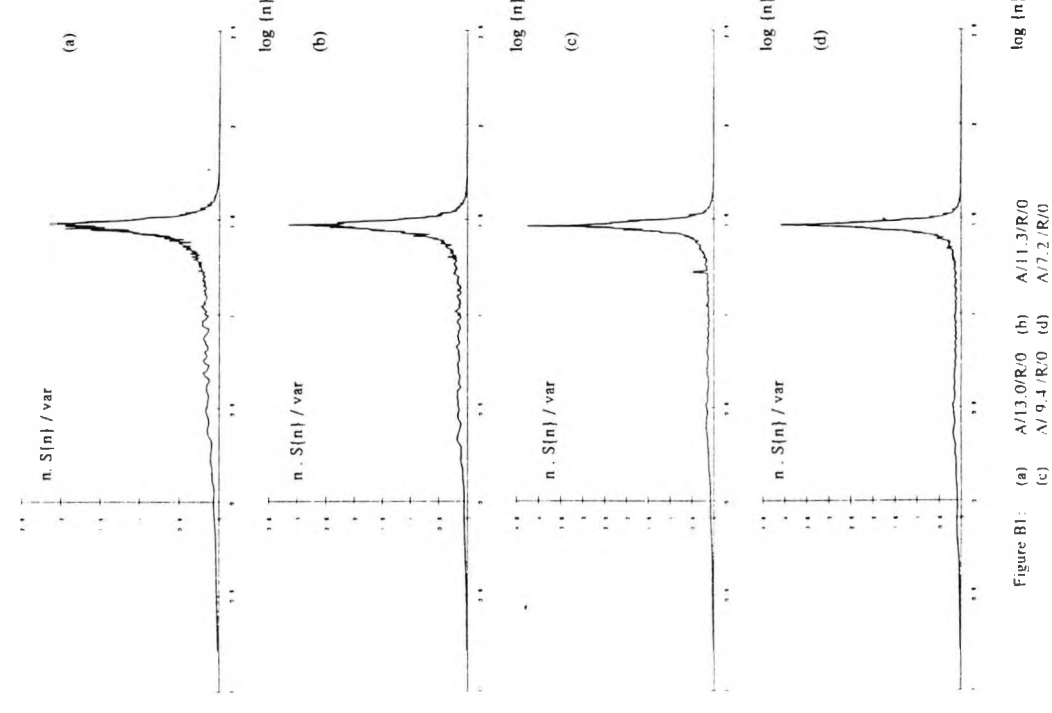

Figure B1: (a) A/13.0/R/0 (b) A/11.3/R/0
(c) A/ 9.4 /R/0 (d) A/7.2 /R/0

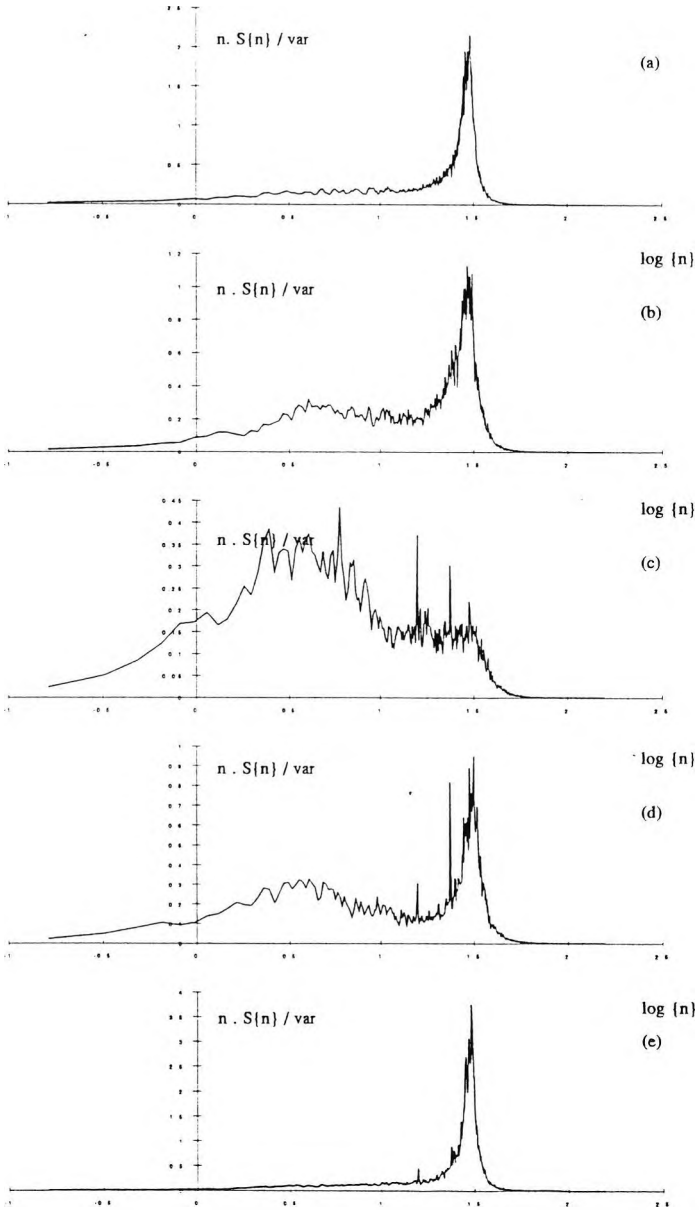

Figure B3: (a) A/13.0/R/0 (b) A/13.0/R/45 (c) A/13.0/R/90
(d) A/13.0/R/135 (e) A/13.0/R/180

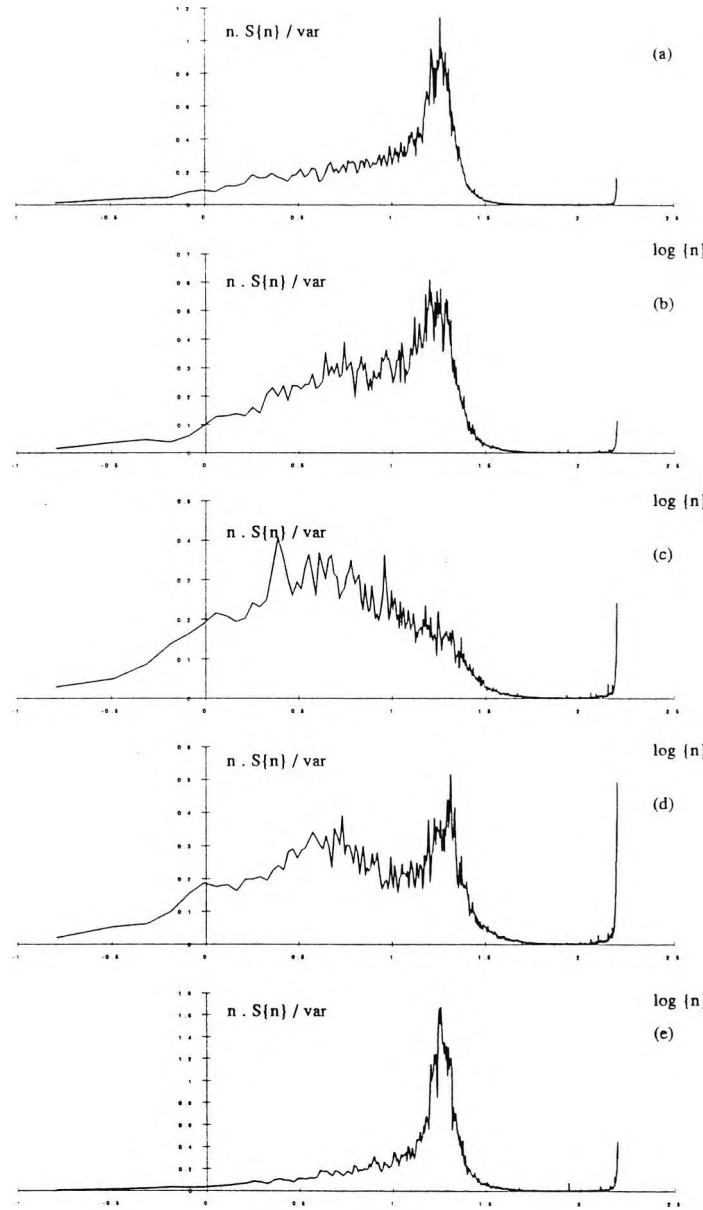

Figure B4: (a) A/13.0/A/0 (b) A/13.0/A/45 (c) A/13.0/A/90
(d) A/13.0/A/135 (e) A/13.0/A/180

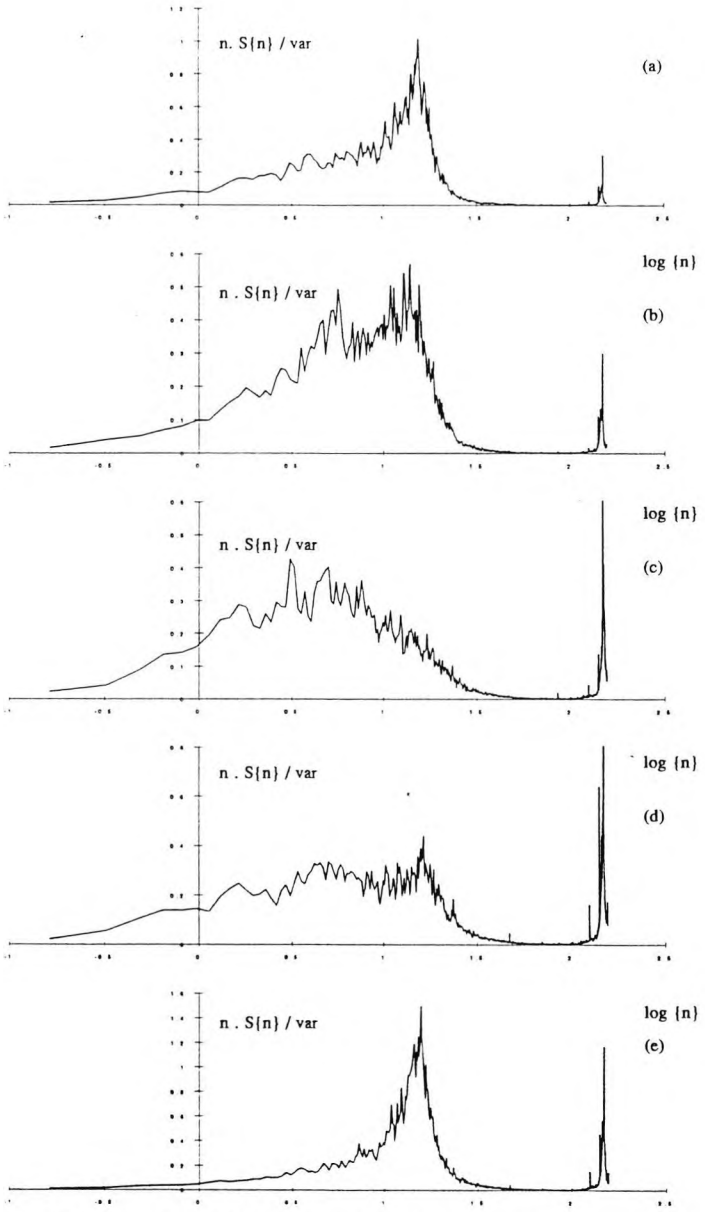

Figure B5: (a) A/13.0/B/0 (b) A/13.0/B/45 (c) A/13.0/B/90 (d) A/13.0/B/135 (e) A/13.0/B/180

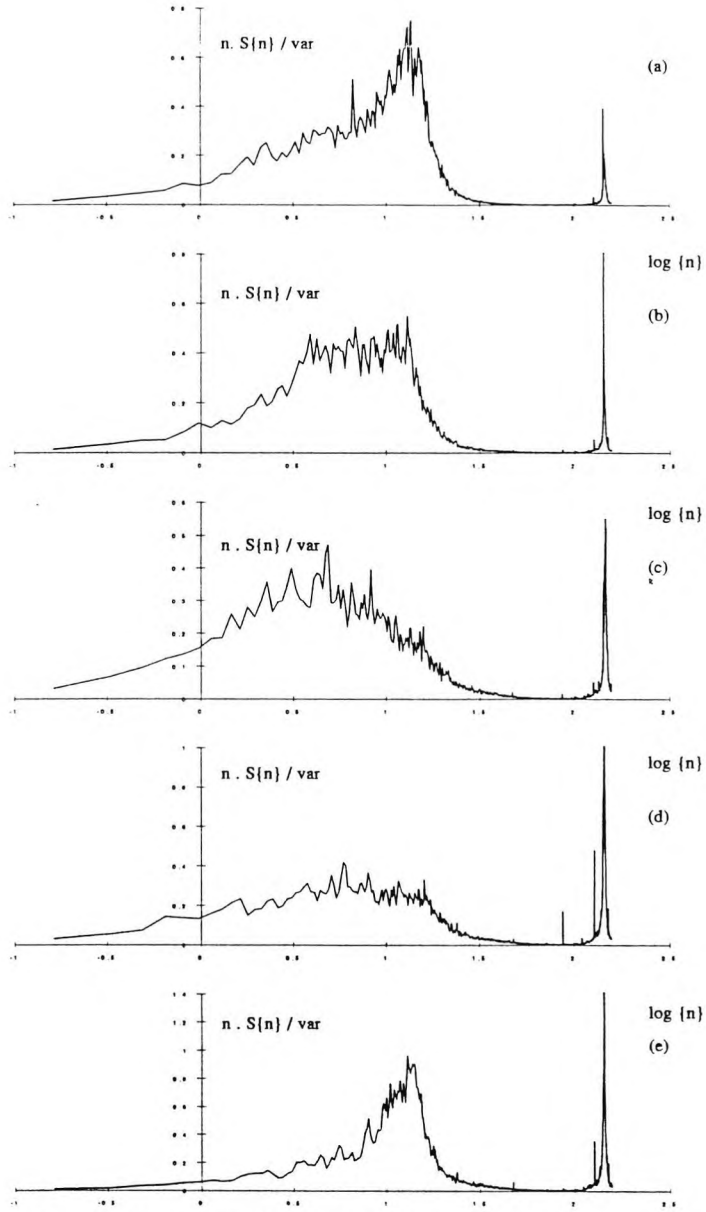

Figure B6: (a) A/13.0/C/0 (b) A/13.0/C/45 (c) A/13.0/C/90 (d) A/13.0/C/135 (e) A/13.0/C/180

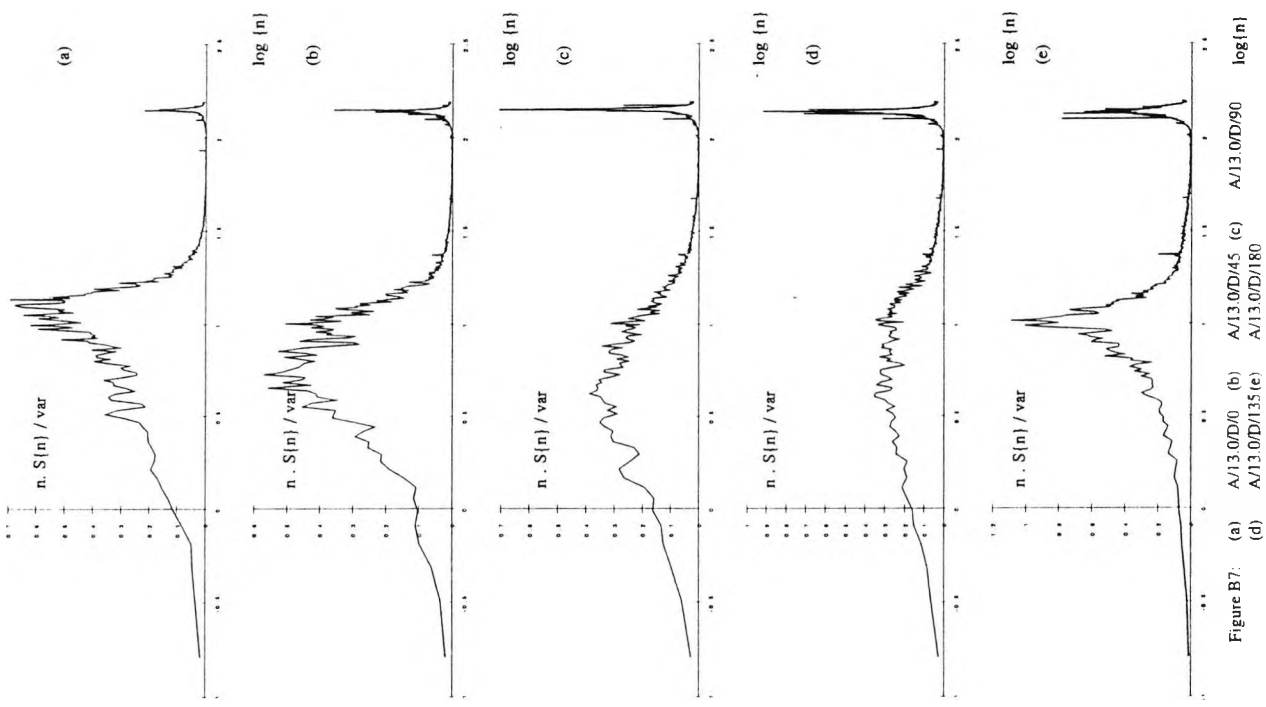

Figure B7: (a) A/13.0/D/0 (b) A/13.0/D/45 (c) A/13.0/D/90 log{n}
(d) A/13.0/D/135 (e) A/13.0/D/180

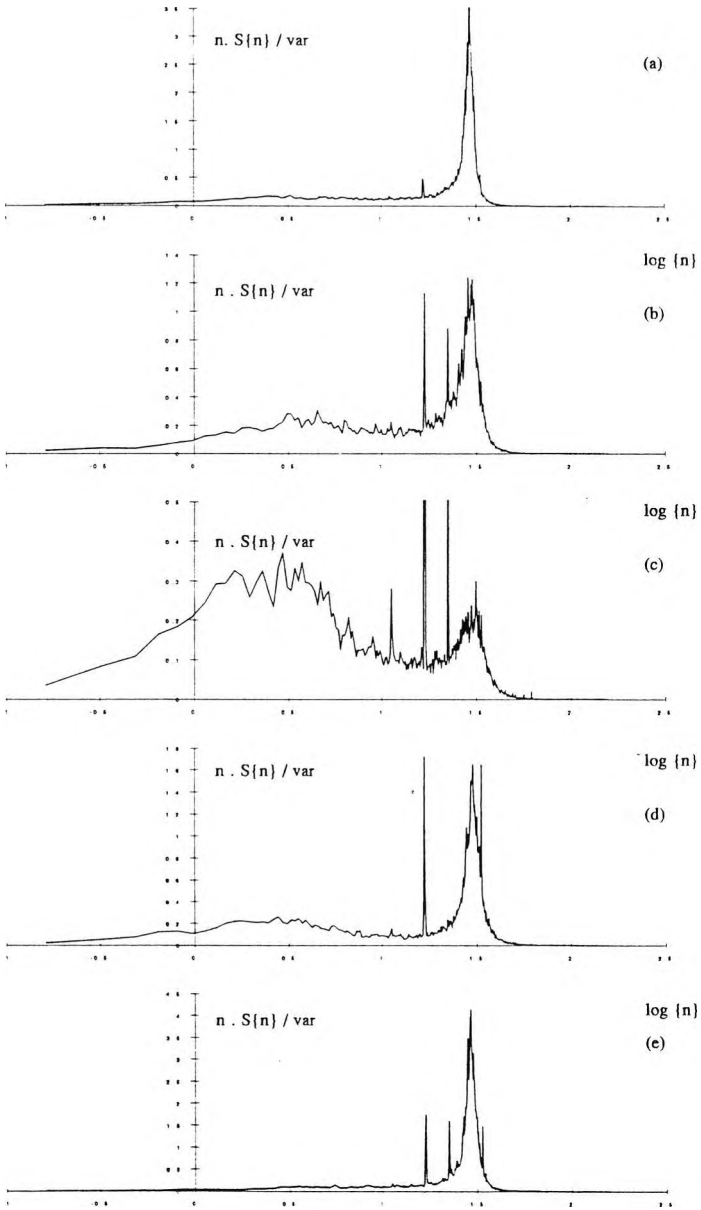

Figure B8: (a) A/9.4 /R/0 (b) A/9.4 /R/45 (c) A/9.4 /R/90
(d) A/9.4 /R/135 (e) A/9.4 /R/180

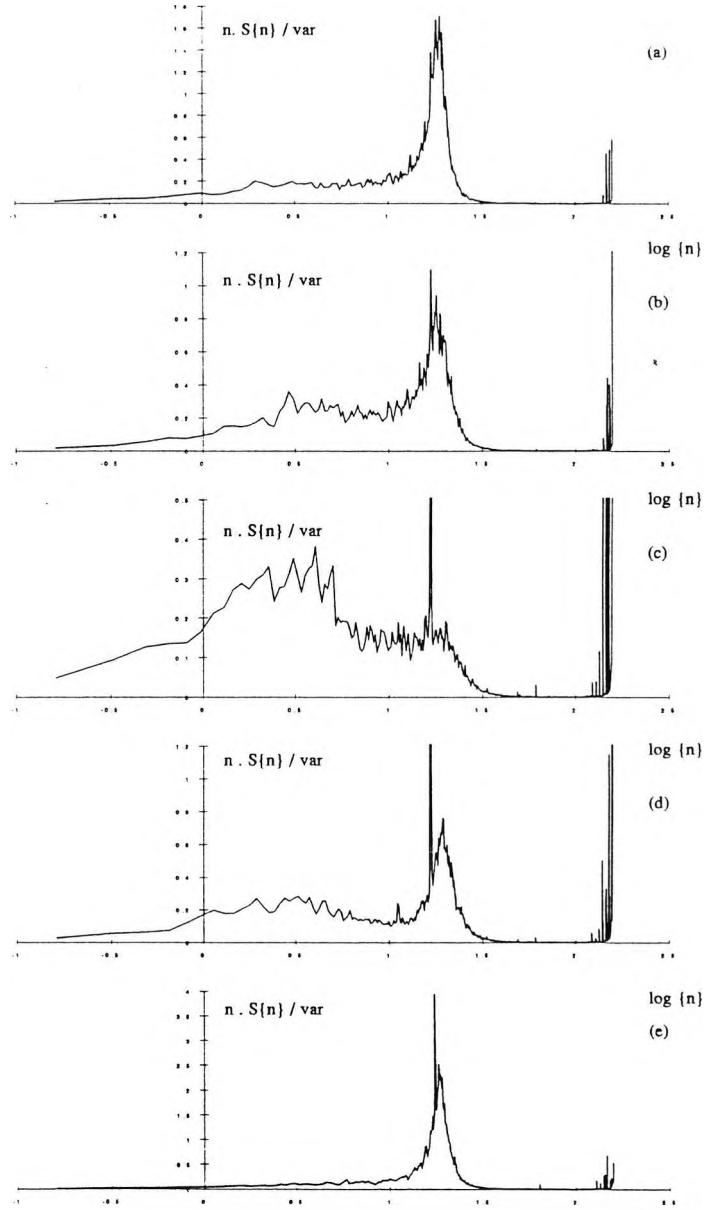

Figure B9: (a) A/9.4 /A/0 (b) A/9.4 /A/45 (c) A/9.4 /A/90
(d) A/9.4 /A/135 (e) A/9.4 /A/180

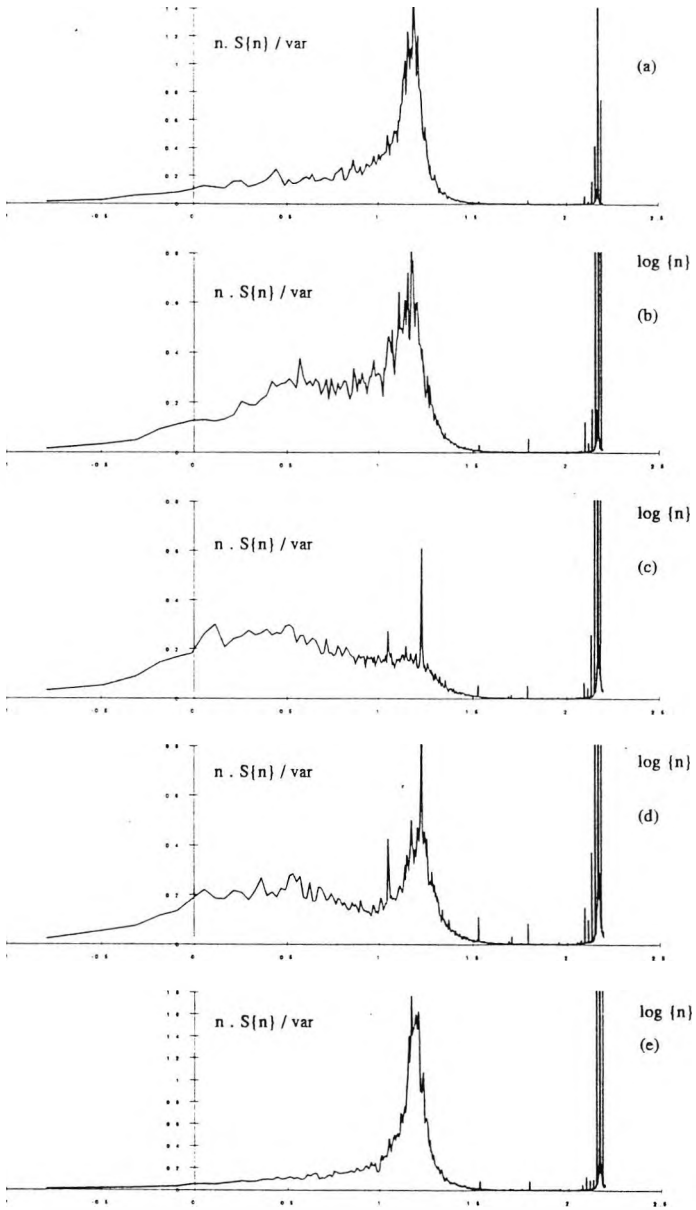

Figure B10: (a) A/9.4 /B/0 (b) A/9.4 /B/45 (c) A/9.4 /B/90
(d) A/9.4 /B/135 (e) A/9.4 /B/180

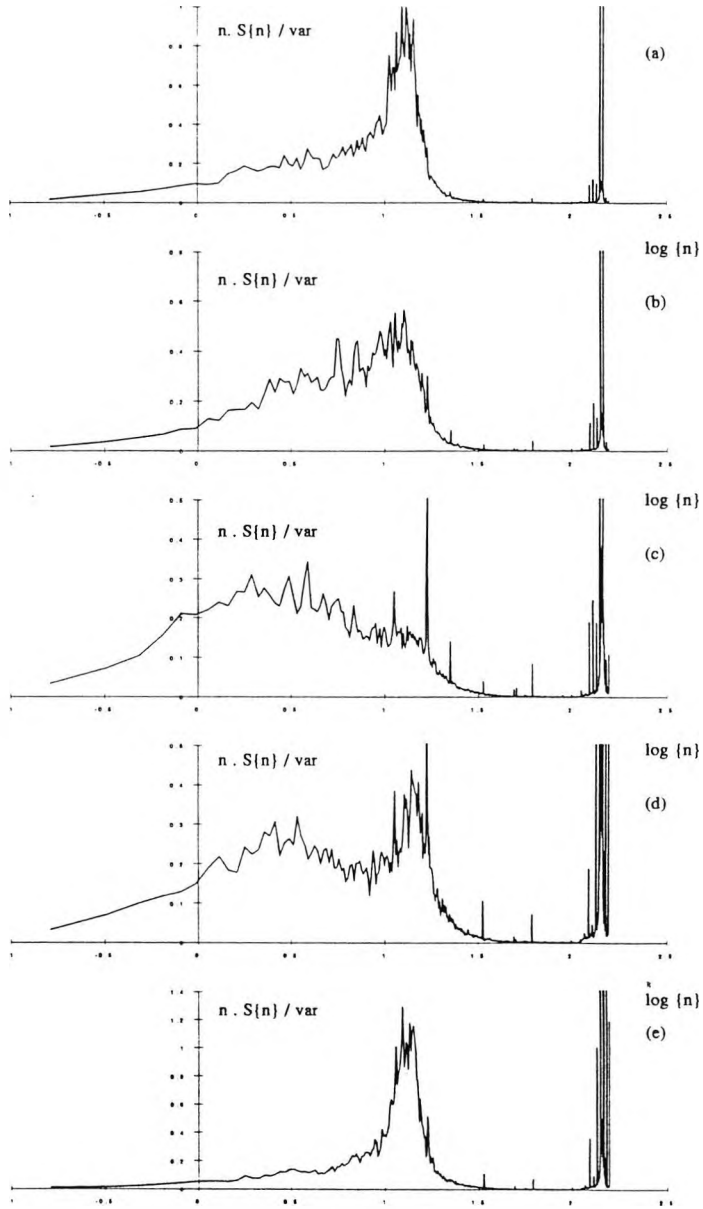

Figure B11: (a) A/9.4 /C/0 (b) A/9.4 /C/45 (c) A/9.4 /C/90
(d) A/9.4 /C/135 (e) A/9.4 /C/180

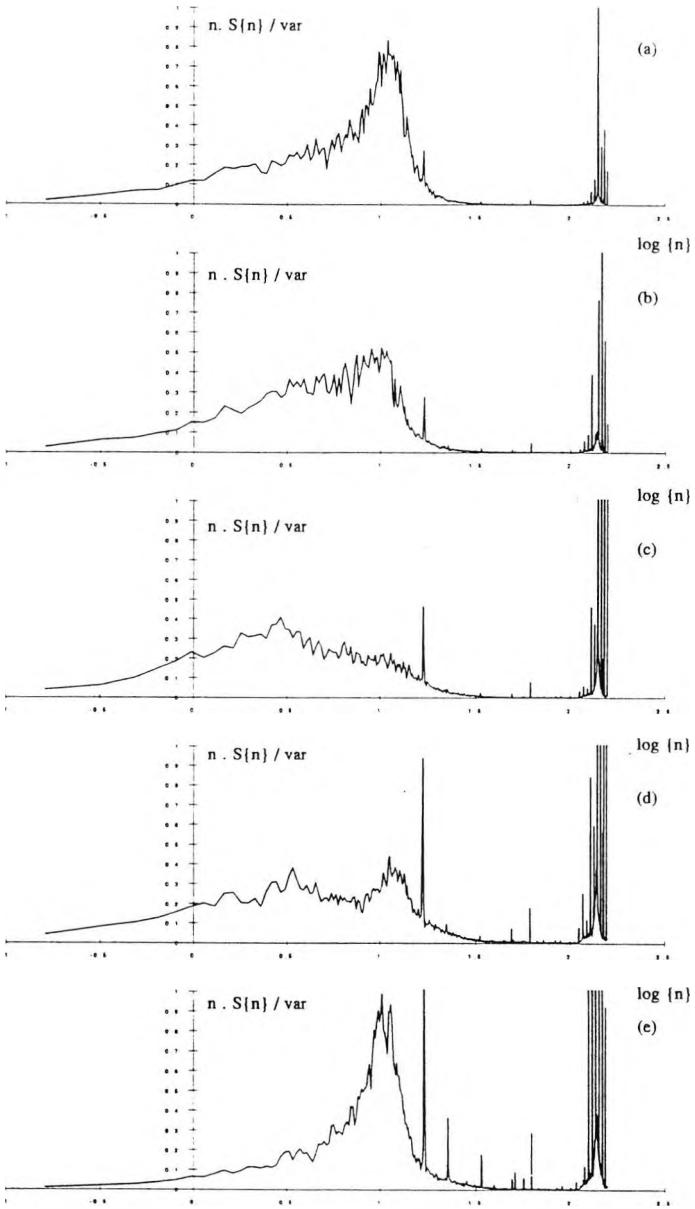

Figure B12: (a) A/9.4 /D/0 (b) A/9.4 /D/45 (c) A/9.4 /D/90
(d) A/9.4 /D/135 (e) A/9.4 /D/180

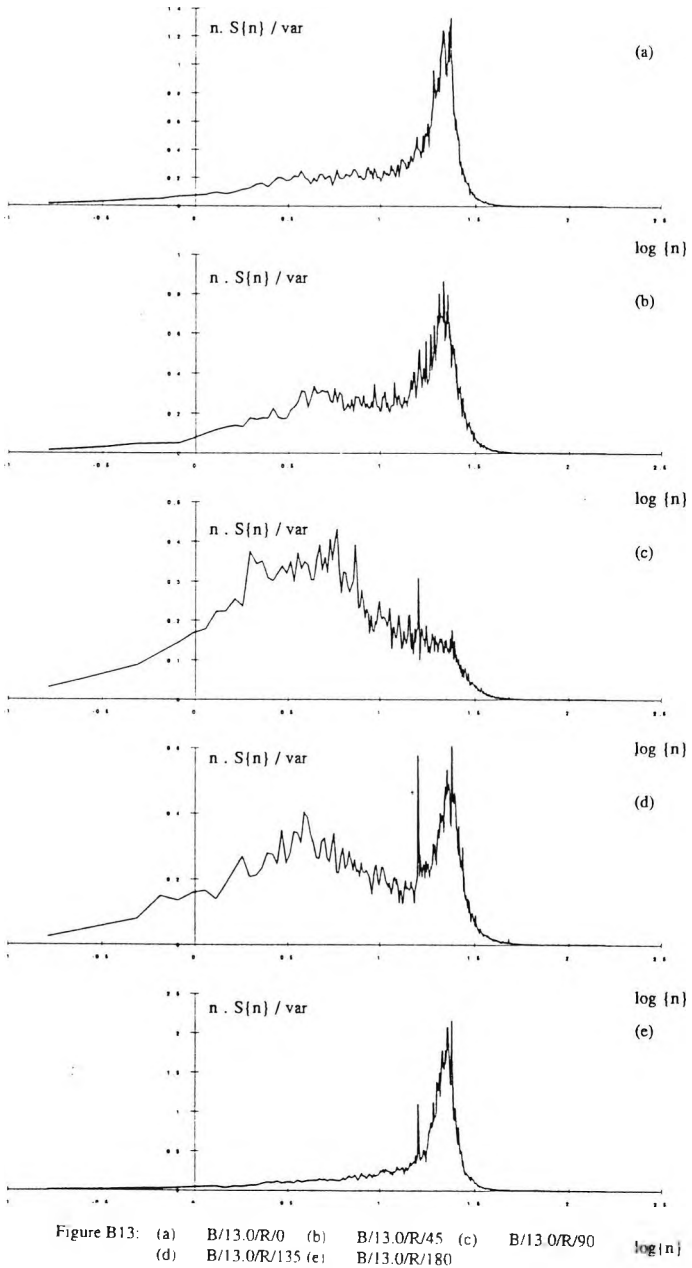

Figure B13: (a) B/13.0/R/0 (b) B/13.0/R/45 (c) B/13.0/R/90
(d) B/13.0/R/135 (e) B/13.0/R/180

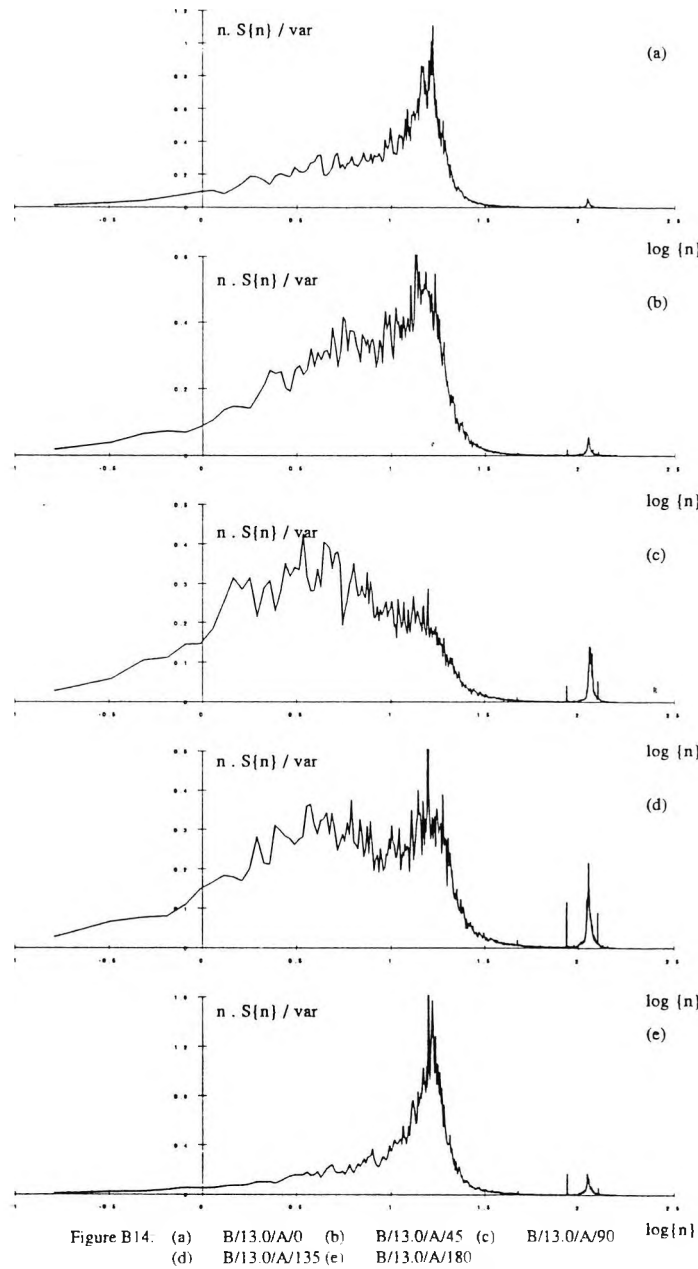

Figure B14: (a) B/13.0/A/0 (b) B/13.0/A/45 (c) B/13.0/A/90
(d) B/13.0/A/135 (e) B/13.0/A/180

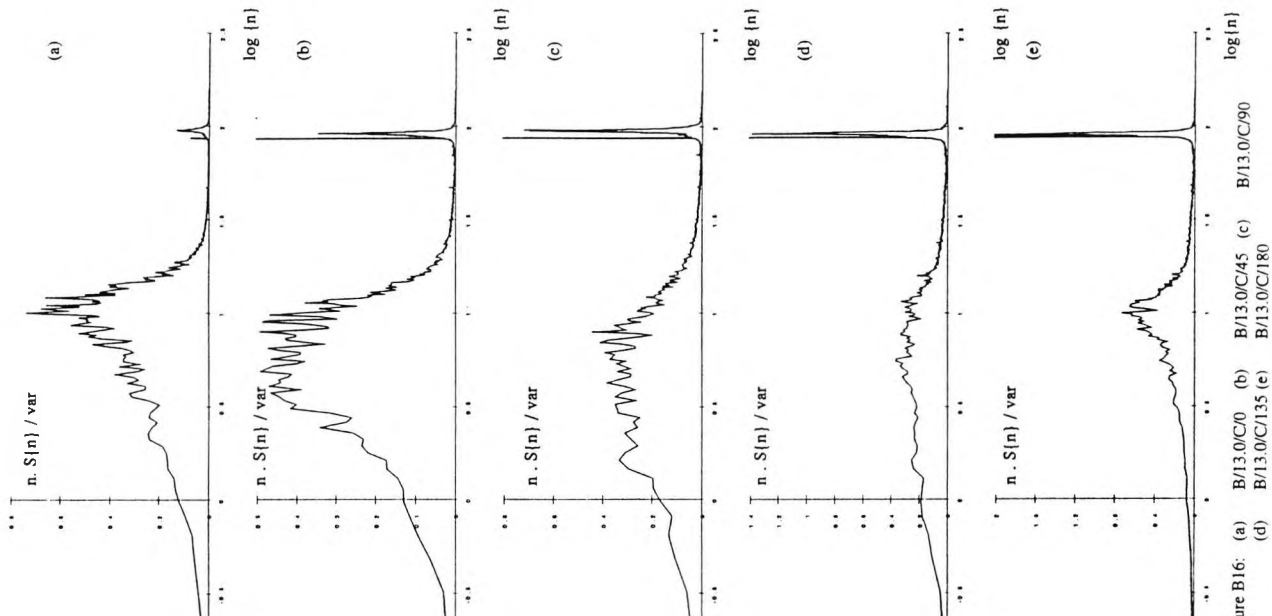

Figure B16: (a) B/13.0/C/0 (b) B/13.0/C/45 (c) B/13.0/C/90
(d) B/13.0/C/135 (e) B/13.0/C/180

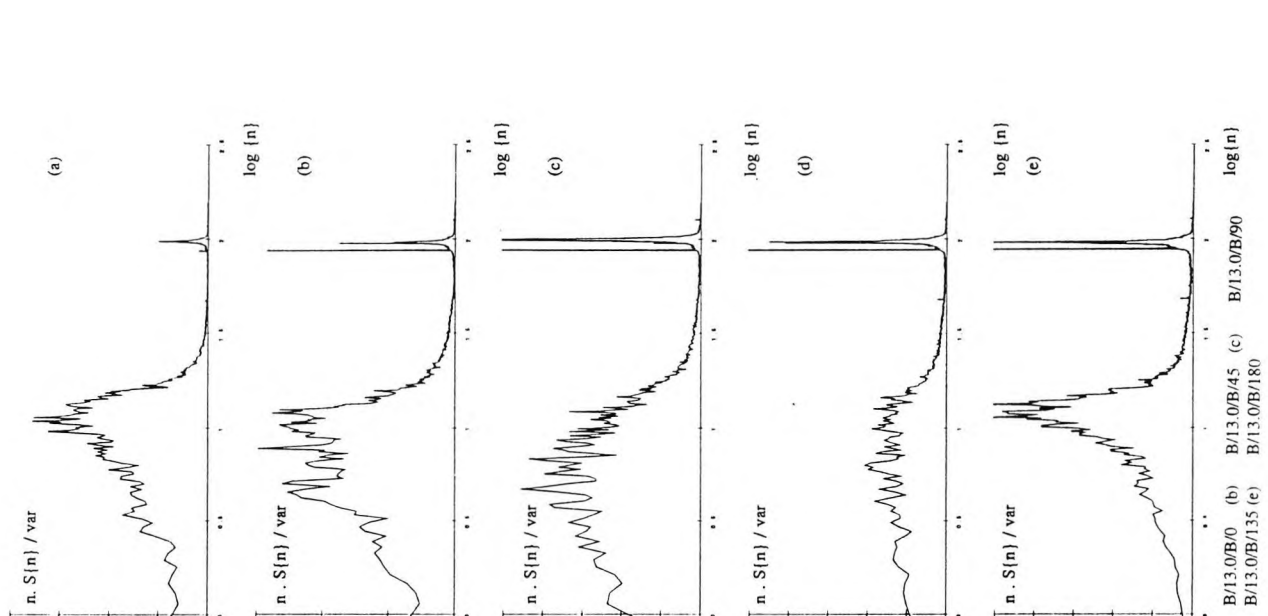

Figure B15: (a) B/13.0/B/0 (b) B/13.0/B/45 (c) B/13.0/B/90
(d) B/13.0/B/135 (e) B/13.0/B/180

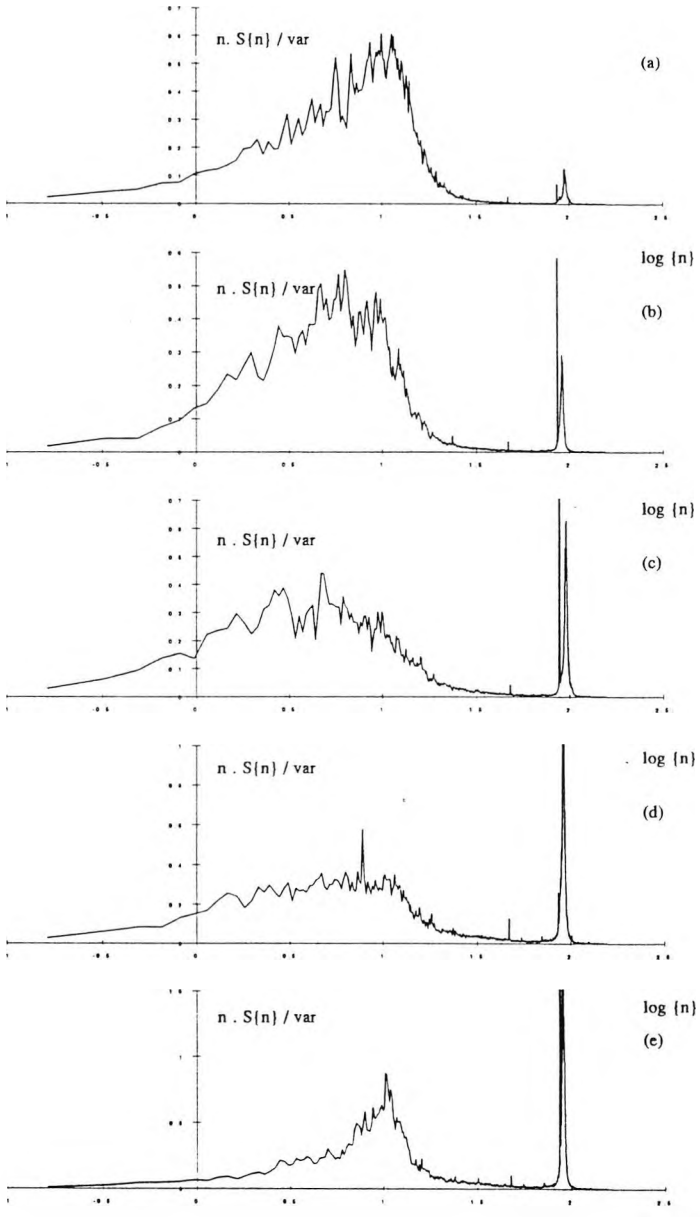

Figure B17: (a) B/13.0/D/0 (b) B/13.0/D/45 (c) B/13.0/D/90
(d) B/13.0/D/135 (e) B/13.0/D/180

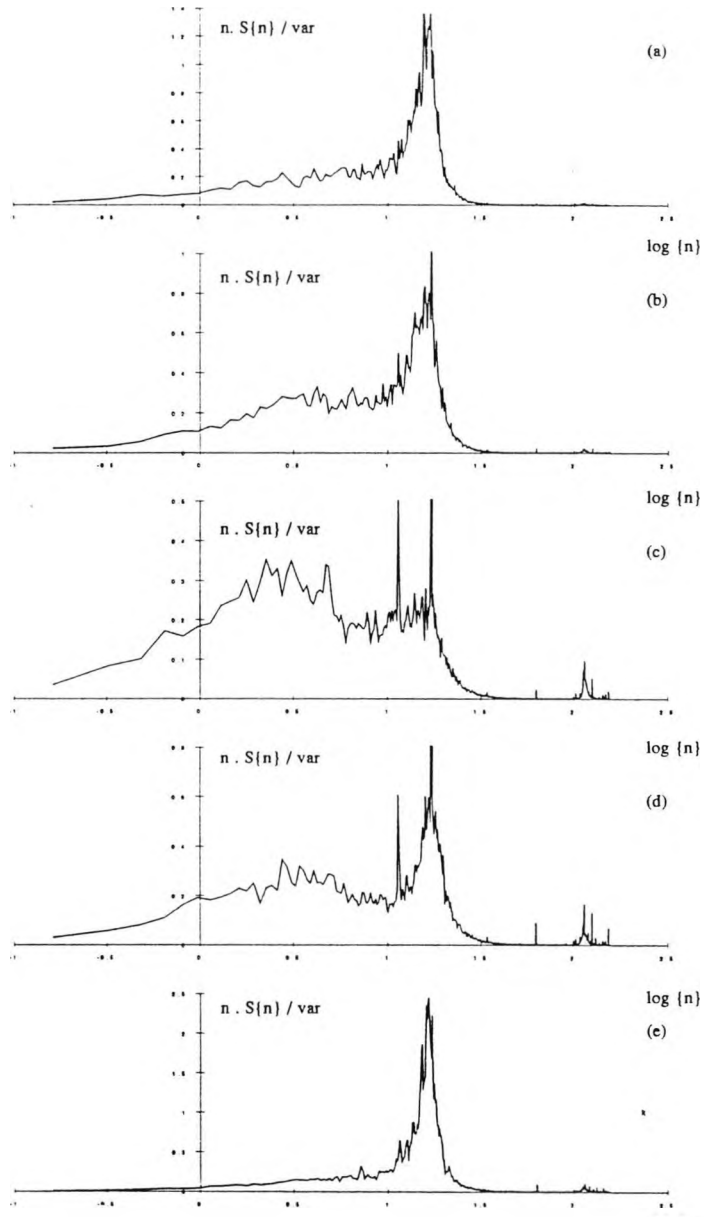

Figure B19: (a) B/9.4 /A/0 (b) B/9.4 /A/45 (c) B/9.4 /A/90
(d) B/9.4 /A/135 (e) B/9.4 /A/180

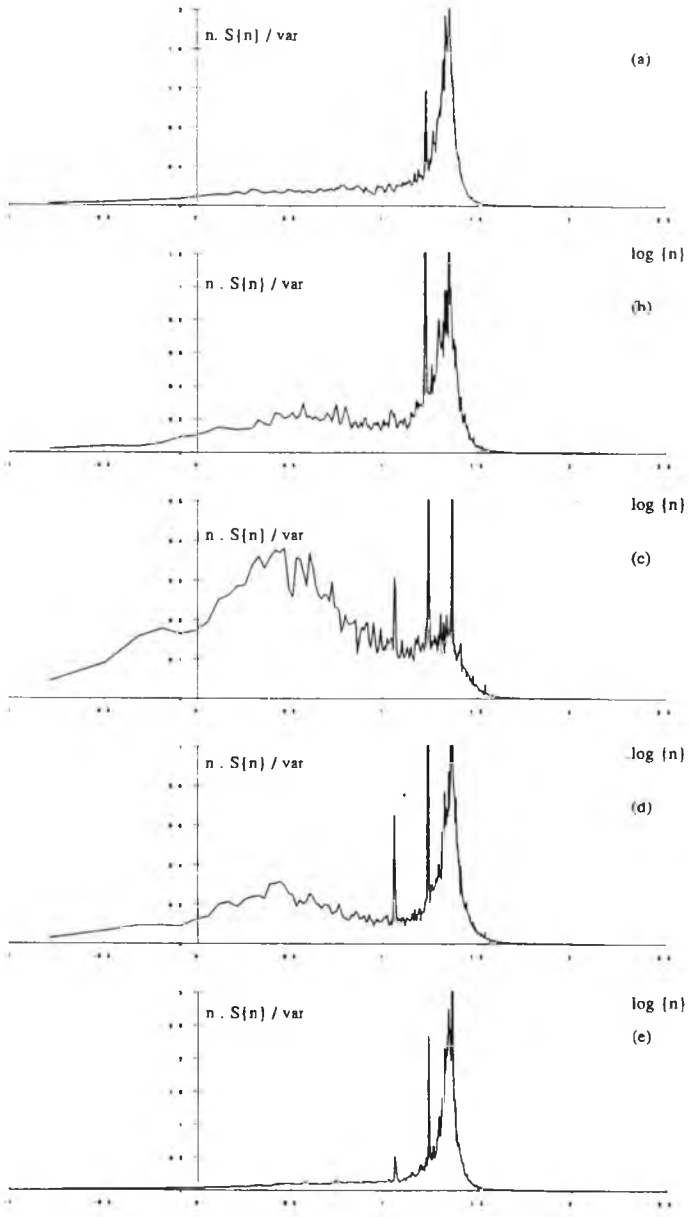

Figure B18: (a) B/9.4 /R/0 (b) B/9.4 /R/45 (c) B/9.4 /R/90
(d) B/9.4 /R/135 (e) B/9.4 /R/180

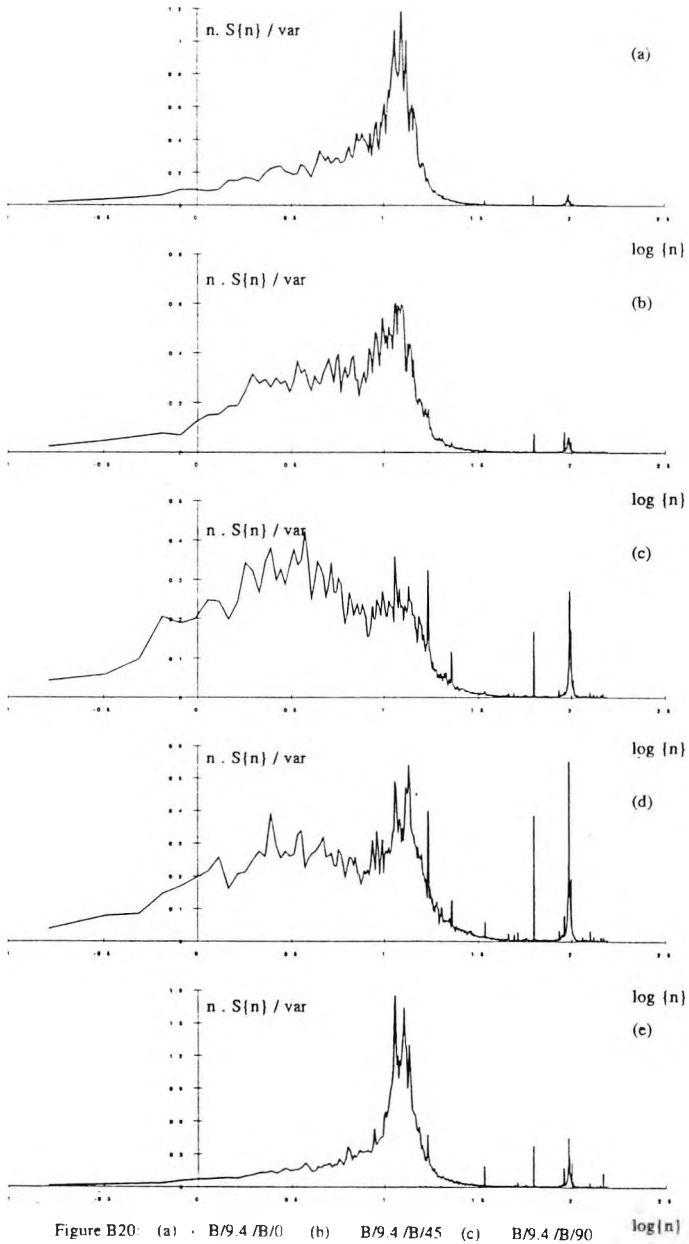

Figure B20: (a) B/9.4 /B/0 (b) B/9.4 /B/45 (c) B/9.4 /B/90
(d) B/9.4 /B/135 (e) B/9.4 /B/180

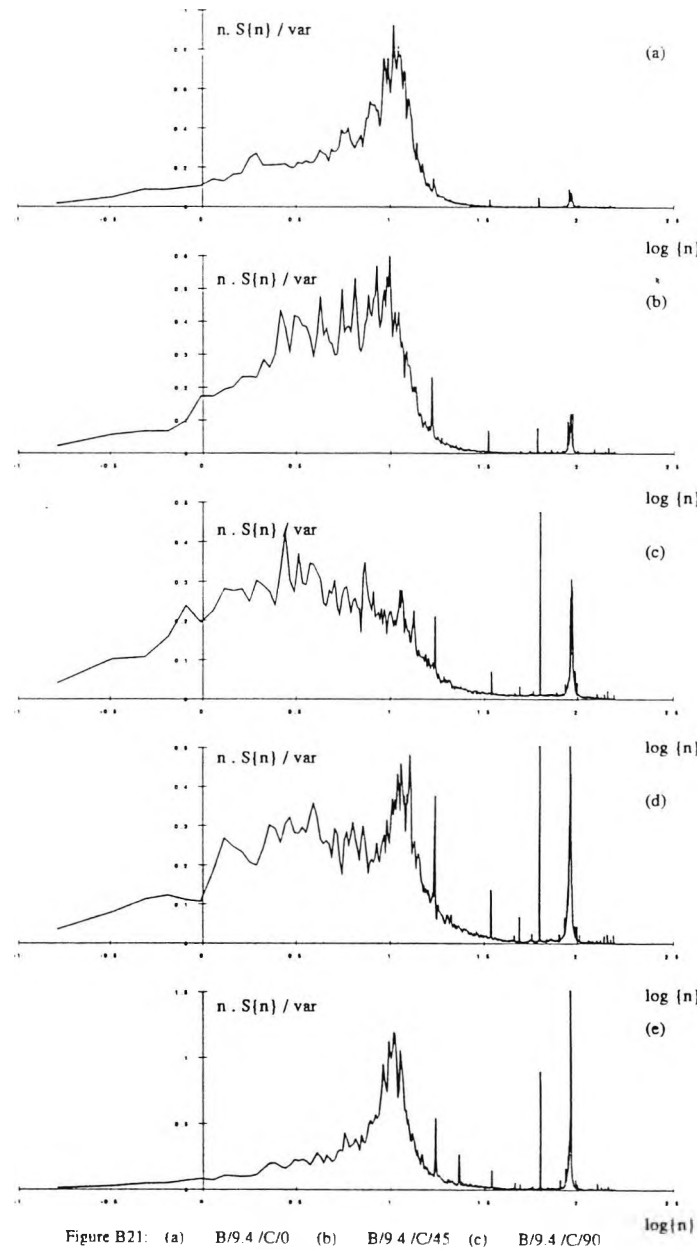

Figure B21: (a) B/9.4 /C/0 (b) B/9.4 /C/45 (c) B/9.4 /C/90
(d) B/9.4 /C/135 (e) B/9.4 /C/180

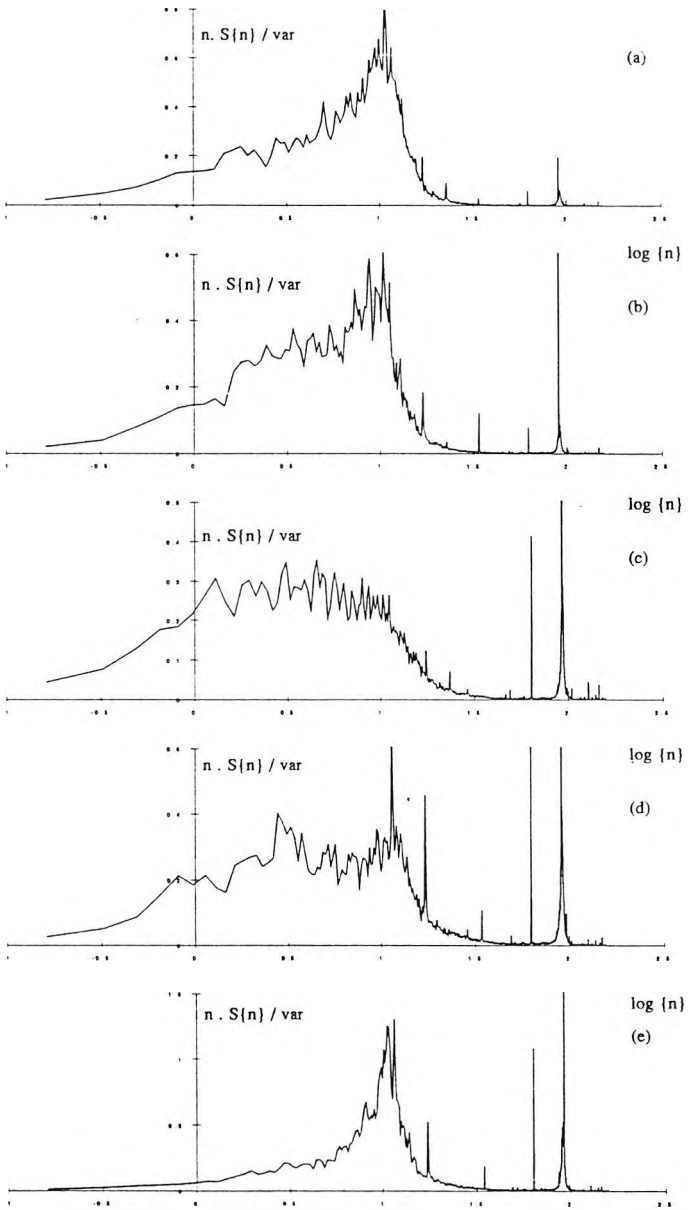

Figure B22: (a) B/9.4 /D/0 (b) B/9.4 /D/45 (c) B/9.4 /D/90
(d) B/9.4 /D/135 (e) B/9.4 /D/180

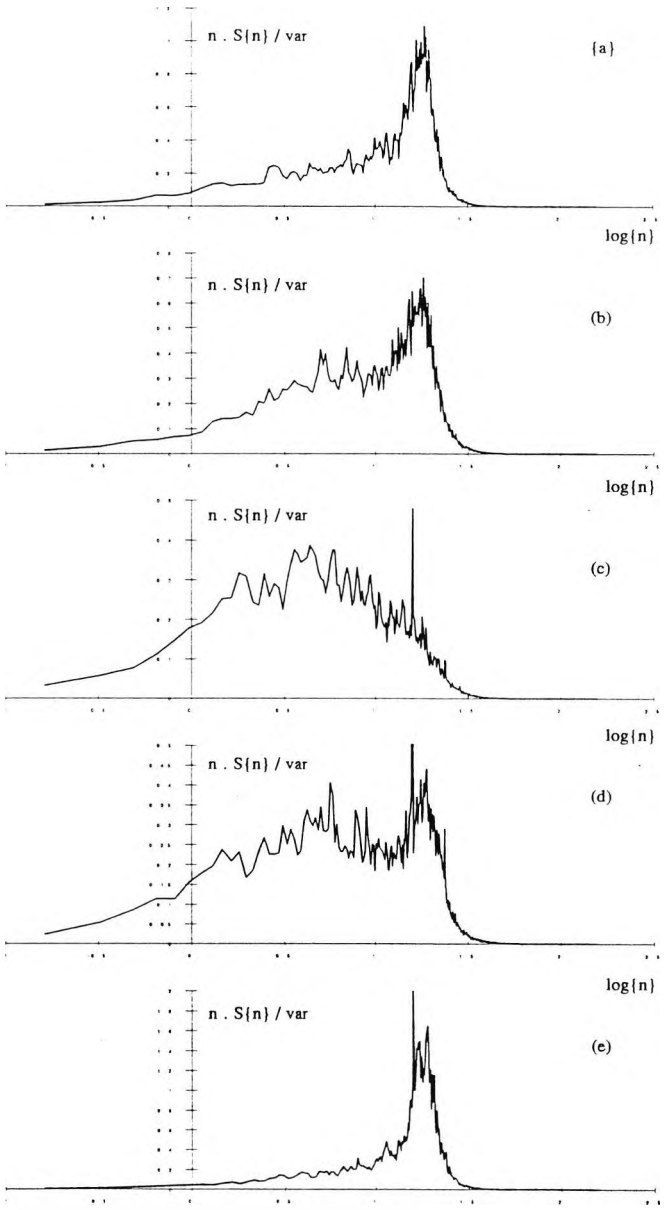

Figure B23: (a) C/13.0/R/0 (b) C/13.0/R/45 (c) C/13.0/R/90
(d) C/13.0/R/135 (e) C/13.0/R/180

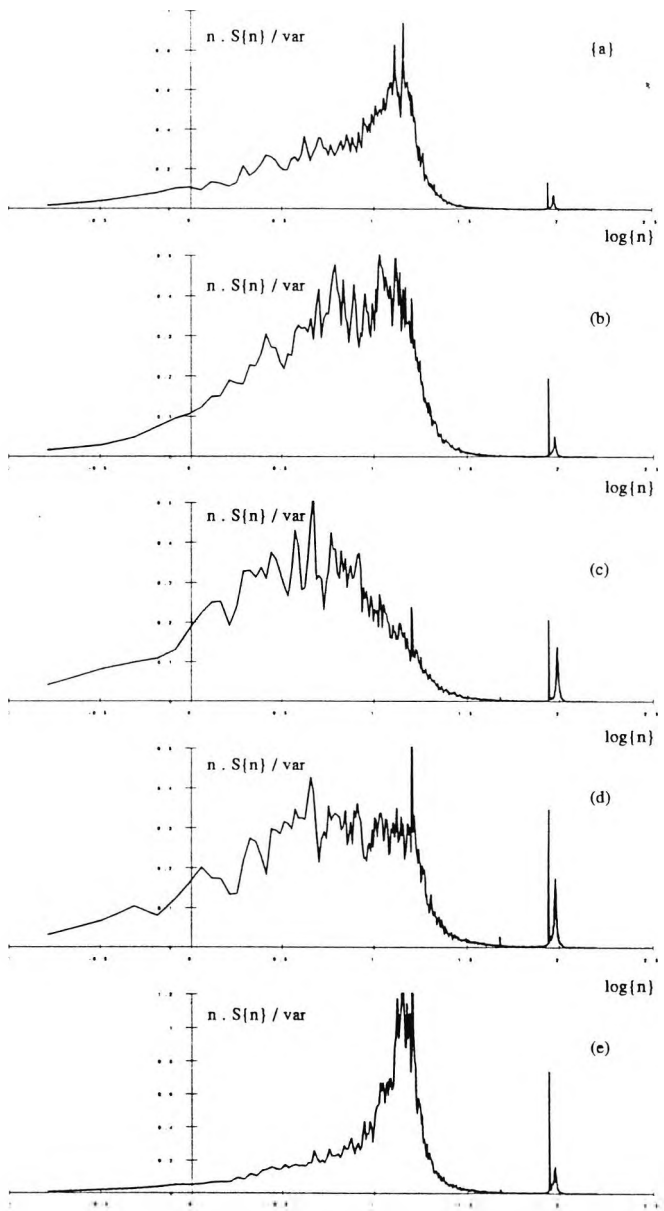

Figure B24: (a) C/13.0/A/0 (b) C/13.0/A/45 (c) C/13.0/A/90
(d) C/13.0/A/135 (e) C/13.0/A/180

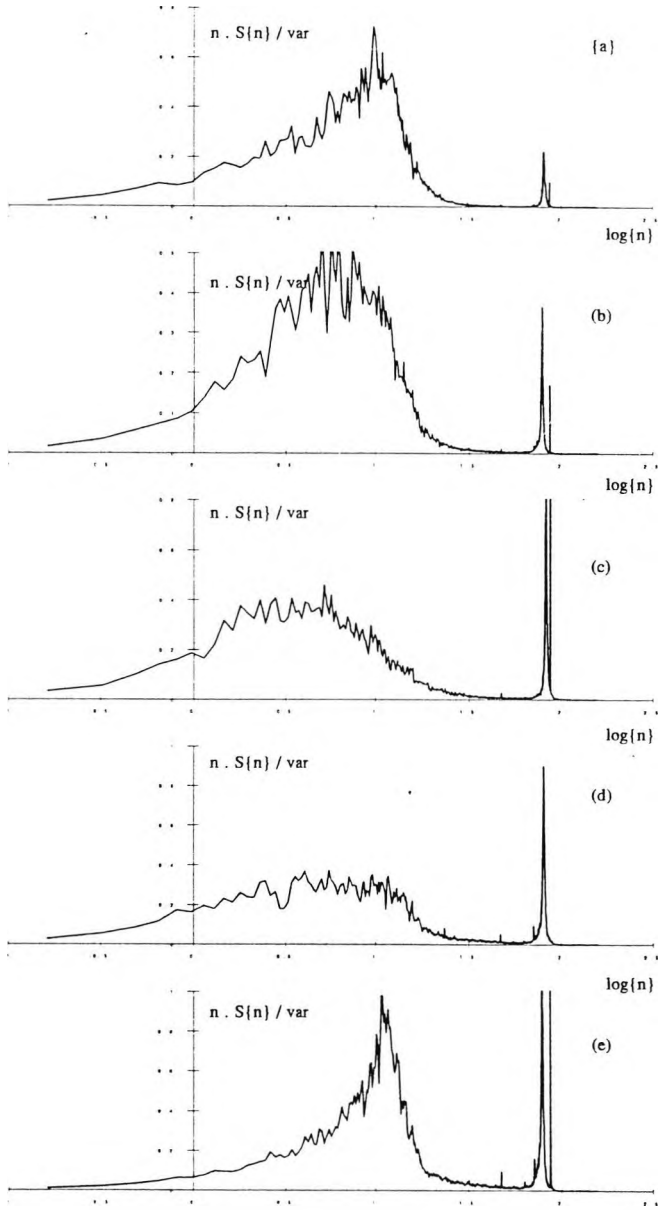

Figure B25: (a) C/13.0/B/0 (b) C/13.0/B/45 (c) C/13.0/B/90 (d) C/13.0/B/135 (e) C/13.0/B/180

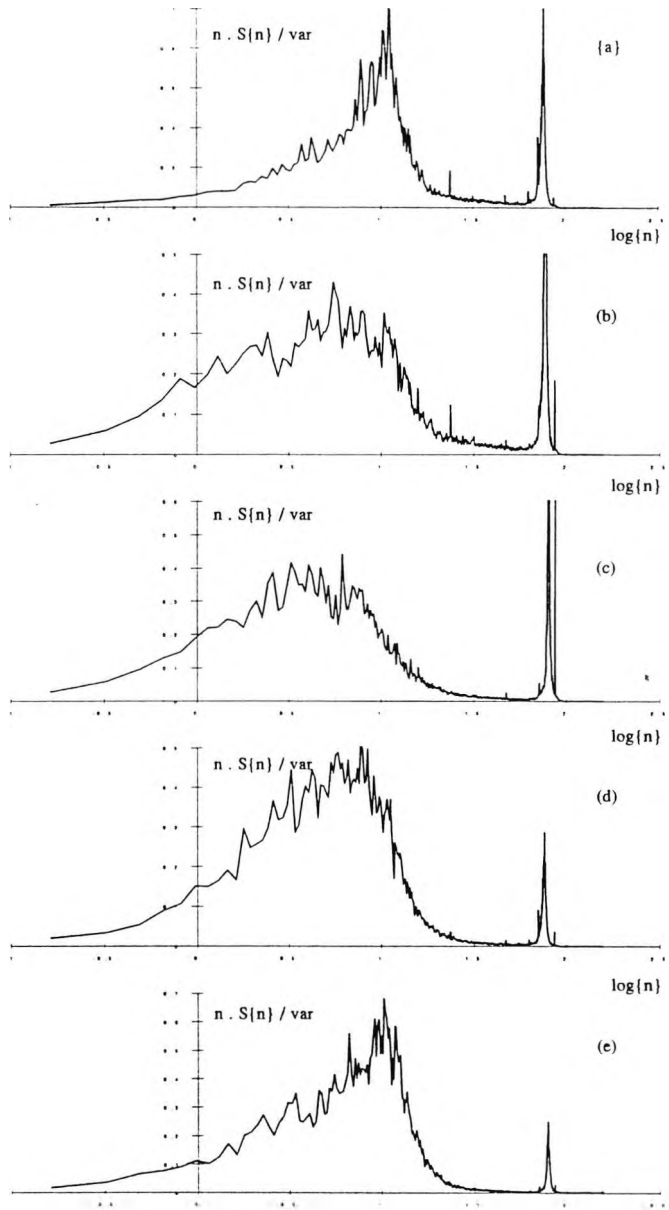

Figure B26: (a) C/13.0/C/0 (b) C/13.0/C/45 (c) C/13.0/C/90 (d) C/13.0/C/135 (e) C/13.0/C/180

Figure B27: (a) C/13.0/D/0 (b) C/13.0/D/45 (c) C/13.0/D/90
(d) C/13.0/D/135 (e) C/13.0/D/180

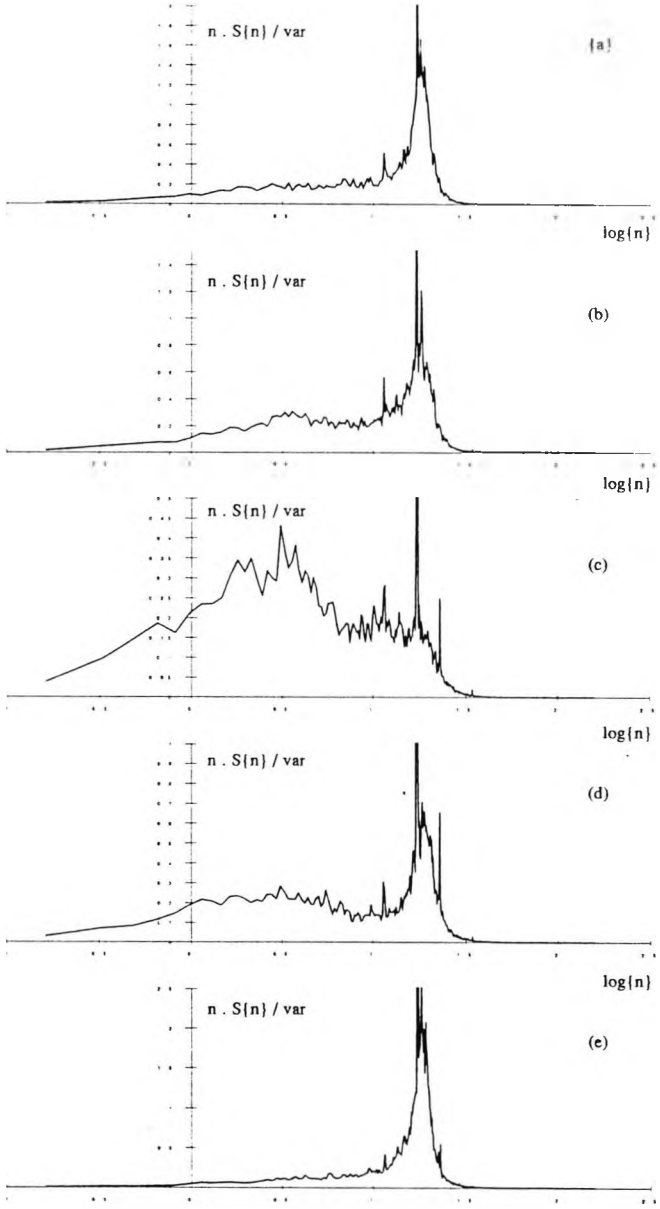

Figure B28. (a) C/9.4 /R/0 (b) C/9.4 /R/45 (c) C/9.4 /R/90 (d) C/9.4 /R/135 (e) C/9.4 /R/180

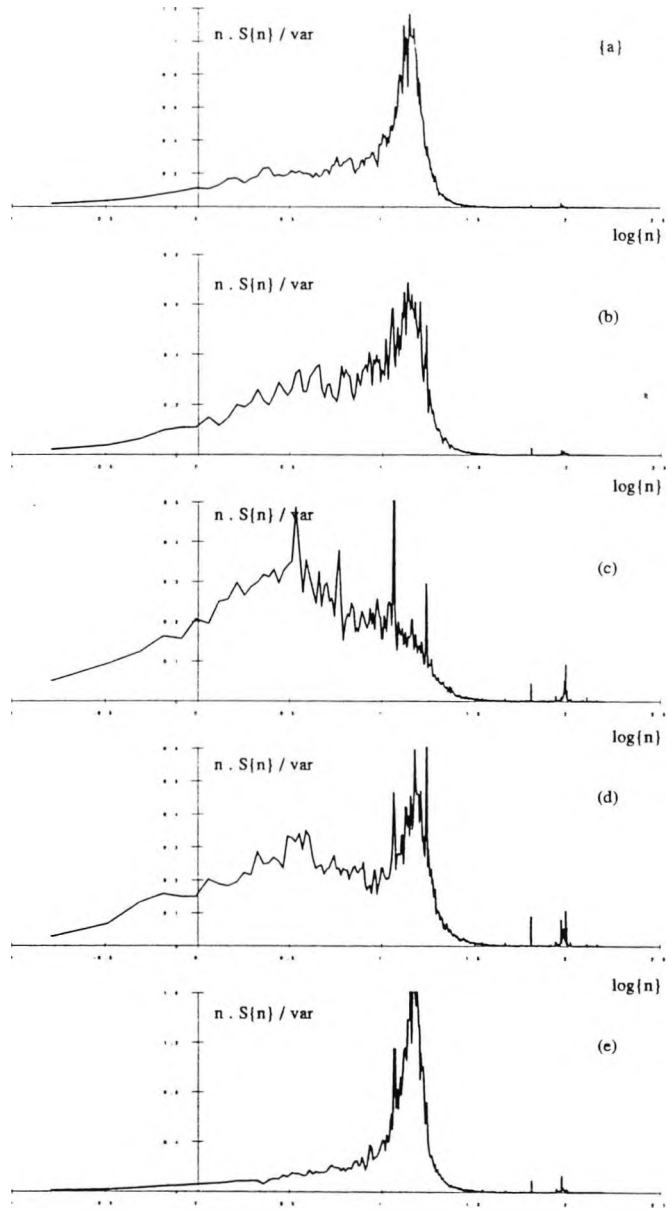

Figure B29: (a) C/9.4 /A/0 (b) C/9.4 /A/45 (c) C/9.4 /A/90 (d) C/9.4 /A/135 (e) C/9.4 /A/180

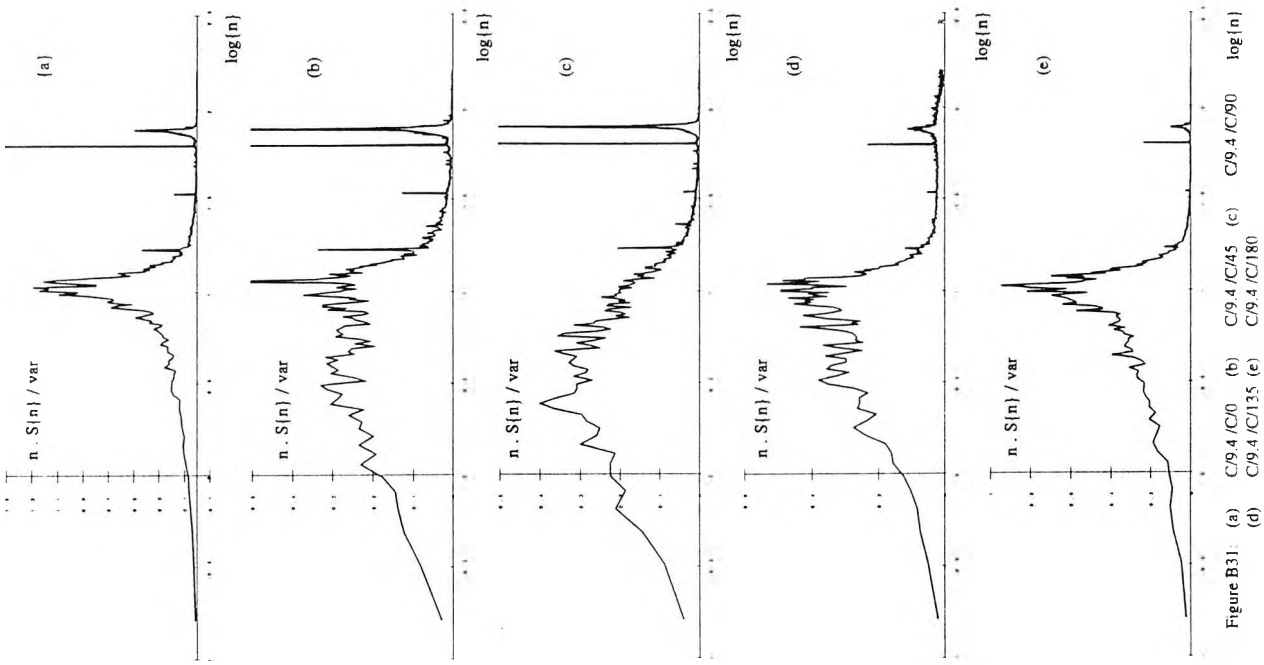

Figure B31: (a) C/9.4 /C/0 (b) C/9.4 /C/45 (c) C/9.4 /C/90
(d) C/9.4 /C/135 (e) C/9.4 /C/180

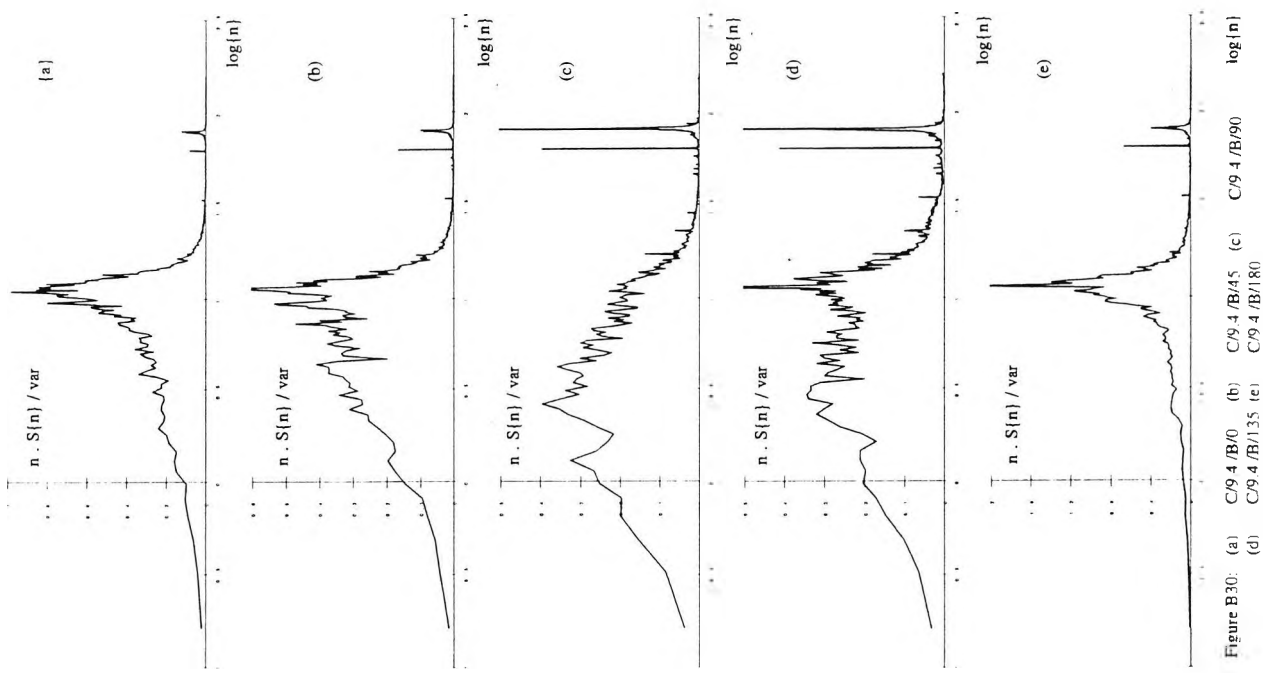

Figure B30: (a) C/9.4 /B/0 (b) C/9.4 /B/45 (c) C/9.4 /B/90
(d) C/9.4 /B/135 (e) C/9.4 /B/180

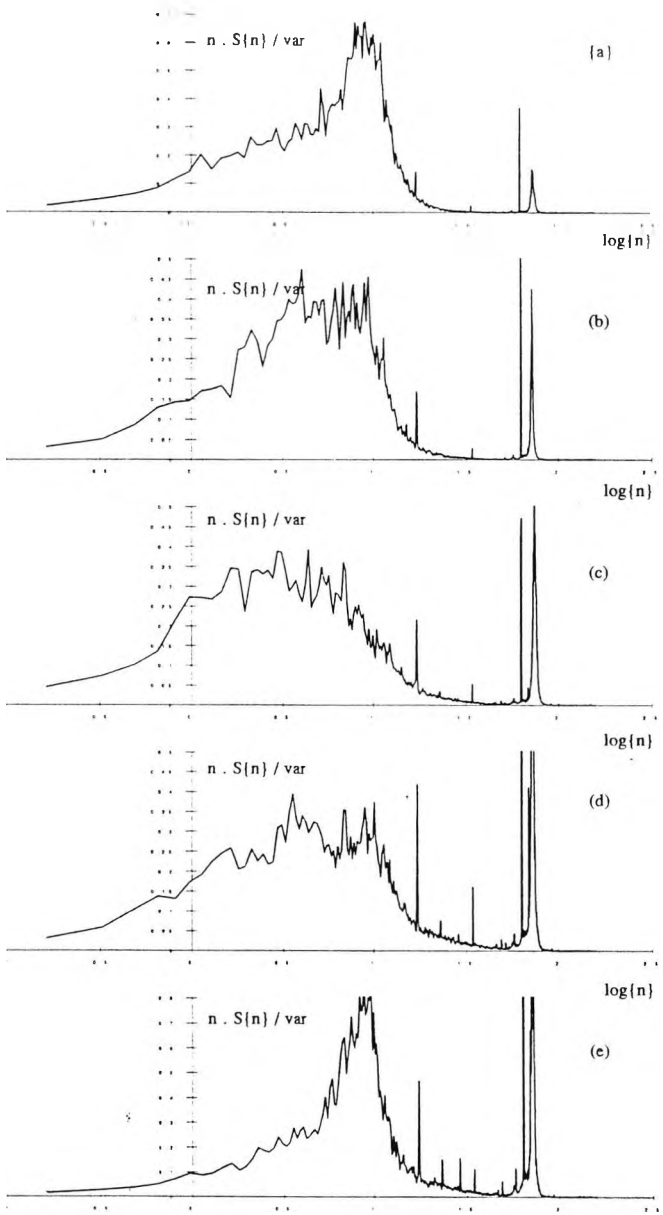

Figure B32: (a) C/9.4 /D/0 (b) C/9.4 /D/45 (c) C/9.4 /D/90
(d) C/9.4 /D/135 (e) C/9.4 /D/180

Appendix C: Cavity Pressure Gain Functions

The results in this appendix comprise the complete set of gain functions (defined by equation 7.1) obtained by dividing the cavity pressure spectra by the external pressure spectra measured at a point 0.27H up the wall of the model.

Results were plotted as gain (on a linear scale) against the logarithm to base 10 of the frequency (at model scale).

The key to each graph is best explained by giving an example,

Figure C1(c) **A/9.4 /R/0** cavity volume **A**,
mean reference windspeed **9.4**m/s,
roof tension, **R** (rigid),
opening azimuth angle **0** degrees

		0			45			90			135			180		
		Va	Vb	Vc	Va	Vb	Vc	Va	Vb	Vc	Va	Vb	Vc	Va	Vb	Vc
L	R	.07	.08	.10	.10	.05	.14	.15	.25	.24	.10	.12	.14	.06	.09	.10
	Ta	.09	.18	.14	.18	.21	.21	.27	.25	.38	.10	.14	.14	.09	.10	.13
	Tb	.11	.21	.26	.16	.23	.22	.42	.29	.47	.15	.22	.31	.12	.18	.21
	Tc	.20	.28	.30	.28	.44	.39	.41	.46	-	.17	.25	.36	.15	.22	.22
	Td	.28	.34	.33	.41	.42	.59	.27	.64	-	.31	.34	.57	.30	.26	.34
H	R	.08	.14	.17	.12	.24	.25	.31	.47	.41	.12	.18	.27	.07	.13	.17
	Ta	.18	.24	.23	.27	.27	.48	.52	.38	-	.14	.25	.36	.15	.18	.22
	Tb	.22	.42	.39	.41	.32	-	.67	.59	-	.29	.33	.25	.19	.29	.37
	Tc	.29	.39	.39	.36	-	-	-	-	-	.45	.42	.54	.25	.62	.38
	Td	.29	.44	.42	-	-	-	-	-	-	.30	.34	.51	.42	.41	.54

Table C1: Experimental estimates of damping, as a fraction of critical, at the Helmholtz frequency.

The results in table C1 were estimated from the following graphs using the half-amplitude method.

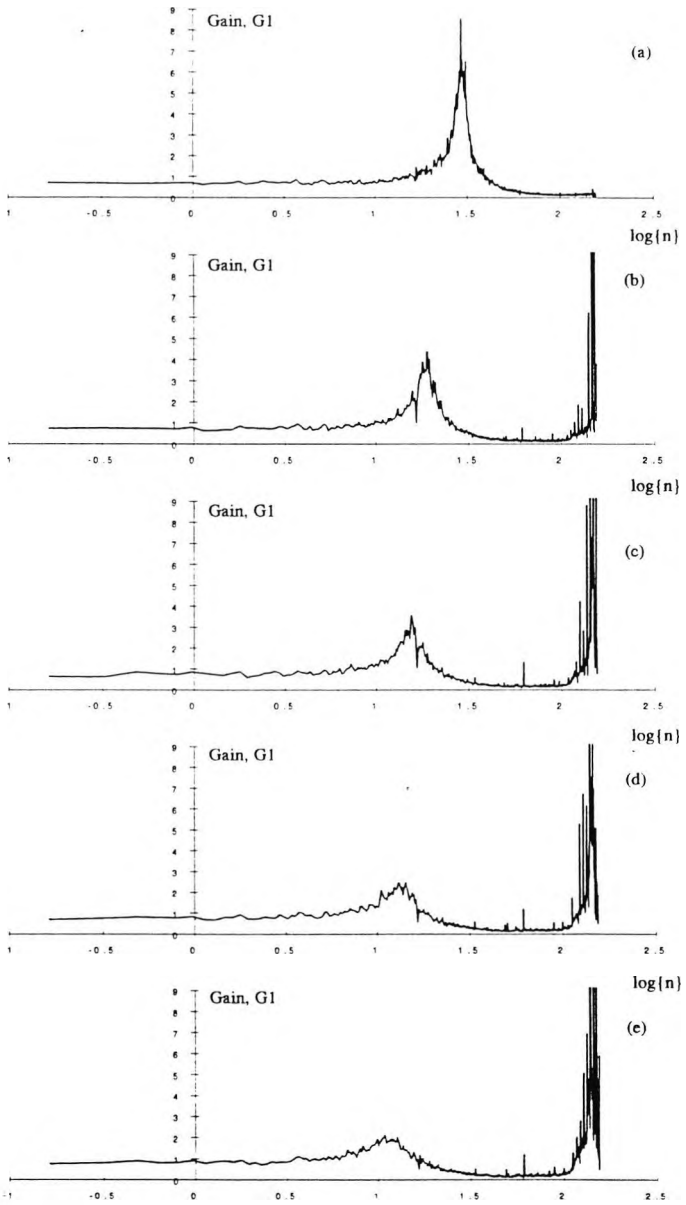

Figure C1: (a) A/9.4 /R/0 (b) A/9.4 /A/0 (c) A/9.4 /B/0 (d) A/9.4 /C/0 (e) A/9.4 /D/0

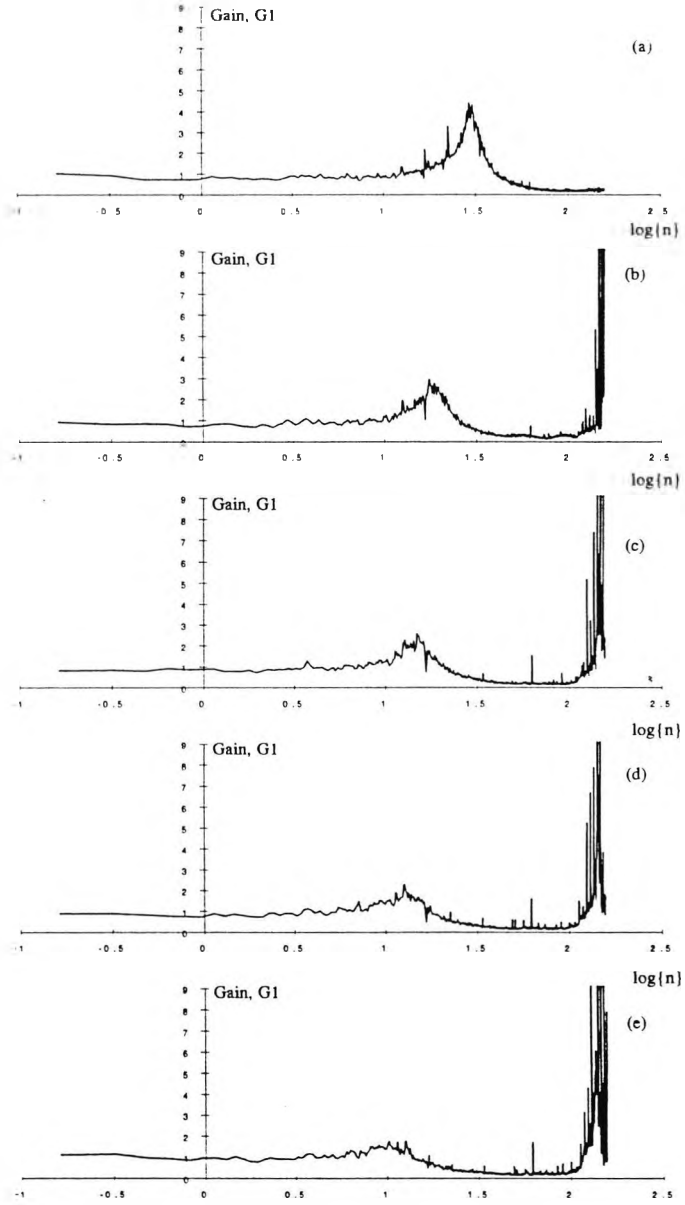

Figure C2: (a) A/9.4 /R/45 (b) A/9.4 /A/45 (c) A/9.4 /B/45 (d) A/9.4 /C/45 (e) A/9.4 /D/45

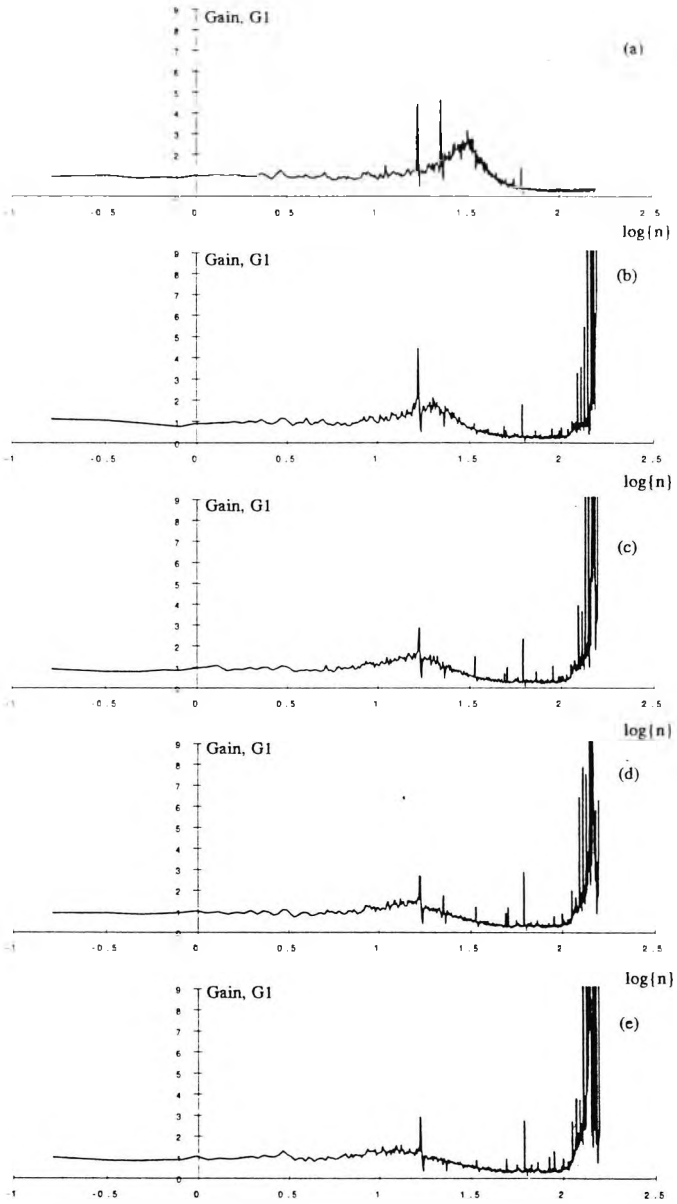

Figure C3: (a) A/9.4 /R/90 (b) A/9.4 /A/90 (c) A/9.4 /B/90
(d) A/9.4 /C/90 (e) A/9.4 /D/90

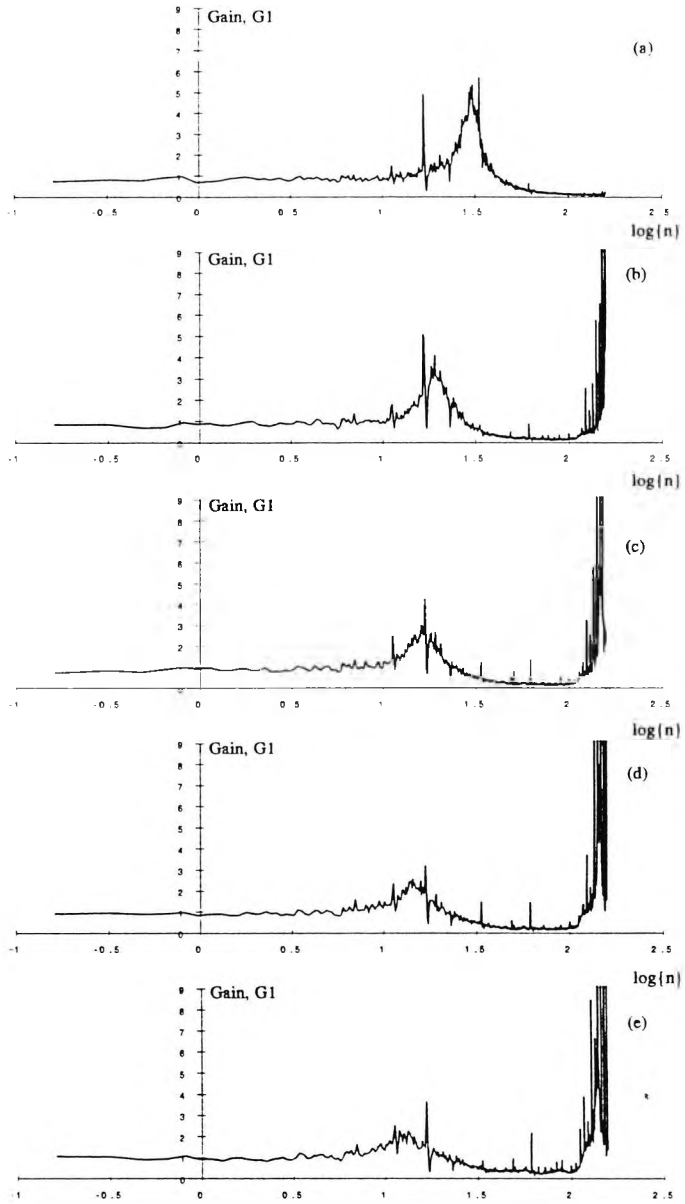

Figure C4: (a) A/9.4 /R/135 (b) A/9.4 /A/135 (c) A/9.4 /B/135
(d) A/9.4 /C/135 (e) A/9.4 /D/135

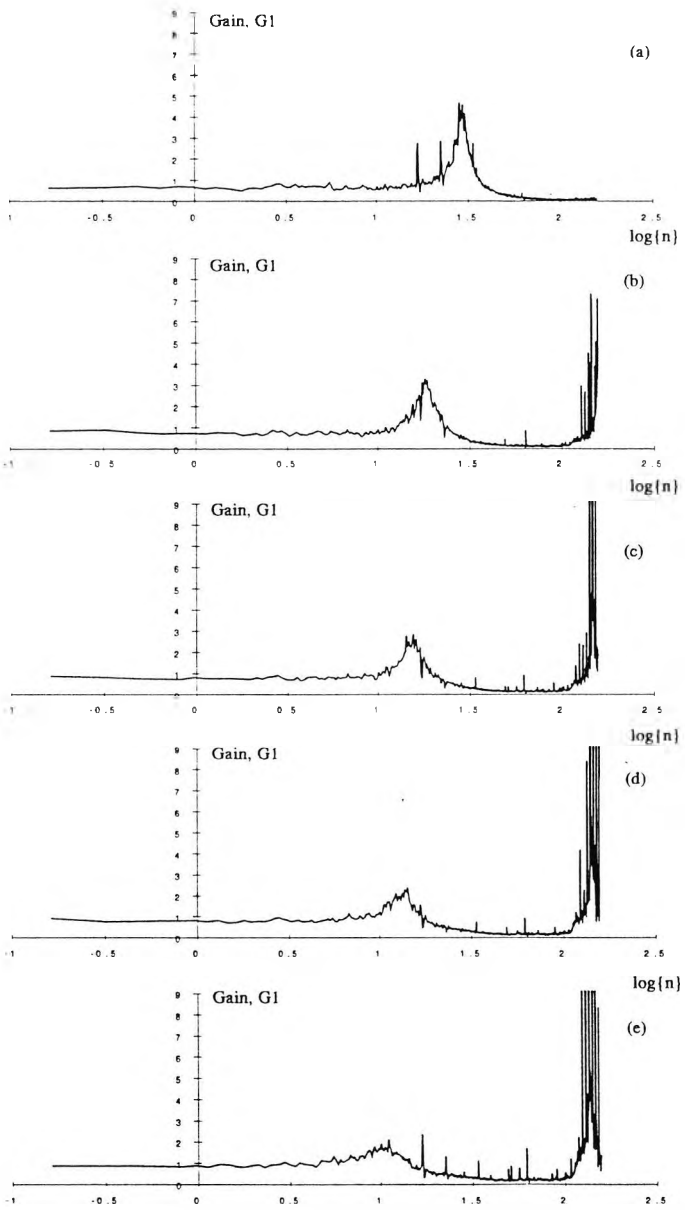

Figure C5: (a) A/9.4 /R/180 (b) A/9.4 /A/180 (c) A/9.4 /B/180
(d) A/9.4 /C/180 (e) A/9.4 /D/180

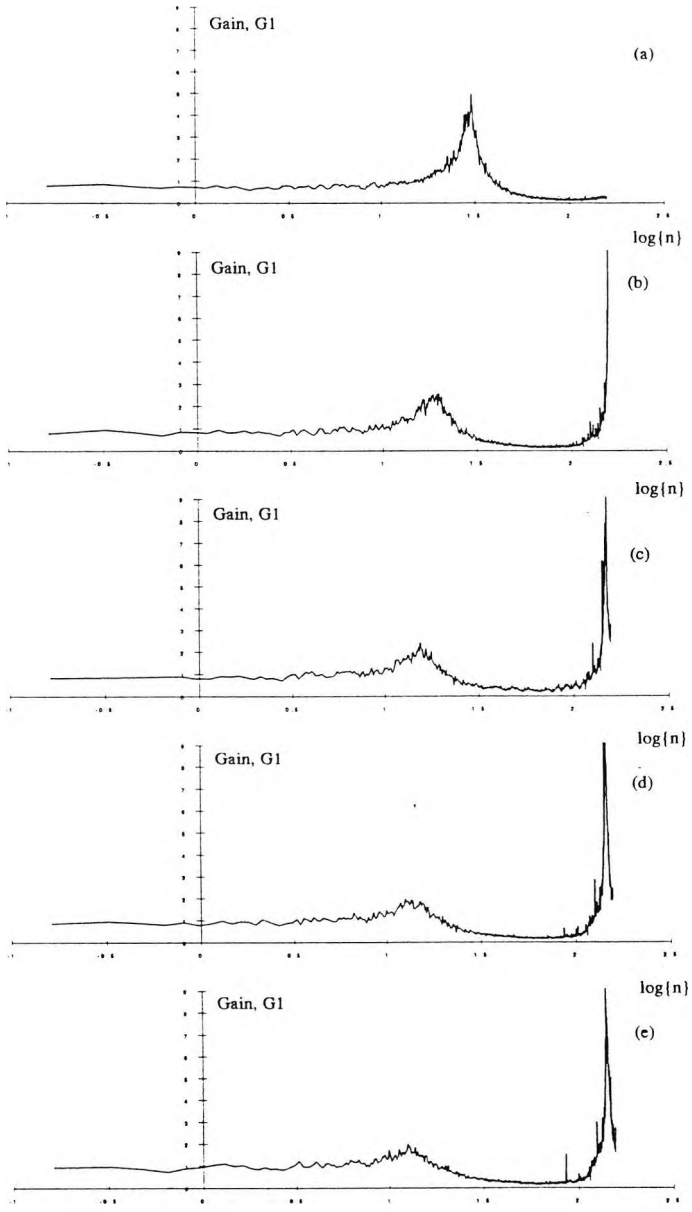

Figure C6: (a) A/13.0/R/0 (b) A/13.0/A/0 (c) A/13.0/B/0
(d) A/13.0/C/0 (e) A/13.0/D/0

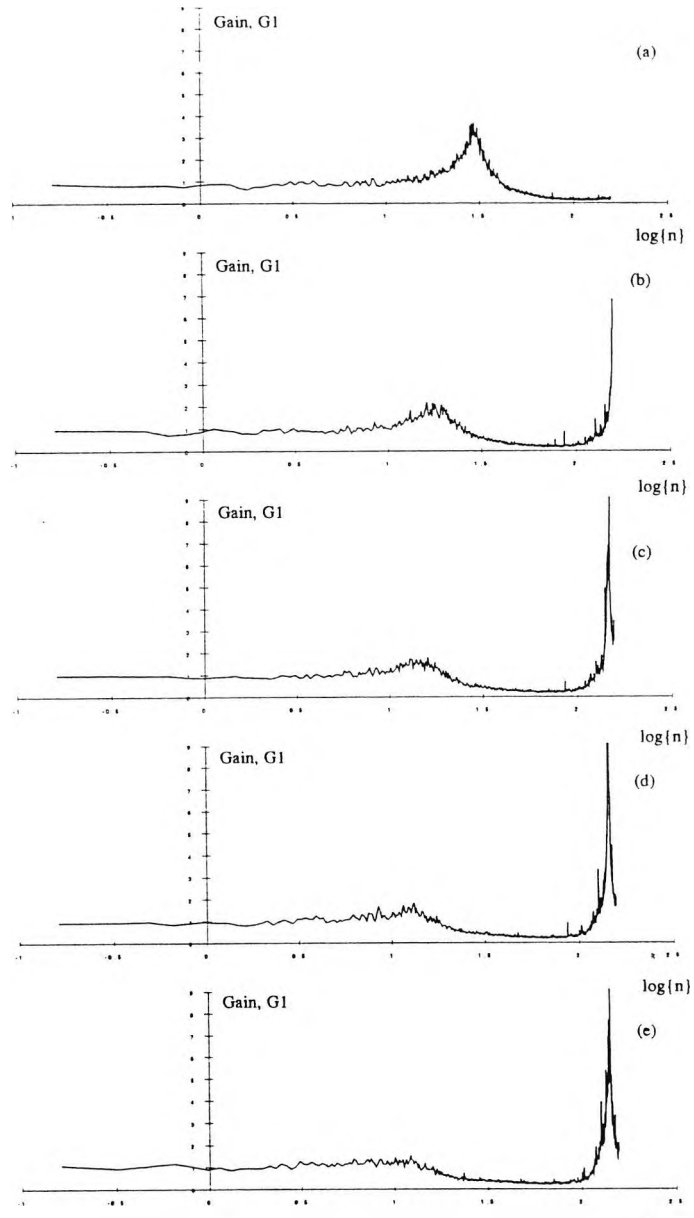

Figure C7: (a) A/13.0/R/45 (b) A/13.0/A/45 (c) A/13.0/B/45
(d) A/13.0/C/45 (e) A/13.0/D/45

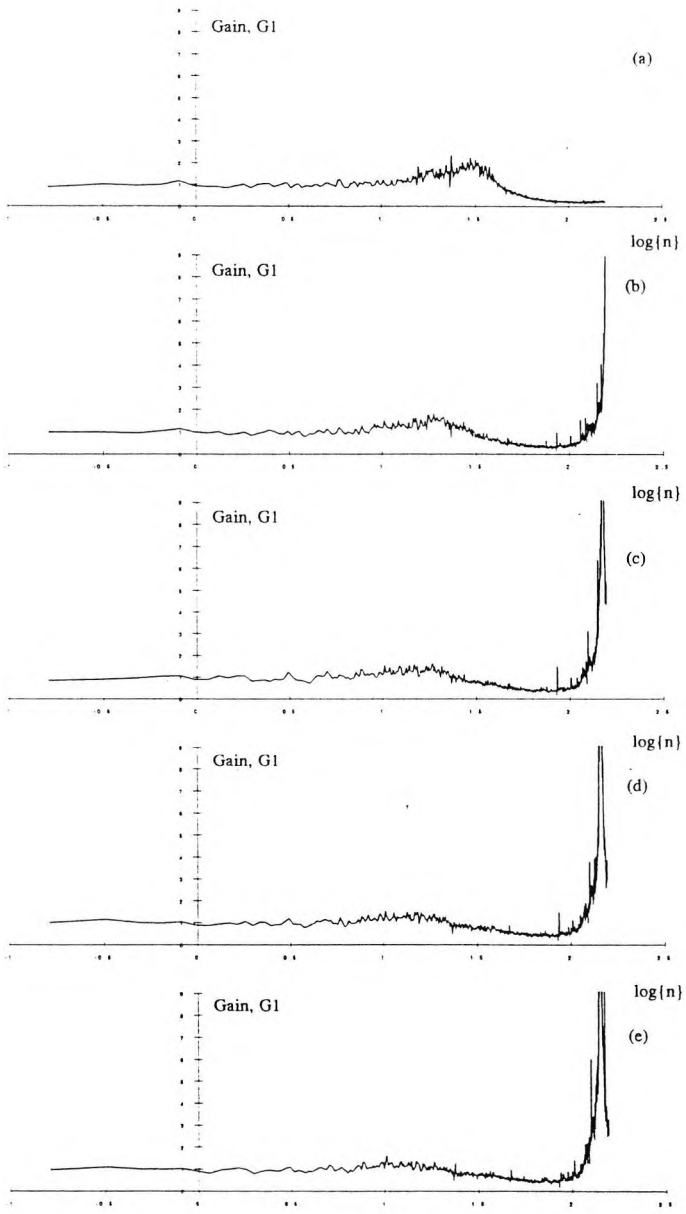

Figure C8: (a) A/13.0/R/90 (b) A/13.0/A/90 (c) A/13.0/B/90
(d) A/13.0/C/90 (e) A/13.0/D/90

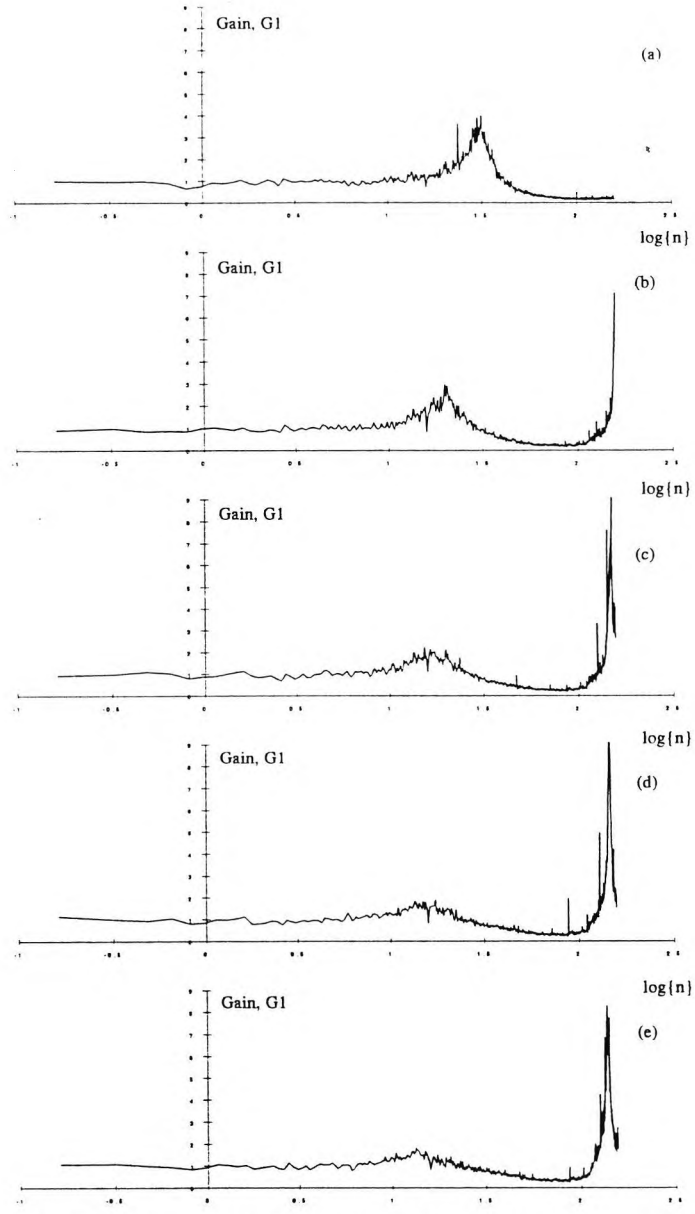

Figure C9: (a) A/13.0/R/135 (b) A/13.0/A/135 (c) A/13.0/B/135
(d) A/13.0/C/135 (e) A/13.0/D/135

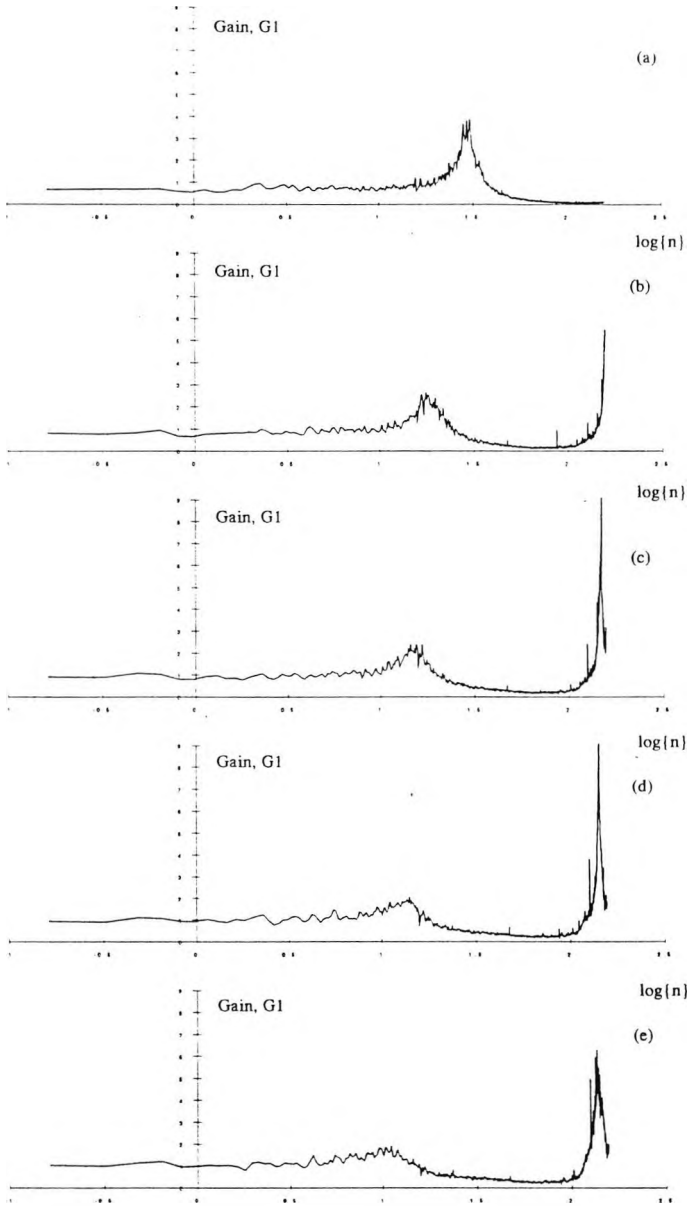

Figure C10: (a) A/13.0/R/180 (b) A/13.0/A/180 (c) A/13.0/B/180
(d) A/13.0/C/180 (e) A/13.0/D/180

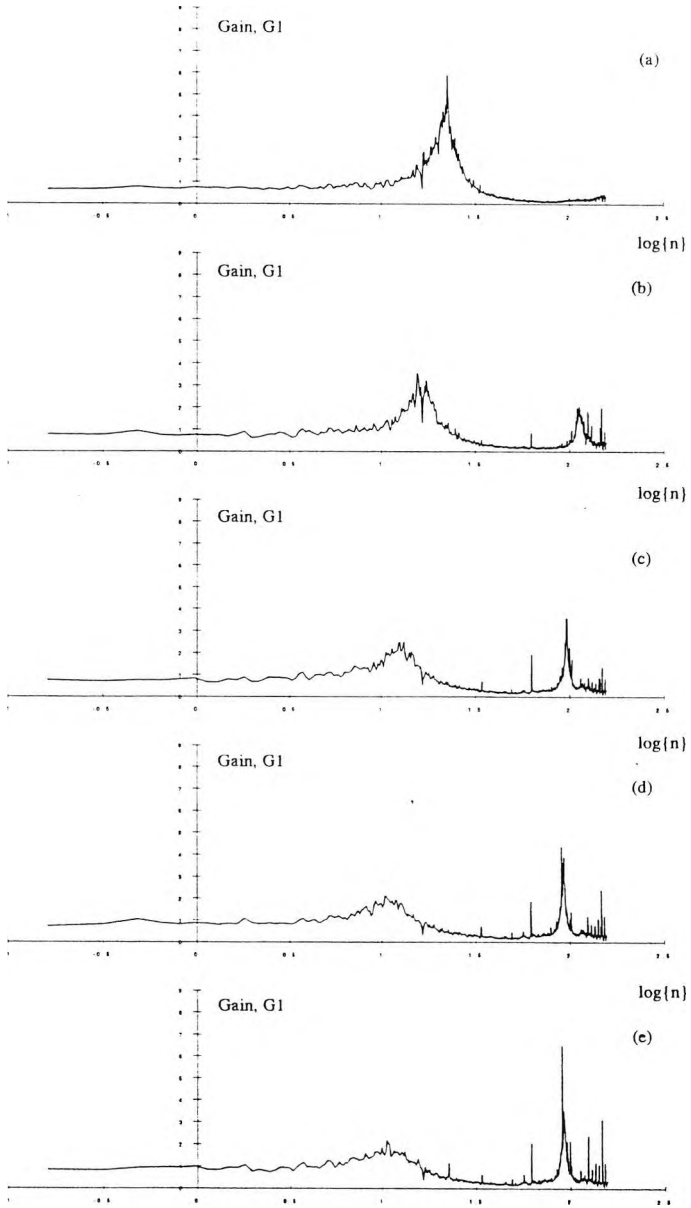

Figure C11: (a) B/9.4 /R/0 (b) B/9.4 /A/0 (c) B/9.4 /B/0
(d) B/9.4 /C/0 (e) B/9.4 /D/0

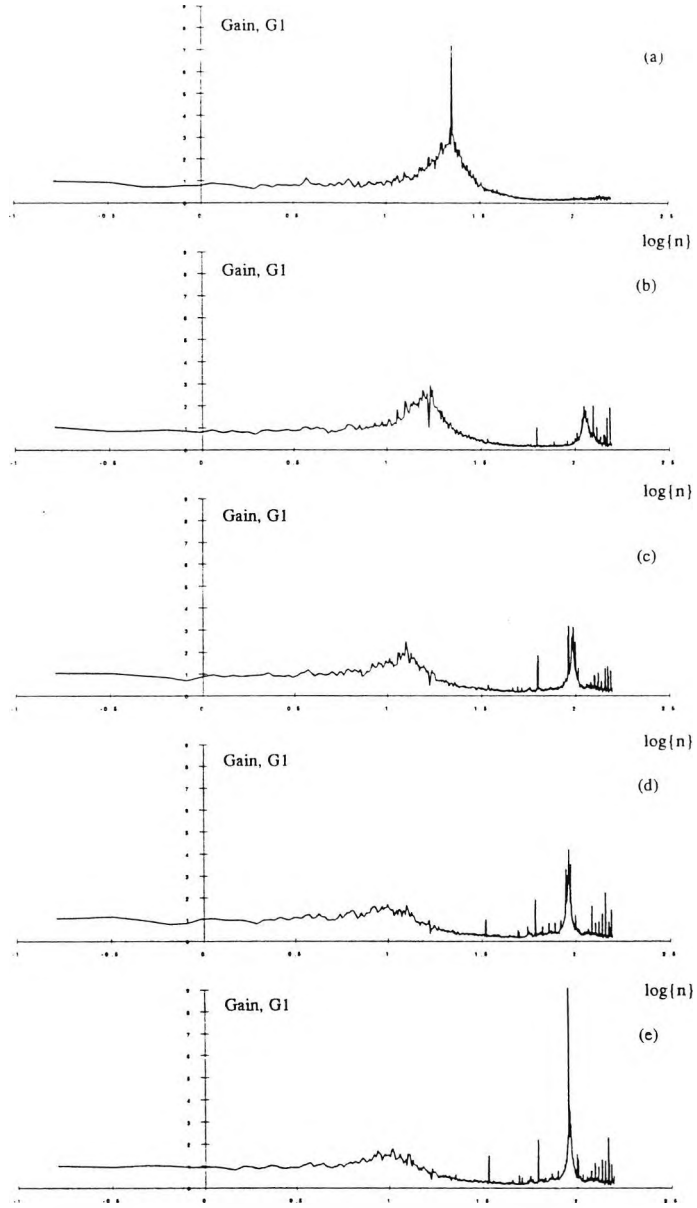

Figure C12: (a) B/9.4 /R/45 (b) B/9.4 /A/45 (c) B/9.4 /B/45
(d) B/9.4 /C/45 (e) B/9.4 /D/45

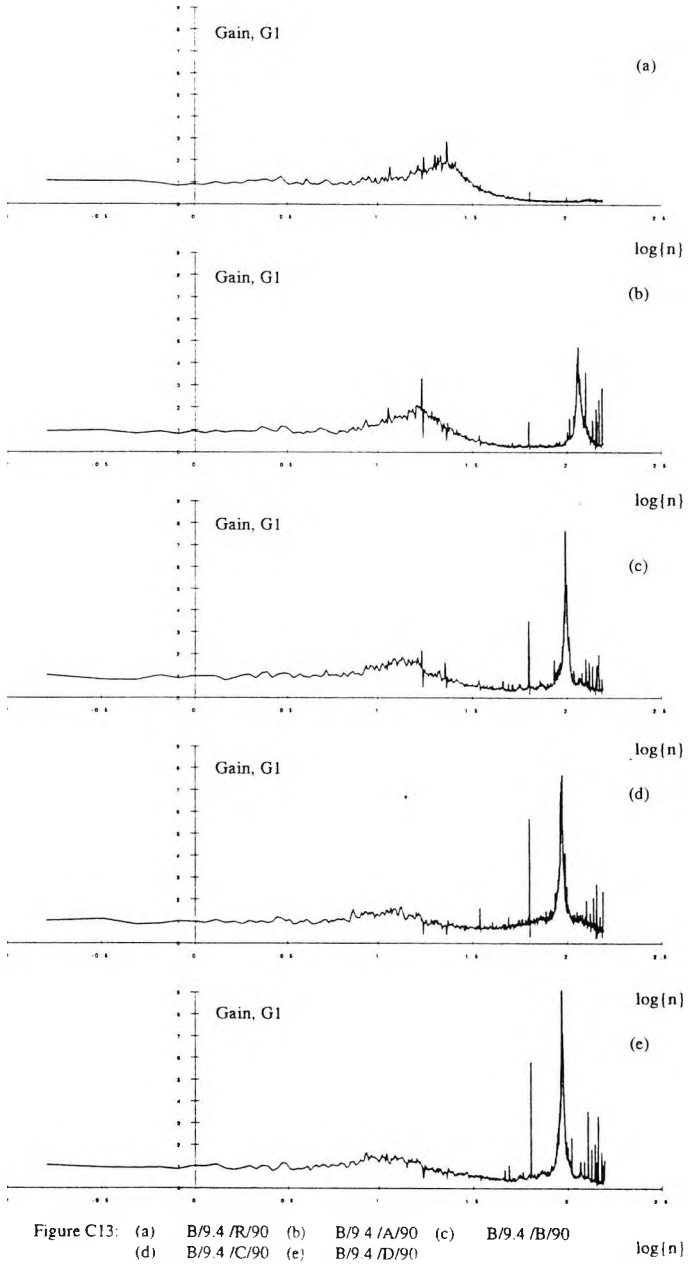

Figure C13: (a) B/9.4 /R/90 (b) B/9.4 /A/90 (c) B/9.4 /B/90
(d) B/9.4 /C/90 (e) B/9.4 /D/90

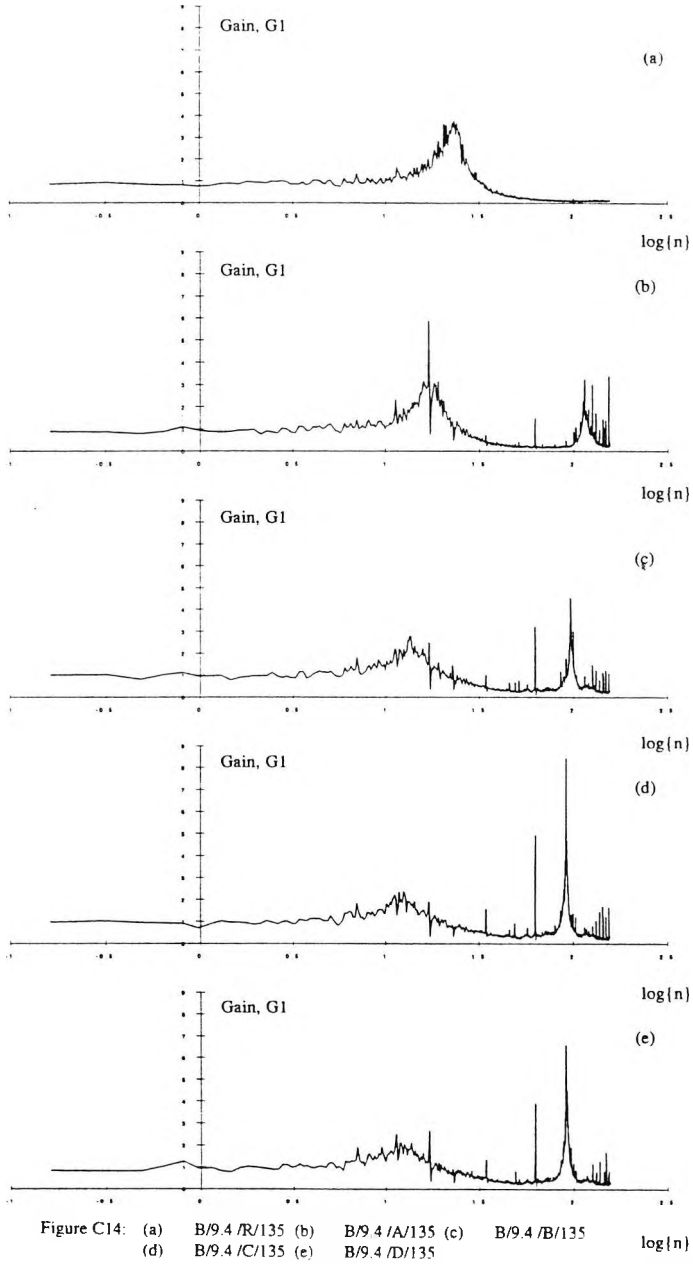

Figure C14: (a) B/9.4 /R/135 (b) B/9.4 /A/135 (c) B/9.4 /B/135
(d) B/9.4 /C/135 (e) B/9.4 /D/135

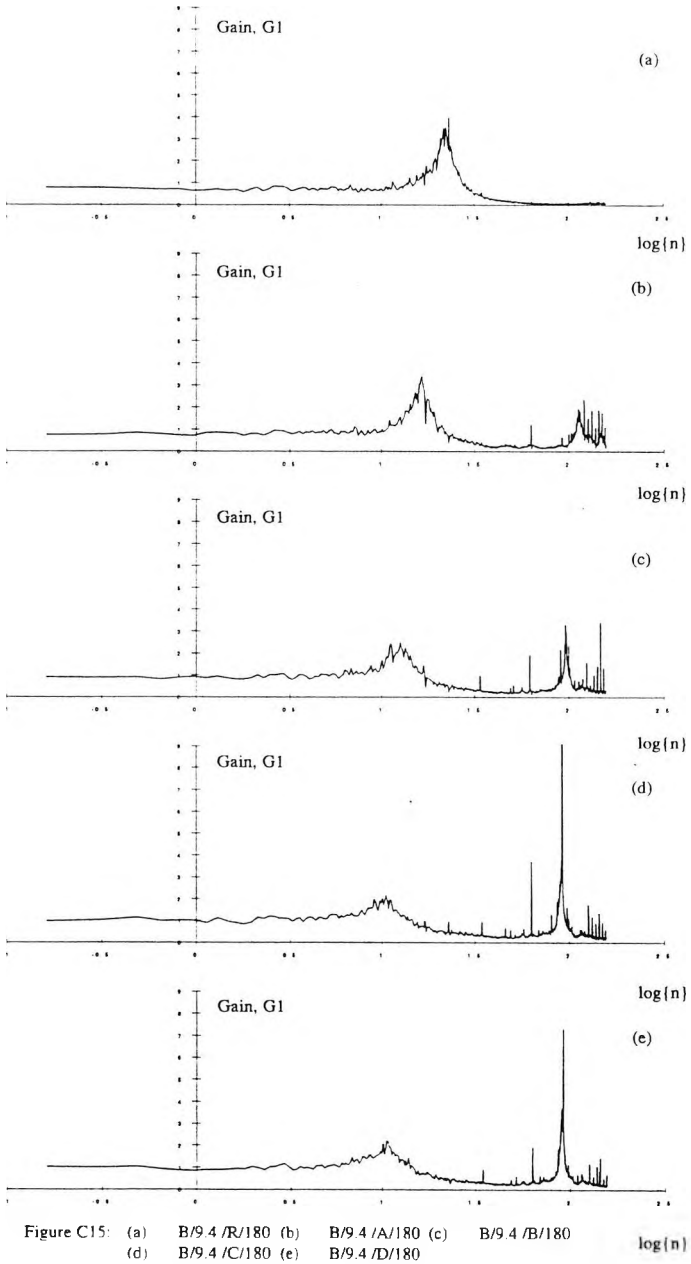

Figure C15: (a) B/9.4 /R/180 (b) B/9.4 /A/180 (c) B/9.4 /B/180
(d) B/9.4 /C/180 (e) B/9.4 /D/180

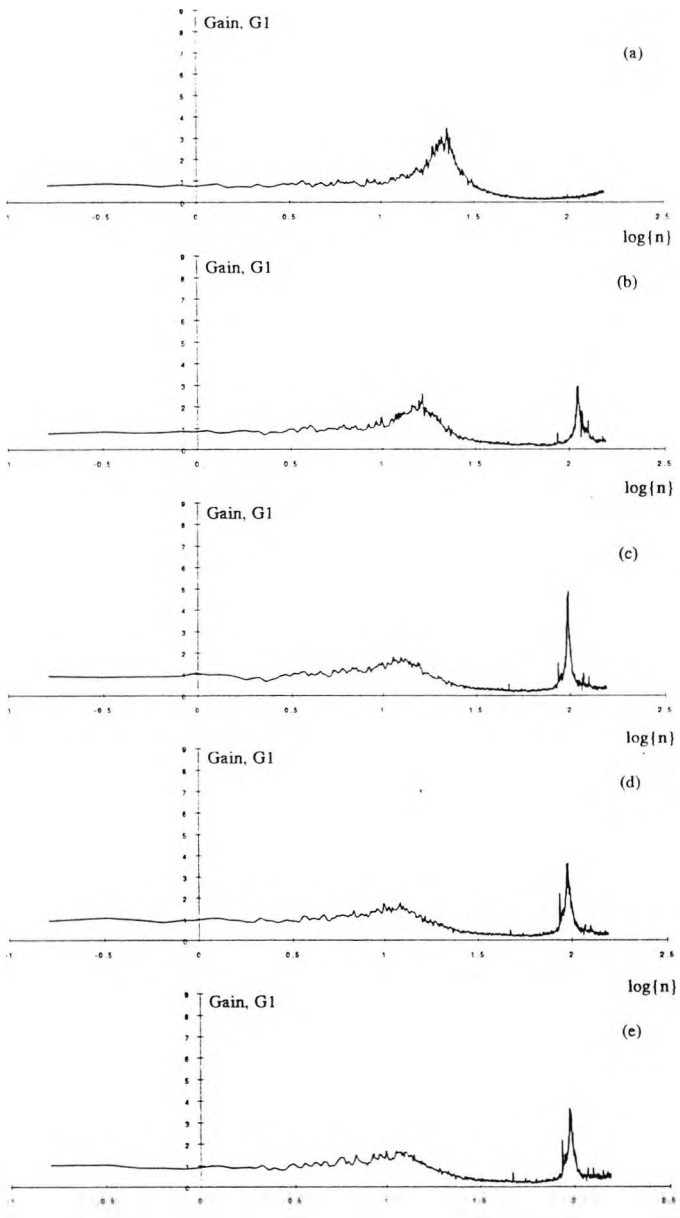

Figure C16: (a) B/13.0/R/0 (b) B/13.0/A/0 (c) B/13.0/B/0
(d) B/13.0/C/0 (e) B/13.0/D/0

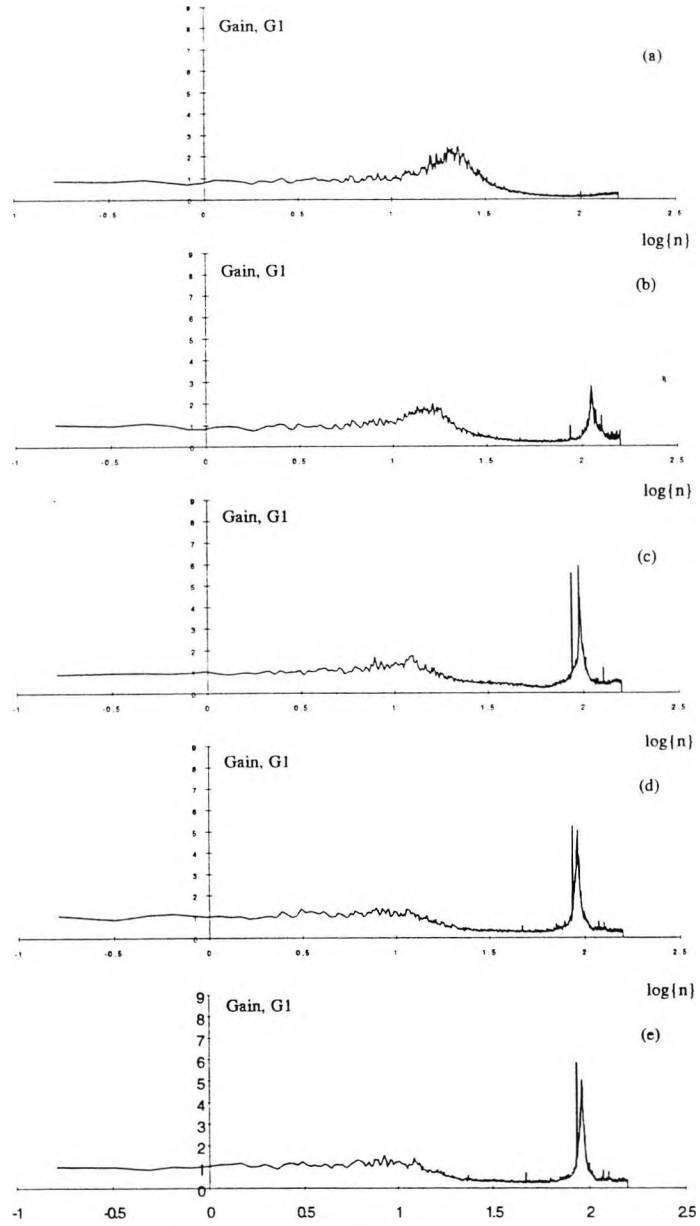

Figure C17: (a) B/13.0/R/45 (b) B/13.0/A/45 (c) B/13.0/B/45
(d) B/13.0/C/45 (e) B/13.0/D/45

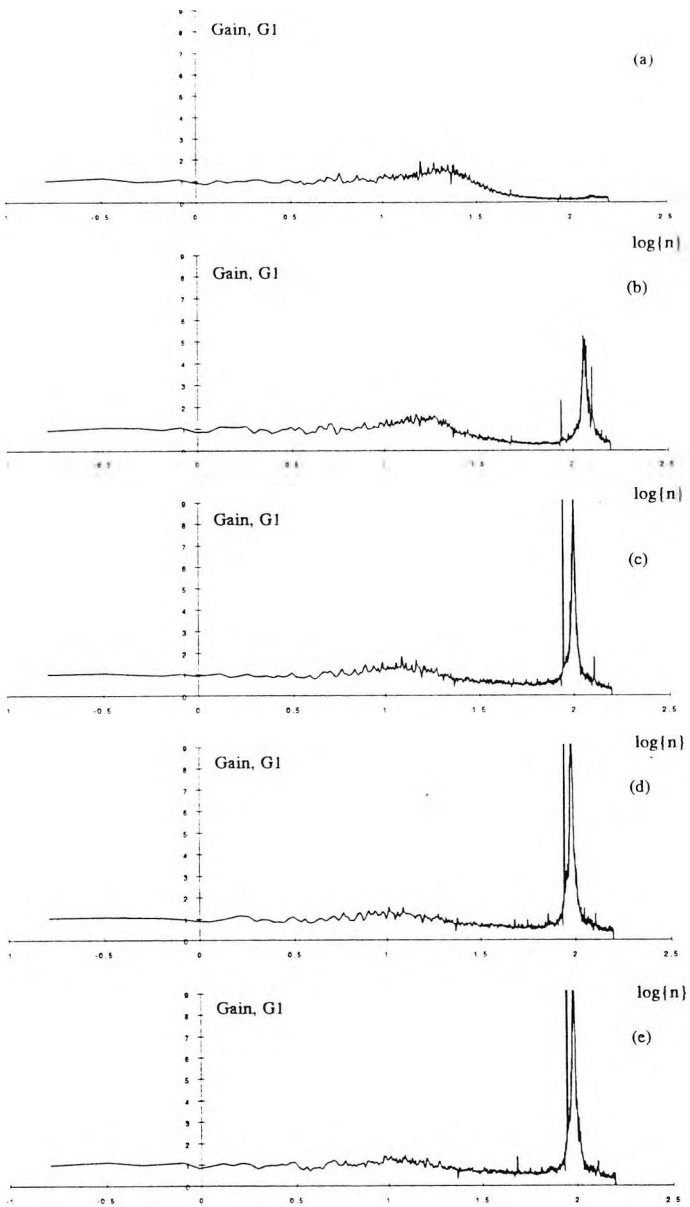

Figure C18: (a) B/13.0/R/90 (b) B/13.0/A/90 (c) B/13.0/B/90 (d) B/13.0/C/90 (e) B/13.0/D/90

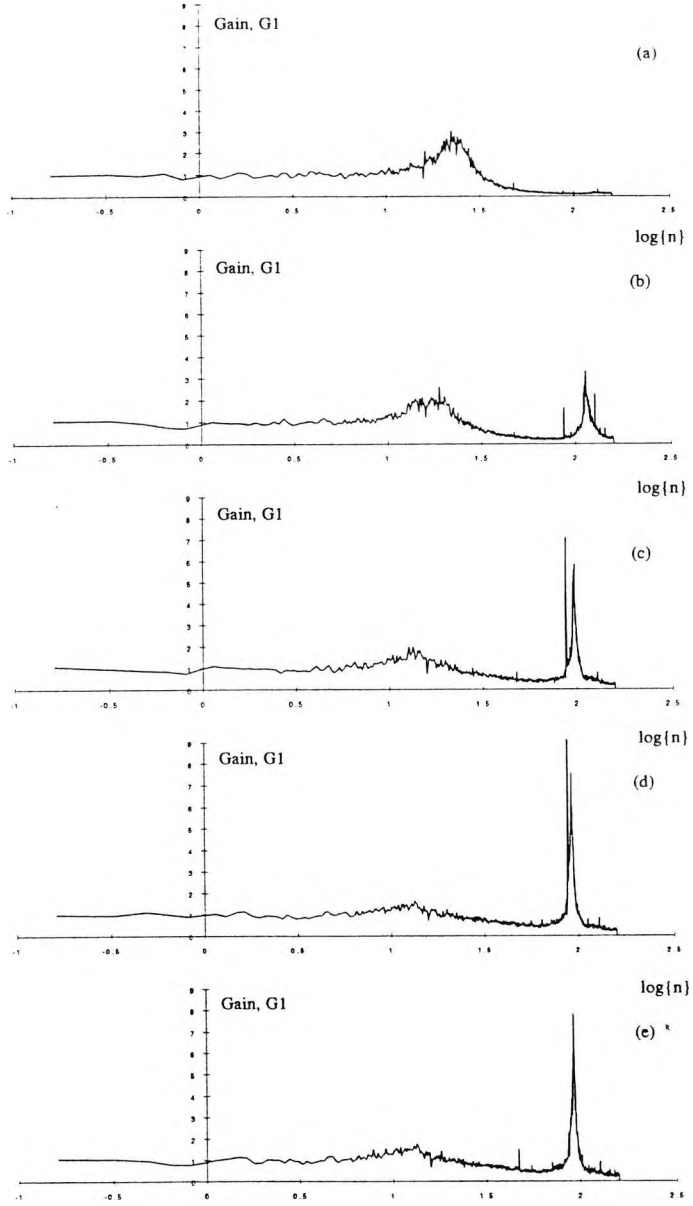

Figure C19: (a) B/13.0/R/135 (b) B/13.0/A/135 (c) B/13.0/B/135 (d) B/13.0/C/135 (e) B/13.0/D/135

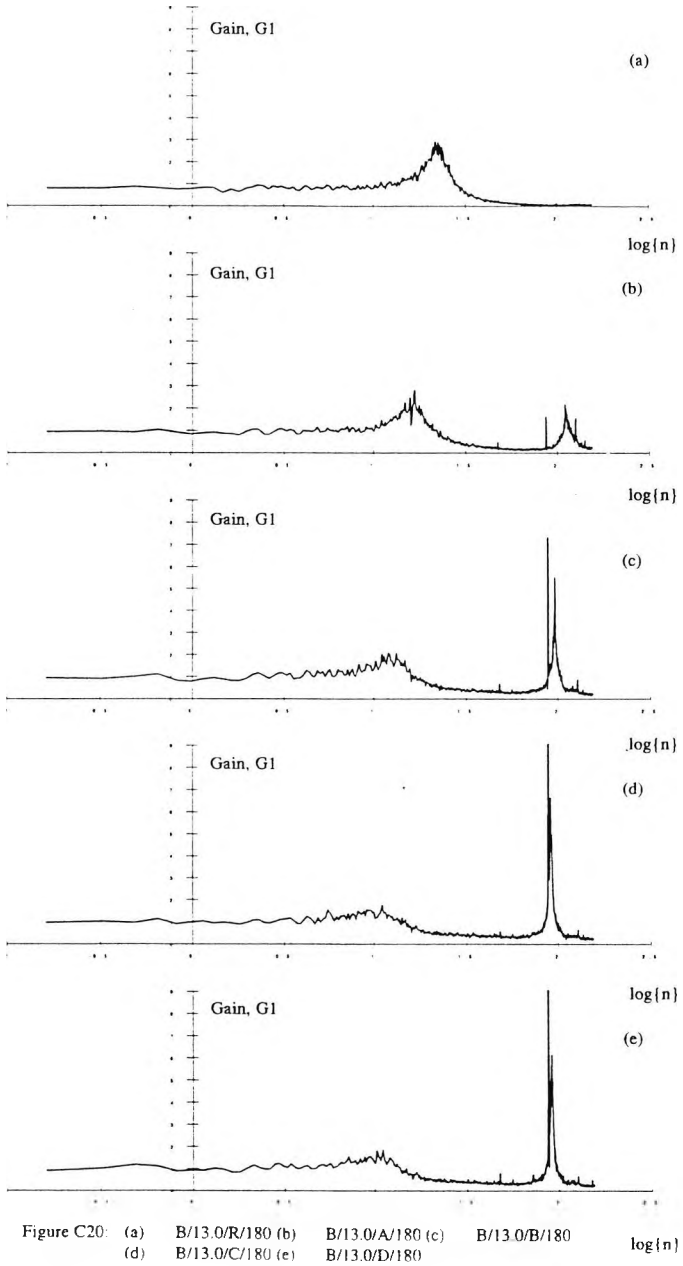

Figure C20: (a) B/13.0/R/180 (b) B/13.0/A/180 (c) B/13.0/B/180
(d) B/13.0/C/180 (e) B/13.0/D/180

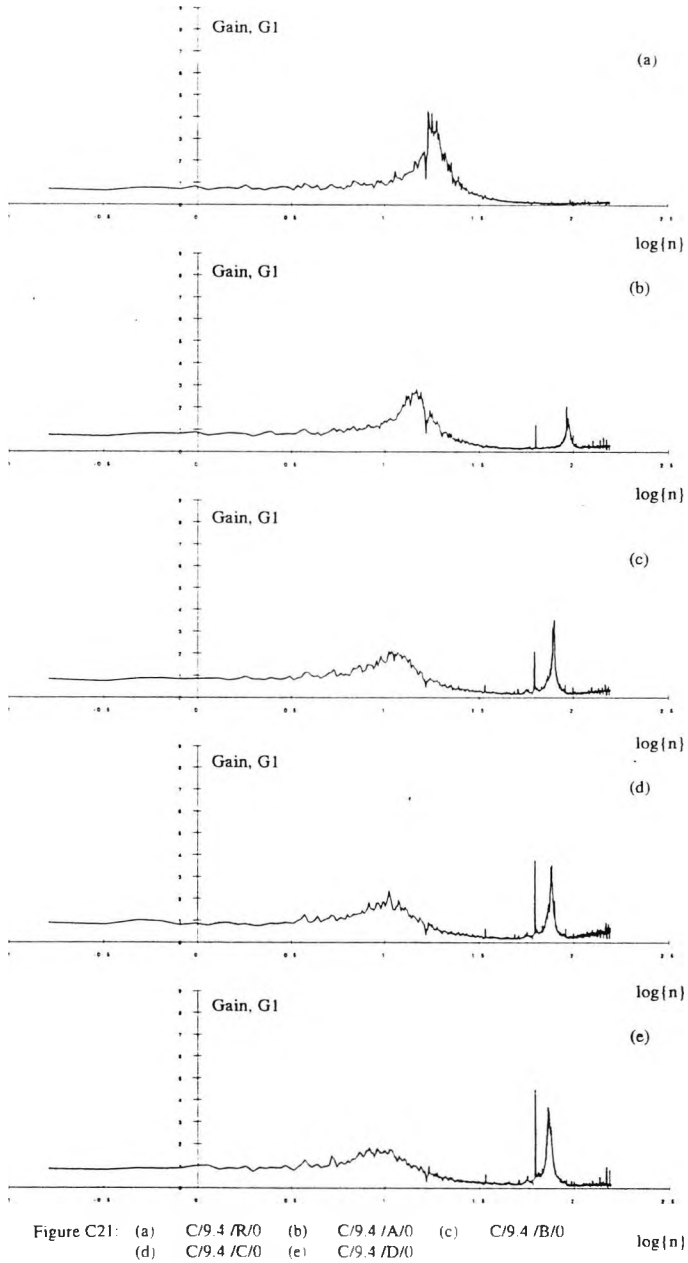

Figure C21: (a) C/9.4 /R/0 (b) C/9.4 /A/0 (c) C/9.4 /B/0
(d) C/9.4 /C/0 (e) C/9.4 /D/0

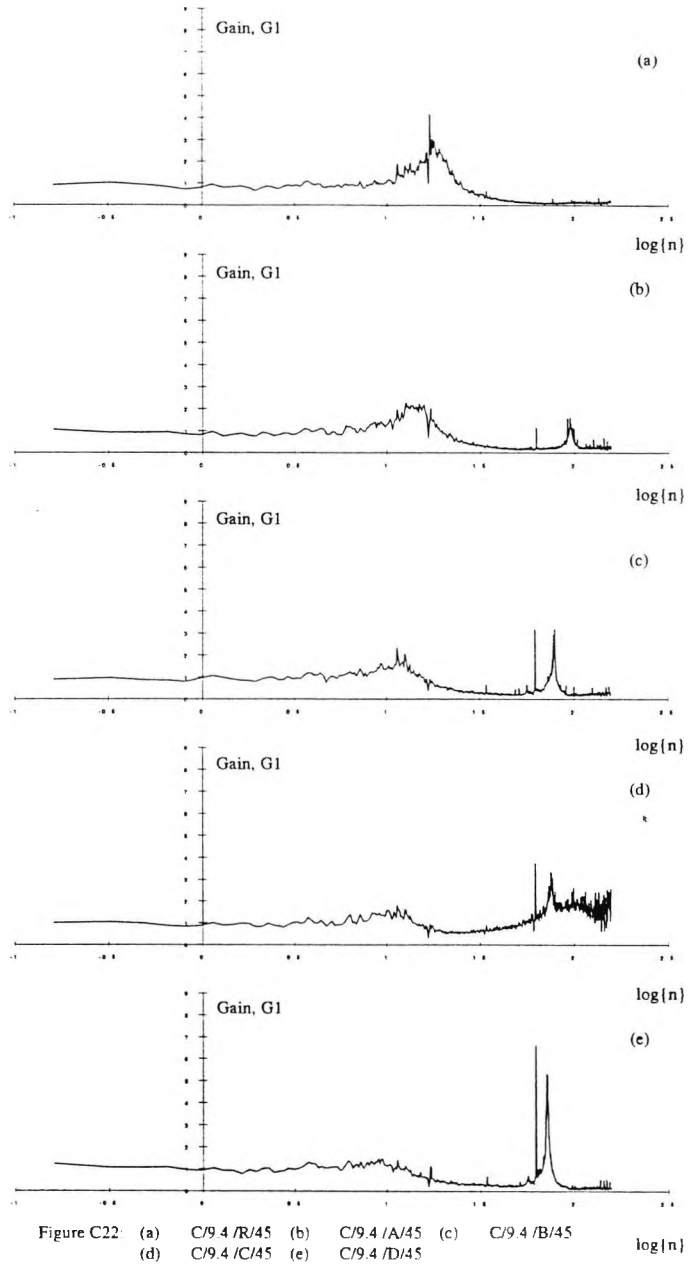

Figure C22: (a) C/9.4 /R/45 (b) C/9.4 /A/45 (c) C/9.4 /B/45
(d) C/9.4 /C/45 (e) C/9.4 /D/45

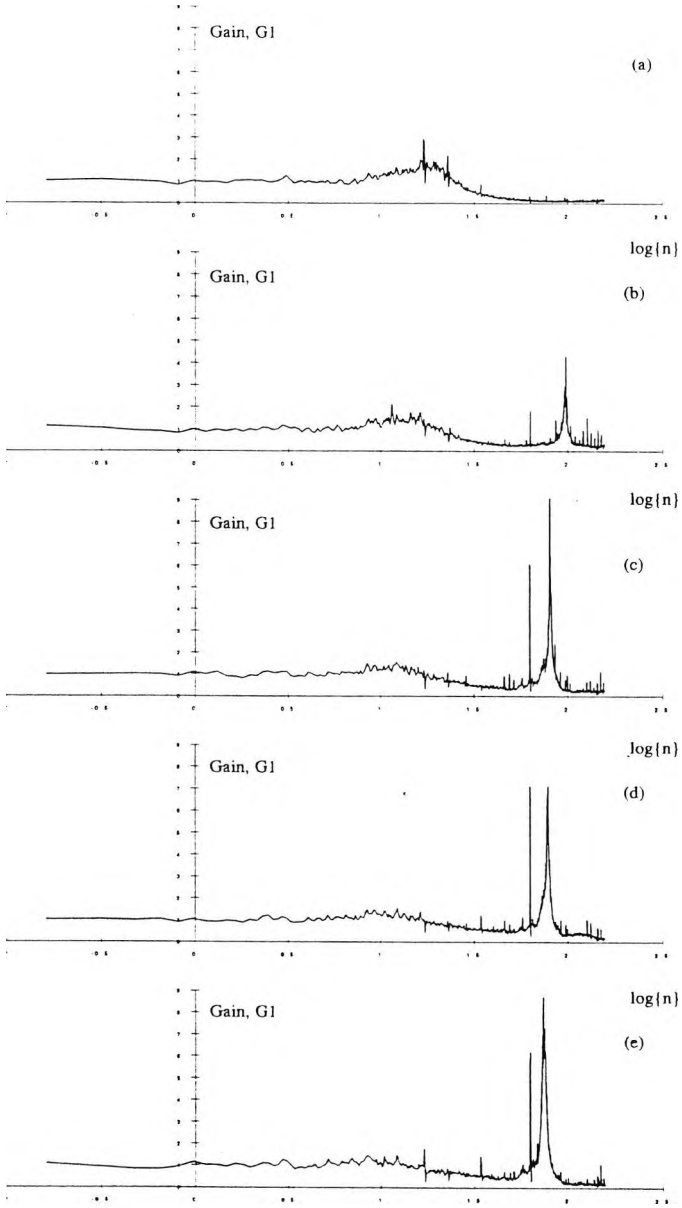

Figure C23: (a) C/9.4 /R/90 (b) C/9.4 /A/90 (c) C/9.4 /B/90
(d) C/9.4 /C/90 (e) C/9.4 /D/90

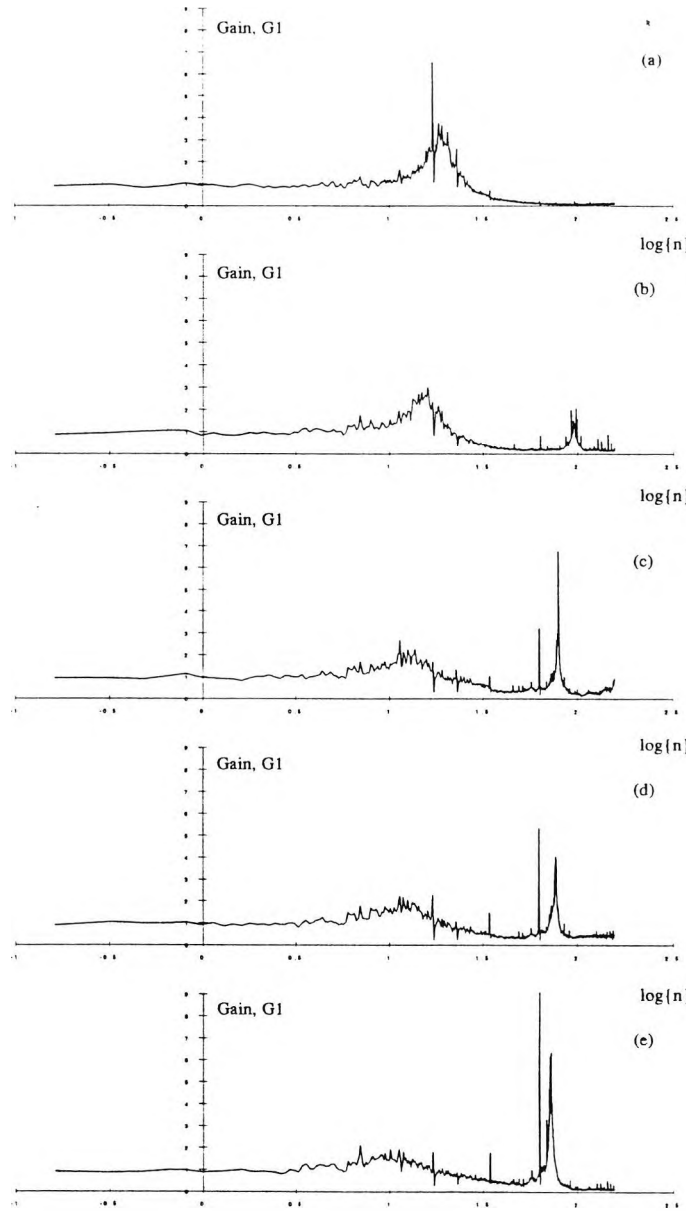

Figure C24: (a) C/9.4 /R/135 (b) C/9.4 /A/135 (c) C/9.4 /B/135
(d) C/9.4 /C/135 (e) C/9.4 /D/135

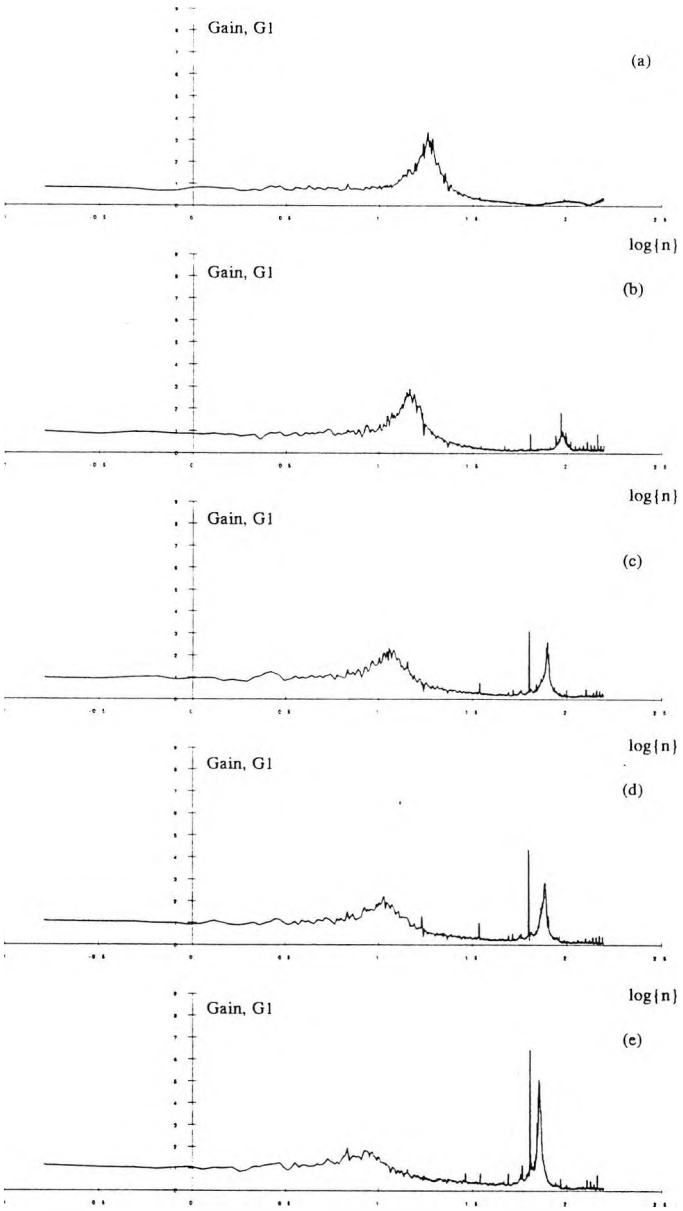

Figure C25: (a) C/9.4 /R/180 (b) C/9.4 /A/180 (c) C/9.4 /B/180
(d) C/9.4 /C/180 (e) C/9.4 /D/180

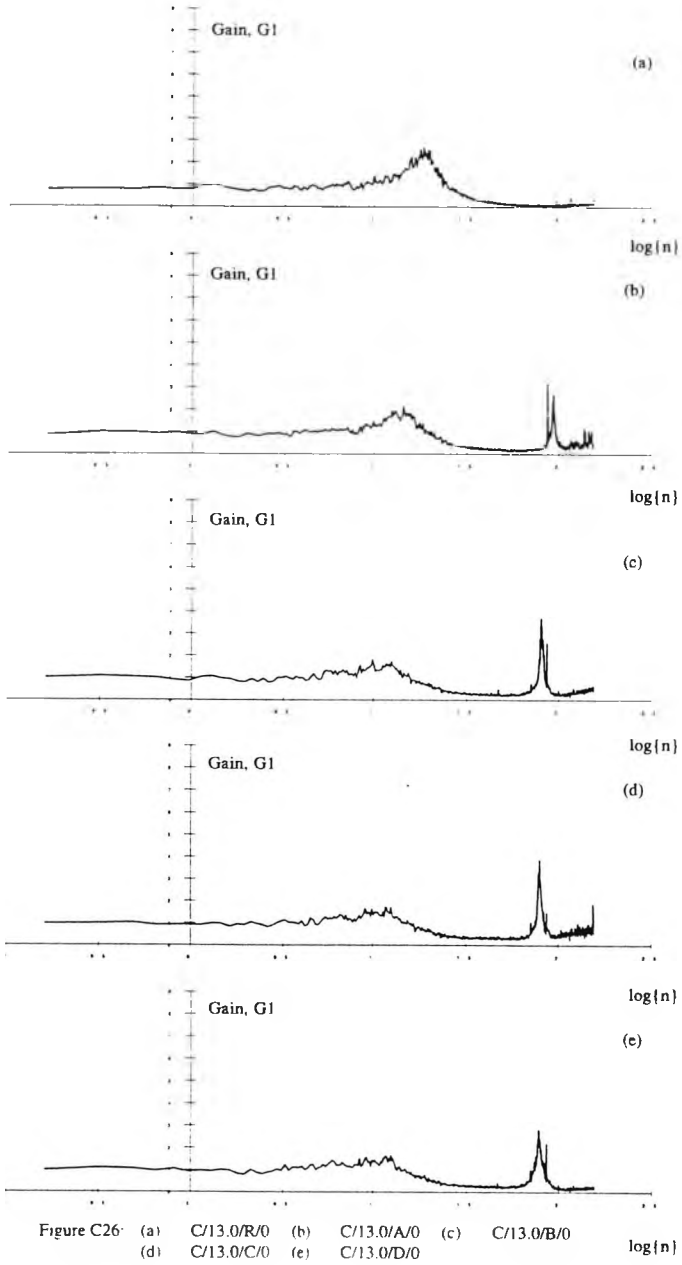

Figure C26: (a) C/13.0/R/0 (b) C/13.0/A/0 (c) C/13.0/B/0
(d) C/13.0/C/0 (e) C/13.0/D/0

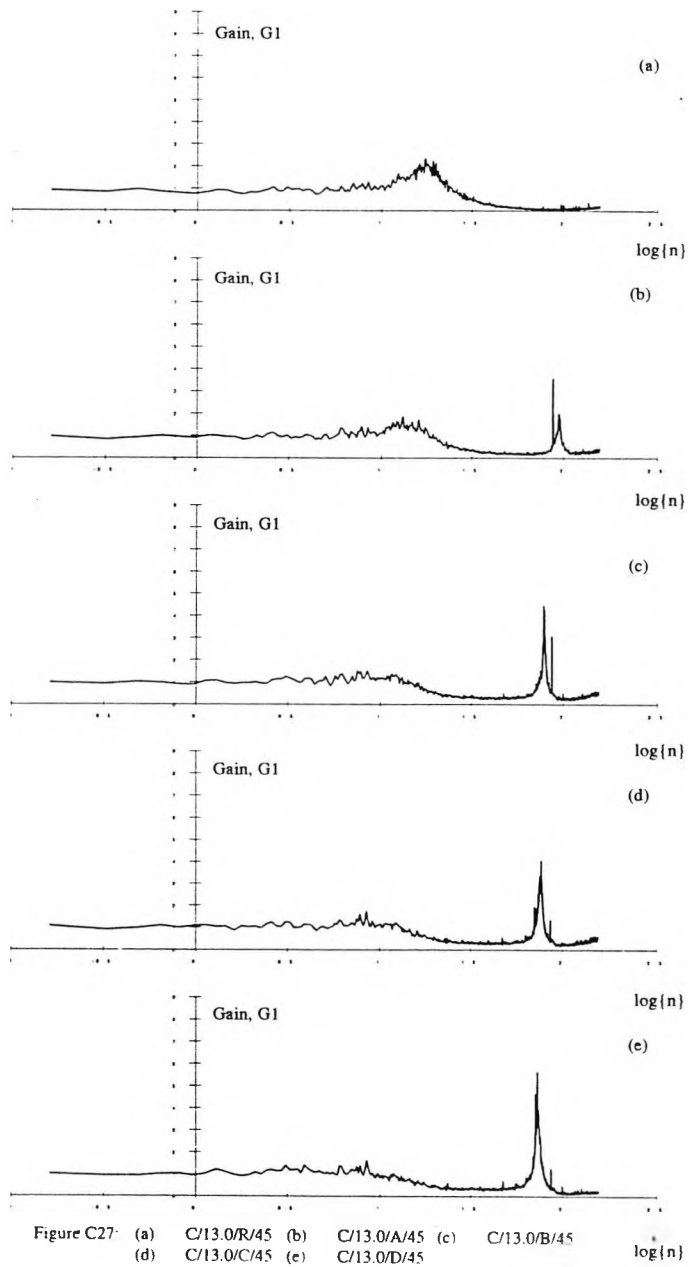

Figure C27: (a) C/13.0/R/45 (b) C/13.0/A/45 (c) C/13.0/B/45
(d) C/13.0/C/45 (e) C/13.0/D/45

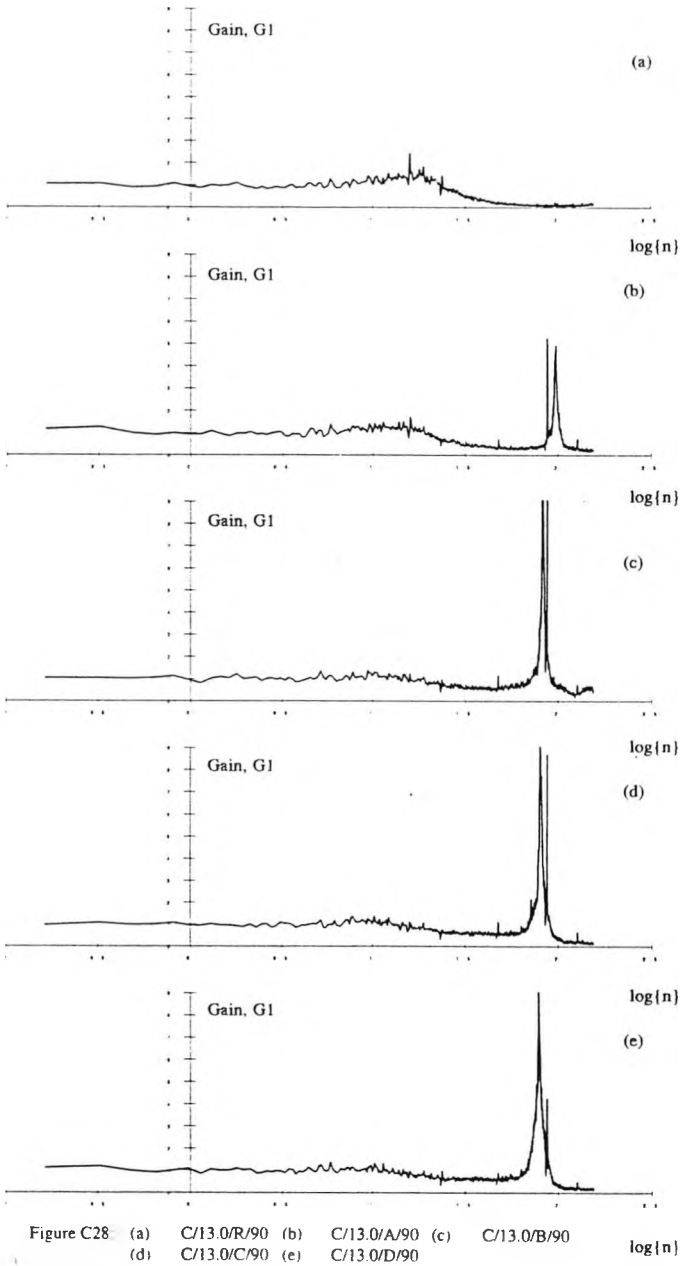

Figure C28: (a) C/13.0/R/90 (b) C/13.0/A/90 (c) C/13.0/B/90
(d) C/13.0/C/90 (e) C/13.0/D/90

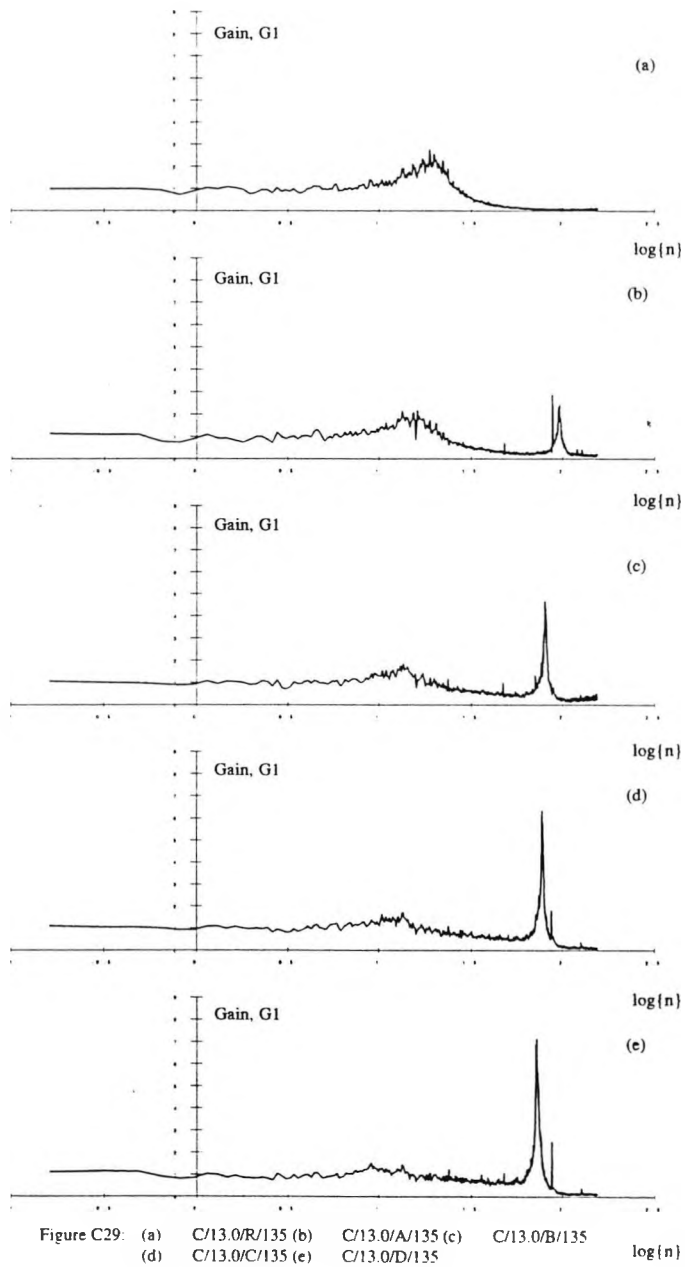

Figure C29: (a) C/13.0/R/135 (b) C/13.0/A/135 (c) C/13.0/B/135
(d) C/13.0/C/135 (e) C/13.0/D/135

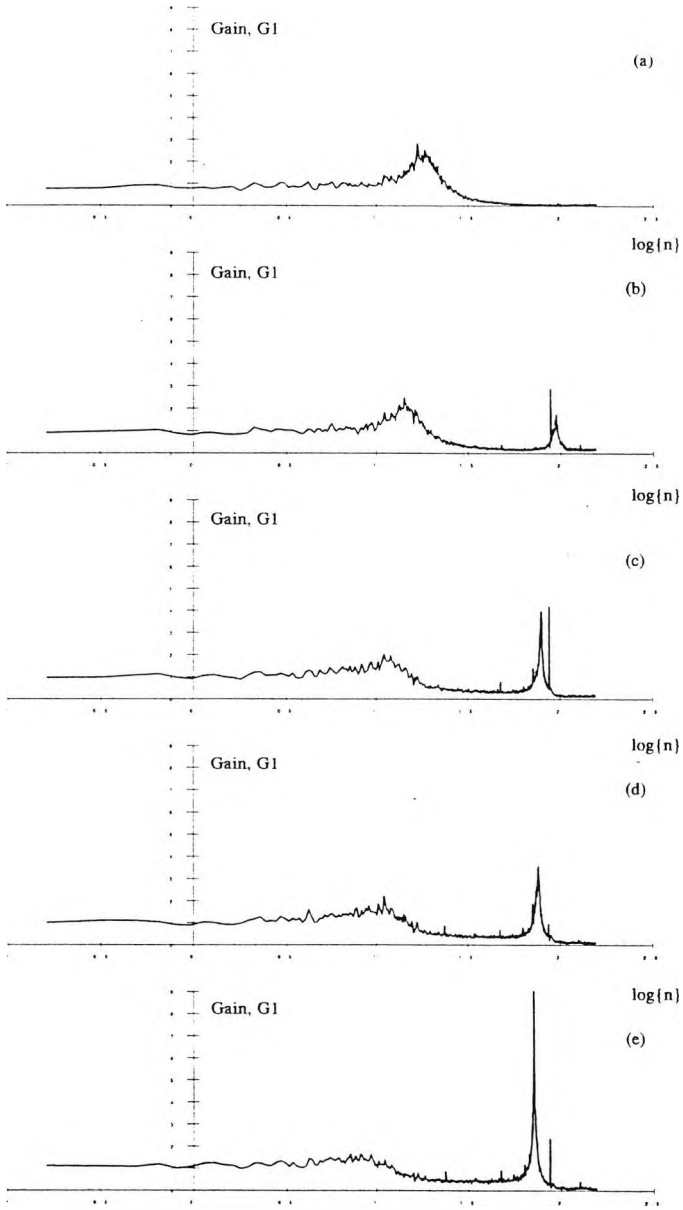

Figure C30: (a) C/13.0/R/180 (b) C/13.0/A/180 (c) C/13.0/B/180 (d) C/13.0/C/180 (e) C/13.0/D/180

Appendix D: Analysis of Extreme Value Data

[D-1] Analysis Procedure

Peak internal and external pressure coefficient data were obtained for selected configurations of model A (see chapter 8). These data were analysed using the method of order statistics which is described in detail below using a set of extreme values, chosen at random.

The data were ranked in ascending order from 1 to N, where N is the total number of extreme data points (N=20 in this example, though the results in chapter 8 utilised 24 extreme values) as shown in table D.1. After ranking the data an estimate of the cumulative distribution function (C.D.F.), P, was obtained from the expression,

$$P = \frac{m}{N+1} \tag{D.1}$$

and subsequently tranformed to the reduced variate, y, where for the Fisher-Tippett Type I distribution

$$y = -\ln\{-\ln[m/(N+1)]\}. \tag{D.2}$$

A graph was then plotted with the reduced variate as abscissa and the corresponding extreme values as ordinates (see figure D.1).

The Fisher-Tippett Type I distribution when plotted against the reduced variate, y, is defined by an equation of the form

$$X = \frac{1}{a}.y + U \tag{D.3}$$

where X are the extreme values, and the parameters 1/a and U are constants called the dispersion and mode respectively and are unique functions of the extreme value distribution. The mode is the value with the greatest likelihood of occurrence and thus corresponds with the peak of the probability density function. The dispersion is a measure of the spread of the data. These two parameters are similar to the more familiar measures of mean and variance which are associated with the Gaussian distribution.

Although it is possible to fit a straight line to the experimental results by the method of least squares this is generally not recommended because of the statistical bias introduced to the data points by the ranking procedure (Lawson, 1980; Cook, 1985). Instead, the numerical approach developed by Lieblein can be employed where the ordered list of extremes is multiplied by the two sets of Lieblein "best linear unbiased estimators" ("B.L.U.E.") to produce two series of values, as shown in the end columns of table D.1. This process is discussed in detail by Cook (1985) where values of the "B.L.U.E." for sets of extremes up to 24 points are presented. A simple summation of the individual columns of Leiblein products enables the mode and dispersion to be quantified and the resulting best-fit line is shown on figure D.1.

	Rank m	C_{pmax}	Probability P=m/(N+1)	Reduced Variate y = -ln(-ln(P))	Lieblein A x C_{pmax}	Lieblein B x C_{pmax}
	1	1.190	0.0476	-1.113	0.132	-0.207
	2	1.239	0.0952	-0.855	0.120	-0.140
	3	1.328	0.1429	-0.666	0.114	-0.096
	4	1.367	0.1905	-0.506	0.107	-0.059
	5	1.421	0.2381	-0.361	0.099	-0.033
	6	1.459	0.2857	-0.225	0.093	-0.013
	7	1.461	0.3333	-0.094	0.086	0.004
	8	1.462	0.3810	0.036	0.080	0.018
	9	1.479	0.4286	0.166	0.074	0.028
	10	1.495	0.4762	0.298	0.069	0.036
	11	1.517	0.5238	0.436	0.065	0.044
	12	1.540	0.5714	0.581	0.060	0.049
	13	1.569	0.6190	0.735	0.056	0.055
	14	1.575	0.6667	0.902	0.053	0.060
	15	1.599	0.7143	1.089	0.048	0.062
	16	1.647	0.7619	1.302	0.043	0.066
	17	1.716	0.8095	1.554	0.039	0.070
	18	1.727	0.8571	1.870	0.034	0.071
	19	1.756	0.9048	2.302	0.032	0.070
	20	1.824	0.9524	3.020	0.027	0.071
N = 20	Mean	1.519		Totals	**1.433**	**0.159**
	Std.devn. S_y	0.028			MODE, U	DISPN., 1/a

Table D.1: Example of the analysis of extreme internal pressure coefficients.

The mean and variance for the set of twenty data points was also calculated and following the procedure outlined by Lawson (1980) it was possible to determine the 99.7% confidence limits associated with the data shown in table D.1. These limits are plotted on figure D.1. According to Lawson (1980), Gumbel found that the distribution of the extreme values at a single value of the reduced variate, y, was Gaussian with a variance that could be approximated by

$$\sigma_x^2 = \frac{\{0.2643+0.1166y+0.6687y^2)S_x^2}{N} \qquad (D.4)$$

where S_x is the standard deviation of the set of extremes. So, if the value of S_x for a set of N extreme values is known then the variance of the extremes at each value of y can be calculated and confidence limits set which bound a specified percentage of all the expected readings, for example, it would be expected that

68.0% of all readings lie within the limits of $X_y + \sigma_x$

95.0% of all readings lie within the limits of $X_y + 2\sigma_x$

99.7% of all readings lie within the limits of $X_y + 3\sigma_x$

where X_y is the magnitude of the ordinate at a value of y and σ_x the standard deviation of X_y.

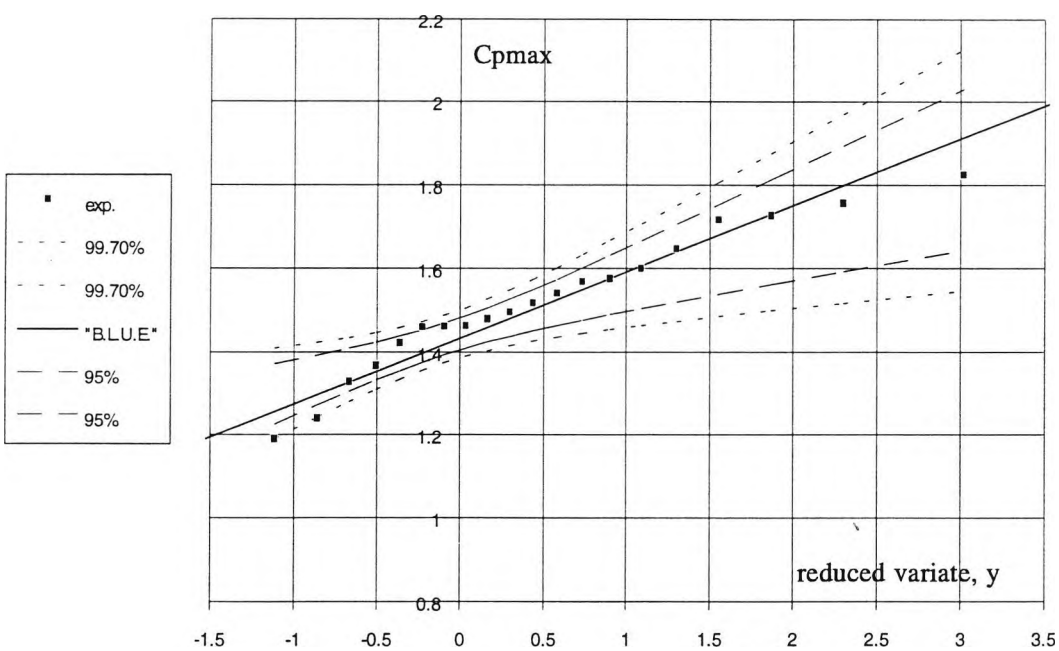

Figure D.1: F.T.1. plot of the data shown in table D.1; the "B.L.U.E." line and confidence limits are also shown.

Appendix E: Membrane Roof Deflections

[E-1] Introduction

A brief summary and description of the results from a limited series of wind tunnel tests on model A is presented where the deflection of the roof membrane was monitored at a single location.

[E-2] Experimental Details

The deflections of the membrane roof were monitored for cavity volume C only. A "Kaman" non-contact displacement transducer was used to sense the motion of the roof via the deflections of a small annulus, made from thin foil, that was attached to the membrane. Tests showed that the transducer response was linear over a range from 0 to around 3.1mm for an annulus with an internal diameter of 10mm and an outer diameter of 12.5mm. The sensitivity of the transducer to such an annular target was around 5mm/volt. The restricted linear range of the displacement transducer dictated that the foil target should be located away from the centre of the roof. The output from the displacement transducer was amplified by a factor of approximately three prior to recording on the FM tape recorder.

In order to further optimise the range of the transducer it was necessary to change the offset distance between the target foil and the transducer head depending upon the model configuration under test. For example, those configurations where the mean membrane deflection was likely to be negative (i.e. when $\phi=90^{o}$) required a large initial offset, whereas, positive deflections dictated a small initial offset.

In general, this procedure appeared to produce satisfactory results, however, those cases where the mean deflection was high, say greater than 1mm, were likely to be in error because of their associated extremes. Large positive deflections were likely to be non-linear with transducer output, whereas, large negative deflections were limited by contact between the membrane and the head of the transducer. Fortunately, the lightweight of the vibrating membrane was insufficient to cause damage to the tranducer.

[E-3] Results

The author was concerned with the quality of the data obtained when the membrane was at its most flexible, tensions C and D, and in particular for the cases when the opening

was oriented at azimuth angles of 0° and 90°., corresponding with the occurrence of maximum mean positive and negative deflections respectively. For these reasons the membrane deflection results were not included in the main body of this thesis. However, Table E.1 summarises the first four moments of the deflection data for different model configurations.

[E-3-1] Mean , R.m.s., Skew & Kurtosis of the Membrane Deflections

		9.4 m/s				13.0 m/s			
	ϕ^o	mean	r.m.s.	skew	kurtosis	mean	r.m.s.	skew	kurtosis
Ta	0	.3136	.115	.56	3.44	.5920	.1842	.43	3.01
	45	.1081	.1014	.49	3.60	.2186	.1789	.44	3.39
	90	-.1915	.0666	-.48	3.40	-.3587	.1100	-.31	3.14
	135	-.0341	.0557	-.27	3.75	-.0653	.0976	-.16	3.16
	180	.0750	.0557	.02	3.45	.1457	.0946	.04	3.29
Tb	0	.7528	.3111	.03	2.60	1.320	.3111	.03	2.60
	45	.2523	.2429	.35	3.69	.5006	.3947	.21	2.80
	90	-.4892	.1446	-.37	3.40	-.8818	.2285	-.30	6.41
	135	-.1051	.1281	.82	42.37	-.1859	.2013	-.61	10.89
	180	.1480	.1109	-.01	3.50	.2836	.1799	-.01	0.49
Tc	0	.1755	.1264	.04	3.18	.3226	.2033	-.10	2.95
	45	-.1295	.1393	-.20	3.23	N/A	N/A	N/A	N/A
	90	N/A	N/A	N/A	N/A	N/A	N/A	N/A	N/A
	135	.3171	.2901	.31	3.37	.5930	.4453	.12	2.62
	180	.9286	.2685	0.21	2.75	1.532	.3094	-.12	2.64
Td	0	1.318	.3457	.11	2.66	2.084	.3588	-.24	2.70
	45	.4793	.4000	.38	2.74	.8823	.5945	.09	2.36
	90	-.7348	.2076	-.35	3.14	-1.325	.3076	-.06	2.83
	135	-.1651	.1709	-.23	3.22	-.3204	.2892	-.21	2.98
	180	.2248	.1412	-.16	3.01	.3696	.2117	-.43	3.15

Table E.1: Membrane deflection data (in mm) for cavity volume C

The displacement transducer was located on a radius that was 0.16D from the centre of the roof of the model so that when the opening was at an azimuth angle of 0°, 45°, 90°, 135° & 180° the corresponding azimuth angles of the transducer were 163.3°, 118.3°, 73.3°, 28.3° & 16.7° respectively (angles measured from the windward generator).

Both the mean and root-mean-square deflections increased when the mean windspeed was increased. The magnitude of the mean membrane deflection was largely dependent upon the location of the opening with the largest mean uplifts occurring when the opening was orientated to windward and large mean downward motions occurring for ϕ equal to 90°. The standard deviation of the membrane deflection generally reduced as the opening was moved from windward to leeward, a trend that was qualitatively similar

to that observed in the magnitude of the internal pressure fluctuations. The mean suction which acted over the roof resulted in a net uplift on the membrane when the opening was in the base region of the model and the mean internal pressure was only slightly negative.

[E-3-2] Spectra

Deflection spectra were computed in the same way as the pressure spectra so that each was an ensemble average of fifty separate spectra; spectra were normalised by the variance of the deflection and plotted as the product of frequency and normalised spectral density versus the logarithm (base 10) of frequency (figures E.1 to E.4).

For all the configurations the roof responded to the low frequency broad-band turbulent buffetting component that was evident in the cavity pressure spectrum; this component of the cavity pressure had its origins in the pressure fluctuations that occurred on the external walls of the model. Indeed it appeared that the energy apparent at high frequencies in the pressure spectra measured on the surface of the rigid roof of the model had little effect on the membrane deflection spectra.

The resonant phenomenon of Helmholtz oscillation was apparent for most opening azimuth angles apart from the 90° case where, as for the cavity pressure fluctuations, this mode was heavily damped. Moving the opening from 90° to either windward or leeward increased the resonant response of the Helmholtz oscillation.

A second higher frequency mode was apparent on each of the frequency domain plots but the energy it contained was negligible compared with that due to both turbulent buffetting and Helmholtz oscillation. It was noted that increasing the mean windspeed generally reduced the energy contained in the Helmholtz mode of vibration. These trends were in general agreement with those reported in chapter 7 where the cavity pressure spectra were described.

[E-4] Summary

A non-contact displacement transducer was used to measure the motion of the membrane roof at a single point, however, reservations about the linear range of this transducer lead the author to include the roof deflection data as a brief appendix only. Extreme value membrane deflections were not presented. The roof deflection was monitored on the model configured with cavity volume C only.

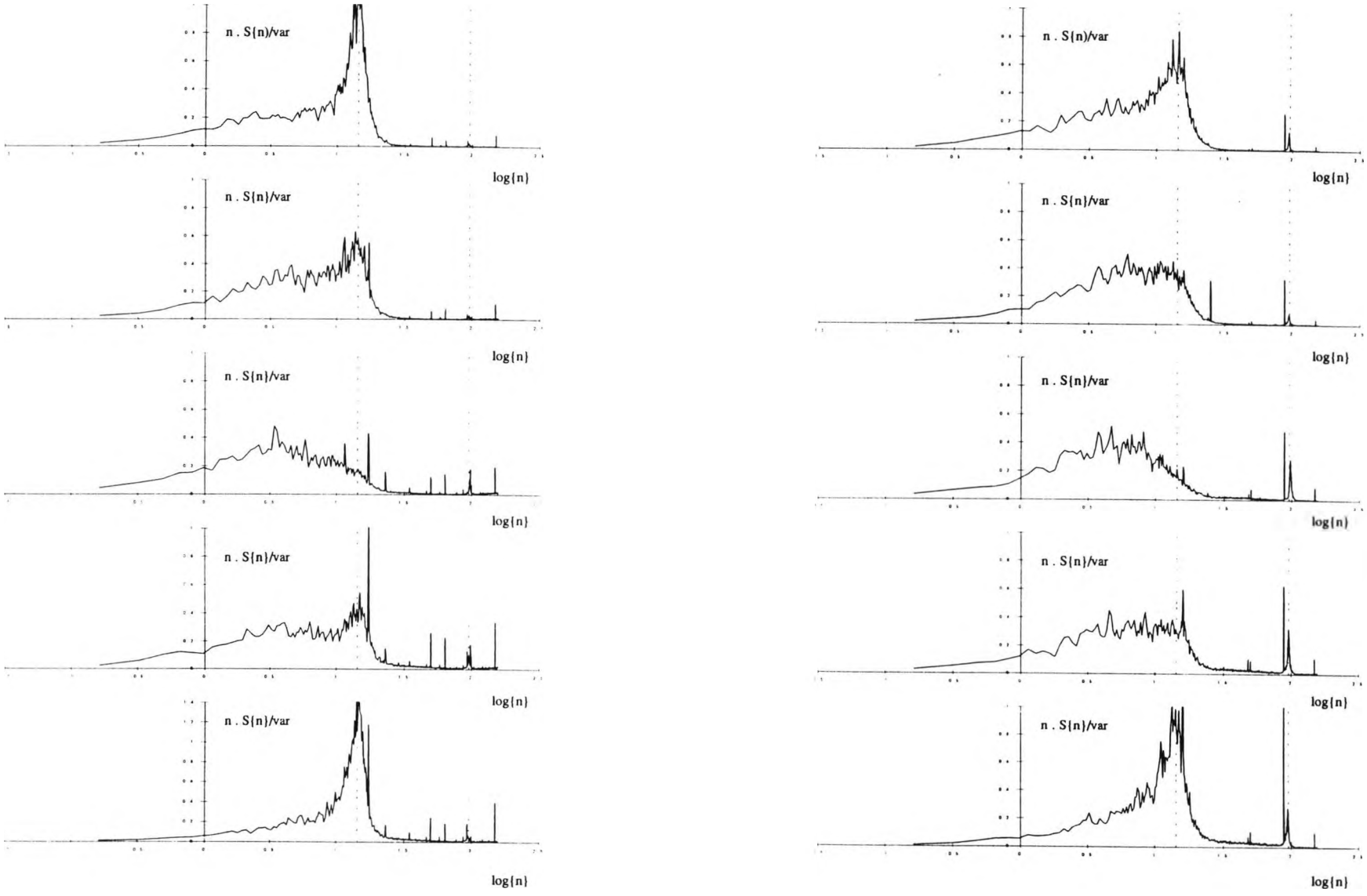

Figure E.1: Membrane deflection spectra for cavity volume C, membrane tension T_a and ϕ= 0° (top) to 180° (bottom); l.h.s. U_{ref}=9.4m/s, r.h.s. U_{ref}=13.0m/s.

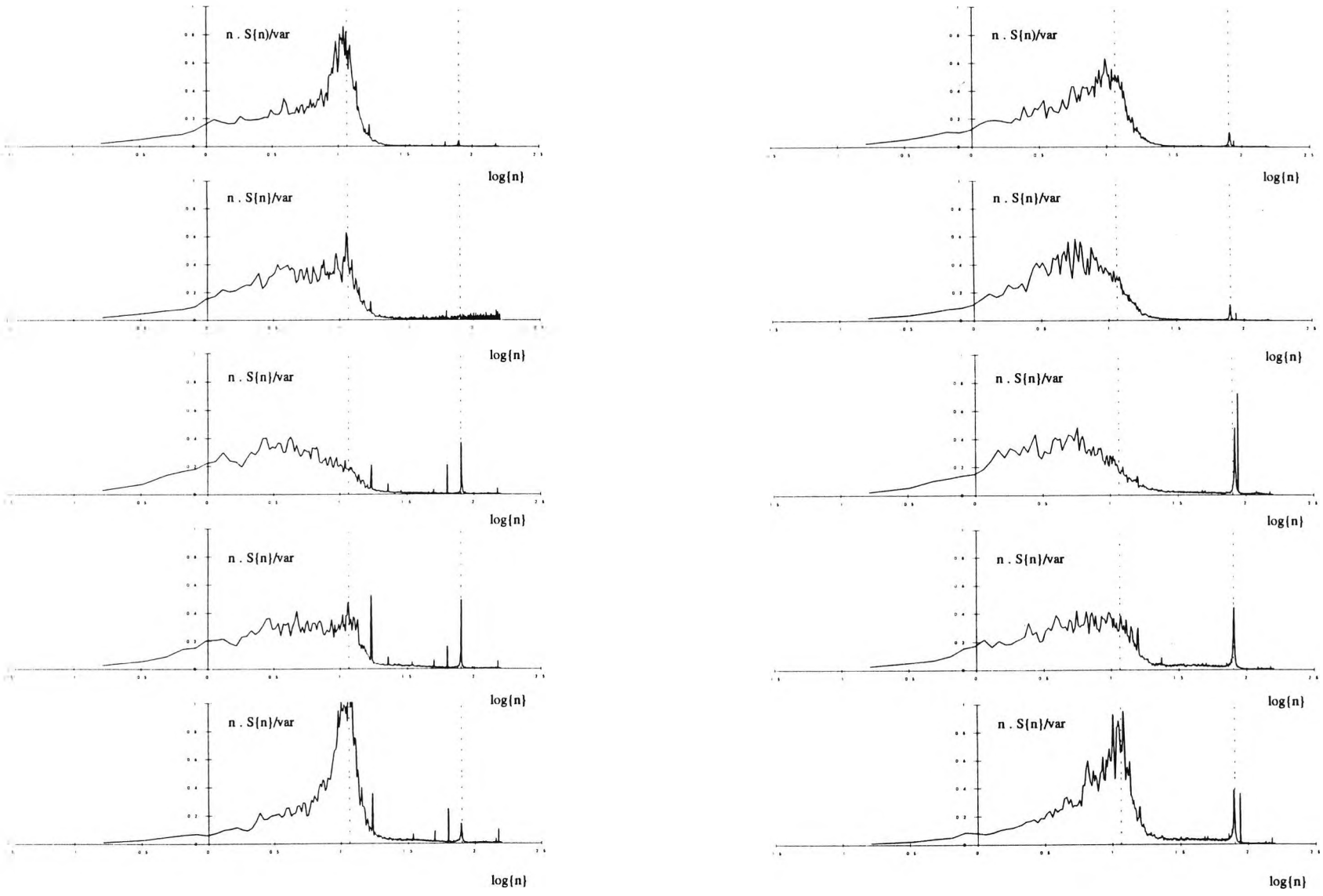

Figure E.2: Membrane deflection spectra for cavity volume C, membrane tension T_b and ϕ= 0° (top) to 180° (bottom); l.h.s. U_{ref}=9.4m/s, r.h.s. U_{ref}=13.0m/s.

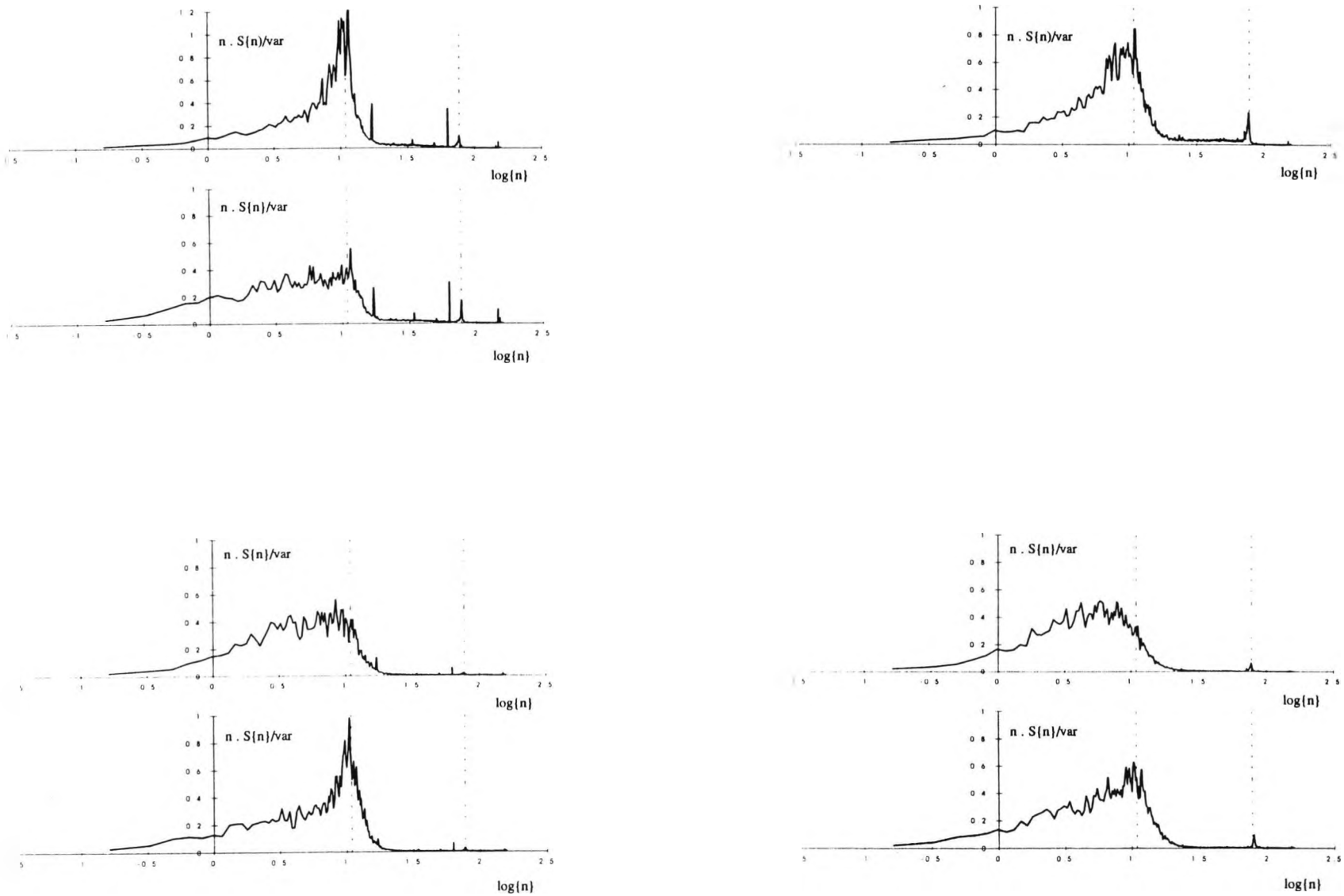

Figure E.3: Membrane deflection spectra for cavity volume C, membrane tension T_c and ϕ= 0° (top) to 180° (bottom); l.h.s. U_{ref}=9.4m/s, r.h.s. U_{ref}=13.0m/s.

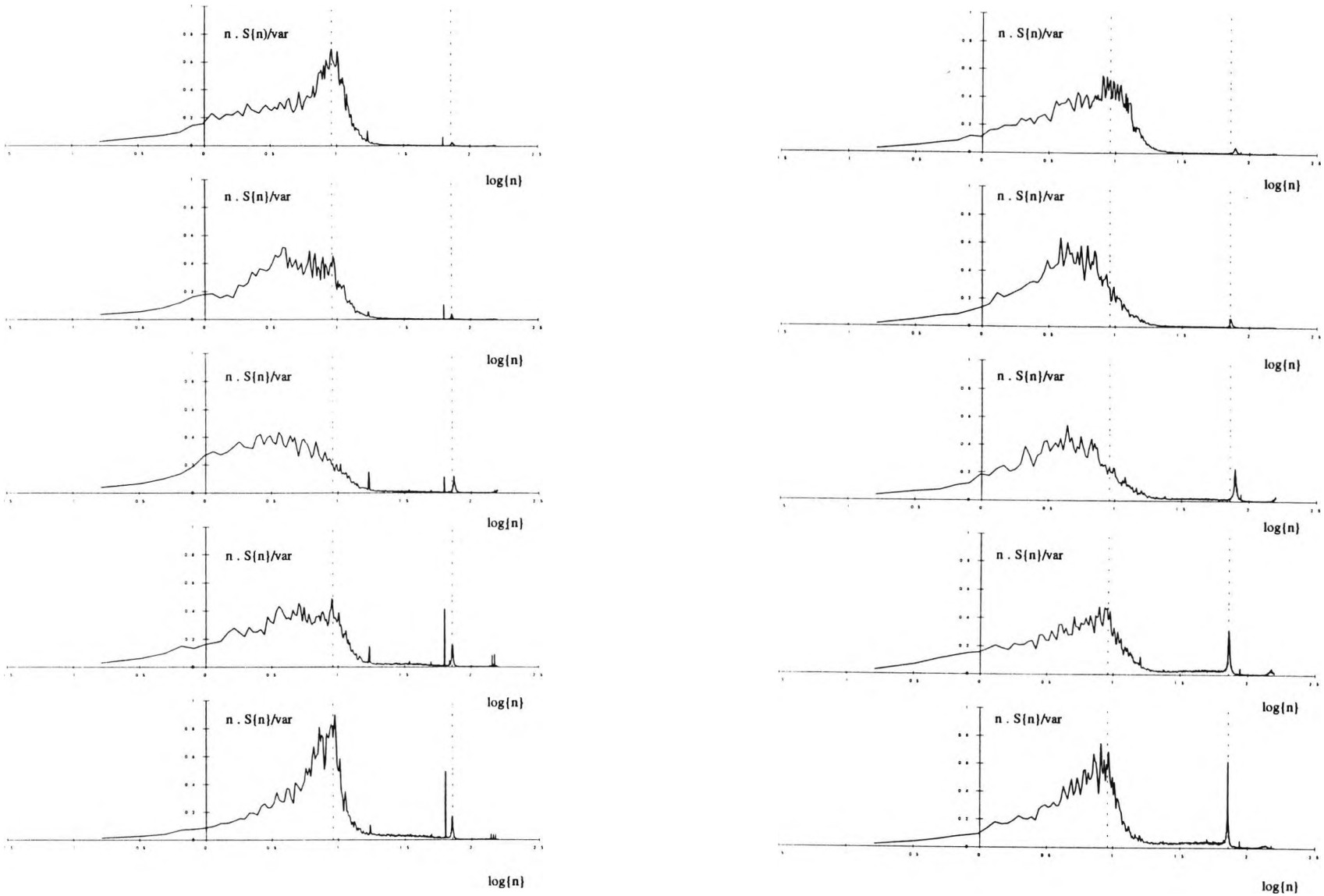

Figure E.4: Membrane deflection spectra for cavity volume C, membrane tension T_d and ϕ= 0° (top) to 180° (bottom); l.h.s. U_{ref}=9.4m/s, r.h.s. U_{ref}=13.0m/s.

The mean roof deflection appeared to be dominated by the magnitude of the cavity pressure, whilst in the frequency domain the response of the membrane was seen to follow that of the cavity pressure fluctuations. Resonance was exhibited at both the Helmholtz frequency and higher frequencies with the former generally being the dominant resonant mode. Trends apparent in the membrane spectra were similar to those reported in the cavity pressure spectra.